Technical University of Denmark

Implementation of Deep Ultraviolet Raman Spectroscopy

Ph. D. Thesis

Chuan Liu

Supervisor:

Rolf W. Berg

December 2011

DTU Chemistry

Department of Chemistry

Implementation of Deep Ultraviolet Raman Spectroscopy

Ph. D. Thesis

Chuan Liu

Supervisor:

Rolf W. Berg

Technical University of Denmark

December 2011

Preface

Fluorescence interference is an important limitation in Raman spectroscopy. This problem can be avoided when the wavelength of the exciting light source is in the range of deep ultraviolet (DUV). DUV Raman spectroscopy expands the application field of Raman scattering technology, especially in catalysis, biological sciences, food and petroleum analysis.

Raman spectroscopy is an optical method that reveals the molecular structure by measuring the inelastic scattering of light. The development of Raman spectrometry has often depended on a serious of newly generated optical techniques. Over the last decade, the laser technology has been developed rapidly. Progress in semiconductor technology has occurred and various ultraviolet solid-state and gas lasers have appeared, and lasers with different properties, such as pulsed or continuous wave, working in single or multi mode have appeared in the commercial market. Different lasers could be suitable only for one particular application. A dedicated spectrometer and special optical components may be required, so in order to implement a DUV Raman system in practice, one has to deal with much optical knowledge.

The work presented in this thesis is the result of a Ph.D.-project carried out during a period of about three years from November 2008 – December 2011 at the Department of Chemistry, Technical University of Denmark. The thesis was written as part of the requirements for obtaining the doctor of philosophy degree. It describes the establishment of a DUV Raman system and briefly a few examples of its application to some kinds of chemical analysis.

Chapter 1 is a short introduction to Raman spectroscopy done with visible as well as ultraviolet light. Chapter 2 is devoted to the introduction of all different types of deep ultraviolet (DUV) lasers and the corresponding optical properties, including a representative overview of the state-of-the-art DUV lasers and possible development of new DUV sources. Chapter 3 aims at the describing and understanding of the detailed function of the DUV spectrometer and some of its associated DUV optical components. Furthermore the thesis reports a chapter 4 describing original work done to make it possible to easily compare the spectral resolution of a DUV Raman spectrometer with that of a similar visible instrument. This part of my work has recently been accepted for publication (after some minor changes) in a well-estimated international journal (Applied Spectroscopy). The developed software needed to do the calculations is included in an appendix. Chapter 5 is devoted to a chemical analysis example: the analysis of gasoline. Chapter 6 is concerned with other applications, including such varied research areas as Sudan I, Melamine, Germanium nanocrystals and Silicon Carbide analysis. Some of these examples are not treated in depth in this thesis because the subjects have been described by us in recently published research papers (see the list on the last page).

Many people have contributed valuable help and support to my work during the last three years. I would like to take the opportunity to express my true gratitude to all of them. First of all, I would like to thank my supervisor Dr. Rolf W. Berg for highly consistent and inspirational guidance. I would also like to acknowledge Dr. Jens. E. T. Andersen for giving me access to his UV-Vis spectrophotometer, Ishaq Khaliqdad for providing the help and excellent mechanical assistance in the workshop, Preben Buchhave for fruitful discussions with respect to the DUV light sources, Haiyan Ou and Yiyu Ou for stimulating discussions and sharing with me the knowledge about Germanium nanocrystals and Silicon Carbides, Dr. Boriana Mihailova for technical assistance during my stay at the Institute of Mineralogy and Petrography, in Hamburg University.

Finally I would like to express my special appreciation to my family, my wife Li Yang and our daughter Amy for their understanding and support through these years.

Chuan Liu

28th of December, 2011, Technical University of Denmark, Kgs. Lyngby

Abstract

The present thesis, “Implementation of Deep Ultraviolet Raman Spectroscopy”, mainly contains two sections. Deep Ultraviolet here is named DUV standing for the wavelength range from 200 to 300 nm. The first section, Chapters 1, 2, 3 and 4, is about the instrumental technology of the DUV Raman system; the second section, Chapters 5 and 6, is devoted to some application examples of the DUV Raman spectroscopy.

Chapter 1 is a brief introduction of Raman spectroscopy in general and its relation to DUV. The DUV Raman spectrometry has many remarkable advantages. The major limitations are the difficulty of the DUV Raman instrumentation, the DUV excitation laser source, DUV optical components, eventual instability of the sample and the non-transparency of ordinary glass containers. With respect to the first limitation, most lasers do not directly emit the DUV lines. The DUV lines can typically be obtained by means of frequency conversions that are implemented by optical nonlinear processes as well as Second Harmonic Generation (SHG) or higher order harmonic generations. Chapter 2 aims at investigating three main type lasers, semiconductor, solid-state and gas lasers, to recognize the different ways to implement the DUV emission. The important optical properties as well as the laser beam quality, line width, emission wavelength, output power and pulsed / CW operation of each kind of laser were discussed to help to choose the best suitable light source. With respect to semiconductor lasers, the most compact DUV laser has been reported to be the use of the waveguide SHG technique with a 266 nm emission wavelength. This deeper wavelength has become possible to be obtained due to recent developments of blue semiconductor lasers. However, at present the probably best commercial laser - at the price – is a DUV laser in which the line is achieved by a highly complex frequency quadrupling device. Such a laser is obtainable as a product from TOPTICA Photonics. With respect to the solid-state laser possibility, we devoted ourselves to distinguish between wavelength tuneable and un-tuneable lasers. With respect to gas lasers, we have focused on introducing two types of lasers: hollow cathode metal ion lasers and Argon ion lasers. The hollow cathode metal ion lasers emit DUV lines directly, however one should consider the poor beam quality and the relatively weak output powers possible and only for particular applications. A frequency-doubled Argon ion laser (95-SHG-QS) manufactured in USA by LEXEL-lasers, Inc. was finally adopted for our project. The basic structure and technological principles of the laser are discussed in detail as these are important requisites to safely understand the physics needed to change among the several lines (257.3, 244.0 and 229.0 nm) possible for a frequency-doubled Argon laser.

Chapter 3 is devoted to establishing a DUV Raman system - made by Renishaw PLC - associated with the adopted DUV laser. The chosen Renishaw InVia Reflex spectrometer was the best spectrometer that could be obtained for the available amount of money. Compared with a traditional Raman system working in the range of visible or near Infrared, the chosen DUV Raman system requires more stringent conditions for the optical components. The various DUV optical components have been described, with particular focus on obtaining high quality of the final measurements. This naturally involves themes such as spectral resolution, sensitivity, elimination of background noise, and so on. Compared to Raman spectra excited with visible light, the DUV excited Raman spectra tend to have a markedly lower spectral resolution. The spectral resolution is an important factor to consider when using the DUV excited Raman spectroscopy. In line with this insight is the fact that we found a way to improve the knowledge on the spectral resolution of the DUV excited spectrum. A new method was invented during the project to determine the spectral resolution of Raman spectrometers by means of principal experimental factors and one equation. This equation is described in detail in chapter 4, and the associated *Mathematica* program is detailed in the appendixes. A manuscript on the same subject has been accepted for *Applied Spectroscopy*.

The DUV Raman system was established so that it is possible to apply several different excitation lines, and even some visible lines can be included. The operating convenience was considered carefully to realize the most user-friendly Raman system. The laser safety was also discussed, because DUV light is a potentially extremely dangerous kind of invisible radiation, and several personnel protection methods have necessarily to be presented.

The fluorescence interference is a persistent problem in Raman spectroscopy. It was met before many times when the wavelengths of excitation lasers are located in the visible range, e.g. for petroleum product analysis. Deep Ultraviolet Raman spectroscopy applied to this research field was claimed to be able to solve the problem. Chapter 5 is devoted to gasoline analysis by the use of the DUV Raman spectroscopy. Firstly, some sampling difficulties (absorption, condensation) are described. We have found a way to solve the problems, and our solution, using a special designed gas gap cell to obtain measurements of extraordinary high quality, are presented. The DUV Raman spectra of gasoline were excited by three different wavelengths, 257.3, 244.0 and 229.0 nm were measured. The results showed that the spectra obtained by use of the 257.3 nm excitation line are useless because of strongly fluorescent interferences; the spectra of the 244.0 nm excitation contained less fluorescent backgrounds and obtainment of clear Raman bands were possible; finally the fluorescent interference was completely eliminated by use of the 229.0 nm excitation line. Obviously, the spectra were different when using the 244.0 and 229 nm excitation lines.

By study of the Raman spectra of Toluene / Pentane mixtures using the 229 nm excitation, it is clear that Toluene dominated spectra of the mixtures because of resonance Raman scattering. By study of the Raman spectra of Toluene / Naphthalene mixtures using the 229 nm excitation, the results showed that Naphthalene has an even stronger resonance. It was concluded that a small content (~0.5%) of Naphthalene was able to mainly dominate the Raman spectra of the gasoline samples. It is virtually unimportant what the rest of the sample consisted of. The most intense characteristic band is located at 1381 cm^{-1}. The Raman spectra of home-made artificial gasoline mixtures - with gradually increasing Naphthalene contents - can be used to determine the concentration of Naphthalene by use of the 229.0 nm excitation. For the Raman spectra of gasoline excited by the 244 nm line, Toluene and Naphthalene have comparable contributions. The intensity of the respective characteristic bands at 1004 cm^{-1} and 1381 cm^{-1} indicate the relative concentrations of the aromatics, Toluene and Naphthalene, in the gasoline.

Chapter 6 shows examples of other applications of DUV Raman spectroscopy, for instance for the illegal red food additive: *Sudan I*. For this dye Raman spectra - useful to indicate an unwanted presence - could not be obtained with green or blue laser line excitation because of fluorescence interferences. Raman spectra of Sudan I - without fluorescence interferences - could be achieved by use of the 244.0 nm excitation. The DUV Raman spectrometry could thus be a potential detection method for Sudan I, as an illegal food colorant. The fluorescence-free DUV Raman spectrometry was further applied to detect another illegal food additive, Melamine, in milk sample. It was shown that the DUV constitutes a more sensitive measurement method than traditional Raman spectrometry and realizes a direct detection in liquid milk. In another research field regarding solid state analysis of Germanium and Silicon Carbide nanocrystals, the application of the DUV excited Raman spectroscopy as a research tool has also been demonstrated and the results are only rather briefly discussed because the results have already been published.

Obviously many more uses can be predicted.

Resumé

Denne afhandling, "Implementation of Deep Ultraviolet Raman spectroscopy", består i hovedsagen af to dele. Deep Ultraviolet – også kaldt DUV – står for bølgelængdeområdet 200 til 300 nm. Første del, kapitlerne 1 til 4, handler om den instrumentelle teknologi i DUV Raman-systemet. Anden del, kapitlerne 5 og 6 fokuserer på nogle få anvendelser af DUV Ramanspektroskopien.

Kapitel 1 giver en kort introduktion til Ramanspektroskopi i almindelighed og DUVs relation hertil. DUV Ramanspektrometrien har mange bemærkelsesværdige fordele. De største begrænsninger ved DUV Raman er sværhedsgraden med hensyn til instrumentering, eventuel ustabilitet af prøverne ved belysningen og den manglende gennemsigtighed af almindelige glasbeholdere. Med hensyn til det første problem: De fleste lasere er ikke direkte i stand til at udsende DUV-lys. Dybt ultraviolet laserlys opnås i mange tilfælde bedst ved hjælp af frekvenskonvertering af andet laserlys. Dette kan typisk ske ved anvendelse af optisk ulineære processer, herunder såkaldt Second Harmonisk Generering (SHG) eller eventuelt højere orden af harmonisk generering. Kapitel 2 tager sigte på at beskrive de tre grundtyper af lasere der kan komme på tale: halvlederlasere, faststoflasere og gaslasere. Formålet har været at fastslå de mest hensigtsmæssige måder at fremskaffe anvendelig DUV emission. Vigtige optiske egenskaber ved laserstråler, så som kvalitet, liniebredde, bølgelængde, udgangseffekt og tidsforløb - pulserende / eller kontinuert (såkaldt CW-emission) - af hver laser-type diskuteres med det formål at vælge den bedst egnede DUV lyskilde til projektet. Med hensyn til halvlederlasere nævnes, at den mest kompakte DUV laser udviklet til dato, bruger den såkaldte waveguide SHG teknik til at opnå 266 nm emission. Den formentlig bedste laser på markedet – prisen taget i betragtning - er et system der frembringer DUV linier ved en meget kompleks frekvens-4-doblings teknik. En sådan laser produceres af TOPTICA Photonics. Med hensyn til faststoflasere, har vi helliget vi os beskrivelse af to typer af lasere, nemlig dels dem hvis bølgelænde er vilkåligt justerbar (tuneable) og dels dem der har faste karakteristiske bølgelængder (diskrete laserlinier). Med hensyn til gaslasere, er hovedvægten lagt på to typer af lasere: hul-katode metal-ion-lasere og argon-ion gas-lasere. Hul-katode metalion lasere er i stand til direkte at udsende DUV-linier, men man bør overveje den dårlige strålekvalitet og den relativt svage intensitet, der begrænser anvendelsen. Det endelige valg til vores projekt – prisen taget i betragtning – faldt på en frekvens-fordoblet argon ion laser (95-SHG-QS) produceret i USA af firmaet LEXEL-lasers, Inc. Den grundlæggende struktur og de teknologiske principper omkring en sådan laser er diskuteret i detaljer, således at de fysiske aspekter ved omskiftning mellem SHG linierne (257.3, 244.0 og 229.0 nm) kan ske sikkert.

Kapitel 3 er afsat til en detaljeret indførelse i, hvordan et DUV Ramansystem - fremstillet og leveret af Renishaw, Plc. - fungerer, under anvendelse af den anskaffede DUV laser. Det valgte Renishaw InVia Reflex spektrometer var det bedste, der kunne opnås for det disponible beløb. Sammenlignet med et traditionelt Ramansystem i det synlige eller nært-infrarøde område stiller det valgte DUV-Ramansystem strengere krav til optikken. De forskellige DUV optiske komponenter er gennemgået med særlig fokus på kvaliteten af de endelige målinger. Dette indebærer naturligvis temaer så som spektralopløsning, følsomhed, eliminering af baggrundsstøj, og så videre. I sammenligning med Ramanspektre ekciteret med synligt lys er der en tendens til, at DUV Ramanspektre fremstår med markant lavere spektralopløsning. Dette vigtige emne er nærmere studeret. I løbet af projektet er der blevet udviklet en ny metode til at fastslå spektralopløsningen af et givet Ramanspektrometer ved hjælp af de vigtigste eksperimentelle parametre og brug af én eneste ligning. Den spektrale opløsning er en vigtig faktor at tage i betragtning ved anvendelse af DUV Raman. I denne forbindelse anføres det faktum, at vi på denne måde har forbedret vores kendskab til den spektrale opløsning i DUV-Ramanspektre, som ellers havde tendens til at være ret begrænset. Detaljerne er beskrevet i kapitel 4 og det tilhørende *Mathematica* computer-program er gengivet i appendixes. En artikel om spektralopløsningen i et Ramanspektrometer er antaget til publicering i *Applied Spectroscopy*.

DUV Ramansystemet er etableret, således at det er muligt at anvende flere forskellige excitationslinier, og endda kan nogle synlige linier også omfattes. Betjeningen er blevet nøje overvejet, så Ramansystemet er blevet så brugervenligt som muligt. Det vigtige punkt omkring lasersikkerheden er ligeledes blevet diskuteret, eftersom DUV lys er en potentielt meget farlig form for usynlig stråling. Flere metoder til personbeskyttelse har nødvendigvis måttet præsenteres.

Indflydelsen fra fluorescens er et vedvarende problem i Raman, f.eks. møder man problemet under analyse af olieprodukter med lasere med excitationsbølgelængder i det synlige område. DUV Ramanspektroskopi anvendt inden for dette felt har været hævdet at kunne løse fluorescensproblemet. Dette undersøges i Kapitel 5, der er helliget emnet "benzinanalyse ved brug af DUV Ramanspektroskopi". I begyndelsen af kapitlet beskrives nogle uforudsete problemer med prøvetilberedelsen (absorption og kondensation) og deres løsning. Vi har fundet en måde at løse problemerne på ved hjælp af en specielt designet celle med et "gasgab". Med denne celle er det lykkedes at gennemføre målinger på benzin af en hidtil ukendt kvalitet. DUV Ramanspektrene af benzin blev forsøgt opnået med de tre forskellige bølgelængder, 257,3, 244,0 og 229,0 nm. Resultaterne viser, at spektre opnået ved brug af 257,3 nm linien er ubrugelige på grund af for stærke interferenser af fluorescens; spektret fra 244,0 nm excitation indeholder en mindre fluorescensbaggrund og tydelige Ramanbånd kan ses. Endelig er interferens fra fluorescens elimineret ret meget ved brug af 229,0 nm excitationslinien. Spektrene er klart forskellige, også når blot 244,0 og 229 nm excitationslinierne bruges.

Ved undersøgelsen af Ramanspektrene af Toluen / Pentan blandinger ved hjælp af 229 nm excitation, er det blevet klarlagt, at toluen dominerer spektrene af alle blandingerne på grund af resonans-Ramanspredning. Ved undersøgelse af Ramanspektrene af Toluen / Naphthalen blandinger ved hjælp af 229 nm excitationen viser resultaterne yderligere, at Naphthalen har en endnu stærkere resonans-Ramanspredning. Det er blevet konkluderet, at et lille indhold (0,5 %) af Naphthalen hovedsageligt dominerer Ramanspektrene af almindelige benzinprøver. Det er sådan set ligegyldigt hvad resten er. Det mest intense karakteristiske band er placeret ved 1381 cm^{-1}. Ramanspektre af hjemmelavede kunstige benzinprøver med gradvist stigende indhold af Naphthalen kan bruges til at bestemme koncentrationen af Naphthalen ved brug af 229,0 nm excitationen. I Ramanspektre af benzin ekciteret af 244 nm-linien, giver Toluen og Naphthalen bidrag der er sammenlignelige. Intensiteten af de respektive karakteristiske bånd ved 1004 cm^{-1} og 1381 cm^{-1} angiver de relative koncentrationer af de aromatiske stoffer Toluen og Naphthalen i benzinen.

Kapitel 6 viser nogle andre eksempler på anvendelser af DUV-Ramanspektroskopien, herunder studiet af ulovlig tilsætning af det røde farvestof *Sudan I* til fødevarer. For dette farvestof kunne anvendelige Ramanspektre ikke opnås med grønt eller blåt laserlys på grund af fluorescens. Derimod kunne Ramanspektre af *Sudan I* opnås uden fluorescens ved brug af 244,0 nm excitation. Dette eksempel viser at DUV Ramanspektrometri således kan benyttes som påvisningsmetode for *Sudan I* som et ulovligt farvestof i mad. Fluorescens-fri DUV Raman-spektrometri blev yderligere anvendt til at detektere et andet ulovligt tilsætningsstof, Melamin, tilsat til prøver af fødevaren mælk. Det er blevet vist, at DUV i dette tilfælde udgør en mere følsom målemetode end traditionel Raman spektrometri og muliggør en direkte påvisning i flydende mælk. I et andet forskningsfelt (inden for solid state science) er det tilsvarende blevet påvist at DUV Ramanspektroskopi kan bidrage til forståelsen af egenskaberne i Germanium og Siliconcarbide nanokrystaller, der anvendes som fotoniske materialer. Disse resultater gennemgås kun ret summarisk fordi resultaterne allerede er publiceret.

Det er klart at man må forudse mange flere fremtidige anvendelser.

Contents

1 Introduction to DUV Raman spectroscopy

1.1 Brief Introduction to Raman Spectroscopy

The *Raman scattering effect* was discovered in 1928 by the Indian physicists Raman and Krishnan [1.1]. Raman scattering may be defined as "instantaneous" inelastic scattering of light (electromagnetic radiation). When a *light quantum* (a kind of particle in the light, called a *photon*) collides with a sample, the *photon* may be scattered, either elastically (called *Rayleigh scattering*) or inelastically (called *Raman scattering*). In the Raman process an amount of energy is exchanged with the sample as shown schematically in the quantum energy level diagram in Fig. 1.1. Accordingly, the outgoing photon has less or more energy than the incoming one (Stokes or anti-Stokes Raman processes). The energy is measured by the frequency ν or the wavenumber ω, according to the relation $E = h\nu = h\,c\,\omega$ (here *h* is Planck's constant and c is the speed of light). A Raman process corresponds to a (fundamental) transition among certain group vibrational states as described in the theory of quantum mechanics (quantum number v changing ± 1). For a peak (a Raman band) to occur in the Raman spectrum with a significant intensity, the molecular bond stretching or angle deformation vibration must cause a change in the so-called "polarizability" of the molecule (the polarizability is the ability of a molecule to become polar when subject to an electric field). The ensemble of light scattering bands constitutes the Raman spectrum. Most often only Stokes-shift Raman spectra are measured and shown; i.e. the scattered photons have lower frequency (energy) than the incident radiation.

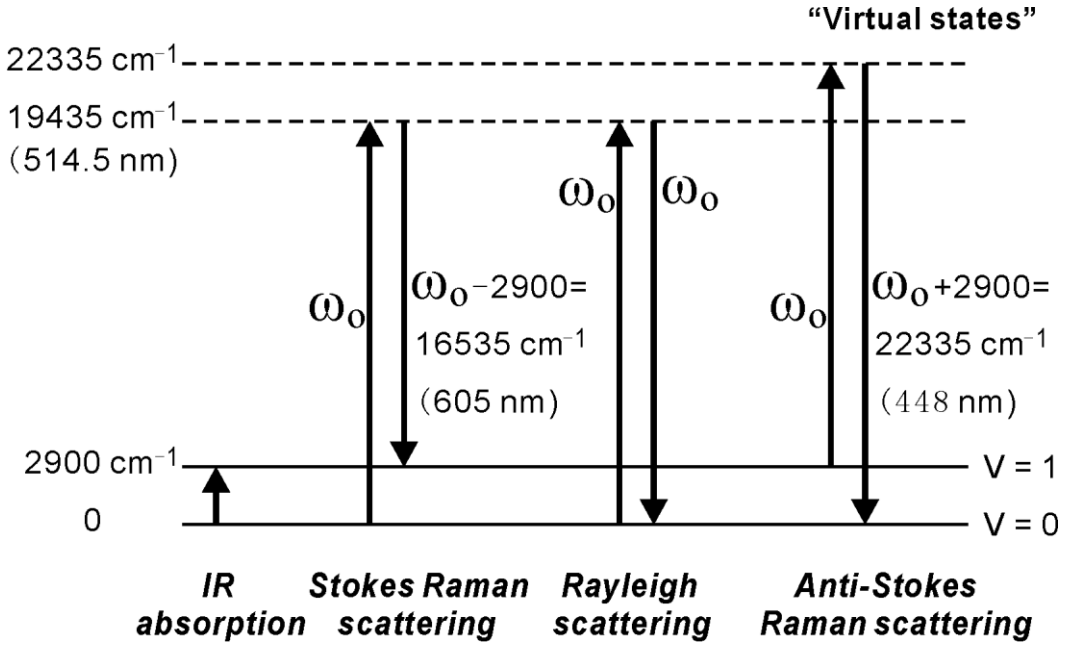

Fig. 1.1: The relationships between infrared absorption, Rayleigh and Raman scattering; see the below text for details. The energy levels of the states are exemplified for a green laser and for a vibration occurring at a wavenumber of 2900 (cm^{-1}). ω_o is the wavenumber of the exciting photons.

During an *infrared (IR) absorption* process, a photon of IR radiation is absorbed. The molecular system most often undergoes a transition from the ground state (quantum number v = 0) to an excited state (v = 1). In

the case shown it may correspond to e.g. a bond stretching in a CH_3 group and a fundamental wavenumber shift of ca. 2900 cm^{-1}. In contrast to this IR absorption, during *Rayleigh* and *Raman* scattering typically an exciting photon of much higher energy (visible light) hits the molecular system and raises it to a virtual state, from where it "immediately" falls back. There are two possibilities, as illustrated in Fig. 1.1 with green Ar^+ light of 514.5 nm wavelength, corresponding to a wavenumber of 19435 cm^{-1}. In the so-called *Stokes Raman scattering* (not so likely), the system falls back to the v = 1 state (emitting a 16535 cm^{-1} photon). In *Rayleigh scattering* (more likely) it falls back to the v = 0 ground state (emitting light at ~19435 cm^{-1}), producing the so-called Rayleigh wing. If the system is starting from the v = 1 state (not so likely at room temperature because of the Boltzmann distribution), a similar *Rayleigh* transition can happen. But now also a so-called *anti-Stokes Raman* process is possible, producing photons at 22335 cm^{-1}. Most Raman spectroscopy studies report data corresponding to *Stokes* Raman transitions. Samples or impurities therein having energy states near the ones labelled "virtual" in Fig. 1.1 (at e.g. ~20000 cm^{-1}) may absorb photons from the incident light and later re-emit the light as a broad intensive background. This is the phenomenon called *fluorescence*.

Dramatic improvements in instrumentation (lasers, detectors, optics, computers, etc.) during recent years have raised the Raman spectroscopy technique to a level where it can be used for "species specific'' quantitative chemical analysis. Although the Raman technique many times is not as sensitive as e.g. infrared absorption, the Raman technique has the advantage that it can measure samples directly without touching or any sample preparation. Furthermore, by use of polarized light techniques, one can derive molecular information that cannot be obtained from infrared spectra [1.2].

Raman and Infrared techniques are closely interrelated in that they both depend on vibrational transitions in sample molecules. The spectral bands arise from characteristic *"group"* motions in the molecules present in the sample. One may say that the vibrational bands in the spectra give rise to a "fingerprint" of the molecules. As an example, bands occurring near 2950 cm^{-1} often arise from transitions for aliphatic C-H stretching vibrations (although sometimes perturbed by "Fermi-resonance" with overtones and other nonfundamental transitions). So-called empirical group frequency charts are available, specifying the "fingerprint" bands. These charts may be used to identify pure materials or to judge the presence of a particular component in a mixture [1.3], [1.4].

Although similar transitional energy ranges occur in IR and Raman spectroscopy, the selection rules that govern the intensities in Raman scattering and IR absorption spectra are not identical. Hence both types of spectra are of value when one wants to characterise a substance: A necessary requirement for a molecular motion (such as a vibration, rotation, rotation/ vibration, or lattice normal mode) to be measurable in IR spectra is that an oscillating dipole moment must be produced during the motion. In Raman the motion within the molecular system should produce a variation in the polarizability. Combinations, differences or overtones of these transitions may occur, but such transitions normally only occur with weak intensities. The selection rules of the transitions are described in great details in famous quantum mechanics and group theory texts [1.5], [1.6].

1.2 Introduction to DUV Raman Spectroscopy and Instrumentation.

Applications of Raman spectroscopy have been limited by the presence of fluorescence originating from the samples. One common way to eliminate the fluorescence is to use less-energetic near-IR lasers as the excitation source because the near-IR photon is too weak to excite most molecules into the first excited electronic state. Since the standard CCDs are not sensitive for near-IR detection, a common way to do near-IR Raman spectroscopy is to detect the spectrum by the Fourier-transformation principle. Such FT-Raman instruments have a single energy sensing detector and involve a Michelson interferometer [1.7].

The fluorescence interference can also be addressed in the opposite way, i.e. by shifting the excitation source to the high-energetic deep ultraviolet (DUV) range. It was examined in a pioneering paper in 1984 by S. A. Asher's group [1.8]. It was discovered that the fluorescence usually prevailed in Raman spectra, if excitation was done in the wavelength range from 300 to 700 nm, or longer. A cut-off wavelength was found to exist, at the short wavelength side in the UV region. Therefore the Raman signals and the fluorescence spectrum could be separated, resulting in the fluorescence interference being greatly diminished. The tick was to choose an excitation wavelength so short, that the excited Raman signals also occur at wavelengths shorter than the fluorescence spectrum.

There are further advantages of using UV excitation. One of these is that the Raman signal intensity is much enhanced because the signals are proportional to the fourth power of the light frequency [1.9]. Another important advantage of using DUV light sources in Raman spectroscopy is the possibility of a significant improvement of the signal strengths by means of resonance enhancements. The resonance enhancement is realized in situations when the energy of the excitation photon energy is close to an electronic transition between two states. These situations are often realized when an absorption band exists in the absorption spectrum. In the situation of resonance enhancement, certain Raman band intensities can be increased dramatically. A resonance-enhanced signal can be several orders of magnitude more intense than the normal Raman signal [1.10], [1.11].

Because of the above advantages DUV Raman spectroscopy has a great potential to expand the application field and value of the Raman scattering technology, especially in catalysis, biological sciences, art items, food and petroleum analyses. However, DUV Raman technology at present still has not been widely popularized. The major limitation to the widespread use of DUV Raman is the high cost of the instrumentation, especially the laser sources, as motioned by the Asher group in 2002 [1.12], and the DUV laser systems are inconvenient for the operator. Over the last ten years, the laser technology has evolved rapidly, especially with respect to the semiconductor lasers. It is worth to consider if one could adopt a semiconductor laser as the DUV Raman excitation source. Other types of lasers, such as fiber lasers and solid-state bulk lasers have also been evolved into compact, long lifetime, reliable and low power consuming lasers due to the developed semiconductor provided a good optical pumping for these lasers. Most semiconductor and solid-state based DUV lasers are still of high cost. DUV lasers for our present project seemed to be the gas DUV lasers: HeAg or NeCu hollow-cathode lasers (made by Photon Systems Inc. and sold by the Laser2000 company) and the Argon-ion gas laser.

In Chapter 2, the state-of-the-art laser technology to achieve DUV radiation is represented in detail, including some kind of lasers that have not been reported of use for DUV Raman application. We propose a highly compact setup to obtain useful DUV laser light. The suggested system is a diode laser combined with a nonlinear crystal waveguide, which could be an excitation source for a future portable type of DUV Raman instrument. We also provide an evaluation method for any suggested laser update in order to implement a new DUV laser in an existing laboratory. A newly developed laser designed software, *Intarsia* software package, was used to study the laser beam properties and laser cavity structure.

Other parts of the instrumentation than the light source of the DUV Raman system have also evolved rapidly in recent decades. However, according to the recent literature, DUV-specifications promised by manufacturers should not always be trusted.

An example that we have experienced personally is that the InVia Reflex spectrometer system was stated by the Renishaw manufacturer to have a ~1 cm^{-1} spectral resolution on their website, but actually it is, by our investigation, impossible to reach this number in the DUV range of their spectrometer. Another example that we have experienced was that a TriVista TR 557 A&S UV spectrometer failed to achieve Raman spectra by use of hollow-cathode lasers as the excitation light source. We are not sure why this could not be done, but surely it is essential to discuss (in Chapter 3) all optical elements such as gratings, mirrors, filters etc. It is not an easy job to adopt suitable optical elements for the DUV Raman system. It is essential to optimize the working condition because the *DUV Raman system to function must have very stringent conditions for the optical components. A major reason for this is that the output power levels of the DUV lasers are rather week.*

References to Chapter 1

[1.1] Raman, C. V. and Krishnan, K. S., "*A new Type of Secondary Radiation*", Nature, 121, (**1928**), pp. 501.

[1.2] Smith, E. and Dent, G. "*Modern Raman Spectroscopy - A practical Approach*", J. Wiley & Sons, Ltd., ISBN 0-471-49668-5, (**2005**), pp. 1-210.

[1.3] Nyquist, R. A., Kagel, R. O., Putzig, C. L, Leugers, M. A., "*Handbook of Infrared and Raman Spectra of Inorganic Compounds and Organic Salts*" (4 vols.), Academic Press, New York and London, **1996**.

[1.4] Socrates, G, "*Infrared and Raman Characteristic Group Frequencies, Tables and Charts*", 3rd ed., J. Wiley & Sons, Chichester UK, (**2001**), pp. 1-249.

[1.5] Carter, R. L. "*Molecular Symmetry and Group Theory*", John Wiley & Sons, New York, **1998**.

[1.6] Atkins, P. W. and Friedman, R. S., "*Molecular Quantum Mechanics*", 4th edition, Oxford University Press, ISBN: 13978-0-19-927498-7, (**2004**), pp. 1-608.

[1.7] P.R. Griffiths. *Introduction to Vibrational Spectroscopy*. In "*Handbook of Vibrational Spectroscopy*" eds J. M. Chalmers and P. R. Griffiths, Wiley, USA, first edition, (**2001**). Vol. 1, pp. 33-43.

[1.8] S. A. Asher and C. R. Johnson, "*Raman spectroscopy of a coal liquid shows that fluorescence interference is minimized with ultraviolet excitation*", Science, Vol. 225, (**1984**), pp. 311–313.

[1.9] P. R. Griffiths, *Introduction to Vibrational Spectroscopy*, in "*Handbook of Vibrational Spectroscopy*", eds. J. M. Chalmers and P.R. Griffiths, Wiley, USA, 1st edition, Vol. 1, (**2001**), pp. 33-43.

[1.10] Spiro, T. G., "*Resonance Raman Spectroscopy. New Structure Probe for Biological Chromophores*", *Acc. Chem. Res.* (**1974**), *7*, pp. 339–344.

[1.11] E. Smith and G. Dent. "*Modern Raman Spectroscopy - A Practical Approach*". Wiley, England, first edition, (**2005**). Chapter 4.

[1.12] S. A. Asher, *Ultraviolet Raman Spectrometry*, in "*Handbook of Vibrational Spectroscopy*", eds. J. M. Chalmers and P.R. Griffiths, John Wiley & Sons Ltd., Chichester, **2002**.

2 Deep Ultraviolet (DUV) Light Sources

The development of Raman spectroscopy has been benefiting much from laser technology. Since the first working laser was invented in 1960 [2.1], laser technology and Raman spectroscopy have been improving rapidly. Today, for Raman applications, various types of lasers are used. They can mainly be classified in three categories: gas lasers, solid-state lasers, and semiconductor lasers. However, not all wavelength regions of interest are directly accessible with these simple lasers, especially in the range of UV. Most common laser lines are located in the range of visible and infrared. Only few types of gas lasers have the direct DUV emission lines. Other ways of getting lasers emitting the DUV lines are obtained by means of frequency conversions that are implemented by optical nonlinear processes, such as Second Harmonic Generation (SHG), Sum Frequency Generation (SFG), Third Harmonic Generation, 4th Harmonic Generation and even 5th Harmonic Generation.

Table 2.1 shows the direct emission lines for some typical lasers. With regard to direct DUV laser sources, there are two types of gas lasers, Excimer lasers and Hollow Cathode ion lasers. Excimer lasers are based on noble gas halide (eximers, like KrF) molecules that may exhibit several DUV lines. However, Excimer lasers do not suit for Raman spectroscopy application because of the poor coherence of the lasing process, i.e. poor laser beam quality and broad line-width. Hollow cathode ion lasers have been applied for Raman spectroscopy [2.8], [2.9]. There are two typical types of hollow cathode ion lasers that have been commercialized, HeAg and NeCu, emitting at 224.3 nm and 248 nm, respectively. Hollow cathode lasers are pulsed lasers, and their average power are emitting relatively weekly (< 1mW). They can probably just be adopted for particular setups.

Other more useful kind of lasers for DUV generation are the frequency converted DUV laser sources. They are based on optical nonlinear processes and are implemented by propagating light through a nonlinear crystal. A requirement for the nonlinear effect to function is that they demand that the fundamental pumping laser has certain qualities such as a high power density. There are four main kinds of methods to achieve a high power density pumping laser: the use of *pulsed*, *external power-enhancement cavity* [2.10], *intra-cavity* [2.11] and *nonlinear crystal waveguide* [2.12] techniques. Pulsed lasers are normally implemented by a *Q-switch* or *mode-locking* technology [2.13]. *External power-enhancement cavity* and *intra-cavity* are suitable for Continuous-Wave (CW) laser frequency conversion. *Nonlinear crystal waveguide* is a newly rising technology, suitable for both pulsed and CW lasers; combined with a fundamental diode laser, it is the most convenient way to achieve a compact DUV laser device.

As mentioned above, there are many combinations and various methods to obtain fundamental frequency conversion. Therefore, property of each of the various DUV lasers should be considered for choosing the most suitable and cheapest DUV laser source. In the following section, the discussion will be mainly around three properties, i.e. power level, laser line width and beam quality.

Some DUV laser light may be achieved just by upgrading already existing lasers in our or other laboratories with frequency doubling. Frequency doubling attachments can be achieved commercially from e.g. Spectra Physics, Inc. Such a device is actually an external power-enhancement cavity equipped with a second harmonics generation (SHG) crystal. It normally requires – to obtain a useful amount of intensity of DUV

light - that the fundamental laser operates in the single-frequency longitudinal and TEM_{00} mode [2.13]. Also the power level of the fundamental laser should exceed a certain level below which no useful amount of DUV intensity is emitted. Some of above mentioned DUV lasers are still under development, such as the techniques of nonlinear crystal waveguiding. In order to examine if we should choose to buy a suitable new commercial DUV laser, or try to modify/upgrade an already existing argon-laser in our laboratory, most possible DUV laser sources and the responding optical properties will be discussed in the following section. The discussion will also give a view of the useful future DUV laser sources.

As an interesting note, we mention that Light Emitting Diodes (LED) emitting in the DUV range are already commercial available (e.g. from Sensor Electronic Technology, Inc.), and a wavelength as deep as 222 nm has been reported [2.14]. These light sources may be used in a similar way like Deuterium Lamps, but the LED is a low coherent light source. Also because of the small emission area, it is possible to use such a LED DUV light source for Raman spectroscopy applications when the monochromator is equipped with a narrow line width filter.

Another interesting way to achieve the DUV laser light is by use of a so-called Raman shifter. The mechanics of Raman shifting is based on Simulated Raman Scattering. Stimulated Raman Scattering occurs in most of substances when a high intensity laser beam passes through the medium [2.56]. As the excitation medium, a tube with Hydrogen gas at a high pressure (> 10 atm) is often adopted (a so-called H_2 shifter) because of the large shifting distance, 4155 cm^{-1}, that Hydrogen can give and because of the low self-focusing effect which affects directly the beam quality and the conversion efficiency [2.56]. Since the power of the stimulated Stokes (or anti-Stokes) wave is exponentially proportional to the incident power density and the propagation distance during *steady-state* operation [2.57], pulsed lasers with high peak power [2.48], [2.58] are normally required as an excitation laser for a single-pass H_2 shifter.

Table 2.1: Typical emission lines from lasers and other light sources. [2.2]-[2.7].

	Light source types	**Emission wavelength (nm)**
Gas lasers	Helium neon (He-Ne) laser	632.8
	Argon-ion laser	351.1 , 363.8, 454.6, 457.9, 465.8, 476.5, 488.0, 496.5, 501.7, 514.5, 528.7, 1092.3
	Nitrogen laser	337.1
	Hollow Cathode ion lasers	(HeAg) 224.3, (NeCu) 248
	Excimer lasers	(F_2) 157, (ArF) 193, (KrCl) 222, (KrF) 248, (XeCl) 308, (XeF) 351
Solid-state lasers	Nd:YVO_4 lasers	1064, 914
	Nd:YAG lasers	1064, 946
	Nd:YLF lasers	1053, 1047
	Ce:LiSAF lasers	280-316
	Ti:sapphire lasers	650 - 1100
	Yb:YAG laser	1020-1050
Semiconductor lasers	Diode lasers	336-2680
LED	AlGaN LED	222-282

2.1 General discussion of lasers

2.1.1 Laser line widths and longitudinal modes

The term "line width" of the exciting light source implicates the *Full width at half maximum* (FWHM) of the laser output spectrum. It distinguishes the single-longitudinal mode (also called the single frequency) from the multi-longitudinal mode. In order to understand the laser output spectrum, we have to start with the basic principles of the laser.

The simplest structure of a laser is shown as Fig. 2.1 (A). In general a laser consists of a gain medium inside a highly reflective optical cavity (an optical resonator). The gain medium is a material with properties that allow it to amplify light by stimulated emission. The cavity consists of two mirrors arranged such that light bounces back and forth, each time passing through the gain medium. Typically one of the two mirrors is partially transparent. The output laser beam is emitted through this mirror. In an optical cavity, only the frequencies of light satisfying the *resonance condition* [2.15] can be oscillating. As shown in Fig. 2.1 (B), these discrete frequencies are so-called longitudinal modes of laser resonance. The gain medium has a gain band or response function. It turns out that the profile of the laser output spectrum has a shape as shown in Fig. 2.1 (C). Normally, there are several longitudinal modes included in the laser output spectrum, so it is a multi-longitudinal mode laser. The laser output spectrum must be considered carefully, depending on the resolution if not single mode. The line width of a multi-longitudinal mode laser must be defined by the FWHM of the envelope curve of the laser output spectrum. Most lasers are multi-longitudinal mode lasers, such as Ar-ion lasers, with mode separation of about 0.33 cm^{-1} and an overall line width containing about 60 longitudinal modes, analogously to what was shown in Fig. 2.1 (D).

Various laser media have different laser gain bandwidths, therefore the FWHMs of laser output spectra are different. It should be noted that the FWHM of the laser output spectrum is not same as the FWHM of laser gain band because there are many factors that have not been considered in the schematic diagram in Fig. 2.1, such as optical losses, modes competitions and so on.

Some kinds of laser media have very broad laser gain bandwidths. Consequently, the output wavelength of the laser becomes widely tuneable, such as for the Ti: Sapphire laser and the dye laser. Thus Ti: Sapphire lasers allow tuning over hundreds of nanometers, from ~650 nm to ~1100 nm. Most solid state diode lasers can be tuned over a few nanometers just by changing the temperature.

For high resolution Raman applications, a narrow line width or a single-longitudinal mode laser is required. It is so because the laser output spectrum has a convolution effect on the Raman spectrum measurements. In other words, the Raman band can be broadened by the line width of the laser source. Such effects must therefore be taken into consideration to improve the spectral resolution. Use of an external enhancement SHG cavity provides a method to achieve DUV laser light (200 nm – 300 nm) from a suitable visible light source (400 nm – 600 nm). It requires however that the fundamental wave has enough narrow line width to oscillate and enhance the fundamental wave in the external-cavity. But also the solution features should be considered. This will be discussed in the following section.

In order to achieve the single longitudinal mode operation, one must consider implementing different methods depending on the various lasers. For Argon-ion lasers the common method is to insert an etalon in to the laser cavity. The principle of these methods can be considered to induce an optical loss factor to limit the laser oscillation in the different longitudinal modes. *An Etalon* is actually a small optical resonator that provides a comb-like loss in the laser cavity to select one particular longitudinal mode, as shown in Fig. 2.1 (F). For diode lasers, the single mode operation can be implemented by use of so called *Distributed-feedback* (DFB) diode lasers or *Grating-feedback External-cavity* diode lasers. As shown in Fig. 2.1 (E), the grating provides a loss window to select a particular longitudinal mode.

For deuterium lamps and DUV LEDs the line widths are depending on the spectral resolution (line width) of the output monochromators which are adapted as an integral part of the light source [2.16].

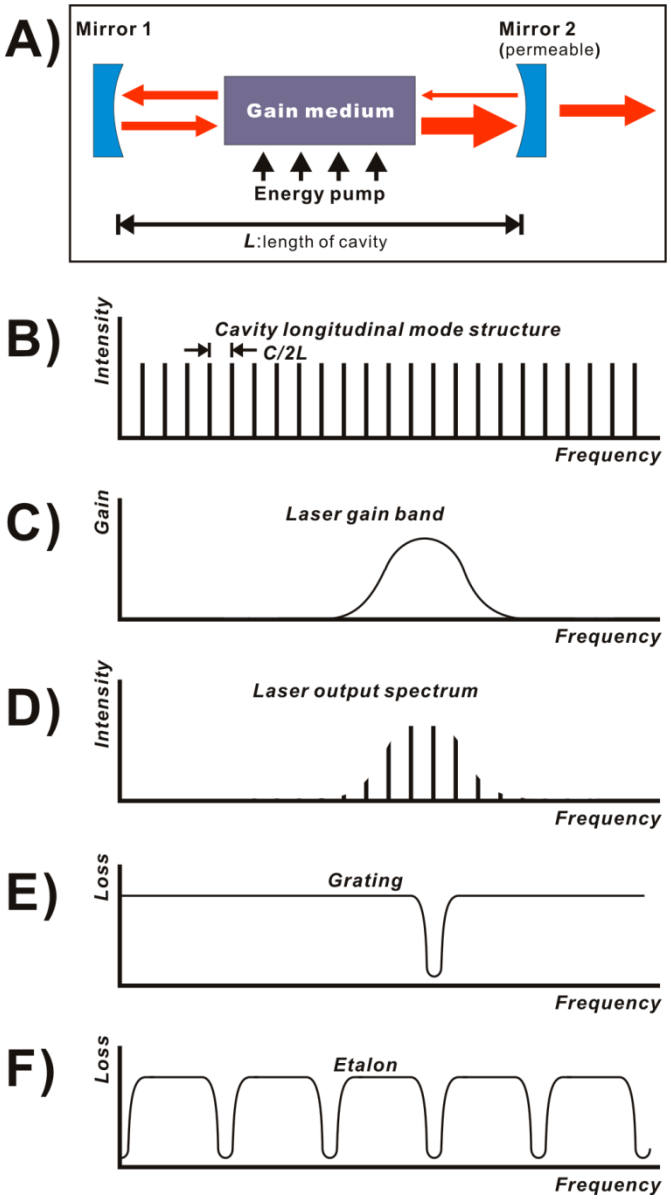

Fig. 2.1: (A) Simplest structure of laser; (B) Laser cavity longitudinal mode structure. The frequency separation of longitudinal modes depends on the length L of the laser cavity by c/*L,* where *c* is

the light speed. (C) The laser active medium has a certain gain band structure. (D) The laser output spectrum mainly depends on the laser gain band of the active medium and the optical loss factor in the laser cavity. (E) The induced loss structure of the grating results in a frequency selection window. (F) The induced loss of an etalon has a comb-like structure.

2.1.2 Laser beam quality and Transverse modes

In addition to the longitudinal modes lasing structure, lasers also exhibit transverse laser modes that determine the intensity distributions in the cross-section of the beam and the wave front of the beam. The laser beams are normally generated from a laser cavity or a waveguide (e.g. a fiber). Light may be considered as an electromagnetic field. The physical meaning of the existence of transverse modes is that the cavity or the waveguide can allow a series of laser beams - oscillating in the cavity or propagating in the waveguide - with a stable intensity (the cross-section) and phase (wave front) distribution. With the energy pump activated, such laser beams will be amplified and emitted. In mathematical terms, the modes refer the specific solutions of the wave equation that satisfy the appropriate boundary conditions of the cavity or the waveguide.

In a laser with cylindrical cavity symmetry, such as most gas lasers, the transverse mode patterns are described by a combination of a Gaussian profile with a Laguerre polynomial [2.13]. The modes are denoted TEM_{pl} (Transverse ElectroMagnetic mode) where p and l are integers labelling the radial and angular mode orders, respectively. Cylindrical transverse mode patterns TEM_{pl} are shown in Fig. 2.2 (a). With $p = l = 0$, the TEM_{00} mode is the lowest order, or fundamental transverse mode of the laser resonator and has the same form as a Gaussian beam.

In a laser with rectangular cavity symmetry, such as most of solid-state lasers, the transverse mode patterns are described by a combination of a Gaussian beam profile with one or more Hermite polynomials [2.13]. These modes are designated TEM_{mn} with m and n being the horizontal and vertical orders of the pattern. Rectangular transverse mode patterns TEM_{mn} are shown in Fig. 2.2 (b). With $m = n = 0$, one has the TEM_{00} mode of the lowest order that corresponds to exactly the same fundamental mode as in the cylindrical cavity geometry. The single mode operation normally is implemented by inserting a pinhole into the cavity or reducing the cross-section area of energy pumping, because the high order modes have a bigger size of the beam.

For optical waveguide laser systems, one distinguishes multi-mode waveguides from single-mode waveguides. A single-mode waveguide only allows the fundamental mode to propagate in the appropriate range of wavelengths. The number of possible modes depends of the cross-section refractive index distribution and the cross-section dimension of the core. For a single-mode waveguide the cross-section dimension of the core can be from a few micrometers to decades of micrometers. The transverse modes of a single-mode waveguide, for example of a step-index fiber, contain only the lowest-order mode (LP_{01}, Linear Polarization modes). The intensity profile of the LP_{01} mode is similar to that of a Gaussian beam, and it may reasonably well be approximated as the TEM_{00} mode [2.17].

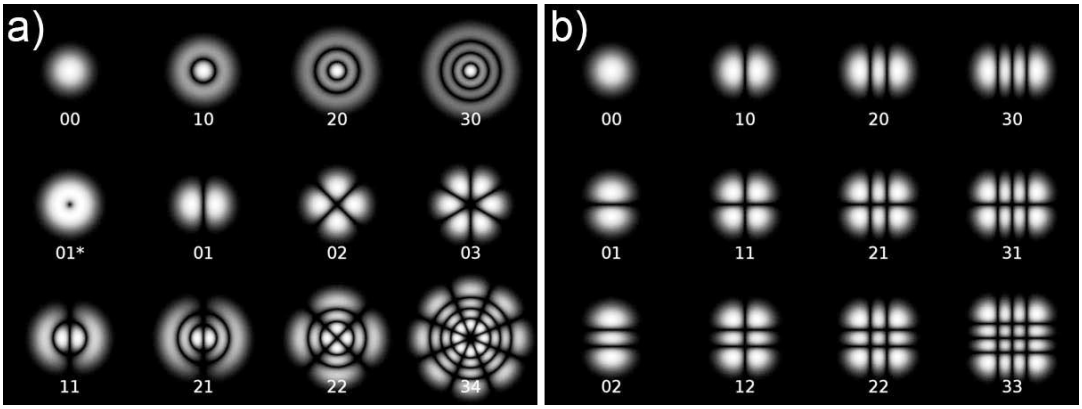

Fig. 2.2: (a) Cylindrical transverse mode patterns TEM_{pl}. (b) Rectangular transverse mode patterns TEM_{mn}.

The laser *Beam Quality factor* (M^2, also called the laser *beam propagation factor*) is a parameter that indicates how close a laser beam is to being running in the TEM_{00} single mode, as well as an indicator to show how small a laser can be focused. For the best beam quality, $M^2 = 1$, it means that such a laser beam contains only the TEM_{00} mode, also called a Gaussian beam. The closer to 1 the value of M^2 is, the better is the beam quality. For a practical laser beam, the beam quality factor, M^2, must be bigger than 1, because a practical laser beam always contains more or less of the high order modes. Also it must be affected by aberrations of the optical components, diffractions of aperture, *spatial wall-off* and so on. The phenomenon of *spatial wall-off* appears at the frequency conversion process as well as SHG, and this phenomenon has a dominating effect on the beam quality of frequency converted lasers.

Sometimes, laser beams are not described by the value of M^2, but instead by the beam divergence angle and the beam diameter. Therefore, in order to recognize the description of a laser beam, it is necessary to know the propagating behavior of a Gaussian beam and the definition of M^2.

A Gaussian beam propagating in free space retains its Gaussian profile; it remains Gaussian. For a monochromatic Gaussian beam, propagating in the *z* direction with the wavelength λ, the transverse profile of the optical intensity of the beam expressed by means of the power *P* can be described as [2.13]:

$$I(r,z) = \frac{2P}{\pi w(z)^2} exp\left(-\frac{2r^2}{w(z)^2}\right) \qquad \text{------ (2.1)}$$

$$w(z) = w_0\sqrt{1+\left(\frac{z\lambda}{\pi w_0^2}\right)^2} \qquad \text{------ (2.2)}$$

Here the beam radius $w(z)$ is the distance from the beam axis to a point where the intensity has dropped to $1/e^2$ (≈ 13.5%) of the maximum value, w_0 is the radius of the laser beam waist (as shown in Fig. 2.3). As we can see from Equation (2.1), when the wavelength λ is given, the beam radius $w(z)$ along the propagating direction *z* are totally defined by the value of the laser beam waist w_0. In Fig. 2.3, the blue curve shows the variation of the beam radius $w(z)$ along the beam propagating direction *z*.

The divergence half-angle Θ can be found by letting $z \to \infty$:

$$\theta = \lim_{z\to\infty}\frac{w(z)}{z} = \lim_{z\to\infty}\frac{w_0\sqrt{1+\left(\frac{z\lambda}{\pi w_0^2}\right)^2}}{z} = \frac{w_0\sqrt{\left(\frac{z\lambda}{\pi w_0^2}\right)^2}}{z} = \frac{\lambda}{\pi w_0} \qquad \text{------ (2.3)}$$

Therefore, for an ideal Gaussian beam

$$\frac{\theta\pi w_0}{\lambda} = 1 \qquad \text{------ (2.4)}$$

For a practical Gaussian beam the value of M^2 can be found by measuring the divergence half-angle and the beam radius. They are denoted as Θ' and w_o' respectively (dashes are added because of the nonideality). Then the value of M^2 is given by

$$M^2 = \frac{\theta' \pi w_0'}{\lambda} \qquad \text{------ (2.5)}$$

However, Equation (2.5) is not the definition description of M^2 because the practical value of Θ' and w_o' can only be measured at a place where the intensity has dropped to $1/e^2$ (≈ 13.5%) of the maximum value which is only a precise measuring method for an ideal Gaussian beam. Therefore, for an arbitrary beam (a practical more or less Gaussian beam) we need a well defined definition of the beam radius. Such a definition is the so called *second moment width* [2.18].

Since the measurement of a second moment width is sensitive for background subtraction on the detector, it requires a specific standard for the measuring method, and such a standard is the ISO standard 11146 [2.18].

Here, we are not going to describe the ISO standard 11146 in detail. However, Equation (2.5) may still provide a rough method to estimate the beam quality parameter M^2.

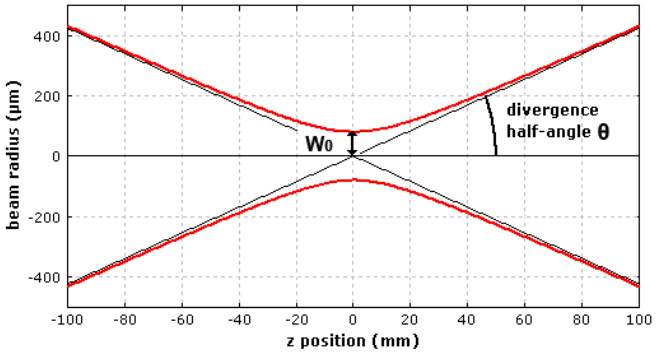

Fig. 2.3: The red curve shows the variation of the beam radius $w(z)$ along the beam propagating direction z for an example beam with waist radius w_0 = 80 μm and λ = 1064 nm. The half-angle divergence Θ of a Gaussian laser beam is defined via the asymptotic variation of the beam radius (red curves) along the beam direction.

2.1.3 Generating UV light by Photon Mixing Frequency Conversion

Instead of directly generating the UV light by a direct physical process, as mentioned previously one may generate UV photons from other photons. Such a process may be called Frequency conversion. The conversion is implemented by one or more nonlinear optical processes in a nonlinear medium, normally an optical nonlinear crystal.

Light can be regarded as electromagnetic waves. When an electric field $\boldsymbol{E}$ (a vector) is applied to a dielectric medium, a separation of bound charges is induced, resulting in a collection of induced dipole moments. The dipole moment is the product of the net separated charge times the distance in units of Debye. The electric polarization $\boldsymbol{\mathcal{P}}$ (a vector) is defined as the net average dipole moment per unit volume. The relation between $\boldsymbol{\mathcal{P}}$ and $\boldsymbol{E}$ is approximately linear for small $\boldsymbol{\mathcal{P}}$. It becomes nonlinear when $\boldsymbol{E}$ acquires a value comparable with the interatomic electric fields (typically on the order of 10^5 to 10^8 V/m). Under these circumstances, it is customary to write $\boldsymbol{\mathcal{P}}$ in the form:

$$\boldsymbol{\mathcal{P}} = \boldsymbol{\mathcal{P}}_L + \boldsymbol{\mathcal{P}}_{NL} \qquad \text{------ (2.6)}$$

where $\boldsymbol{\mathcal{P}}_L$ is the linear polarization and $\boldsymbol{\mathcal{P}}_{NL}$ is the nonlinear polarization. They are given by

$$\boldsymbol{\mathcal{P}}_L = \varepsilon_0 \chi^{(1)} \boldsymbol{E} \qquad \text{------ (2.7)}$$

$$\boldsymbol{\mathcal{P}}_{NL} = \varepsilon_0 \left(\chi^{(2)} \boldsymbol{EE} + \chi^{(3)} \boldsymbol{EEE} + \cdots\cdots \right) \qquad \text{------ (2.8)}$$

where ε_0 is the vacuum permittivity of free space and $\chi^{(1)}$ is the linear response tensor. $\chi^{(2)}$ and $\chi^{(3)}$ are the second and third order nonlinear susceptibility response tensors. Since $\boldsymbol{EE}$ and $\boldsymbol{EEE}$ can be considered as six and ten dimensional vectors respectively, $\chi^{(1)}$, $\chi^{(2)}$ and $\chi^{(3)}$ are 3x3, 3x6 and 3x10 tensors respectively. $\chi^{(2)}$ governs the processes of *Second Harmonic Generation* (SHG) and *Sum frequency generation* (SFG). For *Frequency Tripling*, in principle, this can be achieved with a $\chi^{(3)}$ nonlinearity for direct *third-harmonic generation* [2.19], [2.20], but this is difficult due to the small size of the $\chi^{(3)}$ nonlinearity of optical media and because of so called phase-matching constraints. Therefore, frequency tripling (if wanted) is usually realized as a cascaded process, beginning with frequency doubling (FD) of an input beam and subsequent sum frequency generation of both waves, with both processes being based on nonlinear crystal materials with a $\chi^{(2)}$ nonlinearity. For *Frequency Quadrupling*, this can be accomplished by two sequential frequency doublings or a frequency tripling followed by a SFG with the fundamental wave. Similarly, Frequency Quintupling is accomplished by frequency quadrupling followed by a SFG process with the fundamental wave. Therefore, Frequency Quadrupling and Frequency Quintupling are also based on the $\chi^{(2)}$ nonlinearity.

For the second order $\chi^{(2)}$ nonlinearity, the optical parametric processes are involving three interacting beams, two incoming and one outgoing ones. SHG is the degenerate case of SFG where the two fundamental waves are having the same frequency.

In all these generation processes, both energy and momentum of the involved photons need to be conserved. The energy conservation condition can be written as:

$\nu_1 + \nu_2 = \nu_3$ (For SFG process)

$2\nu_1 = \nu_3$ (For SHG process)

where ν_1, ν_2 and ν_3 are frequencies of the two fundamental waves and the converted wave, respectively. Momentum conservation is achieved by satisfying the *Phase Matching* [2.34] condition:

$\Delta k = k_3 - k_2 - k_1 = 0$ (For the SFG process)

$\Delta k = k_3 - 2k_1 = 0$ (For the SHG process)

Where k_1, k_2 and k_3 are the wave vectors, respectively. A wave vector is a vector pointing in the propagation direction and with a magnitude of 1/λ.

In the following we will focus on the case of frequency conversion by the process of SHG. The power conversion between the fundamental wave photons and the frequency doubled wave, and the phase matching condition are the two topics that we are concerned with.

1.1.3.1 The SHG conversion efficiency τ_{SHG} and the Frequency doubling efficiency τ_{FD}

By assuming that the starting laser light is traveling as plane waves in the *z* direction in a suitable nonlinear crystal with the property of phase-matching and with negligible power loss. The laser power conversion via SHG can then be described as below [2.54]:

$$\frac{P_1(z)}{P_1(0)} = sech^2\left(\gamma\sqrt{\frac{P_1(0)}{A}}z\right) \quad \text{------ (2.9)}$$

$$\frac{P_3(z)}{P_1(0)} = tanh^2\left(\gamma\sqrt{\frac{P_1(0)}{A}}z\right) \quad \text{------ (2.10)}$$

$$\gamma = \sqrt{\frac{2\omega_1^2 d_{eff}^2}{\varepsilon_0 c^3 n_1^3}} \quad \text{------ (2.11)}$$

Here

***P₁*(0)** is the input power of fundamental wave,

***P₁*(*z*)** is the attenuated power of incoming fundamental wave along the propagating direction *z*.

***P₃*(*z*)** is the power of frequency doubled wave outgoing along the propagating direction *z* (the number 3 is referring to the third photon in the SHG generation process). Here *z* actually is the length of the nonlinear crystal.

sech² *x* and **tanh² *x*** are the usual squared hyperbolic secant and tangent functions of *x.*

A is the cross-section area of the laser beam.

γ is a constant that depends on the specific properties of the nonlinear crystal.

ω₁ is the angular frequency of the fundamental wave.

ε₀ is the permittivity of free space.

C is the light speed of free space.

n_1 is the refractive index of the nonlinear crystal.
d_{eff} is the so called *d*-coefficients that refers the second order response tensor.

According to Equation (2.10), there are four parameters that affect the efficiency of the SHG: The power of the fundamental wave $P_1(0)$, the property of the nonlinear crystal γ, the size of the beam cross section *A* and the length of the crystal *z*. Therefore, various methods can respectively be used to increase the efficiency.

1. To increase the power of fundamental wave, there are several methods that could be used:
    - Put the nonlinear crystal inside the laser cavity, so called intra-cavity SHG
    - Attach an enhancement cavity to increase the power, so called external-cavity SHG
    - Use a pulsed laser, to temporary increase the instantaneous power extremely
2. Choose a high *d*-coefficient nonlinear crystal to obtain a high value of γ.
3. *A* and *z* are two contradictory parameters for a laser beam because a smaller beam waist create a bigger beam divergent angle, as shown in Fig. 2.3 In order to find the optimum beam size, the Boyd-Kleinman factor should be considered [2.21]. A new rising technology, the so called poled nonlinear crystal waveguide SHG device methodology, can avoid this problem. Therefore >99% power conversion has been achieved on a low power level (<1 W) [2.22]. This technology will be discussed in a following section (2.1.3.5).

On the condition of low conversion efficiency, the approximation $tanh(x) \approx x$ can be used to simplify the Equation (2.10).

$$\mathrm{P}_3(z) = \frac{\gamma^2 z^2}{A} P_1^2(0) \qquad \text{------ (2.12)}$$

Here it is clear that the power of the frequency doubled beam depends on the square of the power of the fundamental wave. It is usual to define a SHG conversion efficiency τ_{SHG} as below:

$$\tau_{SHG} = \frac{\mathrm{P}_3(\mathrm{z})}{\mathrm{P}_1(0)} = \frac{\gamma^2 z^2}{A} P_1(0) \qquad \text{------ (2.13)}$$

Therefore the SHG conversion efficiency τ_{SHG} is linearly depending on $P_1(0)$. It should be noted that the SHG conversion efficiency τ_{SHG} and the Frequency Doubling (FD) efficiency τ_{FD} should be distinct. The definition of the FD efficiency τ_{FD} for a frequency doubler device is the input power of the fundamental laser $P_0(0)$ divided by the output power of the frequency doubled laser.

$$\tau_{FD} = \frac{\mathrm{P}_3(\mathrm{z})}{\mathrm{P}_0(0)} \qquad \text{------ (2.14)}$$

For the case of the external enhancement cavity doubling, $P_0(0)$ means the input power of the fundamental laser outside the enhancement cavity, but $P_1(0)$ means the enhanced power inside the enhancement cavity. For the case of pulsed laser frequency doubling, $P_0(0)$ means the average power of the fundamental laser, and $P_1(0)$ means the peak power of fundamental laser.

Concerning the *enhancement rate* e_r for the external enhancement cavity doubling,

$$e_r = \frac{P_1(0)}{P_0} \quad \text{------ (2.15)}$$

the relation between τ_{SHG} and τ_{FD} is

$$\tau_{FD} = e_r \cdot \tau_{SHG} \quad \text{------ (2.16)}$$

2.1.3.2 Phase Matching

Due to the chromatic dispersion in most optical elements, the fundamental wave and the frequency doubled wave may have different velocities of propagation in the nonlinear applied crystal. Therefore the SHG from the different parts of the crystal can cancel each other, as shown in Fig. 2.4. However, it is possible to find a propagation direction where these two waves (the fundamental and the doubled wave) have the same velocity independent of the anisotropism of the nonlinear crystal. Under such condition the so-called Phase matching, the SHG can grow up quite substantially, see Fig. 2.4 (b). The usual technique for achieving phase matching in nonlinear crystals is to use birefringent phase matching [2.34], where one exploits the crystal property of birefringence to cancel the phase mismatch. This birefringent phase matching technique comes mainly in two variations:

- *Type I phase matching* meaning that, e.g. in sum frequency generation, the two fundamental beams have the same polarization direction, perpendicular to that of the sum frequency wave.

- *Type II phase matching*, in which the two fundamental beams have perpendicular polarization (*Type II* type phase matching can also be adopted for un-polarized fundamental laser. In such a case, the two perpendicular polarization directions refer to the projections of the fundamental polarization).

For the *intra-cavity frequency doubling* method of SHG, therefore type I and type II phase-matched frequency doublings are suitable for respectively polarized emission and unpolarized emission [2.23].

For a laser beam propagating in an isotropic medium, the transverse intensity distribution propagates along the beam axis as defined by the *k* wave vector of the medium. In anisotropic (and thus perhaps birefringent) crystals, this is not necessarily the case. It is possible for the intensity distribution and polarization to drift away from the direction defined by the *k* wave vector, as illustrated in Fig. 2.5. Here the gray lines indicate wavefronts and the blue color marks the region with significant optical intensity. This phenomenon, called *spatial walk-off*, could separate and displace the SHG created laser beam of to a different propagating angle, thereby decreasing the power conversion efficiency and the SHG laser beam quality. There are two phase matching techniques that can be used to avoid this problem:

- *Noncritical phase matching* (also called *temperature phase matching* or *90° phase matching*). Here, all polarization directions are along the crystal axes. The interacting beams are aligned such that

they propagate along some direction in axis of the birefringent nonlinear crystal. The phase mismatch is minimized by adjusting the crystal temperature until the phase velocities of the interacting beams become equal. The attribute "noncritical" comes from the fact that this technique is relatively insensitive to slight misalignments of the beams. Another important advantage of this method is that the phenomenon of spatial walk-off is avoided. Therefore, the conversion efficiency can often be very high with noncritical phase matching method, and a high beam quality of SHG can be achieved. Typically, Lithium TriBorate (LBO) crystals are applied for this technique to achieve SHG from 1064 nm neodymium-based lasers [2.24].

- *Quasi Phase Matching* (QPM) is a technique for achieving phase matching by use of a nonlinear crystal material with spatially modulated nonlinear optical properties. The idea is essentially to allow for a phase mismatch over some propagation distance, but to reverse (or disrupt) the nonlinear interaction at positions where otherwise an interaction would take place with a wrong direction of conversion.
  In Fig. 2.6 it is illustrated with green arrows how the complex amplitude contributions from different parts in the nonlinear frequency doubling crystal add to form the harmonic wave.
  The most popular technique for making a quasi-phase-matched crystal is to use *periodic poling* of a ferroelectric nonlinear crystal material such as lithium niobate ($LiNbO_3$), lithium tantalate ($LiTaO_3$) or potassium titanyl phosphate (KTP, $KTiOPO_4$). The technique is also called *ferroelectric domain engineering*. A strong electric field is applied to the crystal for some time, using microstructured finger-like electrodes, so that the crystalline domain orientation and thus the sign of the nonlinear coefficient are permanently reversed, but only below the electrode fingers. The electrode size (the periodicity of the electrode pattern) determines the wavelengths for which certain nonlinear processes can be quasi-phase-matched. It can work with a very wide range of nonlinear interactions, even in crystals which have e.g. too weak a birefringence for birefringent phase matching, and without spatial walk-off.

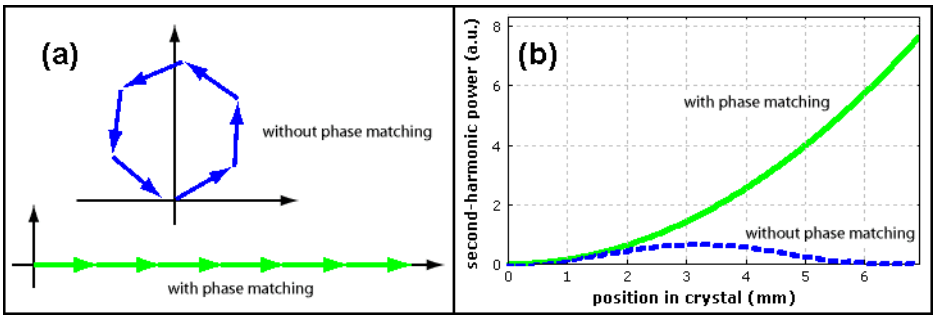

Fig. 2.4: The sketch of growth of second harmonic power in a crystal. (a) illustrates with arrows how the complex amplitude contributions from different parts in the nonlinear frequency doubling crystal add to form the harmonic wave. Without phase matching, the amplitude contributions from different parts of the crystal will cancel each other (blue arrows). With phase matching, the amplitude contributions will superimpose on each other, resulting in the second-harmonic wave growing up in intensity (green arrows). (b) Growth of second harmonic power in a crystal along the propagation direction, assuming a constant pumping intensity. Solid greed curve: the phase-matched case, with the power

growing in proportion to the square of the propagation distance; Dashed blue curve: the non phase-matched case, with the SHG power oscillating between zero and a small value.

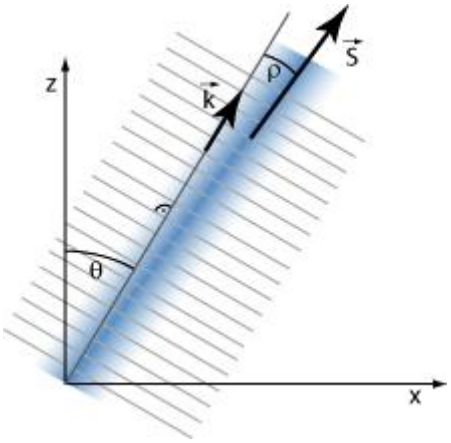

Fig. 2.5: Spatial walk-off: The intensity distribution of a beam in an anisotropic crystal emitting SHG radiation propagating in a direction which is slightly different to that of the wave vector.

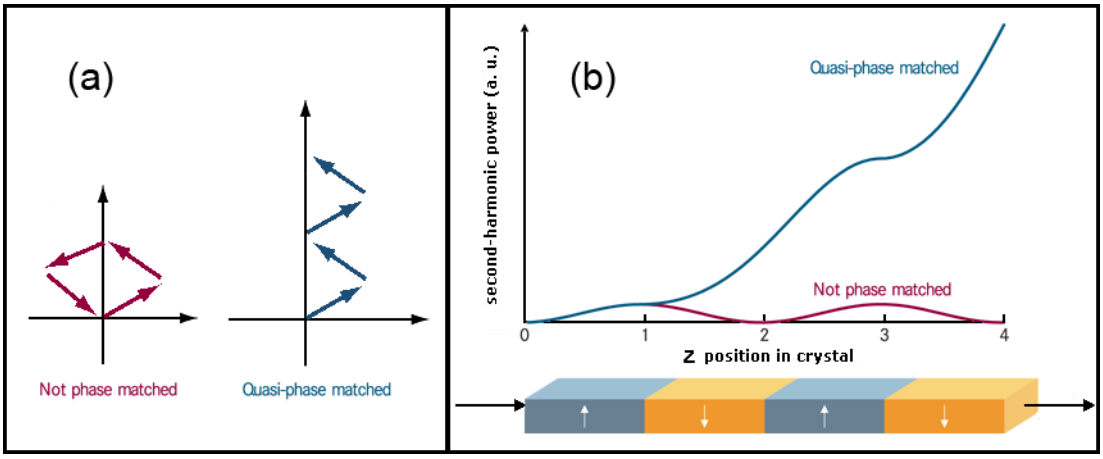

Fig. 2.6*:* With quasi-phase matching, each section of the crystal is not in prefect phase-matching. Instead, the amplitude contributions from different sections cancel each other as dark blue arrows show. Therefore the second-harmonic amplification wave cannot grow up. (b) Growth of the second harmonic power in a crystal along the propagation of direction, assuming a constant pumping intensity in the case of quasi-phase matching.

2.1.3.3 Selecting Nonlinear Crystals for DUV SHG

Selecting suitable nonlinear crystals for the SHG at certain wavelengths and calculating the phase matching angles is a complex task. Fortunately, there is nowadays software that can be used as aiding tools. SNLO (Select Non-Linear Optics) is such public domain software developed at Sandia National Laboratories in USA for selecting a nonlinear crystal and in modeling the nonlinear frequency conversion processes in those crystals. Over sixty crystals are contained in the database of the SNLO program [w2-6].

The first step to select a nonlinear crystal for DUV generation is to investigate the transparency in the range of 200 nm - 300 nm and 400 nm - 600 nm, because most of crystals are not DUV transparent. There are only few crystals that satisfy the transparency condition, such as BBO (β-barium borate, β-BaB_2O_4), LBO (lithium triborate, LiB_3O_5,), CLBO (Cesium Lithium Borate, $CsLiB_6O_{10}$), $Na_2CsBe_6B_5O_{15}$ [2.25] and $KBe_2BO_3F_2$ [2.26]. Secondly, the *d*-coefficients and the angle of the spatial wall-off should be considered. We choose two crystals, BBO and CLBO, as the investigation targets, because these two crystals have distinct advantages over the others, namely excellent transparency in the range of blue and shorter wavelength light; otherwise they cannot be suitable for intra-cavity frequency doubling.

Fig. 2.7 shows the curves of transparency versus wavelength that are obtained as results from SNLO software. Other properties of these two crystals are shown in Table 2.2 read from the SNLO program. The main disadvantage of BBO is the spatial walk-off angle that is bigger than for CLBO's. The decisive disadvantage of CLBO is the SHG phase matching cut off wavelength that is 471 nm. Therefore the CLBO crystal cannot be used to achieve DUV light deeper than 235.5 nm (half of 471 nm).

Table 2.2: Comparison of the properties of BBO and CLBO.

Nonlinear crystals	Cut off SHG	*d*-coefficients @ 244 nm	Spatial walk-off angle @ 244 nm	Optical damage threshold @ 1064 nm
BBO	411 nm	1.56 pm/V	83.11 mrad	1-2 GW/cm^2
CLBO	471 nm	0.895 pm/V	19.76 mrad	25 GW/cm^2

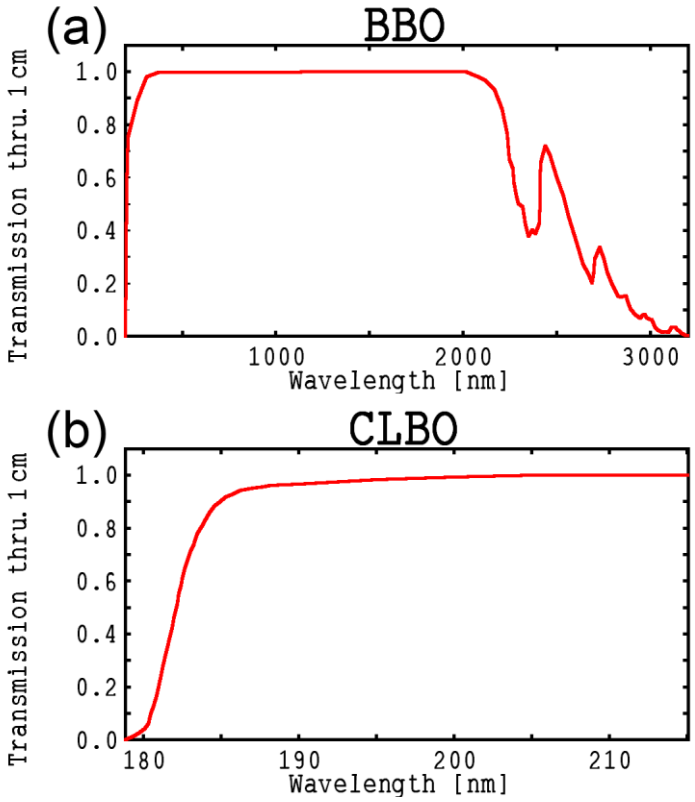

Fig. 2.7: Transparency curves of crystals of 1 cm length: (a) BBO i.e. β-barium borate, β-BaB_2O_4. (b) CLBO i.e. cesium lithium borate, $CsLiB_6O_{10}$.

2.1.3.4 Frequency doubler

There are some laser manufacturers that also provide frequency doubling attachments, such as Spectra-Physics, Inc. (the WaveTrain attachment [w2-1]), Coherent, Inc. (the MBD-200 unit [w2-2]) and TOPTICA Photonics, AG (the SHG pro module [w2-3]).

These frequency doublers are SHG devices equipped with an enhancement cavity and a nonlinear crystal. The schematics of a typical unit are shown in Fig. 2.8. The enhancement cavity is an optical cavity which is used for resonant enhancement of the optical power: if the incident light is resonant with the cavity, i.e. the frequency of laser is equal to one of mode of the cavity (the so-called *resonant condition*), then the intra-cavity power can be far above the incident power, particularly for a cavity with high *finesse* [2.35]. Finesse depends on the reflectivity of the cavity mirrors, meaning that a high finesse cavity can trap a fundamental photon for longer time and therefore a higher power can be obtained inside the cavity. The "active piezo control" is used to adjust the optical length of cavity in order to make the frequency of the incoming laser satisfying the resonant condition. When an appropriate nonlinear crystal is placed inside the enhancement cavity, a high SHG conversion efficiency can be achieved. However, there are some other quite demanding conditions for the fundamental laser to make a well working system.

1. The linewidth of the fundamental laser should be narrow enough. Normally, a single-longitudinal mode is required. It is because the enhancement cavity has its own longitudinal mode structure. When the fundamental laser is operated in a multi-longitudinal mode, only that particular mode may reach the resonance condition. It is impossible to make all the longitudinal mode frequencies of laser satisfy the resonance condition unless the longitudinal modes of the laser and the attachment are of the same spacing, i.e. the optical length of the laser cavity should be equal to the optical length of the enhancement cavity.
2. The laser beam quality should be as good as possible. In order to couple the laser beam into the enhancement cavity, the laser transverse mode must be matching the transverse mode of the cavity. It can be achieved by adjusting the mode-coupling lens as shown in Fig. 2.8 (B). The high order transverse modes are difficult to couple into the enhancement cavity. Except for the TEM_{00} mode, other modes of the laser beam will be lost in the enhancement cavity.
3. The power of the fundamental laser should be as high as possible. As mentioned above, the output power of SHG depends on the quadratic power of the input intensity power. Typically, 1 Watt of fundamental wave input is required to achieve about 10% power conversion for the frequency doubled wave.

Concerning the types of enhancement attachments, the MBD-200 and SHG pro units are using the traditional (so-called) bow-tie cavity for the SHG enhancement, as shown in the Fig. 2.8 (B). The mirrors M1, M2, M3 and M4 form a cavity looking like a bow-tie. M2 is driven by an *active piezo control* system to ensure that the optical length of cavity saturates the resonance condition. Because the wavelength of the incoming fundamental laser is always shifting more or less and the optical length of enhancement cavity can also be changing due to thermal bending, the presence of the *active piezo control* system is necessary to maintain a stable resonance condition. Such an *active piezo control* was normally implemented by a Pound–Drever–Hall technique [2.37]. The disadvantage of such a design is that the pointing of the output beam is unstable. Since M3 is a concave mirror, a small movement of M2 will cause a small angle change of the output beam. A small angle can cause a signification displacement of laser beam position when the laser beam propagates over a certain distance. In contrast to this the WaveTrain SHG unit utilizes a *DeltaConcept* ring cavity [w2-1] which allows the cavity length to be adjusted with no effect what so ever on the output beam position. The DeltaConcept ring cavity is constructed by M1, M2 and a prism, as shown in Fig. 2.8 (A). The optical length of the cavity can be modified by moving the prism in a way that does not change the angle of laser beams. Therefore the DeltaConcept cavity has a stable pointing of the output beam.

Regarding the frequency doubling efficiency, τ_{FD}, the WaveTrain, MBD-200 and SHG pro units are able to produce SHG radiation on levels of 4-10% at 800 mW, 16% at 1000 mW and 5-10% at 1000 mW, respectively [w2-1],[w2-2],[w2-3] as shown in Table 2.3. All of the three frequency doublers have approximate enhancement rates $e_r \approx 100$ times that of the fundamental laser, (according to the Equation (2.16), $\tau_{FD} = e_r \cdot \tau_{SHG}$). Since the frequency doubling conversion efficiency $\tau_{FD} < 16$ % (see Table 2.3), we get

$$\tau_{SHG} < 0.16\ \% \qquad \text{------ (2.17)}$$

It should be noted here that the power of the fundamental wave has been enhanced, and the power is about 100 W. Therefore, when the input power is 1 W, and the power enhanced wave is ($\approx 100\ Watt$), the

SHG conversion efficiency can also be considered as low SHG conversion case. Then the equations (2.13) and (2.12) can be used to estimate the frequency doubling efficiency τ_{FD} and the output power of doubled frequency, respectively, if the power of input laser cannot reach the demanded power level. For a sample, if the input power of fundamental wave is 100 mW, and a MBD-200 frequency douler is used, the limiting Frequency Doubling conversion efficiency is:

$$\tau_{FD} = 16\,\% \cdot \frac{100\ mW}{1000\ mW} = 1.6\,\%$$

and the output power of the doubled frequency wave is:

$$P = 100\,mW \cdot\ \tau_{FD} = 1.6\,mW$$

On the other hand, we can also estimate the power of the doubled frequency for directly SHG, i.e. for the case of using no enhancement cavity. For example, when the input power of fundamental wave is 1W, the SHG efficiency for the fundamental wave with a power of 100 W is <0.16 % as shown in equation (2.17). Then, according to equation (2.13), the SHG efficiency for a fundamental wave with power of 1 W is

$$\tau_{SHG} < 0.16\,\% \cdot \frac{1\ W}{100\ W} = 0.0016\,\%$$

Since the power of the fundamental wave was not enhanced, $e_r = 1 \Rightarrow \tau_{FD} = \tau_{SHG}$. According to equation (2.12), therefore the output power of the doubled frequency is

$$P < 1\,W \cdot \tau_{FD} = 1\,W \cdot 0.0016\,\% = 1.6 \times 10^{-5}\,W \qquad \text{------ (2.18)}$$

As this above result shows, it is clear that the achieved power of the DUV laser is very low by direct SHG for the case of a 1 W CW fundamental wave.

Table 2.3: compare Frequency Doubling conversion efficiency τ_{FD} of three Frequency doublers.

Frequency doubling unit	Corresponding range of wavelength (nm)	Frequency Doubling conversion efficiency τ_{FD}	Power Demand (mW)	DUV output power (mW)
WaveTrain	410-1600	4~10 %	800	32~80
MBD-200	455-1070	16%	1000	160
SHG pro	410-1600	5~10 %	1000	50~100

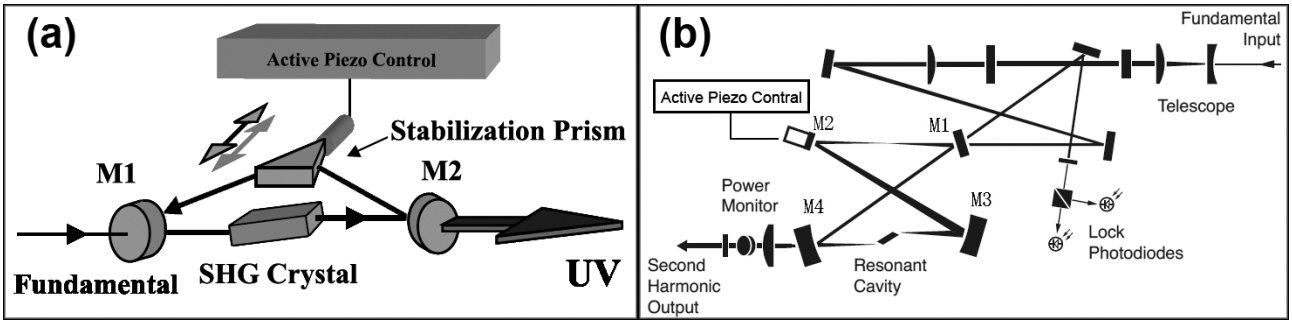

Fig. 2.8: (a) The schematic of frequency doubler equipped with the *DeltaConcept* WaweTrain ring cavity. (b) The schematics of a typical frequency doubler, equipped with a so called bow-tie ring type cavity.

2.1.3.5 SHG in Periodically Poled Nonlinear Crystal Waveguides (PPNCW)

These devices are made by *ferroelectric domain engineering*. The nonlinear crystal waveguide devices are providing very compact and simple devices to achieve enhanced SHG efficiencies [2.12], [2.22]. As high as 99% SHG efficiency has been reported by using this method with a periodically poled ferroelectric lithium niobate ($LiNbO_3$) waveguide [2.22]. It is also suitable for DUV generation when BBO is used [2.12]. Since some kinds of PPNCW has been commercial available, we will focus on discussing this.

Presently, the wavelength limitation of PPNCW is 280 nm because of the transparent edge of the $LiTaO_3$ crystal, the best transparent crystal in the UV range, for which periodically poled waveguides have been implemented by [2.27]. Although wavelength of 280 nm is not short enough for a DUV laser, it is a potential as a method to achieve DUV laser in a future compact device.

The key of this method to achieve enhanced SHG efficiency is to use wave guiding to maintain the high power density of the fundamental wave that is propagating inside the nonlinear crystal. As shown in Fig. 2.9 (a), the optical wave because of diffraction cannot be entirely focused (to a point) and will after the convergence open up again when it propagates in the bulk device, so single-pass high conversion efficiency cannot be achieved. In waveguides, the mode profile is confined (by doping layers) to a transverse dimension on the order of the wavelength, and hence high optical intensities can be maintained over considerable distances and in this way it is possible to improve the conversion efficiency. As shown in e.g. equation (2.10) or (2.13), the SHG efficiency is inversely proportional to the cross-section area A, and quadratically proportional to the interaction length Z in the crystal. Thus a long and low-loss waveguide can achieve a very high SHG efficiency.

Since waveguide SHG is a single-pass (no enhancement cavity is needed) process, there being an advantage is that the fundamental wave of a multi-longitudinal mode laser can be adapted.

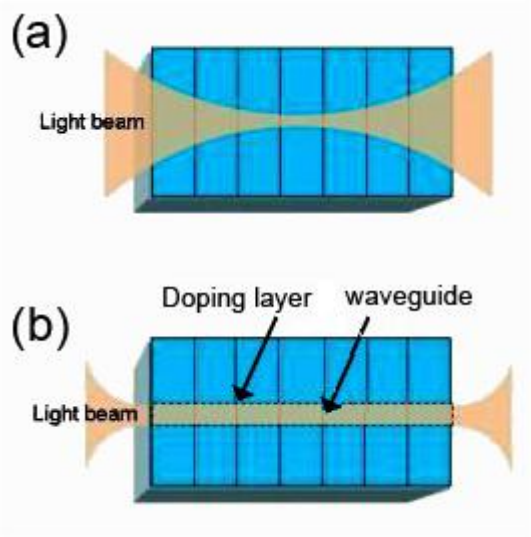

Fig. 2.9: (a) The laser beam is propagating in a bulk chip: The more focussed, the smaller is the beam waist (cross section) but also the shorter the length of high interaction (Rayleigh length). b) The laser beam is confined by means doping layers in the waveguide chip allowing for high power density and hence high SHGs.

2.2 Diode Lasers

Diode lasers (= *laser diodes*) are electrically pumped semiconductor lasers in which the gain is generated by an electrical current flowing through a p–n junction or (more frequently) a p–i–n structure. The structural sketch of a typical semiconductor laser devise is shown in Fig. 2.10. The laser resonator cavity is formed between the p and n type layers and by the two polished coated (or uncoated) end facets. Also so called vertical cavity VCSEL lasers have recently been developed. They are cheaper to mass fabricate because they do not need to be polished [2.36].

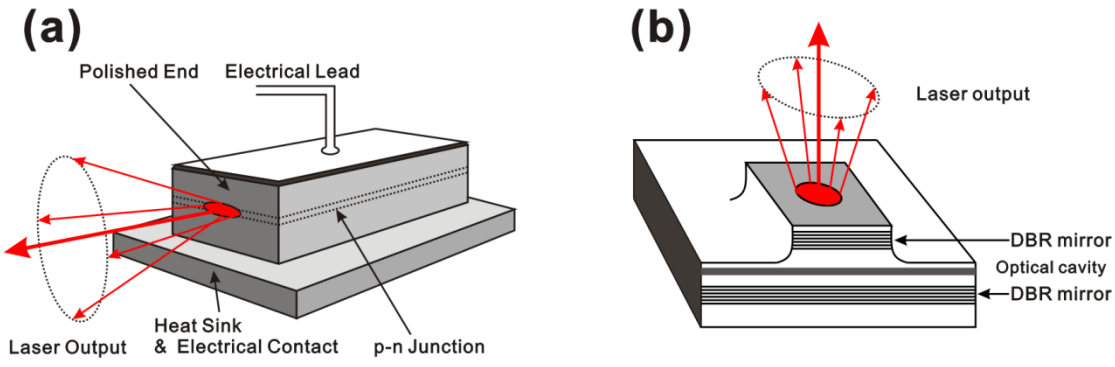

Fig. 2.10*:* Structural sketches of two kinds of semiconductor lasers, (a) edge emitting laser, (b) Vertical-cavity surface emitting laser (VCSEL). DBR: Distributed Bragg reflecting layers.

2.2.1 Emission Wavelengths of diode lasers

The emission wavelengths of diode lasers today cover the range from Infrared to UV. The wavelength of the emission is essentially determined by the band gap of the laser-active semiconductor material: the photon energy is close to the band gap energy. Table 2.4 gives an overview on typical material systems.

Table 2.4: Emission wavelengths of various types of laser diodes.

Laser diode material (active region / substrate)	Typical emission wavelengths (nm)
AlGaN	342 (336)
InGaN / GaN, SiC	380, 405, 450, 470
AlGaInP / GaAs	635, 650, 670
AlGaAs / GaAs	720–850
InGaAs / GaAs	900–1100
InGaAsP / InP	1000–1650

Most laser diodes emit in the near-infrared and red spectral region. Since the successful demonstrations of the electrically driven stimulated emission (laser operation) from GaInN/GaN quantum wells [2.28], [2.29], the nitride semiconductors have been expanding their range of lasing wavelengths from the red and yellow into the green, blue and ultraviolet. These latest colors are of interest, because the SHG of these lights will be in the range of DUV. These lasers all are commercial available. The shortest wavelength ever reported by the end of 2010 for an electrically driven semiconductor laser is 336 nm [2.30], being emitted from an indium-free AlGaN-based laser diode.

2.2.2 Emission Bandwidth of Diode Lasers

Most laser diodes emit a beam with an optical FWHM bandwidth of a few nanometers (hundreds of wavenumber units, cm^{-1}). This bandwidth results from the simultaneous oscillation of multiple longitudinal (and possibly transverse) resonator modes (***multimode laser diodes***). The bandwidth of a laser diode is thus too broad for application as a Raman exciting light source, unless a special design was applied to narrow the emission bandwidth. Distributed-feedback (DFB) diode lasers and External-cavity diode Lasers are two common designs for bandwidth narrowing, therefore perhaps making them more useful for Raman use.

A (DFB) diode laser is a laser where the active region of the device is periodically structured as a diffraction grating. Typically, the periodic structure is made with a phase shift in its middle of the cavity. The structure in this way builds a one dimensional interference grating. The grating acts as the wavelength selective element for at least one of the mirrors and provides feedback, reflecting light back into the cavity to form the resonator. The grating is constructed so as to reflect only a narrow band of wavelengths, and thus produce a single longitudinal lasing mode. Thus the emission bandwidth is much narrower, typically with a line width in the megahertz region (~10^{-4} cm^{-1}).

Further linewidth narrowing is possible with external cavities and particularly with narrow band optical feedback from a reference cavity. Such lasers are called External-cavity Diode lasers. The design is suited for edge emitting lasers as well as Vertical Cavity Surface-Emitting Lasers.

2.2.3 Transverse Mode of Diode Lasers

As mentioned above, the resonance cavity of laser diode is formed by two end facets. These two end facets are plane and parallel. According to the theory of an optical cavity, the setup is often not a stable cavity, meaning that the laser transverse mode is not defined by end the facets. Actually, the transverse mode depends on the optical active medium layer that has a waveguide structure.

A so-called single mode diode laser (also called Ridge waveguide diode laser) implicates that the transverse mode of output laser is single mode and the active area is a single mode waveguide or cavity. The single mode of a waveguide is slightly different from the free space single mode TEM_{00}. Therefore the beam quality of a single mode diode laser is not as good as what is found for a gas laser or a solid-state laser. Normally the value of M^2 for a practice single mode diode laser is above 1.2.

For the single mode diode laser, since the width of the active layer is limited, it is difficult to increase the pump current too much. The maximal output power is hence normally limited to about few hundreds milliwatt. In order to increase the output power the width of active area must be broadened, but then the transverse mode will not be maintained in single mode. A special technique, taking advantage of a tapered amplifier, has been developed to solve this problem [2.31]. Such a technology can increase the output to above 2 W and can maintain the single mode operation in the tapered active area as shown in Fig. 2.11. Combined with a grating external cavity, or a DFB diode laser, it is possible to produce very powerful single frequency diode lasers.

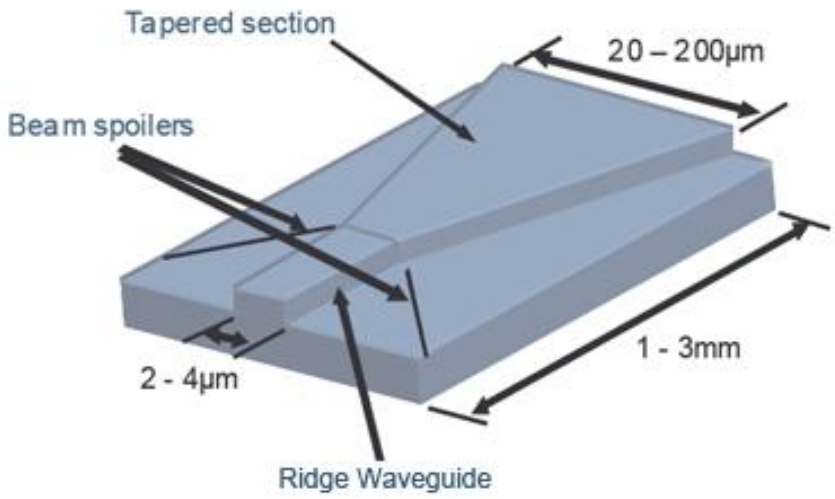

Fig. 2.11: Schematics of a typical tapered diode laser geometry.

2.2.4 Discussion and Conclusion

Until recently, there was still no DUV laser diode available. The shortest wavelength of a diode laser reported was 336 nm. Therefore, a frequency conversion technology must be implemented to achieve the DUV lasing from diodes. In the following, the possible ways to achieve the DUV emission based on diode lasers are presented. To get an overview the information is practically arranged in Table 2.5:

Table 2.5: The possible methods to convert the wavelength of diode lasers down to the DUV.

Frequency conversion	**Fundamental wavelength**	**Methods**
Frequency doubling	400 - 600 nm	1. A single-frequency and single-mode diode laser & a SHG enhancement cavity
		2. A single-mode diode lasers & periodically poled $LiTaO_3$ waveguides (or He^+ implanted BBO waveguides)
		3. A single-mode diode laser & a wavelength selector & an Amplifier & a SHG enhancement cavity
Frequency tripling	600 -900 nm	4. A single-mode diode laser & a wavelength selector & an Amplifier & a Frequency tripling enhancement cavity
Frequency quadrupling	800 -1200 nm	5. A single-mode diode laser & an Amplifier & a 1st SHG enhancement cavity & a 2nd SHG enhancement cavity

The various methods are explained below:

1. Recently, one of the leading diode laser producers (TOPTICA Photonics, AG) claimed that they were able to produce the record highest possible power (50 mW) diode laser with a single-frequency and single-mode (DFB) output at 405 nm [w2-4]. Combined with a frequency doubler, the DUV line of 202.5 nm may be achieved. The output power of 202.5 nm would be estimated as (by using equations 2.12, 2.13, 2.16).

$$50\ mW \times 10\% \times \frac{50\ mW}{1000\ mW} = 0.25\ mW$$

2. A DFB laser combined with a nonlinear crystal waveguide is the most compact setup to achieve DUV laser radiation. However, the SHG cannot with the present technology crate UV radiation deeper than 280 nm by using periodically poled $LiTaO_3$ waveguides, and the emerging He^+ implanted BBO waveguide technology that may do it is not yet commercial available [2.12]

3. The schematics of this setup are shown in Fig. 2.12. Compare with the 1st method, a tapered amplifier is added to increase the power of the fundamental wave. Therefore the power of frequency doubled laser can be significantly increased. However, for the wavelengths of 400-600 nm, the tapered amplifiers are still not commercial available.

4. Frequency tripling can be implement by combining SHG and SFG in one enhancement cavity [2.32]. The schematics of setup 4 are similar to the one shown in Fig. 2.12. Instead of one SHG crystal, a SHG crystal and a SFG crystal were used in the ring cavity.

5. Frequency Quadrupling can be accomplished by two sequential frequency doubling systems as shown in Fig. 2.13. The schematic shows a laser product from TOPTICA Photonics AG. This setup has been fully developed [2.33], and is commercial available. The output power level of the DUV radiation is 10 mW [w2-5].

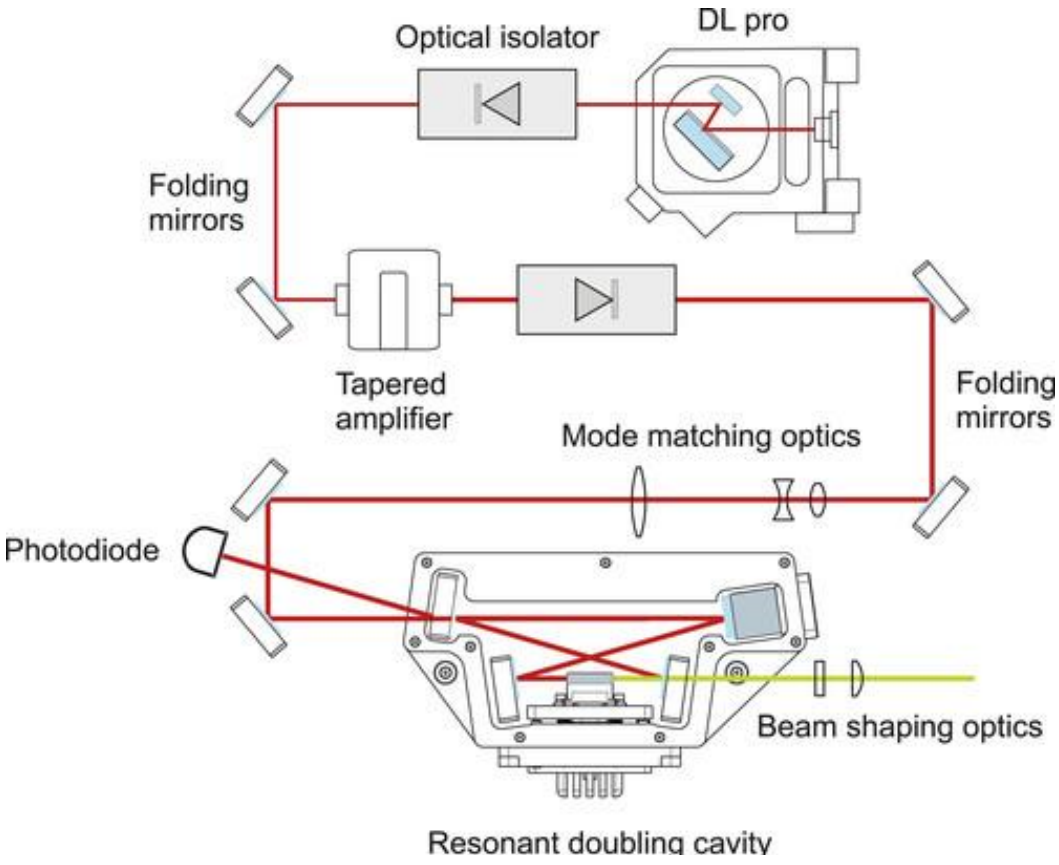

Fig. 2.12: The schematics of the 3th method, *DL pro,* involve a single-mode diode laser combined with a grating wavelength selector. A t*apered amplifier* is adapted as a power amplifier. In the final part of the system a bow-tie enhancement cavity is used for the SHG.

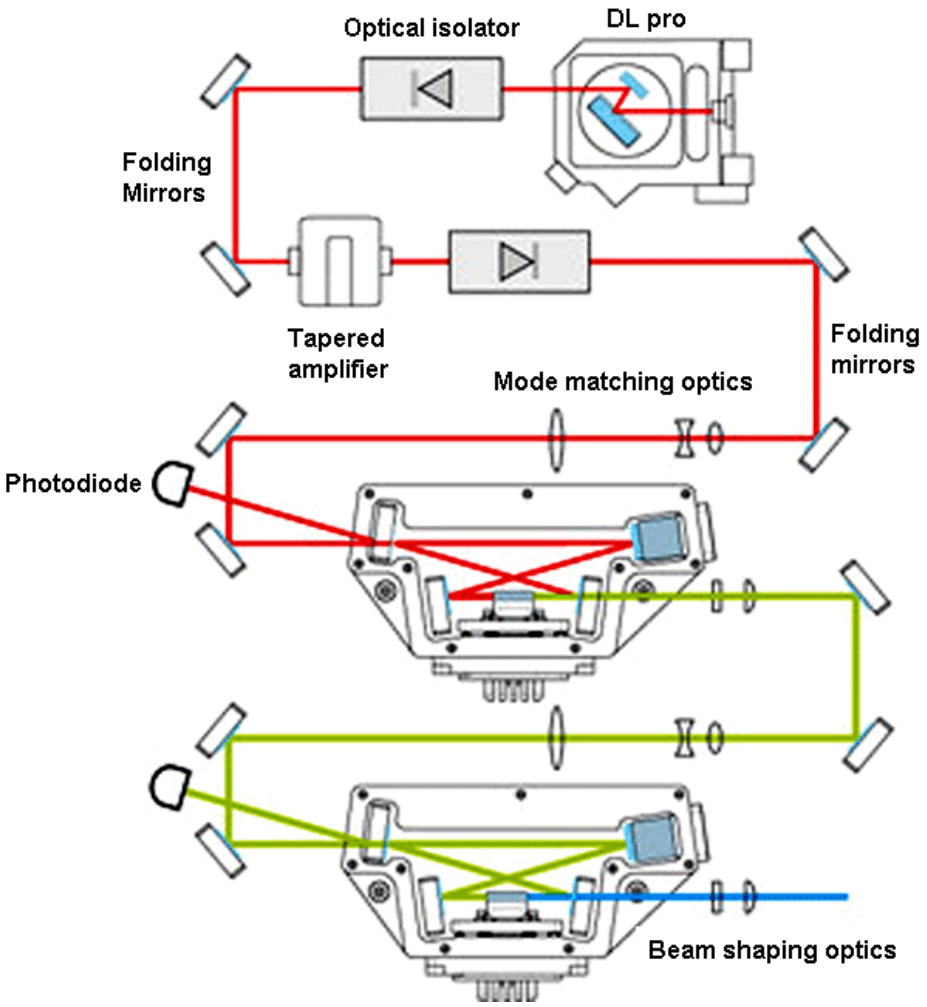

Fig. 2.13: The schematic of the 5th method, *DL pro* is a single-mode diode laser combined with a grating wavelength selector. A *tapered amplifier* is adapted as the power amplifier. Two sequential bow-tie enhancement cavities are applied to implement the frequency quadrupling.

2.3 Solid-State Lasers

Solid-state lasers are lasers based on solid-state gain media such as crystals or glasses doped with rare earth elements such as neodymium, chromium, erbium, or other ions. (Although semiconductor lasers are of course also solid-state devices, they are often not included in the term solid-state lasers.) Many of the common dopants are rare earth elements, because the excited states of such ions are not strongly coupled with thermal vibrations of the crystalline lattice (phonons), and the lasing threshold can be reached at relatively low brightness of pump. Solid state lasing media are typically optically pumped, using either a flash lamp or arc lamp, or by laser diodes. Diode-pumped solid-state (DPSS) lasers [2.38] tend to be much more efficient, and have become much more common as the cost of high power semiconductor lasers has decreased. DPSS lasers have many advantages, in particular a compact setup, long lifetime, and often very

good beam quality. Solid-state lasers can be made in the form of bulk lasers, fiber lasers, or other types of waveguide lasers. In the following we will mainly discuss the DPSS lasers in the bulk form.

Most DPSS lasers emit their lines in the range from red to near infrared (600-3000 nm) [2.39]. In order to achieve DUV laser light with present day techniques, frequency tripling, quadrupling or even higher order conversion must be used. Higher order frequency conversion is rather difficult to implement and the conversion efficiency is very low. Therefore when we are interested in wavelengths below, say, 300 nm and want to use a technique not more complicated than quadrupling we should apply a fundamental wave which is shorter than 1200 nm. Table 2.6 shows some typical solid-state lasers in these wavelength ranges. The lasers can be classified in two types by the width of the laser gain band. The lasers with narrow gain band media emit narrow and specific laser lines. Oppositely, the lasers with broad gain band media allow achieving of the laser light in a tuneable certain range.

Table 2.6: Emission lines of solid-state lasers with wavelengths shorter than 1200 nm.

		Lasers host medias	Pump wavelengths (cm)	Emission wavelengths (nm)	DUV lines (nm)
Solid-state lasers	Narrow gain band, wavelength un-tuneable.	Nd:YVO_4	808 nm	1064, 914	266, 213, 229
		Nd:YAG	808 nm	1064, 946	266, 213, 237
		Nd:YLF	797, 792	1053, 1047	263, 211, 262,210
	Broad gain band, wavelength tuneable.	Ce:LiSAF	266	280-316	280-316, 223-243*
		Ti:sapphire	488 (400-600)	650 – 1100	193-270*
		Cr:LiSAF	--	780 - 1010	--
		Cr:$BeAl_2O_3$	--	700 - 820	--
		Yb:YAG	--	1020-1050	--

*For particular setups, see [2.45], [2.48].

2.3.1 Wavelength Un-tuneable Solid-state Lasers

Among narrow gain band (wavelength un-tuneable) laser host media, Nd:YVO_4 (Neodymium Doped Yttrium Orthovanadate) is the most efficient laser host crystal for diode pumping among the current commercial laser crystals, and this applies especially for low to middle power density, mainly because of the absorption and emission features for Nd:YVO4. It exhibits much higher pump absorption and gain (due to the very high absorption and laser cross sections), a broader gain bandwidth (around 1 nm), and a much broader wavelength range for pumping (often eliminating the need to stabilize the pump wavelength) [2.40], [2.41]. Another famous laser crystal, Nd:YAG (Neodymium Doped Yttrium Aluminium Garnet) is one of earliest laser crystals used, popular since 1964 [2.42], 2 years earlier than the first report on Nd:YVO_4 [2.43]. Although the Nd:YAG material is not as good as Nd:YVO_4 in many properties, it is however outstanding for high energy pulsed laser applications.

Both laser crystals, Nd:YVO_4 and Nd:YAG, have their strongest emission wavelength at 1064 nm and the used pump wavelengths are around 808 nm. When high power and low cost 808 nm semiconductor LDs appeared, Nd:YVO_4 and Nd:YAG came in widespread use. Their wavelength at 1064 nm has become the

most common wavelength for solid-state lasers. The corresponding frequency converted lasers (doubled, tripled and quadrupled, at respectively at 532, 355 and 266 nm) are also getting much in use. Therefore, the 266 nm line is the typical DUV one among solid state lasers, and it can be obtained from many laser manufacturers as a most reliable DUV laser source. Other important wavelengths, 914 nm for Nd:YVO_4 and 946 nm for Nd:YAG, require higher pump energy compared with 1064 nm generation, and they are therefore not so common. However they allow generating DUV lines at 229 nm and 237 nm by frequency quadrupling. Another neodymium wavelength generator, is the birefringent Nd:YLF (Neodymium-doped yttrium lithium fluoride), which eliminates thermally induced depolarization losses. The gain and the emission wavelength of Nd:YLF are polarization dependent. There are two lines, 1047 nm or 1053 nm (the 1047 nm line is the stronger one). Therefore the frequency quadrupled DUV laser lines from Nd:YLF are at 262 or 264 nm, and the 262 nm line is also a common DUV line of solid-state lasers.

The above motioned lasers can be operating either pulsed or in continuous mode (CW). The pulses are normally generated by the Q-switching technique. Compared with the CW lasers, the pulsed lasers are easier to use for frequency quadrupling. Therefore, the price of pulsed DUV laser is lower than the for CW DUV lasers.

As shown in Fig. 2.14 (A) a typical configuration for frequency quadrupling of a pulsed laser may begin with a pulsed Nd:YAG laser at 1064 nm, generating frequency doubled 532 nm light by directly passing the beam through a SHG crystal (normally, LBO or KTP) (so-called single pass SHG). Then frequency quadrupled 266 nm light is generated in a second stage SHG crystal (normally consisting of BBO or CLBO). There is still quite an amount of power of 1064 and 532 nm light remaining in the output beam. The different lines can be separated by a prism or by use of two edge mirrors. Therefore 1064 and 532 nm laser lines can also be achieved as by-product lines at the same time. For a CW laser, the first frequency doubling is normally achieved by use of intra-cavity SHG; then in a second stage SHG is performed once more by use of an external enhancement SHG cavity, as shown in Fig. 2.14 (B). Such lasers are produced by Crastech Laser and Coherent Radiation Inc. [w2-7], [w2-8]. Compared with the pulsed lasers, there is no 1064 and 532 nm laser lines output from the CW frequency quadrupling laser systems because the 1064 and 532 nm lines are trapped in the laser intra-cavity and the external enhancement cavity, respectively, with the purpose of generating as high power intensity inside the resonators as possible.

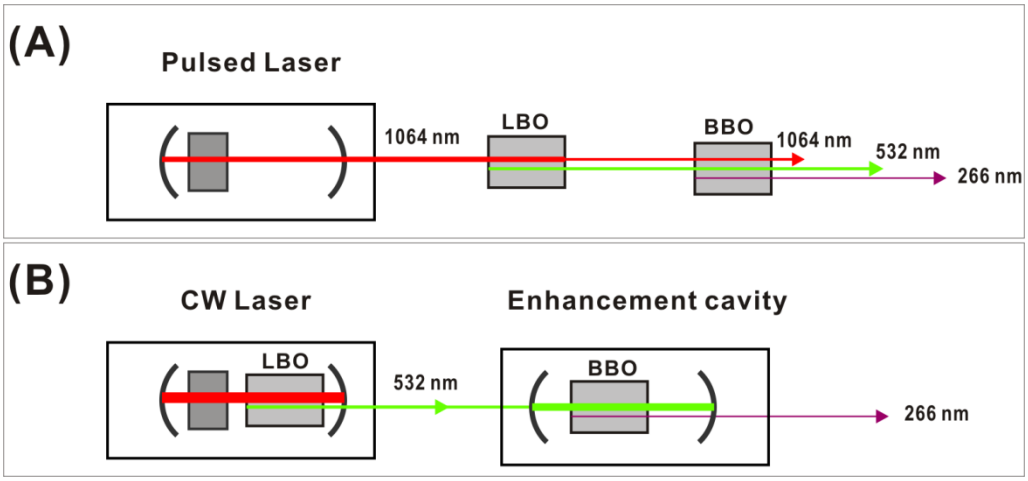

Fig. 2.14: (A) A typical configuration of frequency quadrupling for a pulsed laser: an infrared input beam at 1064 nm generates a green 532 nm wave in a first SHG crystal, and a second SHG crystal converts this to light at 266 nm. (B) A typical configuration of frequency quadrupling for a CW laser: the first frequency doubling is achieved by use of intra-cavity SHG. Then, second stage frequency doubling is implemented by use of external enhancement cavity SHG.

2.3.2 Wavelength tuneable solid-state lasers

Ce:LiSAF (Ce^{3+}:$LiSrAlF_6$) is an attractive laser host medium of this category, since it directly emits the tuneable DUV lines, although the tuneable range of 281– 315 nm [2.44] is not deep enough for our purpose. The deeper wavelength range of 223 – 243 nm can be achieved by frequency sum mixing with a 1064 nm laser [2.45]. In such a procedure, a Ce:LiSAF laser is typically pumped by a frequency quadrupled Nd:YAG pulsed laser (at 266 nm); then the generated 281 – 315 nm laser beam from the Ce:LiSAF is sent into a SFG (Sum frequency Generation) BBO crystal together with the fundamental wave of the Nd:YAG pulsed laser (1064 nm laser), resulting in a 223 – 243 nm radiation output. However, such complicated lasers are not commercially available.

Titanium-doped sapphire is an outstanding medium for broad gain band (wavelength tuneable) laser host media, working in the range from red to near-infrared. Another potential rival laser type is based on the Cr^{3+}:LiSAF (Cr^{3+}:$LiSrAlF_6$) crystal [2.46]. The gain bandwith of the latter type is inferior as shown in Table 2.6. Ti: sapphire was introduced in 1986 [2.47], and thereafter Ti:sapphire lasers quickly replaced most of the dye lasers, which until then had dominated the fields of ultra short pulse generation and widely wavelength-tuneable laser emission. The wavelength of the Ti:sapphire laser is widely tuneable in the range of 650-1100 nm and by frequency tripling or quadrupling, tuneable DUV laser radiation can be achieved. The Ti:sapphire laser is usually pulsed, generated by the mode-locking technique or pulsed pumping laser. It has previously been applied for DUV Raman spectroscopy in some important research groups, such as the Asher group and the Spiro group [2.48], [2.49].

In the following, we present two interesting tuneable UV laser systems that the Asher group used to realize tuneable DUV laser radiation in a broad range of 193 – 270 nm [2.48]. The lasers are of the kind Indigo-S from

Positive Light Co. (Los Gatos, CA.) The two laser systems are based on Ti: sapphaire wavelength tuneable lasers, and utilize frequency conversion techniques, second harmonic generation (SHG) and sum frequency generation (SFG). Two laser systems are required because BBO is not of use for frequency doubling below 206 nm due to no phase-matching exist below this wavelength. By using the other way to achieve frequency quadrupling, i.e. SFG of the 3rd harmonic generated wave and the fundamental wave to achieve the 4th harmonic wave generation, BBO can be used to generate the deeper wavelength. However, it needs three stages of SFG to reach the 4th harmonic generated wave. The power conversion is therefore relative lower.

Both of these laser systems are pumped by an acousto-optically Q-switched Nd:YLF system, operating at a 5 kHz frequency to generate the 1053 nm wavelength fundamental in pulsed mode - with pulses of 100 to 350 ns duration - depending on the pulse energy. The Nd:YLF system is intra-cavity frequency doubled using a lithium tri-borate (LBO) crystal. Although the absorption peak of the Ti:sapphire is at 488 nm, the Ti:sapphire crystal has a broad absorption range of 400 – 600 nm. Therefore, this frequency doubled Nd:YLF laser - emitting radiation at 527 nm - can be adopted as a pumping laser.

The first system (shown on Fig. 2.15 (a.1) and (a.2)) uses two successive frequency doublers (two sequential SHGs) to generate tuneable light from 210 to 240 nm. The first stage of frequency doubling was achieved by means of intracavity SHG. The laser cavity of the fundamental wave is constructed by three mirrors, M1, M2 and M3, as shown on Fig. 2.15 (a.1). For a normal cavity with two mirrors, there is only one possible beam waist where the laser crystal (Ti:sapphire) could be placed. In order to generate a second beam waist for placing another SHG crystal in the laser cavity, a cavity with three (or more) mirrors was therefore adopted. The frequency selector is formed by two prisms combined with the set of etalons. The laser pulse is generated by mode-locking. In the layout of the further SHG (denoted as FHG shown in Fig. 2.15 (a.2)) the lenses are placed in the beam to focus the first order SHG wave on the *FHG* (actually SHG crystal) to generate the quadrupled frequency. The SHG crystals should have precisely controlled temperature to achieve phase matching conditions for the different fundamental waves. Such temperature controlled phase matching is the so-called noncritical phase matching. The overall efficiency is about 20%, which results in about 10 – 40 mW of UV radiation within the range of 210 nm to 240 nm.

The purpose of the second system is to generate even shorter wavelengths, in the range of 193- 210 nm, and also the tripled frequency in the range of 240 – 270 nm. The layout is shown in Fig. 2.15 (b.1) and (b.2). The fundamental laser cavity is a normal two mirrors laser cavity, constructed with M1 and M2 (M2 is the output coupler). The 193–210 nm laser harmonics package consists of a second-harmonic generator (SHG) unit that converts the 772–820 nm Ti:Sapphire IR fundamental to light of 386–410 nm with an efficiency of about 20%. The THG crystals mix the 386–410 nm light with the IR fundamental to produce the 257–273 nm third harmonic with an efficiency of up to 10%. The final stage mixes the third harmonic with the residual fundamental to produce 193–210 nm light with a somewhat lower efficiency of about 5%. The deep UV output power depends on the wavelength and varies from about 9 mW at 200 nm to 3 mW at the edges of the 193–210 nm spectral region.

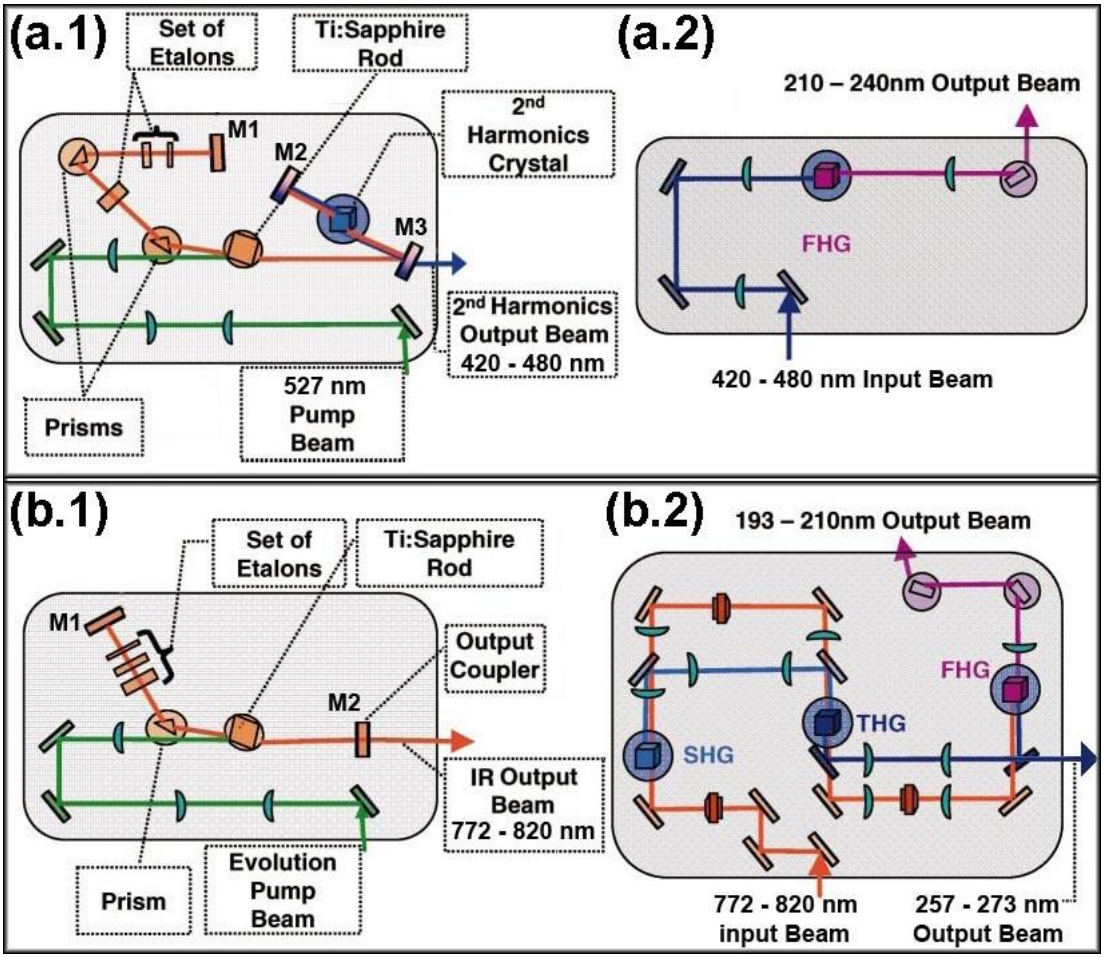

Fig. 2.15: Optical layouts for two pulsed laser systems to provide a broad tuneable DUV range of 193 -270 nm. **(a.1)** An intra-cavity doubled Ti:Sapphire laser; **(a.2)** The frequency doubling for 210 - 240 nm generation **(b.1)** Fundamental Ti:Sapphire laser; **(b.2)** Sum frequency generation provide 257 – 273 nm output by mix of SHG with fundamental wave; further sum frequency generation provides 193 – 210 nm output by mix of THG with fundamental wave. The graphics are courtesy of Asher et al. [2.48].

2.4 Gas Lasers

Gas lasers are based on gases as the gain media. The types of gases not only include normal gases such as N_2, CO_2, and noble gases such as He, Ne, Ar and Kr, but also include metal vapors such as Cu (Copper), Ag (Silver) and Cd (Cadmium). The laser-active entities are either single atoms or molecules, and are often used in a mixture with other substances having auxiliary functions. In most cases the energy pumping is implemented by an electric discharge. During operation, the gas is often in the state of plasma, containing a significant concentration of electrically charged particles. It usually requires a high-voltage high-current supply.

Most gas lasers emit with a high beam quality, since the gas introduces only weak optical distortions, despite considerable temperature gradients. Gas laser examples are e.g. the He-Ne laser and Argon-ion

Laser with excellent beam quality. However other gas lasers have poor beam quality, such as several hollow cathode gas lasers and *excimer* lasers (obtained from excited dimers in noble gas - halogen gas mixtures).

2.4.1 Hollow cathode metal ion lasers

Hollow cathode metal ion lasing was first demonstrated at the University of Budapest in 1974 [2.50]. The emission wavelength can be 224.3 nm (from a helium silver (HeAg) hollow cathode laser) or 248.6, 260.0 and 270.3 nm (from a neon copper (NeCu) hollow cathode laser). The linewidths of all of these semi-CW emission lines are narrow, less than 0.1 cm^{-1}. These lasers have been previously applied for resonance Raman spectroscopy studies of the nucleic acids and the aromatic amino acids [2.9].

The presented lasers differ significantly from other metal vapor lasers in that the metal vapor pressure is generated by sputtering of a metal from a cathode in a low pressure precious gas rather than by evaporation from a hot metal source, as for the He-Cd lasers [w2-9]. The hollow cathode sputtering metal ion lasers operate at room temperature and require no preheating or standby power. The laser can be built as compact as the He-Ne lasers as shown in Fig 2.16 (a). Fig. 2.16 (b) illustrates the structure of the HeAg 224.3 nm hollow cathode laser tube. The active medium of this laser consists of singly ionized silver ions formed by sputtering within a silver hollow cathode tube, with an about 3 mm inside diameter. Helium and other dopant gases are employed as buffer gases to ionize and excite the sputtered silver atoms to an excited state from where lasing occurs.

The hollow cathode discharge is formed between the hollow cylindrical silver cathode and an opposite anode via a slot in the side of the cathode. The pressure of the buffer gas mixture is optimized for the output at 224.3 nm. The threshold discharge current for the laser output can be less than 1 A. The laser cavity is constructed from a flat 0.75% transmission output-coupling mirror, and a 2 m focal length concave high reflecting mirror. The distance between the two mirrors of the cavity is 40 cm [2.8]. According to the above parameters of the laser cavity, the beam profile of the laser operating in an ideal TEM_{00} mode can be found by the *Intarsia* program [w2-10] which is a laser cavity design software, as shown in Fig. 2.16 (c). The software shows that the radius of the TEM_{00} laser beam should be 0.239 mm on the output-coupling mirror. However, the radius of an actual output laser beam is about 1.25 mm that is much bigger than the radius of an ideal TEM_{00} laser beam as motioned above. The mode quality of the output beam was determined from the measured, focused spot size, and it gave a value of $M^2 = 18$. Accordingly, the area of the focused spot is 18^2 times larger than the ideal TEM_{00} focused beam spot, meaning that we had a bad beam quality [2.52]. The bad beam quality might be caused by strong disturbances of the puttering.

Presently, these lasers cannot stand for high current (such as >10 A) continuously, because the heat effects. In order to minimize the heating, typically the lasers should be operated at a 1 % duty cycle, and the pulse width of the laser output can be varied from a few microseconds to a millisecond. The pulse rate can be from 2 pulses per second to 20 pulses per second. Since the laser output behaves like a CW wave during the pulse duration, it is so-called quasi-CW.

The power can reach peak values as high as 200 mW [w2-11]. In a typical 1% duty cycle, the average power is 2 mW. Considering the low laser output power and the poor laser beam quality under these conditions, the beam will be too weak for measuring of most of the traditional Raman experiments, especially unsuitable for the confocal microscopy because of the poor beam quality.

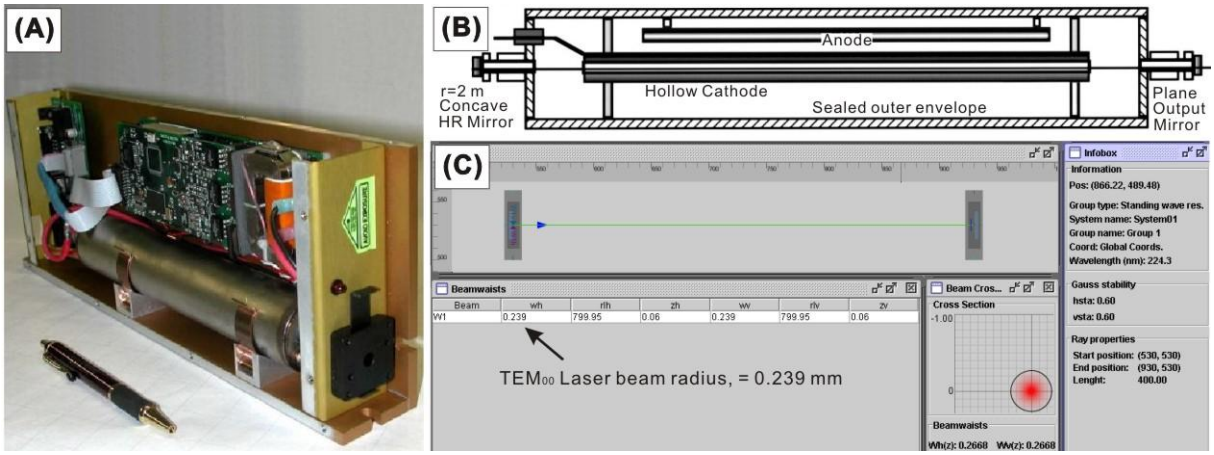

Fig. 2.16: Details of a typical hollow cathode metal ion laser: (a) Photo of the unit with the cover removed. The compact power supply is integrated in the laser head. (b) The schematic structure of laser resonator. (c) The corresponding TEM_{00} laser beam profiles can be found by use of the *Intarsia* software [w2-10].

2.4.2 Argon-ion lasers

The Argon laser was invented in 1964 by William Bridges at Hughes Aircraft Co. [2.51]. Argon lasers may emit at 13 different wavelengths from the visible, near-visible, and ultraviolet spectrum, including: 351.1 nm, 363.8 nm, 454.6 nm, 457.9 nm, 465.8 nm, 476.5 nm, 488.0 nm, 496.5 nm, 501.7 nm, 514.5 nm, 528.7 nm, 1092.3 nm. The lines arise from the different transitions in the Ar^+ ion, sometimes called Ar(I)-lines [2.55]. These can be preferentially selected using an intra cavity prism. This prism selects the specific wavelength. Removal of the prism allows for broadband operation, that is, several wavelengths are running rather than only a particular wavelength.

The most prominent and most used wavelengths in the argon laser are the 514.5 nm green line and the 488.0 nm blue line. Fig. 2.17 shows the typical wavelengths and relative power levels from a usual size 4 Watt Argon laser [w2-12]. Argon lasers are normally rated by the power level sum produced by the lasing wavelengths from 514.5 nm to 454.6 nm. The wavelengths outside of this standard visible range, including an infrared line at 1090 nm and the two rather intense UV lines at 351.1 nm and 363.8 nm are available by changing the laser cavity mirrors. These two UV lines are produced from transitions between states in double-ionized argon which require higher than normal laser current levels, and are therefore available only from the highest power models.

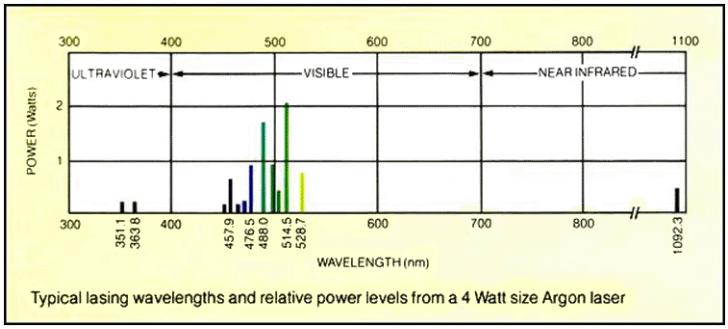

Fig. 2.17: The typical wavelengths and relative power levels from a 4 Watt size Argon laser.

The structure of a usual Argon laser is shown on Fig. 2.18. The key component of the argon ion laser is an argon-filled tube, made of e.g. quartz or beryllium oxide ceramics, in which an intense electrical discharge between two hollow electrodes generates plasma with a high density of Argon (Ar^+) ions. A solenoid around the tube is used for generating a magnetic field, which increases the output power by better confining the plasma. The intracavity prism is used to select the lasing line. Without an intracavity prism, argon ion lasers have a tendency for multi-line operation with simultaneous output at various wavelengths. When the intracavity prism is used, the output laser line is in so-called *single wavelength mode*. It should be noted that it is different from the so called *single frequency mode. Single frequency* commonly means single longitudinal mode operation. *Single wavelength* just means single laser line output, probably running in multi-longitudinal mode operation. For a typical Argon-ion laser, a single wavelength laser line is actually made up of a large number of longitudinal modes spaced over a frequency bandwidth of approximately 5 GHz, as shown on Fig. 2.2. These modes are related to the distance between the two mirrors making up the optical cavity. The frequency spacing between these longitudinal modes is *c/2L*, where *c* is the velocity of light and *L* is the mirror spacing. Thus a 1 meter cavity length has a 150 MHz longitudinal spacing between the modes.

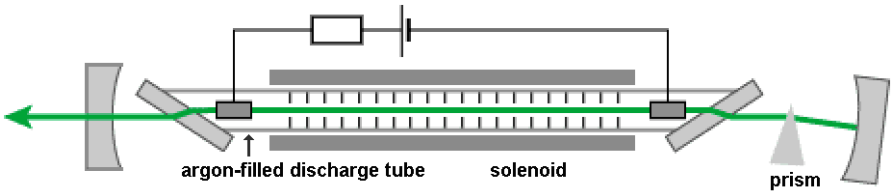

Fig. 2.18: the typical structure of Argon laser oscillator.

A laser device, containing a tube with a length of the order of 1 m, can generate some Watts of output power at the line of 514.5 nm, thereby using several kilowatts of electric power [w2-13]. The voltage drop across the tube may be about 100 V (or a few hundred volts), whereas the current can be several tens of amperes DC, as the gas has to be ionized. It normally requires a three-phase electric power supply. The dissipated heat must be removed with a water flow around the tube. Commonly one uses a closed-circle cooling system containing a chiller, which further adds to the power consumption. On sale are also smaller air-cooled argon ion lasers, generating some hundred of milliWatts of output power from several hundred Watts of electric power [w2-14], [w2-15].

For such power levels, it is to achieve a few mW of the DUV lines by use of intracavity frequency doubling. The mW scores of e.g. the lines at 257.3 or 244 nm are shown later in Table 2.7.

Since Argon-ion lasers emit several laser lines in the range of 400 nm – 600 nm that can be used as the fundamental pumping laser line for SHG to achieve several DUV lines at the wavelengths of 227.3 nm, 229.0 nm, 232.9 nm, 238.2 nm, 244.0 nm, 248.3 nm, 250.9 nm, 257.3 nm and 264.4 nm.

As mentioned in equation (2.16), for a 1 Watt fundamental wave, the maximum power of doubled frequency wave (DUV light) is only about $1.6 \times 10^{-5}\ Watt$ by using a direct SHG process. Therefore, in order to obtain a useful amount of intensity of DUV light, a frequency doubling technique with higher power conversion efficiency is required. There are two techniques that can be used to increase the frequency doubling efficiency, i.e. use of either an external SHG enhancement cavity or use of intracavity SHG.

2.4.2.1 External enhancement cavity SHG for an Argon-ion laser.

Since the external enhancement cavity is a separate device, external enhancement cavity SHG may be suitable for upgrading a pre-existing laser. As mentioned above, the external enhancement cavity SHG method requires that the fundamental laser should be running in single-frequency mode (single-longitudinal mode). If the pre-existing laser is a multi-longitudinal mode laser, firstly, the laser must be upgraded to a single-frequency laser. This can be obtained by implanting an etalon assembly in the laser as a longitudinal mode selector. Normally, the manufacturers of Argon-ion lasers also provide such etalon assembly extra complements, such as the *LEXEL™* Model 503 Temperature-Controlled Etalon Assembly [w2-16]. The Etalon Assembly utilizes normally a solid fused-silica plate in a precisely temperature-controlled oven to provide ultimate frequency stability and controlled mode tuning. When installed in a *LEXEL™* ion laser, extremely stable single frequency operation can be achieved, with an output linewidth of approximately 10^{-4} cm^{-1} (3 MHz). However, the output power will be reduced to approximately 50% because the etalon induces an intra-cavity loss from surface reflections. Because of the power reduction, except for 488 and 514.5 nm lines, other lower power lines for a 4 W level laser will be difficult to use for achieving external enhancement cavity SHGs by frequency doubling.

2.4.2.2 Intracavity SHG for an Argon-ion Laser

Intracavity SHG (or intracavity frequency doubling) is an optical nonlinear process that involves placing a nonlinear crystal within the laser resonator. There are actually two different reasons why this procedure works well:

- Within the laser resonator, the optical powers and thus the intensities achievable are much higher (also higher than the external cavity enhancement), because of increased conversion efficiency per path by often more than an order of magnitude.

- It is normally sufficient to achieve a single-pass-conversion-efficiency of just a few percent, because the unconverted power remains in the laser resonator and can be reused rather than being lost.

Since we already have an existing laser in our laboratory, at first, we investigated if it would be possible to utilize it for frequency doubling. During our investigation, it becomes clear that two main modifications must be made for the already existing Ar-laser to implement intracavity SHG.

1. **The output coupling mirror must be changed to a totally-reflective mirror for the fundamental wave and highly-transparent for SHG.**

For our typical Argon-ion laser (a Coherent Innova CR4), the output coupling mirror is a partly-transparent dielectric mirror. The output coupler mirror transparency is about 5% for the fundamental wave [2.52], meaning that the laser power inside the resonator is 20 times higher than the output power. This power is obviously not enough to achieve useful SHG. In order to increase the laser power inside the resonator, the output coupling mirror should be changed to a totally-reflective mirror for the fundamental wave. In this case, the fundamental wave would be trapped in the cavity and the power inside cavity will be extremely increased. On the other hand, the mirror should be highly transparent for the DUV light, thus the DUV light can be obtained from outside.

2. **The laser cavity should have a beam waist of $radius \approx 20\ \mu m$ to achieve a high enough power density for making the BBO crystal work in SHG.**

Being a gas laser, the output power is affected by the quantity of active ions in the plasma tube: the more ions involved the more output power. The quantity of ions depends on the volume of the laser beam propagating in the plasma tube. Therefore the laser beam is designed to have a large radius in the plasma tube. Normally, for a 2-mirror laser cavity with the length of 1 meter, the rear mirror (M1) is a plane mirror and the front mirror (M2) is a concave mirror with r = 10000 mm, respectively. The beam radius is about 0.7 mm, as shown in Fig. 2.19 (a). The figure shows the interface panel of the laser cavity design software of *Intarsia,* for the case example of the optical parameters of a typical 2-mirror laser cavity of an Argon-ion laser.

The optical parameters for a typical Argon-ion laser cavity (for 488 nm emission) as obtained by use of the Intarsia program are shown below:

- M1: the rear end mirror, a plane mirror.
- M2: the front end mirror, a concave mirror with a radius of curvature *r* = 10 m.
- Length of cavity: 1 m.
- Beam waist: horizontal radius = 0.681 mm, vertical radius= 0.680 mm, located on rear end mirror M1.
- Beam radius on M2 is 0.6911 mm and 0.6922 mm on horizontal and vertical respectively.

As motioned above, a minimal radius of 0.68 mm of a laser beam is too large for SHG. An optimal laser beam should have a tiny beam waist because the SHG efficiency is inversely proportional with the cross section area of the beam, as shown in equation (2.13). However the laser beam waist should not be too small because the smaller beam waist responds the shorter Rayleigh length. The optimized size of the beam

waist can be found by the Boyd-Kleinman expression [2.53]. It requires further optical knowledge to do such a calculation. However the result that can be found from the literature is $\approx 20\ \mu m$ for a nonlinear crystal with a length of 10 mm [2.52]. Therefore, when designing a laser cavity for intra-cavity SHG, on the one hand it is needed to keep the laser beam radius large in the plasma tube (radius = 0.691 mm) to maintain the efficiency of the energy pumping of the fundamental wave, and on the other hand it is also needed to have a tiny beam waist ($radius \approx 20\ \mu m$) for the place of the SHG crystal to achieve a high SHG efficiency. The simplest two-mirror cavity cannot satisfy these two conditions. Therefore, a folded cavity with 3 or 4 mirrors has to be chosen, as shown in Fig. 2.19 (b) and (c).

Typical optical parameters of a 3-mirrors folded laser cavity for the intra-cavity SHG Argon-ion laser are shown below:

- M1: the rear end mirror, a plane mirror.
- M2: the folding mirror, a concave mirror, radius of curvature *r* = 200 mm.
- M3: the front end mirror, a plane mirror.
- Length of cavity: 1.3 m.
- Beam waist 1: horizontal radius = 0.681 mm, vertical radius= 0.706 mm, located on rear end mirror M1.
- Beam radius on M2 is 0.6945 mm and 0.7180 mm on horizontal and vertical respectively. Beam waist 2: horizontal radius = 0.022 mm, vertical radius= 0.021 mm, located on the front end mirror M3.

For a 4-mirrors cavity, the results are shown below:

- M1: the rear end mirror, a plane mirror.
- M2: the folding mirror, a concave mirror, radius of curvature *r* = 200 mm.
- M3: the folding mirror, a concave mirror, radius of curvature *r* = 200 mm.
- M4: the front end mirror, a plane mirror.
- Length of cavity: 1.9 m.
- Beam waist 1: horizontal radius = 0.640 mm, vertical radius= 0.784 mm, located on the rear end mirror M1.
- Beam radius on M2 is 0.6588 mm and 0.7941 mm on horizontal and vertical respectively.
- Beam waist 2: horizontal radius = 0.022 mm, vertical radius= 0.019 mm, location is nearly on the centre of M2 and M3.

Actually, the above 3-mirrors and 4-mirrors cavities are similar to the two different designs which were adopted by the companies Cambridge-Lexel-lasers and Coherent-Radiation-lasers for their lasers, SHG-95-QS and INNOVA- 90C-FRED, respectively. The intrinsic condition for the different designs is the fixed distance between M2 and the BBO crystal, as shown in Fig. 2.19 (b) and (c). This is because a beam radius w(z) = 0.6945 on M2 is required for efficient energy pumping from the plasma tube (see Fig. 2.19 (b)) and a beam radius w0 = 0.022 on the BBO crystal is required for an efficient SHG conversion. As mentioned above, according to equation (2.2) the distance z comes out as $z \approx 9.9\ mm$. But unfortunately, in our already available laser head there was not space enough for this distance and for the mirror mount.

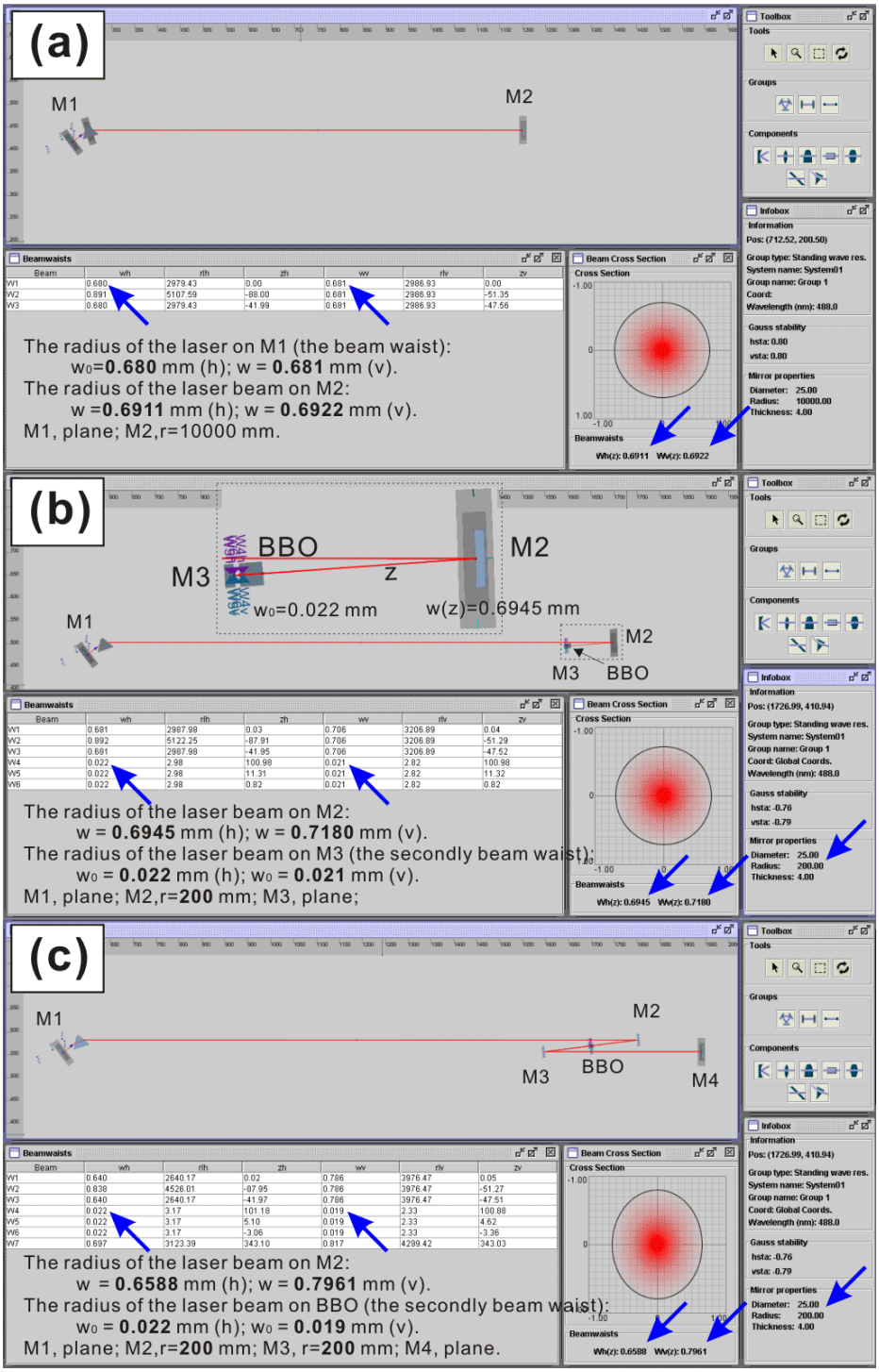

Fig. 2.19: Panels to obtain laser cavities parameters by use of the *Intarsia* program for 3- or 4-mirrors cavity design. (a) This upper panel shows that the profile of the laser beam of a 2-mirror cavity is a nearly collimated beam with a radius of $w_0 \approx 0.7\,mm$. (b) The tasks of a 3-mirrors cavity design is to maintain a $w_0 \approx 0.7\,mm$ beam and to generate a second beam waist with a radius of $w_0 \approx 0.02\,mm$. The parameter for the mirror M2 is calculated as a concave mirror with r = 200 mm. The distance between M2 and BBO is also found as $z \approx 10\,mm$. (c) The function of a 4-mirror cavity is same as the 3-mirror cavity.

2.4.2.3 The Lexel 95-SHG-QS Argon-ion Laser from Cambridge Laser Laboratories Inc. (USA).

The two mentioned lasers, 95-SHG-QS and Innova 90C FRED, are two well known types of intracavity frequency-doubled Argon-ion lasers that are produced by Cambridge Laser Laboratories Inc. and Coherent Radiation, Inc. I have experience with both lasers, and feel that 95-SHG-QS is much easier to operate, switching the output wavelength between the visible and UV, or between different UV lines. In the following we will mainly discuss the 95-SHG-QS laser.

As already mentioned the 95-SHG-QS Argon-ion laser (Fig. 2.20 a) is an intracavity frequency-doubled system, equipped with a nonlinear BBO crystal designed to produce deep-UV coherent laser light by Second Harmonic Generation (SHG). A three-mirror folded cavity design was adopted.

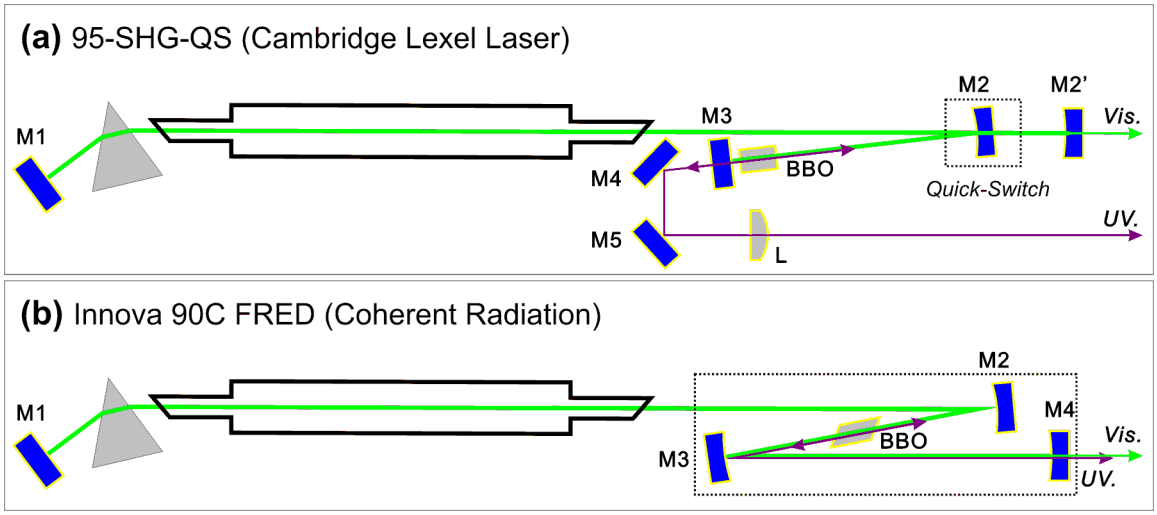

Fig. 2.20: (a) The optical layout of the 3-mirrors cavity of a 95-SHG-QS Argon-ion laser; (b) The optical layout of the 4-mirrors cavity of an Innova 90C FRED Argon-ion laser.

The special feature of 95-SHG-QS is the Quick-Switch design, as also shown in Fig. 2.20. The folding mirror M2 is mounted on a Locating slide shaft (not shown in the figure). When M2 is moved out of the laser cavity, the mirrors M1 and M2' form the normal two-mirrors Argon ion cavity. The M2' is a normal visible output coupler mirror. Therefore, the laser working in this condition is optimized for visible line output. When the M2 is moved back into the cavity, the mirrors, M1, M2 and M3 form a 3-mirrors folded cavity. As motioned above, these three mirrors are totally-reflective for visible light. The mirror M2 is a dielectric mirror. However such so-called totally-reflective mirrors also can transmit a unavoidable small amount of light (such as 0.01%). Since the laser power level inside the cavity is very high (above 100 W under usual operation, we observe the visible laser beam leaking out from the visible output aperture when it is not blocked physically.

The BBO nonlinear crystal is normally placed at the position where the most tiny beam waist is located. However, this tiny beam waist position is located exactly on the mirror M3. Therefore the crystal should be placed ideally as close as possible to M3. But it still needs a gap to avoid scratching during the adjustment. The Lexel Laser company engineers suggest a gap of 2 mm.

When the BBO is placed in the cavity, it will cause the power to drop for the fundamental wave. It is so, not only because of the conversion of power from the fundamental wave to the frequency doubled wave, but also because of the surface reflections of BBO crystal. Since the power of the fundamental wave is very high inside the laser cavity, the power losses by surface reflections become significant. There are two techniques that can be used to reduce the surface reflection losses:

- Brewster angle cutting (adopted for Innova 90C FRED),

The Brewster angle cutting can minimize the surface reflection for the linearly-polarized light. In the Innova 90C FRED there is room for this. However, it is not suitable for the above three-mirror folded 95-SHG-QS cavity, because a tilted surface would require more distance between M3 and the BBO crystal to avoid the touching.

- Anti-reflective coating (adopted for 95-SHG-QS),

The intracavity SHG requires high quality anti-reflective coating to maintain the high internal power in the cavity. A simple one or two layer anti-reflective coating does not satisfy this situation. Therefore multi-layer coating is demanded. Deposition of multi-layer coatings on an anisotropic medium (such as the BBO crystal) is difficult and is therefore increasing the price of the crystal. On the other hand the anti-reflective coating can protect the crystal surface. This is a good thing to avoid deliquescence of slightly hygroscopic materials.

Comparing 95-SHG-QS with Innova 90C FRED, both lasers are allowing us to switch the output wavelength between UV and the visible, or between different UV lines. The former alignment is much easier to achieve in 95-SHG-QS because of the advanced Quick-Switch design. Oppositely, the switching of wavelength for the Innova 90C FRED is inconvenient. Firstly, one needs to replace three mirrors, M2, M3 and M4 as shown on Fig. 2.20 (b). Secondly, it is necessary to start the laser cavity alignment from a zero output light state, meaning that one has to slowly scan the angle of M4 in horizontal and vertical directions. Furthermore, the Brewster angle cutting also makes the alignment troublesome since the acceptable angle of the BBO crystal is quite small.

2.4.2.4 The Operating Cautions for Switching Wavelengths between the DUV Lines.

Due to the Phase-matching condition, SHG for each of various wavelengths requires respective cutting angles matching each particular wavelength. Therefore we have to change between the different BBO crystals to have doubling for the different wavelengths. Our laboratory at present is equipped with a Lexel 95-SHG-QS Argon-ion Laser. Since the operating manual does not specify the details of switching between the DUV wavelength lines we here make some remarks for the cautious operation of these shifts.

There are two main steps to change the UV lines:

1. **Optimize the visible power at the selected wavelength.**

The wavelength selection can be performed by adjusting the rear mirror M1 in horizontal direction as shown on Fig. 2.21 (a). On the rear of laser head we can see the corresponding screw, denoted with “HORIZONTAL & WAVELENGTH”, as shown on Fig. 2.21. There is no indicator to show the running

wavelength. However the wavelengths can be practically distinguished by the relative position (rotation angle) of the screw and the power level (in % of the strongest line of 514.5 nm), as shown in table 2.7.

The "VERTICAL" screw is used for adjusting the vertical direction of M1 for the power optimization. It should be noted that the horizontal screw should be on the optimal position first: **Never try to** adjust the vertical screw when there is *no* output laser *light*.

Fig. 2.21: View of the rear of the laser head.

Table 2.7: Output power and relative position of the horizontal screw for wavelength adjustments.

Wavelength (nm)	The output Power @ 30A (W)	Relative position of the Horizontal screw (degrees)
514.532	2.4	CCW 0
501.716	0.55	CCW 120
496.507	0.85	CCW 180
487.986	2.1	CCW 280
476.486	0.80	CCW 360+60
472.686	0.35	CCW 360+100
465.789	0.2	CCW 360+190
457.935	0.3	CCW 360+300
454.505	0.2	CCW 360+360
CCW: Counter-Clock-Wise		
Note: The power was measured without optimizing the vertical knob		

2. Replacing the corresponding BBO crystal in the laser cavity

The BBO crystal is mounted on a platform. It allows adjusting the horizontal and vertical direction from the top of the platform, as shown in Fig. 2.22 a). The height of crystal is also adjustable from the top via a setting screw in the middle of the platform.

Before installing the BBO crystal in the laser cavity, one should make sure that there is no dust staying on the surface of the crystal. Since the laser will be highly focussed on the BBO, with a radius $w_0 \approx 0.02\ mm$ and the intracavity power can reach hundreds of Watts, it results in above 10^5 W/mm^2 of power density in the laser beam. It will burn or vaporize any dust therefore damage is done to the coating. Although the beam radius is only 0.02 mm, when we adjust the mirrors or the crystal to optimize the lasing, the laser beam is moving around on the surface of the crystal, so no dust particles can escape to be burnt.

Fig. 2.23 shows the laser beam path and the position of the optical components. When the BBO crystal is ready for being installed, one should pay attention to the location of the M2, and to avoid touching the BBO crystal during the installation. Finally one should make sure that the wires do not block the laser beam.

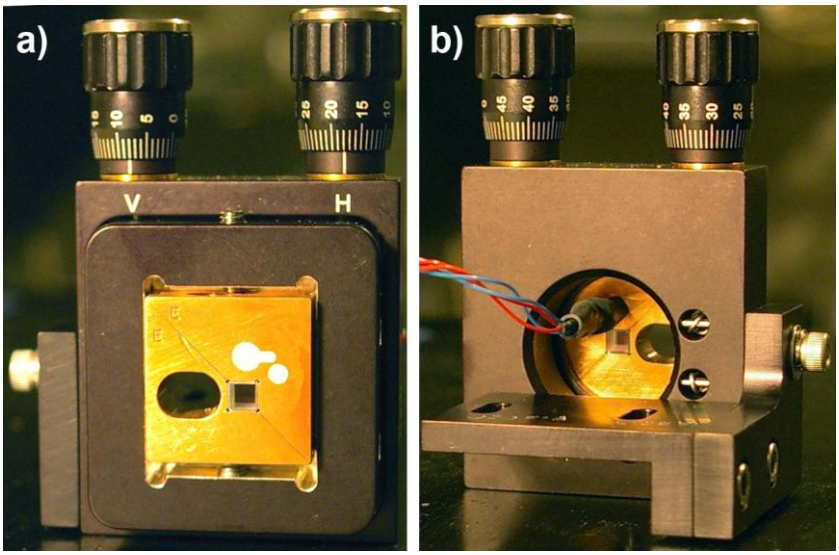

Fig. 2.22: the view of the BBO crystal platform.

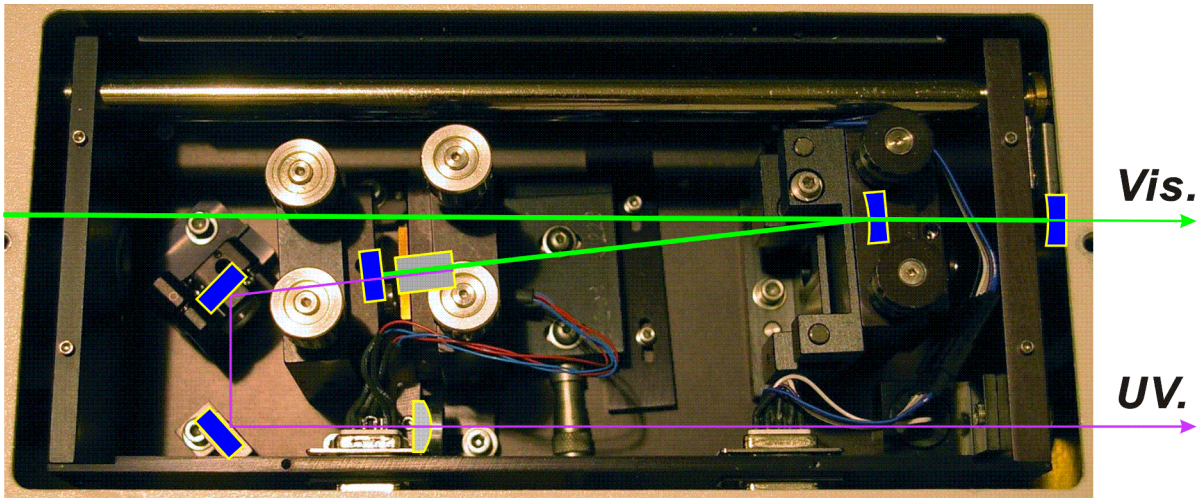

Fig. 2.23: The laser beam path and the location of the optical components in the laser head.

References to Chapter 2

[2.1] T. H. Maiman, "*Stimulated optical radiation in Ruby*", Nature (**1960**), 187, pp. 493-494.

[2.2] A. Javan, W. R. Bennett Jr. and D. R. Herriott, "*Population inversion and continuous optical maser oscillation in a gas discharge containing a He–Ne mixture*", Phys. Rev. Lett. (**1961**), 6 (3), pp. 106.

[2.3] M. S. Shur and R. Gaska, "*III-Nitride Based Deep Ultraviolet Light Sources*", Gallium Nitride Materials and Devices III, edited by Hadis Morkoç, Cole W. Litton, Jen-Inn Chyi, Yasushi Nanishi, Euijoon Yoon, Proc. of SPIE Vol. 6894, (**2008**), pp. 689419-1-8.

[2.4] Schuocker D., "*Handbook of the Eurolaser Academy*", (**1998**), Springer, ISBN: 0412819104.

[2.5] F. J. Duarte and L. W. Hillman, "*Dye Laser Principles*", Academic Press, New York, (**1990**), Chapter 6.

[2.6] P. F. Moulton, "*Spectroscopic and laser characteristics of Ti:Al_2O_3*", J. Opt. Soc. B, vol. 3, (**1986**), pp. 125.

[2.7] G. Huber, C. Krankel, and K. Petermann, "*Solid-state lasers: status and future*", Proc. of SPIE Vol. 7784, (**2010**), pp. 77840K.

[2.8] Mark C. Sparrow, John F. Jackovitz, Calum H. Munro, William F. Hug, and Sanford A. Asher, "*New 224 nm Hollow Cathode Laser–UV Raman Spectrometer*"**,** APPLIED SPECTROSCOPY, Volume 55, Number 1, (**2001**), pp. 66-70.

[2.9] M. C. Storrie-Lombardi, W. F. Hug, G. D. McDonald, A. I. Tsapin, and K. H. Nealson, "*Hollow cathode ion lasers for deep ultraviolet Raman spectroscopy and fluorescence imaging*", REVIEW OF SCIENTIFIC INSTRUMENTS, Volume 72, Number 12. (**2001**), pp. 4452-4459.

[2.10] A. Ashkin, G. D. Boyd, and J. M. Dziedzic, "*Resonant optical second harmonic generation and mixing*", IEEE J. Quantum Electron. QE-2, (**1966**), pp. 109-124.

[2.11] R. G. Smith, "*Theory of intracavity optical second-harmonic generation*", IEEE J. Quantum Electron. QE-6, (**1970**), pp. 215-223.

[2.12] R. Degl Innocent, A. Majkic, F. Sulser, L. Mutter, G. Poberaj, and P. Gunter, "*UV Second Harmonic Generation at 266 nm in He^+ Implanted β-BaB_2O_4 Optical Waveguides*", Optical Express, 15, (**2008**), pp. 11660-11669.

[2.13] Bahaa E.A.Saleh and Malvin Carl Teich, *Fundamentals of Photonics*. Wiley Interscience Publication, (**1991**), pp. 607-618.

[2.14] Hideki Hirayama, Norimichi Noguchi, Sachie Fujikawa, Jun Norimatsu, Norihiko Kamata, Takayoshi Takano, Kenji Tsubaki, "*222-282 nm AlGaN and InAlGaN based deep-UV LEDs fabricated on high-quality AlN template*", Gallium Nitride Materials and Devices IV, Proc. of SPIE Vol. 7216, (**2009**), pp. 721621.

[2.15] A. E. Siegman, *Lasers*, University Science Books, Mill Valley, CA (**1986**).

[2.16] Boivin, Louis-Philippe, "*Study of bandwidth effects in monochromator-based spectral responsivity measurements*", Applied Optics, vol. 41, iss. no. 10, (**2002**), pp. 1929-1935.

[2.17] Govind P. Agrawal, *Fiber-Optic Communication Systems*, Third Edition. (**2002**), John Wiley & Sons, Inc., ISBNs: 0-471-21571-6 (Hardback); 0-471-22114-7 (Electronic)

[2.18] ISO 11146-1:2005(E), "Lasers and laser-related equipment — Test methods for laser beam widths, divergence angles and beam propagation ratios — Part 3: Intrinsic and geometrical laser beam classification, propagation and details of test methods".

[2.19] F. Gravier and B. Boulanger, "*Cubic parametric frequency generation in rutile single crystal*", Opt. Express 14 (24), (**2006**), pp. 11715- 11720.

[2.20] K. Miyata *et al.*, "*Phase-matched pure $\chi^{(3)}$ third-harmonic generation in noncentrosymmetric BiB_3O_6*", Opt. Lett. 34 (4), (**2009**), pp. 500-502.

[2.21] Boyd, G. D. and Kleinman, D. A, "*Parametric Interaction of Focused Gaussian Light Beams*", Journal of Applied Physics, Volume 39, Issue 8, (**1968**), pp. 3597-3639.

[2.22] Krishnan R. Parameswaran, Jonathan R. Kurz, Rostislav V. Roussev, and Martin M. Fejer, "*Observation of 99% pump depletion in single-pass second-harmonic generation in a periodically poled lithium niobate waveguide*", OPTICS LETTERS, Vol. 27, No. 1, January 1, (**2002**), pp. 43-45.

[2.23] C. Czeranowsky, V. Baev, and G. Huber, "*Stabilization of intracavity frequency-doubled lasers with type I phase matching*", OPTICS LETTERS , Vol. 28, No. 21, November 1, (**2003**), pp. 2100-2102.

[2.24] Velsko S.P., Webb M., Davis L., Huang C., "*Phase-matched harmonic generation in lithium triborate (LBO)*", Quantum Electronics, Volume: 27, Issue: 9, ISSN: 0018-9197, (**1991**), pp. 2182 – 2192.

[2.25] Shichao Wang and Ning Ye, "*$Na_2CsBe_6B_5O_{15}$: An Alkaline Beryllium Borate as a Deep-UV Nonlinear Optical Crystal*", Am. Chem. Soc., Volume 133, Issue 30, (**2011**), pp. 11458-11461.

[2.26] C. T. Chen, G. L. Wang, X. Y. Wang and Z. Y. Xu, "*Deep-UV nonlinear optical crystal $KBe_2BO_3F_2$ — discovery, growth, optical properties and applications*"**,** Applied Physics B: Lasers and Optics, Volume 97, Issue 1, (**2009**), pp. 9-25.

[2.27] S. Kase and K. Ohi, "*Optical-Absorption and Interband Faraday-Rotation in $LiTaO_3$ and $LiNbO_3$*", Ferroelectrics, Volume 8, Issue 1-2, (**1974**), pp. 419-420.

[2.28] I. Akasaki, H. Amano, S. Sota, H. Sakai, T. Tanaka, and M., Koike, "*Stimulated Emission by Current Injection from an AlGaN/GaN/GaInN Quantum Well Device*", Japanese Journal of Applied Physics - Part 2 Letters, Volume 34, Issue 11, (**1995**), pp. 1517-1519.

[2.29] S. Nakamura, M. Senoh, S. Nagahama, N. Iwasa, T. Yamada, T. Matsushita, H. Kiyoku, and Y. Sugimoto, "*InGaN multi-quantum-well-structure laser diodes with cleaved mirror cavity facets*", Japanese Journal of Applied Physics - Part 2 Letters, Volume 35, Issue 2 B, (**1996**), pp. L217-L220.

[2.30] Harumasa Yoshida, Masakazu Kuwabara, Yoji Yamashita, Kazuya Uchiyama, and Hirofumi Kan, "*The current status of ultraviolet laser diodes*", Phys. Status Solidi A 208, No. 7, (**2011**), pp. 1586–1589.

[2.31] Alexander Knitsch, Martin Traub, Karsten Rotter, Dieter Hoffmann, Peter loosen, Reinhart Poprawe, "*Characterization of tapered diode laser bars for the use on high power diode laser systems*", Proceedings of the SPIE - The International Society for Optical Engineering, Volume 5336, Issue 1, (**2004**), pp. 56-64.

[2.32] Karl Koch and Gerald T. Moore, "Singly *resonant cavity-enhanced frequency tripling*", Journal of the Optical Society of America - B - Optical Physics, Volume 16, Issue 3, (**1999**), pp. 448-459.

[2.33] L. Goldberg and D. A. V. Kliner, "*Deep-uv generation by frequency quadrupling of a high-power GaAlAs semiconductor laser*," Opt. Lett. 20, (**1995**), pp. 1145-1147.

[2.34] P. D. Maker, R.W. Terhune, M. Nisenoff, and C. M. Savage, "*Effects of Dispersion and Focusing on the Production of Optical Harmonics*", PHYSICAL REVIEW LETTERS, Vol. 8, No. 1, January 1, (**1962**), pp. 21-22.

[2.35] E. Hecht, "*Optics*", Addison-Wesley, San Francisco, CA, 4th edition, ISBN: 0321-18878-0, (**2002**), pp.423.

[2.36] R. A. Morgan, "*Vertical-cavity surface-emitting lasers: present and future*", Proc. SPIE 3003, (**1997**), pp. 14-26.

[2.37] R. W. P. Drever, J. L. Hall, F. V. Kowalski, J. Hough, G. M. Ford, A. J. Munley, H. Ward, "*Laser phase and frequency stabilization using an optical resonator*", Applied Physics B*,* Volume 31, Issue 2, (**1983**), pp. 97-105.

[2.38] R. L. Byer, "*Diode laser-pumped solid-state lasers*", Science, Volume 239, Issue 4841, (**1988**), pp. 742-747.

[2.39] G. Huber, C. Kränkel, and K. Petermann, "*Solid-state lasers: status and future*", Optical Society of America *B,* Vol. 27, Issue 11, (**2010**), pp. B93-B105.

[2.40] X. Délen *et al.*, "*Temperature dependence of the emission cross section of Nd:YVO_4 around 1064 nm and consequences on laser operation*", Optical Society of America *B,* Vol. 28, issue 5, (**2011**), pp. 972-976.

[2.41] D. Sangla *et al.*, "*Highly efficient Nd:YVO_4 laser by direct in-band diode pumping at 914 nm*", Opt. Lett. 34 (14), (**2009**), pp. 2159-2161.

[2.42] J. E. Geusic *et al.*, "*Laser oscillations in Nd-doped yttrium aluminum, yttrium gallium and gadolinium garnets*", Appl. Phys. Lett. 4 (10), (**1964**), pp. 182-184.

[2.43] J. R. O'Connor, "*Unusual crystal-field energy levels and efficient laser properties of YVO_4:Nd*", Appl. Phys. Lett. 9, (**1966**), pp. 407-409.

[2.44] J.F.Pinto, L.Esterowitz and G.J.Quarles, "*High performance Ce3+:LiSrAlF6/LiCaAlF6 UV lasers with extended tunability*", Electronics Letters, Volume 31, Issue 23, (**1995**), pp. 2009-2011.

[2.45] Joseph F. Pinto, Leon Esterowitz, and Timothy J. Carrig, "*223 and 243 nm by Sum Frequency Mixing in β-Barium Borate*", Applied Optics, Vol. 37, Issue 6, (**1998**), pp. 1060-1061.

[2.46] Stephen A. Payne, L. L. Chase, L. K. Smith, Wayne L. Kway, and Herbert W. Newkirk, "*Laser performance of $LiSrAlF_6:Cr^{3+}$*", Applied Physics, Volume 66, Issue 3, (**1989**), pp. 1051-1056.

[2.47] P. F. Moulton, "*Spectroscopic and laser characteristics of Ti: Al_2O_3*", J. Opt. Soc. Am. B 3 (1), (**1986**), pp. 125-133.

[2.48] Bykov Sergei, Lednev Igor, Ianoul Anatoli, Mikhonin Aleksandr, Munro Calum, Asher, Sanford A, "*Steady-State and Transient Ultraviolet Resonance Raman Spectrometer for the 193–270 nm Spectral Region*", APPL. PECTROSC., Vol. 59, Number 12, (**2005**), pp.1541- 1552.

[2.49] G. Balakrishnan, Y. Hu, S. B. Nielsen, and T. G. Spiro, "*Tunable kHz Deep Ultraviolet (193-210 nm) Laser for Raman Application*", Appl. Spectrosc. 59, (**2005**), pp. 776-781.

[2.50] K. Rozsa, L.Csillag, M.Janossy, and T.Salamon, "*INVESTIGATION OF A HELIUM-CADMIUM ION LASER WITH A HOLLOW CATHODE*", Sov J Quantum Electron, Volume 4, Issue 4, (**1974**), pp. 523-524.

[2.51] W. B. Bridges, "*LASER OSCILLATION IN SINGLY IONIZED ARGON IN THE VISIBLE SPECTRUM*", Appl. Phys. Lett. 4, (**1964**), pp. 128-130.

[2.52] S.R. AbduUina, S.A. Babin, A.A. Vlasov, S.I. Kablukov, "*Intracavity frequency doubling in a wide-aperture argon laser*", Quantum Electronics 35(9), (**2005**), pp. 857-861.

[2.53] Boyd, G. D. and Kleinman, D. A. "*Parametric Interaction of Focused Gaussian Light Beams*", J. Appl. Phys., 39, (**1968**), pp. 3597-3639.

[2.54] Robert W. Boyd, "*Nonlinear Optics*", Edition 2, ISBN: 0121216829, 9780121216825, Academic Press, (**2003**). pp. 87-94.

[2.55] F. M. Phelps III, M.I.T. Wavelength Tables, Wavelengths by Element, The MIT Press, Cambridge, Massachusetts, Volume 2, (**1982**), pp. 270-280.

[2.56] P. Lallemand, P. Simova, "*Stimulated Raman Spectroscopy in Hydrogen Gas*", Journal of Molecular Spectroscopy, 26, (**1968**), pp. 262-276.

[2.57] John Reintjes, Mark Bashkansky, "*Stimulated Raman and Brillouin Scattering*", *Handbook of Optics*, Digital Engineering Library @ McGraw-Hill, (**2010**), 15, pp. 8.

[2.58] S. A. Asher, C. R. Johnson, J. Murtaugh, "*Development of a New UV Resonance Raman Spectrometer for the 217-400 nm Spectral Region*", American Institute of Physics, (**1983**), pp. 1657-1662.

[w2-1] http://www.newport.com/WaveTrain-CW-Frequency-Doubler/368121/1033/catalog.aspx
[w2-2] http://www.coherent.com/products/?341/MBD-200
[w2-3] http://www.toptica.com/products/diode_lasers/research_grade_diode_lasers/frequency_converted_diode_lasers/shg_pro_stand_alone_second_harmonic_generator_module.html
[w2-4] http://www.toptica.com/products/diode_lasers/research_grade_diode_lasers/tunable_diode_lasers/bluemode_high_coherence_and_high_power_at_405_nm.html
[w2-5] http://www.toptica.com/products/diode_lasers/research_grade_diode_lasers/frequency_converted_diode_lasers/ta_fhg_pro_frequency_quadrupled_tunable_diode_laser.html
[w2-6] http://www.as-photonics.com/SNLO.html
[w2-7] http://www.klastech.com/verve-266nm-laser_15.html
[w2-8] http://www.coherent.com/Products/index.cfm?874/Azure
[w2-9] http://www.kimmon.com/lasers/overview.html
[w2-10] http://www.intarsiaoptics.dk/
[w2-11] http://www.laser2000.se/index.php?id=366686
[w2-12] http://www.lexellaser.com/NS/techinfo_gas-ion.htm#singlefreq
[w2-13] http://www.lexellaser.com/
[w2-14] https://www.cvimellesgriot.com/Products/Air-Cooled-Lasers.aspx
[w2-15] http://www.laserphysics.co.uk/argon_laser.html
[w2-16] http://www.lexellaser.com/NS/techinfo_features_single-freq_503-etalon.htm#FEATURES

3 DUV Raman system

A DUV Raman system is a Raman system that is able to perform the measurement of a Raman spectrum excited by the DUV light sources. Compared with a traditional Raman system working in the range of visible or near Infrared, the DUV Raman system have more stringent conditions for the optical components. In this chapter, the various DUV optical components will be described, with particular focus on the quality of the measurements. This naturally involves themes such as spectral resolution, sensitivity, eliminating background noise and so on.

On the other hand, operating convenience should be considered because a Raman system for scientific research applications is necessary (or at least it is an advantage) to have several different excitation lines, even including some visible lines. An intracavity frequency doubled Argon-ion laser (Lexel 95-SHG-QS) has been adopted as the DUV excitation laser (described in chapter 2). We have chosen three prime DUV laser lines, 257.3, 244 and 228.9 nm, which are relative strong lines and cover the broadest DUV wavelength range of the frequency doubled Argon laser. There are two advantages of choosing these DUV lines. Firstly, some kinds of samples still have fluorescence for 257.3 and 244 nm excitation [3.1], making it necessary to provide an even deeper wavelength, 228.9 nm, to avoid the fluorescence interference. Secondly, these three lines also provide more opportunity to study possible resonance Raman effects [3.2]. When including the two visible lines, 514.5 and 488 nm, the system in total comprise to work with 5 excitation lines. Therefore it is important to set up a practical layout that will save time when switching different excitation wavelengths.

Furthermore, it is important to consider the laser safety because DUV light is a potentially extremely dangerous kind of invisible radiation.

3.1 DUV Optical Components

3.1.1 Gratings

For a grating based spectrometer the quality of the grating affects almost all the parameters of the spectrometer, such as the measurement sensitivity, the background noise and the spectral resolution. The effect on the measurement sensitivity is caused by the diffractive efficiency of the grating because the diffraction efficiency affects directly the signal intensity. Normally, the spectrometer only utilizes the first order diffracted light. In order to optimize this first order diffraction light, an optimum *blazed* grating is the best choice. A blazed grating can provide 100% efficiency at first order diffraction for certain wavelengths at a certain incident angle, at least theoretically [3.3]. This optimized wavelength is so-called blazed wavelength. Around the blazed wavelength, a relatively high efficiency can be achieved. Fig. 3.1 shows the efficiency curve of a typical blazed grating, produced by the leading company HORIBA Jobin Yvon and blazed at 290 nm [w3-1]. The blazed wavelength of a DUV grating should optimally be chosen not too far from the range where the DUV Raman signals are to be excited.

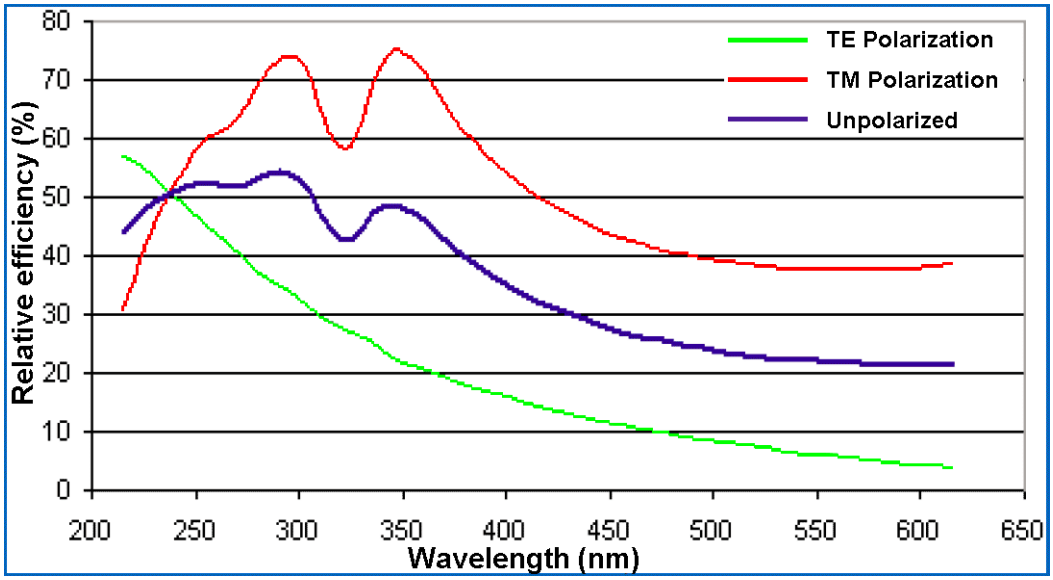

Fig. 3.1: The efficiency curve of a typical blazed grating produced by HORIBA-Jobin-Yvon (blazed at 290 nm). In TE (*transverse-electric*) polarization, also called S-polarization, the polarization of electric field is perpendicular to the *plane of incidence* (the same plane as the incident ray, the surface normal and the reflected ray); In TM (*transverse-magnetic*) polarization, also called P-polarization, the electric field is linearly polarized in the *plane of incidence*. [w3-2]

With respect to the spectral resolution, when comparing visible Raman spectra with the DUV Raman spectra the tendency is in DUV to have low spectral resolution (broad bands) because the spectral resolution is proportional to the square of the absolute wavenumber of the Raman signal [3.4]. The grating groove density is one of the main parameters dominating the spectral resolution of a spectrometer because the resolution is inversely proportional to the groove density of the grating [3.4]. Therefore, for an optimal DUV Raman spectrometer, the grating is required to have a groove density as high as possible to achieve the best (narrow) spectral resolution. However groove densities higher than 3600 groove/mm is rarely found on the commercial market.

There are two typical methods to manufacture grating grooves, the diamond ruling or the holographic recording. The diamond ruling is a purely mechanical method. Oppositely, the holographic recording produces the grooves by recording the pattern from the interference between two laser beams on a photoresist layer. The holographic recording method can completely eliminate any periodic errors of the grooves that – if occurring – may cause the strange diffraction behaviours, so-called *ghosts*. The overall quality of the holographic grating surface is such that imperfections and roughness are considerably less than those found in mechanical ruled gratings. This is important to reducing stray light, because the Raman spectra in general are quite weak. Regarding the background noise of the Raman spectrum, it is important to avoid as much stray light from the grating as possible because it directly increases the background noise. This stray light is depicted on the CCD as shown on Fig. 3.7.

Practically speaking, the diffraction efficiency depends on not only the micro structure of grating grooves but also on the surface reflectance. For the DUV application, the best material of the surface reflector is aluminium with a protective coating.

3.1.2 Mirrors

There are mainly three kinds of different mirrors in the Raman system. One is used for the transportation of the laser line, such as mirrors M1, M2 and M3 in Fig. 3.7; the second is used for the transportation of the Raman signal, such as the double Triangular mirror; the third is dichroic mirrors (a primary filter) as shown on Fig. 3.7. The former two kinds of mirrors are required to have as high as possible a reflectance to reduce the optical losses during the beam transportation. The third kind of mirrors is required to have high reflectance for the laser line. At the same time, it should be transparent for the Raman signal. Actually, this kind of mirror plays a role as a laser line filter, because it also acts to reflect the return laser line from sample, thus being a so-called primary filter. The polarization of the return laser line can however be different from the input laser line. Since the reflectance of this partly transparent mirror is polarization dependent, it may be unable to reflect the entire retuned laser line. Therefore, a further filter is necessary to make the spectrometer work, as shown in Fig. 3.7.

These various functions of the above mirrors are implemented by the various optical coatings. These high reflective coatings mainly consist of three types: metallic, dielectric and enhanced metallic mirrors.

The metallic mirrors are typically made by depositing a thin layer of metal on a glass or other optical substrate material. The metals are commonly aluminium, silver and gold. The metal used determines the reflection characteristics of the mirror; an aluminium coating yields a reflectivity of around 88%-92% from DUV to infrared (200 nm - 5 µm) as shown in Fig. 3.2. Silver has a reflectivity of 95%-99% long into the far infrared, but suffers from decreasing reflectivity (<90%) in the blue and UV spectral regions. Gold gives excellent (98%-99%) reflectivity throughout the infrared (better than silver), but limited reflectivity at wavelengths shorter than 550 nm, resulting in the typical gold colour. Therefore silver and gold are not suitable for DUV coatings, and aluminium is to be preferred.

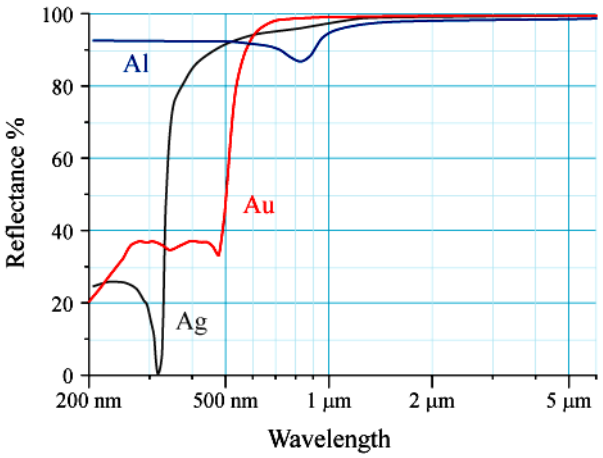

Fig. 3.2: Reflectance vs. wavelength curves for aluminium (Al), silver (Ag), and gold (Au) metal mirrors at normal incidence.

The dielectric mirrors are made by depositing a series of lays having a different refractive index to the substrate. These thin layers are constructed from materials such as magnesium fluoride, calcium fluoride, and various metal oxides. By careful choice of the exact composition, thickness, and number of these layers, it is possible to tailor the reflectivity and transitivity of the coating to produce almost any desired

characteristic. When illuminated the reflective waves from the many boundaries of the layers result in constructive or destructive interference depending on the wavelength. The reflection coefficients of the surfaces can e.g. be reduced to less than 0.2%, producing an *antireflection* (AR) coating. Conversely, the reflectivity can be increased to greater than 99.99%, producing a *high-reflector* (HR) coating. The level of reflectivity can also be tuned to any particular value, over some range of wavelengths. Alternatively, the coating can be designed such that the mirror reflects light only in a narrow band of wavelengths, producing an optical filter [3.5]. For such a dichoric mirror working in DUV, the substrate should be transparent, such as is extremely pure fused silica.

The functionality of a dielectric coating is usually sensitive to wavelength, incident angle, and polarization. A great number of layers are required to achieve high reflectivity. This is increasing the price. Often applied dielectrics have a few layers on the top of a metal film, and such devices can achieve higher reflectance than the simple metal film. The reflectance is then not so sensitive to wavelength, incident angle, and polarization. Since the dielectric layer increases the reflectance and also provide a protection layer to the metal layer, such items are often called *enhanced mirrors*, or sometimes *protected mirrors* (for single dielectric layer).

With their low sensitivity to wavelength, incident angle and polarization, the enhanced mirror is highly suitable for the Raman signal transport. Since the HR dielectric mirrors are excellently working also for laser line (in such a case called laser mirrors), we have chosen to use the HR dielectric mirrors for laser lines transport, but it must be remembered that such mirrors - being optimized for certain wavelengths - are not suitable for transport of the Raman signal.

3.1.3 Filters

Normally, the Rayleigh scattering is much stronger than the Raman scattering. When no filter is applied, the Rayleigh light can easily saturate the CCD array and totally swamp out the Raman spectrum. The excessive saturation can spread to the whole CCD by so-called CCD-crosstalk, and even damage may be done to the CCD. In this way, the strong Rayleigh light can affect the whole spectrum. Even if one records the spectrum in a range far away from laser line, the recording may hence be spoiled by the stray light. Thus, this strong background noise should be avoided. This on the other hand, requires a filter that has a certain shape of transmission curve to obtain filtering of the Rayleigh light but not the low frequency shift Raman signal. The normal absorptive type filter cannot satisfy such condition therefore.

For the application to Raman instrumentation, mainly three types of filters are used as below:

1. Dielectric filters. These filters are actually the dichroic dielectric mirrors as mentioned above. They can be edge or notch type filters depending on the design.

2. Holographic filters. These filters are also having layers structure. The optical principle of these filters is similar to that of dielectric filters, i.e. selective reflection of various wavelengths implemented by optical wave interference from various layers. The main difference is that the layer structure of a holographic filter is obtained by recording the interference pattern of two collimated

ultraviolet laser beams (such as 312 nm) on a *photosensitive glass* [3.6], [3.7]. The filter is called "holographic" because of the method of producing it (two laser beams interfering to generate the layer structure). Thus the spacing of each layer is exactly equal, resulting only one wavelength to have total reflectance like in a Bragg grating. Therefore, holographic filters can only perform a single line type of filtering (notch type filter). The photosensitive glass is sensitive for short wavelengths. The layered structure of the holographic filter is made by exposure of two UV lasers beam interference. The finished products of holographic filters are still photosensitive for UV exposure. The layered structure can be wiped off if the filter was working continually in an UV environment. Therefore the holographic filters are not available for the UV range. Compare to the dielectric filter, in which the layers are made by CVD (Chemical Vapour Deposition), for holographic filters it is easy to achieve a great number of layers that give a sharper edge in the transmission curve.

3. Double monochromator filters. A double monochromator filter is a quite large object composed of two monochromators with their mechanical systems operating in tandem. The first monochromator disperses scattered light - collected from a testing Raman sample and sent in through a *quite narrow entrance slit* - and then separates most of the Rayleigh light spatially from the Raman light, sending it e.g. to the right of the *quite open intermediate slit*. The second monochromator is arranged inversely to the first monochromator. The certain range of the Raman spectrum, passing the intermediate slit, is thereby concentrated at the quite narrow exit slit, then filtering off the light outside the spectral range determined by the intermediate slit. As defined by the intermediate slit width these filters are flexible and wavelength tuneable.

3.1.4 Lenses

For DUV Raman applications, firstly, the medium of the lenses should be highly transparent for the DUV light. Even then the lens can induce a background signal from the lens material, especially for the objective because here much light of the strong laser beam is passing. Use a reflective objective (a Cassegrain type objective) instead of traditional refraction type objective can eliminate such background signal. Secondly, the lenses - if used - should have a broadband DUV AR coating. Without such a coating each surface of lens would have about 4% of reflectance losses. Therefore a one lens alone will induce about 8 % loss in intensity passing once and light has to pass forth and back. In addition to this problem, reflection from the lenses may also add to the stray light.

3.1.5 CCD

Today charge-coupled device (CCD) detectors are commonly known from photographic cameras and mobile phones. Such typical silicon-based gate devices are unresponsive to UV light because of the high absorption of the UV radiation in the polysilicon gate material, which leads to a short penetration depth. Most of the radiation is simply absorbed in the gate material rather than entering within the channels of

the CCD [3.8]. Because of this absorption there has been efforts to reduce the thickness of the silicon material, and illumination from the front (side of the electronics circuits) or from the back of the material. Fig. 3.3 shows typical front-illuminated and back-illuminated CCDs. The gates are made of very thin polysilicon, being reasonably transparent at long wavelengths, but becoming opaque at wavelengths shorter than say 400 nm. Thus, at shorter wavelengths, the gate structure attenuates most of the incoming light.

A useful technique solving the absorption problem is to use a *lumogen* (light-emitting) phosphor coating to convert the UV radiation to visible. This improves the sensitivity of the CCDs in the blue-visible and ultraviolet (UV) wavelength ranges. Fig. 3.4 shows the improved UV sensitivity a e.g. a phosphor-coated UV CCD from Alphalas.

It is worth to note, however, that one has a common problem with such *lumogen* coatings. They exhibit a steady drop in sensitivity with the accumulated UV exposure. Furthermore, the lifetime of the CCD will depend on the ageing of the phosphor coating.

The other solution is the use of a back-illuminated CCD. By using acid-etching techniques from the back of the side with the electronics, it is possible to uniformly thin a CCD to a thickness of approximately 10 µm. This is possible because there is no gate structure on the backside of the CCD as shown in Fig. 3.3 (b). When the incoming light is illuminating the backside of the thinned CCD a high sensitivity to light is obtained, ranging from the soft X-ray to the near-infrared regions of the spectrum.

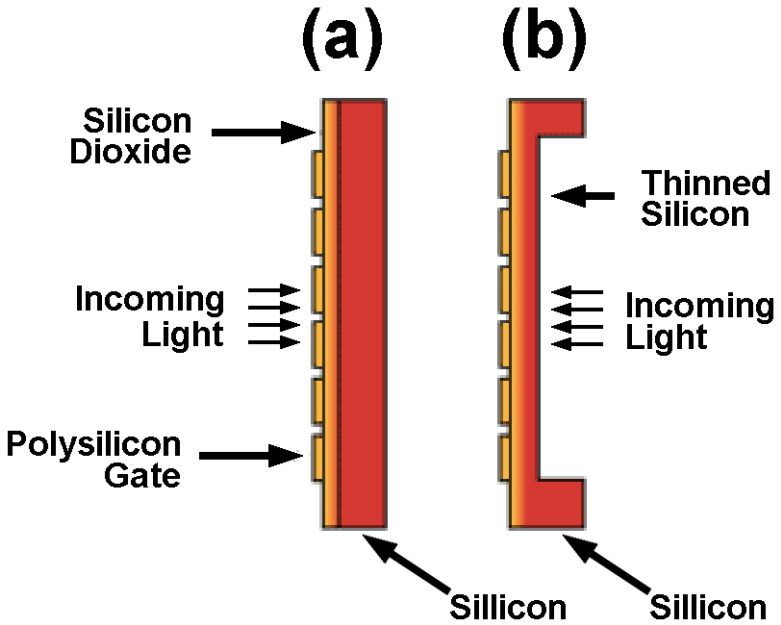

Fig. 3.3: (a) Front Illuminated CCD; (b) Backside Illuminated CCD. [w3-3]

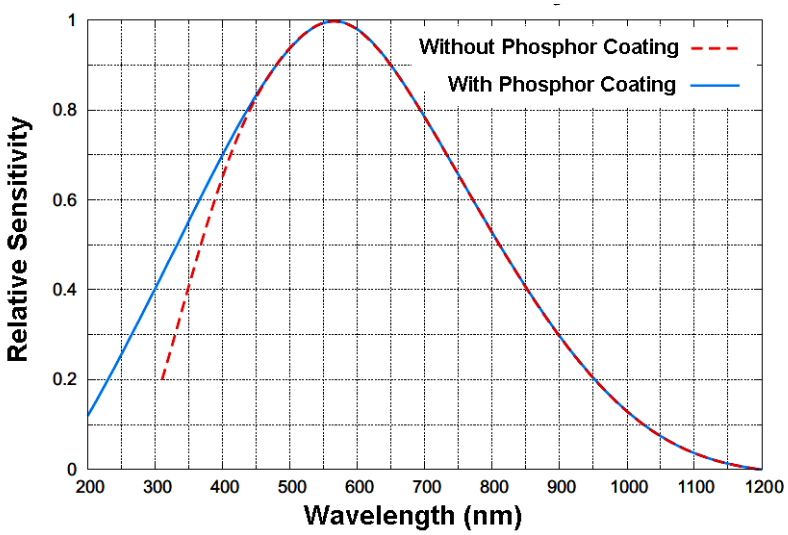

Fig. 3.4: The spectral sensitivity curves of the front illuminated CCD, with and without phosphor coating. [w3-4]

3.1.6 Prism Pre-Monochromator

In many cases, the DUV light sources are obtained by using frequency conversion from visible or infrared light. The output DUV light often contains the fundamental wave, more or less. For the pulsed laser frequency conversions, the output beam contains normally a remarkable amount of the fundamental wave, as shown in Fig. 2.14. As an optical dispersion element, a prism is used to separate the frequency converted beam from the fundamental beam. For the CW laser, the intensity of fundamental wave is present in the output beam in relatively low amount because the end mirror of laser cavity is highly reflective for the fundamental wave, as shown in Fig. 2.14. The fundamental wave itself has such a low wavenumber that it does not appear in the Raman spectrum (within the range of 4000 cm^{-1}, at least). However the fundamental light can pass directly through the filters (see Fig. 3.7) and thus may increase the background noise. Therefore, it is necessary to use prism to eliminate the fundamental wave even for the case of a CW DUV laser source.

For the linearly polarized laser beam, it is possible to design a prism which satisfies the Brewster incidence angle for both the input and the output beam, as shown in Fig. 3.5 (a), thus to minimize the power losses of the reflective beam from the facets of prism. On the other hand it reduces the DUV exposure of the operator because it is difficult to block the internal reflective beam.

The Brewster angle (the special angle maximizing penetration of the light into the medium) depends on the refractive index of the medium. For the fused silica prism, the dispersion equation is shown below:

$$n(\lambda) = \left(\frac{0.6961663 \cdot \lambda^2}{\lambda^2 - (0.0684043)^2} + \frac{0.4079426 \cdot \lambda^2}{\lambda^2 - (0.1162414)^2} + \frac{0.8974794 \cdot \lambda^2}{\lambda^2 - (9.896161)^2} - 1\right)^{\frac{1}{2}} \qquad \text{------ (3.1)}$$

Here, λ is the wavelength in micrometer and n is the refractive index. The expression is valid in the suitable wavelength range of 0.21 – 3.71 μm [3.9].

The Brewster angle is defined by

$$\theta_B = \arctan[n] \qquad \text{------ (3.2)}$$

and the diffractive angle $\Theta_{B'}$ is [3.10]

$$\theta_{B'} = 90^o - \theta_B \qquad \text{------ (3.3)}$$

For the triangular prism, when both facets are satisfying the Brewster's angle incidence as shown in Fig. 3.5 (a), the apex angle (the top angle) Θ_T can be found:

$$\theta_T = 180^o - 2 \cdot \theta_B \qquad \text{------ (3.4)}$$

According to the data curve of the refractive index and equations (3.1) and (3.2) it is possible to present at plot of the Brewster angle versus wavelength, as shown in Fig. 3.6 (a). For the DUV light (in the range of 0.21 - 0.30 μm), the refractive index n and the Brewster angle θ_B are in the range of

$$n \in (1.53836,\ 1.48779\ )$$

$$\theta_B \in (56.9744^o,\ 56.0935^o)$$

According to equation (3.4) the apex angle range of the prism therefore is

$$\theta_T \in (66.0514^o,\ 67.813^o)$$

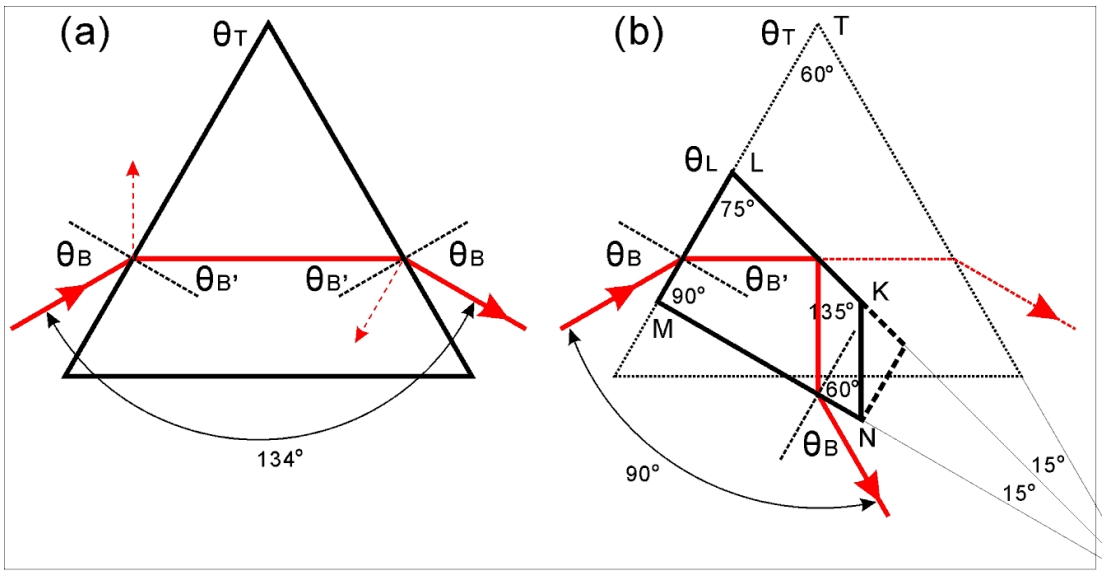

Fig. 3.5: (a) The schematics of the laser beam path in a triangular premonochromator prism; the apex angle Θ_T is defined when both input and output beams satisfy the Brewster angle; (b) The geometry of a Pellin Broca prism and the schematics of the laser beam path; the dispersion ability of the Pellin Broca prism is in principle closely equivalent to a triangular prism, but it is smarter because it forms a 90° deviated angle between the input and output beam.

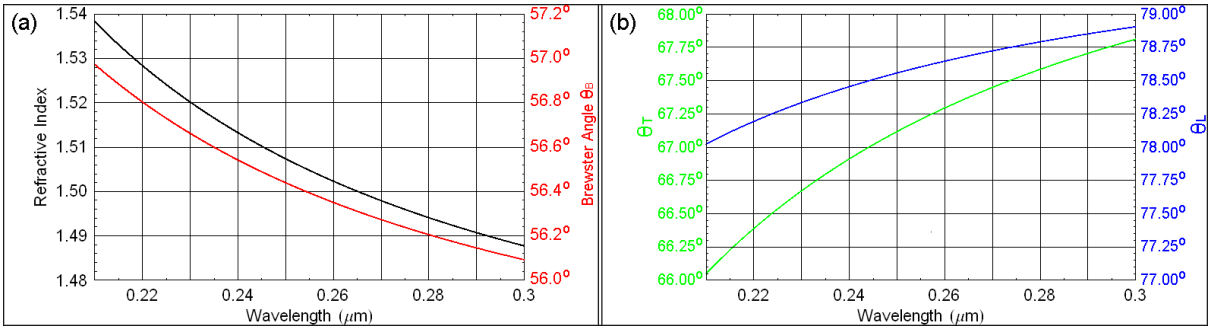

Fig. 3.6: (a) The curves of the refractive index (black) and the Brewster angle (red) versus wavelength in fused silicon. (b) The green and blue curves represent respectively the apex angle of a triangular prism and the Θ_L angle of a Pellin Broca prism versus wavelength under the condition of Brewster angle incidence. [Appendix 1]

3.1.6.1 Pellin Broca prism

The triangle prism may cause an inconvenient layout of the optical path because the incident beam and the dispersion beam form an *"irregular"* angle of about 134° as shown on Fig. 3.5 (a). The Pellin Broca prism was developed for solving this problem.

The main feature of a Pellin Broca prism is the 90° angle between the input beam and the output. The solid shape structure of the original Pellin Broca prism is shown in the Fig. 3.5 (b). The prism consists of a four-sided block of glass, shaped as a right prism with 90°, 75°, 135°, and 60° angles on the end faces. Light enters the prism through the face ML, undergoes total internal reflection from the face LK, and exits through the face NM. The refraction of the light as it enters and exits the prism is such that one particular wavelength of the light is deviated by exactly 90° [3.11]. The angle $\angle KNM$ does not affect the actual beam path. Therefore $\angle KNM$ can also be the (convenient) 90° for as given by the dashed shape shown in Fig. 3.5 (b). With respect to dispersion ability, it is equivalent to a triangle prism (dotted shape) with a 60° apex angle, as shown in Fig. 3.5 (b) [3.12].

For the original Pellin Broca prism, the condition for occurrence of the 90° deflection angle is only that the refractive angle of the input beam is

$$\theta_{B'} = \theta_L - 45^o = 30^o \qquad \text{------ (3.5)}$$

according to the Brewster angle refraction condition.

Therefore the essential condition for a Brewster angle input is that the refractive index of the prism is

$$n = tan[60^o] = 1.732 \qquad \text{------ (3.6)}$$

The refractive index of fused silica cannot satisfy this condition as Fig. 3.6 (a) shows. In order to realize the Brewster angle input and output the angle Θ_L must be modified.

If we substitute equation (3.3) into (3.4), the angle Θ_L required for Brewster incidence can be found:

$$\theta_L = 180^o - 45^o - \theta_B \qquad \text{------ (3.7)}$$

Fig. 3.6 (b) shows the results as:

$$\theta_L \in (78.0256^o,\ 78.9065^o)$$

The optical company Thorlabs has a standard Pellin Broca prism product of with an angle of Θ_L = 78°26' that would be satisfactory for our application [w3-5].

3.2 Transport of Laser Beams from the Laser Head to the Spectrometer.

Our DUV Raman system is composed two main sections, a Lexel 95-SHG-QS Argon gas ion laser from Cambridge Laser Laboratories Inc. (USA) and an InVia Reflex spectrometer system for Raman spectral analysis from Renishaw, plc. (UK). As previously introduced, we have adopted 2 visible and 3 DUV laser lines, 514.5, 488.0, 257.3, 244.0 and 228.9 nm, which are exported from visible and DUV laser output apertures, respectively. Correspondingly, the spectrometer must have two access ports. The spectrometer is very sensitive for the pointing of the incoming laser beam (including position and direction). Furthermore, the pointing of the laser beam can be changed slightly during switching the wavelengths, especially for the DUV laser beams. As shown in Fig. 2.21 (A), when we were optimizing the position of M2, the direction of the laser beam is actually changing. The laser beam can also be changed slightly when inserting of different BBO crystals. Furthermore the prism disperses the different wavelengths to the different directions, and therefore the beam paths for the various DUV lines are slightly different. Therefore, it is required that the laser beams can be adjusted quite freely to let them go through the pinhole pairs as shown in Fig. 3.7. The pinhole pairs are used to fix the position and direction of the incoming beam to a good way for spectrometer.

For a convenient alignment, the laser beam path is normally set to have two 90° deflections by two 45° incident laser line mirrors; see the green beam path in the front of the laser head, shown in Fig. 3.7. The mirrors are mounted on kinematic mirror mounts (Thorlabs products: KM100). We have chosen broad band high reflective dielectric visible and DUV laser mirrors, respectively (Thorlabs products, BB1-E02 and NB1-J02). These mirrors provide above 99% reflectance at 45° incidence.

Compared with visible and DUV laser beams, the situation for the DUV laser is complicated because a prism is needed to be inserted in the laser beam path to remove the fundamental wave and non-lasing plasma lines from the argon gas. The violet lines in the front of the laser head (see Fig. 3.7) show the laser beam path when a triangular prism is used. In such a geometry layout, the three mirrors, M1, M2 and M3, can bear equal shares of the irregular deflection angle (about 134° shown on Fig. 3.5 (a)) that is associated with the use of the triangular prism, resulting in the about 52.3° angle incidence for each of the mirrors:

$$\angle\mathrm{M1} + \angle\mathrm{M2} + \angle\mathrm{M3} \equiv 180^o + 134^o \quad \xrightarrow{\angle M1=\angle M2=\angle M3} \quad \frac{\angle M1}{2} \approx 52.3^o$$

Here, $\angle M1, \angle M2$ and $\angle M3$ are the angles between the incidence and reflectance beams for each mirror, respectively.

Using such a beam path is convenient because the reflectance of the mirrors is as close as possible to the optimum incident angle of 45° typical for the high reflectance dielectric mirrors.

If a Pellin Broca prism is used instead of the normal triangle prism, the laser beam path becomes simple because of the 90° deflection of the Pellin Broca prism, as shown in Fig. 3.7 in the dashed frame. In such a beam setup we suggest that the position of Pellin Broca prism should be on the upper corner of the beam path, because otherwise, it is difficult to control respectively the position and direction of the laser beam during adjusting of the Pellin Broca prism. When the Pellin Broca prism is on the upper corner, it just needs to be responsible for the beam position on the mirror M3' which should be on the extension line of the pinhole pair. The tilt of the mirror M3' is then responsible for the final adjusting of the beam direction to go through the pair of pinholes.

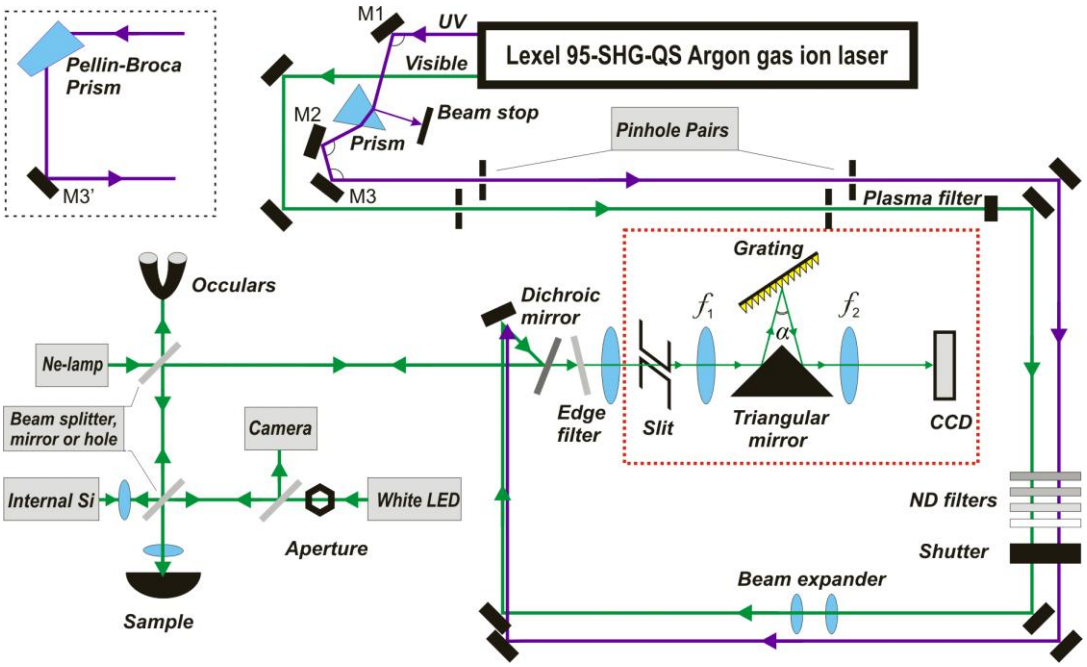

Fig. 3.7: The optical layout of the Raman system for DUV and Visible excitation.

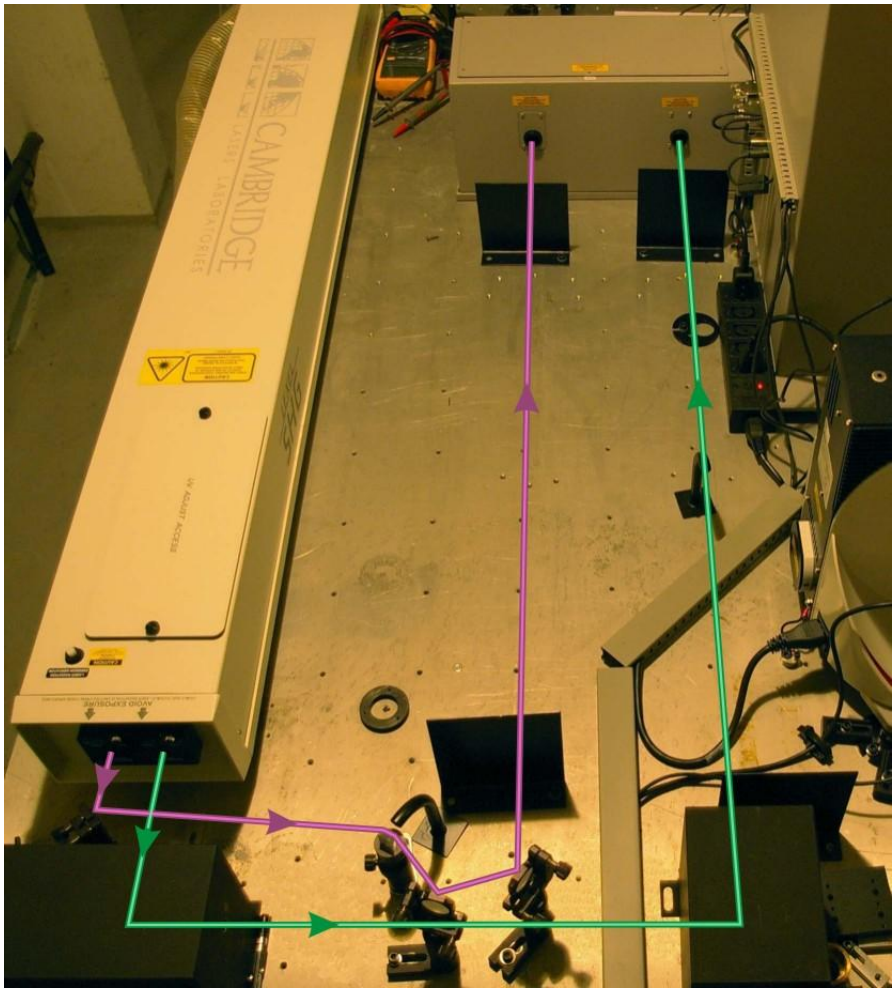

Fig. 3.8: View of the laser beam transport system from the laser head to the spectrometer.

3.3 Horizontal Sampling with “Nose”

Because we use the microscope for the Raman excitation entrance and signal collection, the following two cases of measurements could present difficulties and we have to use the method of Horizontal sampling:

- When it is wished to measure the side face of a sample and it cannot be laid down.
- When the sample is too large to be placed under the microscope.

In the first case, the microscope objective can be taken away and a microscope *“nose” with* a broad band high reflective mirror or a right angle prism, as shown in Fig. 3.9 (a), can be fitted to the microscope, to realize the horizontal sampling. This works because the light beam is parallel when reaching or leaving the objective. The objective is put directly on the “mirror holder” to constitute the “nose”. It can be laterally shifted (or turned) by mounting and applying a lengthening tube on the microscope nose, as shown in Fig. 3.9 (b). This helps for the second case. The principle of the optical layout is depicted in Fig. 3.10, a photograph is given in Fig. 3.10 and details of the setup structure are shown in the [Appendix 2].

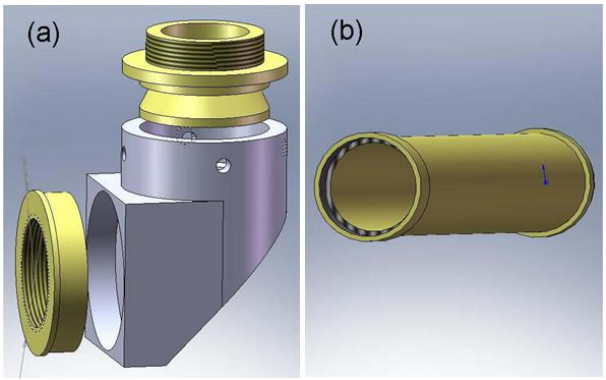

Fig. 3.9: (a) An additional microscope "nose" can be used to realize horizontal sampling; (b) A lengthening tube making a shift of 20 cm of the objective possible.

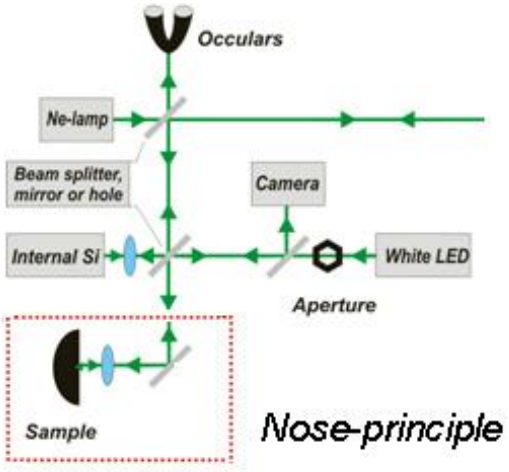

Fig. 3.10: The optical layout of the nose mounted on the Raman microscope system. For the principles of the rest of complete system, see Fig. 3.7.

Fig. 3.11: Photograph of the nose mounted on the Raman microscope system.

References to Chapter 3

[3.1] S. A. Asher and C. R. Johnson, "*Raman spectroscopy of a coal liquid shows that fluorescence interference is minimized with ultraviolet excitation*", Science, Vol. 225, (**1984**), pp. 311–313.

[3.2] S. A. Asher and C. M. Jones "*UV Resonance Raman – Spectroscopy – a New Technique for Speciation of Aromatics in Complex Matrices*", in New Applications of Analytical Techniques to Fossil Fuels, ACS Sym. Ser., Ed. Perry and Retcofsky, *Am. Chem. Soc., Division of Fuel Chemistry, preprints, 31* (1), (**1986**), pp. 170-180.

[3.3] E. Hecht, "Optics", Addison-Wesley, San Francisco, CA, 4th edition, ISBN: 0-321-18878-0, (**2002**), pp. 478.

[3.4] Chuan Liu and Rolf W. Berg, "*Determining the Spectral Resolution of Raman Instruments*", Applied Spectroscopy, Accepted.

[3.5] Ivan Moreno and J. Jesus Araiza, "Thin-film spatial filters", OPTICS LETTERS, Vol. 30, No. 8, April 15, (**2005**), pp.914-916.

[3.6] Parker Sybil P., "*Photosensitive glass*", Dictionary of Scientific and Technical Terms, McGraw-Hill Companies Inc., (**2003**), ISBN: 0-0704231-3-X.

[3.7] T.R. Dietrich, W. Ehrfeld, M. Lacher, M. Krämer and B. Speit, "*Fabrication technologies for microsystems utilizing photoetchable glass*", Microelectronic Engineering 30, (**1996**), pp. 497-504.

[3.8] Wendy A. R. Franks, Martin J. Kiik, and Arokia Nathan, "*UV-Responsive CCD Image Sensors with Enhanced Inorganic Phosphor Coatings*", IEEE TRANSACTIONS ON ELECTRON DEVICES, VOL.50, NO.2, (**2003**), pp.352-358.

[3.9] I. H. Malitson, "*Interspecimen Comparison of the Refractive Index of Fused Silica*" JOURNAL OF THE OPTICAL SOCIETY OF AMERICA, Vol. 55, Issue 10, (**1965**), pp. 1205-1208.

[3.10] E. Hecht, "Optics", Addison-Wesley, San Francisco, CA, 4th edition, ISBN: 0-321-18878-0, (**2002**), pp.348.

[3.11] Pellin, Ph. and Broca, Andre, "*A Spectroscope of Fixed Deviation*", Journal de Physique, Volume 8, (**1899**), pp. 314-319.

[3.12] W. M. McClain, "*How to Mount a Pellin-Broca Prism for Laser Work*", APPLIED OPTICS, Vol. 12, No. 1, (**1973**), pp. 153- 154**.**

[w3-1] http://www.horiba.com/scientific/products/gratings/

[w3-2] http://www.gammadatainstrument.se/_resources/File/Diffraction_Custom_Gratings.pdf

[w3-3] http://www.newport.com/Oriel-InstaSpec-X-CCD/415018/1033/catalog.aspx

[w3-4] http://www.alphalas.com/images/stories/products/laser_diagnostic_tools/ALPHALAS_Digital_CCD_Spectral_Sensitivity.pdf

[w3-5] http://www.thorlabs.de/NewGroupPage9.cfm?ObjectGroup_ID=3217

4 Determining the Spectral Resolution of Raman Instruments

4.1 Introduction:

The wavelength of the light sources used for excitation in modern dispersive Raman spectroscopy most often lies in the range from ~800 nm down to nearly 200 nm. The use of deep ultraviolet (DUV) radiation - in the range below 300 nm - although used occasionally - is a newly rising technology. DUV Raman spectroscopy has a significant advantage, avoiding the common interference from a high fluorescence background, as discovered long time ago [4.1]. There are however also disadvantages by using UV excitation, such as the need for extra security precautions, the non-transparency of glassy containments and often decomposition of the tested samples [4.2], [4.3]. Traditional visible light Raman spectroscopy therefore still plays an important role, first of all because its operation is easier than for DUV Raman, and secondly because some samples have interesting resonance Raman spectra in the visible range [4.4]. Therefore, a scientific research type Raman set-up usually requires flexible instruments and several different light sources with various wavelengths for excitation.

In such an environment it is important to maintain an even and high spectral resolution, when switching between Raman instruments, changing the setup or comparing results from different instruments. It is well known that the spectral resolution of a Raman system is affected by many factors, such as grating groove density, entrance slit width, focal length, and so on. In order to estimate and optimize the spectral resolution of an instrument, one must consider all the factors which affect the system resolution. In this chapter we attempt to combine all the influencing factors into one single expression. Such an expression has the advantage that it clearly shows the dependence of the spectral resolution on the situation of the Raman system under different conditions. As it will be shown, the expression shows that the spectral resolution exhibits a significant change along the Raman shift axis. This behavior, although known for long time, is being constantly overlooked in many contemporary Raman publications.

With respect to applications in some research areas, knowledge of the precise width of a Raman band is important to characterize the structure of materials. For example the properties and behavior of single layer graphite (graphene) can be determined by using a Raman technology, in which the width and the position of certain characteristic Raman bands may be used as criteria [4.5]. In another case, the width of a Raman band could be used to infer the size of germanium nanocrystals [4.6]. In such studies one should remember that the spectral resolution resulting from the applied experimental setup affects directly the determined Raman band width. The measurement of a Raman band width should therefore be considered as a convolution relation between the true Raman band and the experimental resolution in the situation [4.7]. Therefore, one should find the true Raman band width by taking the exact spectral resolution of the instrument into consideration. To do this, data for the true experimental resolution must be determined.

The exact spectral resolution of a Raman instrument is typically determined by using a light source with a narrow-line radiation, such as a low-pressure mercury lamp [4.8], [4.9], or a sample which has a well-defined narrow Raman band. In this way the spectral resolution is determined for the particular wavelength(s) or at

the corresponding Raman shift(s). Since the spectral resolution is not constant but depends on the wavelength, one needs a well-defined expression to predict (by interpolation or extrapolation) the spectral resolution at positions where the important Raman bands are located, as a prerequisite to finally determine the true Raman band width.

A new method is described to express the spectral resolution of an applied CCD Czerny-Turner Raman instrument entirely by means of one equation and principal factors determined by the actual setup. The factors are usual quantities such as wavenumber values for the laser and the Raman band (ω_L and ω_R), the diffraction grating groove density (G), the second focal length (f_2), the angle between the incident and the diffracted light (α) and the full width at half maximum (FWHM) value of the signal on the detector (b_{img}). The basic formula derived to estimate the spectral resolution ($\Delta\omega$ function) of the Raman instrument is given as

$$\Delta\omega\left[\omega_L, \omega_R, G, f_2, \alpha, b_{img}\right] = (\omega_L - \omega_R)^2 \cdot \frac{b_{img}}{G \cdot f_2} \cdot \cos\left(\arcsin\left(\frac{G}{2 \cdot (\omega_L - \omega_R) \cdot \cos\left(\frac{\alpha}{2}\right)}\right) + \frac{\alpha}{2}\right)$$

This validity of this expression has been examined by measuring the band width of the 1332.4 cm^{-1} diamond Raman fundamental band, excited with two quite different wavelengths (deep ultraviolet 257.3 nm and visible green 514.5 nm light). Further use of a low pressure mercury line at 265.2042 nm also gave verification of the given expression. A useful method to find true Raman band widths is provided. The relation between the practical spectral resolution and the true band width is based on a Gaussian band shape approximation. An essential feature of the new method is a proposed way to compensate for non-ideality (slit diffractions, aberrations, etc.) by use of a hyperbola model function

$$b_{img} = M \cdot \sqrt{(b_{ent})^2 + (b_{limit})^2}$$

to describe the relationship between b_{ent} (the width of the entrance slit) and the image signal width on the CCD (b_{img}). M is the spectrometer magnification, given by the focal length f_2 divided by the focal length f_1 of the first concave mirror. b_{limit} is the smallest possible limiting FWHM of the slit image when M = 1. A final finding is that the known significant changes in spectral resolution along the Raman shift axis make static recording and synchronous (extended) scanning modes differ significantly with respect to their resolution properties; this feature has been often overlooked in many contemporary works reporting Raman spectra.

4.2 Derivation of the Expression

We will derive the theoretical expression for the spectral resolution of a spectrometer based on the common Czerny-Turner monochromator [4.10], [4.11]. The schematics are shown on Fig. 4.1. Most currently, the spectrometer is equipped with a multi-channel charge coupled device detector (CCD) [4.12], replacing previous single-channel detectors behind an exit slit. As we shall see this complicates the problem. In the following derivation of the expression for the resolution, we are concerned with the central part of the CCD.

The spectral resolution of a Raman system is affected by many factors. We count up 10 items as shown below:

1. Exciting laser characterized by the wavelength λ_L (or the corresponding wavenumber, ω_L).
2. Raman wavenumber shift, ω_R.
3. Diffraction grating groove density, *G*.
4. Angle α between the incident light and the diffracted light.
5. Focal length, *f*.
6. Entrance slit width, b_{ent}.
7. System magnification, *M*.
8. System diffraction effects of grating and concave mirrors (lenses).
9. System aberrations.
10. Pixels of the CCD.

Among these many factors related to the spectral resolution of a Raman instrument, the wavelength dispersing ability ($\Delta\lambda/\Delta\Theta$) of the grating and the *full width at half maximum* (FWHM) of the slit image of a monochromatic light on the CCD are the two key parameters that link up all the factors. Please note that resolution is not affected by the diffraction efficiency of the grating (blazing angle etc.) [4.13].

The wavelength dispersing ability of the grating, here defined as $\Delta\lambda/\Delta\Theta$, depends on the spacing of the grating grooves (*d,* not shown in Fig. 4.1) and the incident angle (Θ_i). The dispersing ability can be derived from the well-known grating relation (eq. 1) as shown below. Θ is the diffractive angle, and the order of diffraction is set to one (normally the first order is used in Czerny-Turner monochromators to get the most effective monochromator):

$$d \cdot (\sin(\theta_i) + \sin(\theta)) = \lambda \qquad \text{------ (eq. 1)}$$

By differentiation one gets the relation (eq. 2),

$$\frac{\partial\lambda}{\partial\theta} = d \cdot \cos(\theta) \quad \Rightarrow \quad \frac{\Delta\lambda}{\Delta\theta} = d \cdot \cos(\theta) \qquad \text{------ (eq. 2)}$$

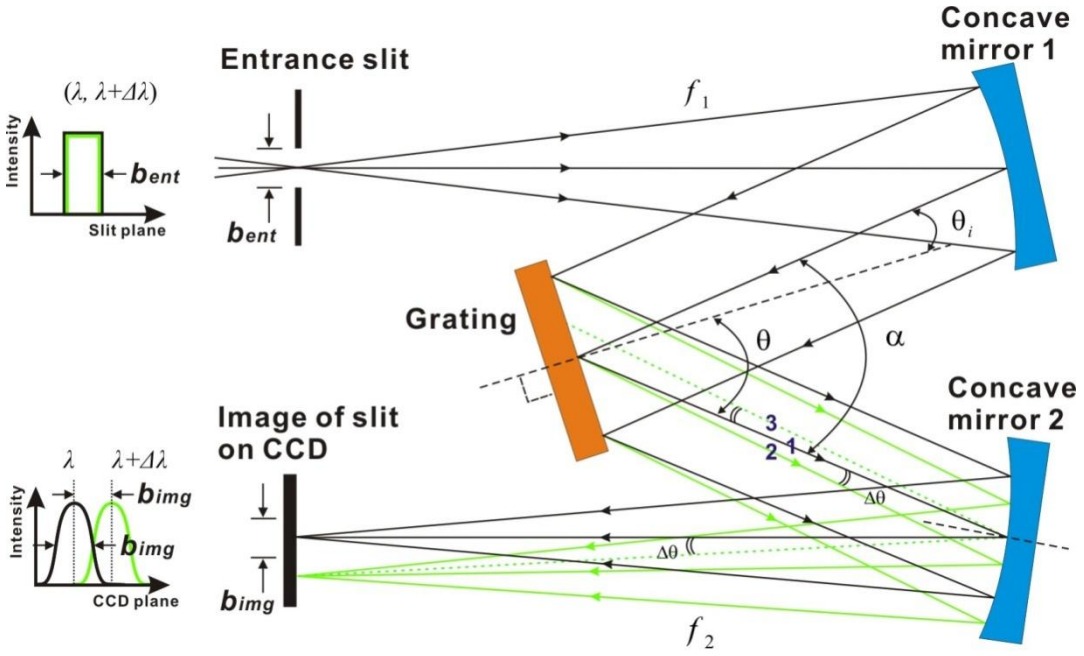

***Fig. 4.1**:* The schematics of a Czerny-Turner monochromator based spectrometer.

Assuming that monochromatic light, say of wavelength λ, is entering through the entrance slit, then an image of the entrance slit (with the physical width, b_{ent} and a color corresponding to λ) will be formed on the detector (CCD), by means of the concave mirrors (see Fig. 4.1). Because of diffractions and aberrations, the intensity profile of the image is not a rectangle curve any more, but will be a bell-shaped curve, corresponding to the signal obtained with a CCD having a sufficiently narrow pixel size (such that at least a few pixels are sensing the curve [4.9], [4.14], [4.15]). The FWHM of the bell-shaped curve is denoted as b_{img}. Furthermore to analyze the situation more carefully, the slit image (or signal *versus* wavelength) due to the angular dispersion of the grating, will be depicted differently by e.g. two different wavelengths, say λ and (λ + Δλ), see Fig. 4.1. When the two images corresponding to different grating diffraction angles, Θ and (Θ + $\Delta\Theta$), are juxtaposed at a distance corresponding to the FWHM, then these two peaks can be considered to be just distinguishable (or resolved, see Appendix 3). This criterion of the resolution is more tolerant than the usual Rayleigh criterion (see Appendix 3) to distinguish two close images [4.14]. However, normally the spectral resolution is dominated by the FWHM. This situation characterizes the resolving power $\Delta\lambda$ of the spectrograph. The opening angle $\Delta\Theta$ at the grating (between the rays **1** and **2** in Fig. 4.1) can be seen (by geometry, because ray **2** and **3** are parallel) to form at the *Concave mirror 2* another angle $\Delta\Theta$ of equal magnitude, because rays **1** and **3** are reflected in the same point. From this and the near right angled hitting of the image on the slit, it therefore follows that b_{img}, $\Delta\Theta$ and the second focal length f_2 are related in this way:

$$\Delta\theta = \frac{b_{img}}{f_2} \qquad \text{------ (eq. 3)}$$

The $\Delta\Theta$ angle is equal to the grating dispersive angle for these two just distinguishable wavelengths, as seen in Fig. 4.1.

By substitution of (eq. 3) into (eq. 2), we therefore get the spatial resolution as

$$\Delta\lambda = \frac{b_{img}}{f_2} \cdot d \cdot \cos(\theta) \qquad \text{------ (eq. 4)}$$

To eliminate Θ from this expression we introduce the angle α, between the direction of the incident light and the diffracted light, as shown in Fig. 4.1.

$$\alpha = \theta - \theta_i \qquad \text{------ (eq. 5)}$$

This angle α is normally kept constant for well designed instruments; the condition for this constancy being that the grating rotation is done around an axis chosen to be parallel with the grating surface and centrally placed. Then we rearrange (eq. 1) from a sum to a product by use of a standard trigonometric formula:

$$d \cdot (\sin(\theta_i) + \sin(\theta)) = \lambda \quad \Rightarrow \quad d \cdot \left(2 \cdot \sin\left(\frac{\theta+\theta_i}{2}\right) \cdot \cos\left(\frac{\theta-\theta_i}{2}\right)\right) = \lambda \qquad \text{------ (eq. 6)}$$

By substituting (eq. 5) into (eq. 6), we get the equation:

$$d \cdot \left(2 \cdot \sin\left(\frac{2\theta-\alpha}{2}\right) \cdot \cos\left(\frac{\alpha}{2}\right)\right) = \lambda \qquad \text{------- (eq. 7)}$$

Then, solving for Θ we have

$$\theta = \arcsin\left(\frac{\lambda}{2 \cdot d \cdot \cos\left(\frac{\alpha}{2}\right)}\right) + \frac{\alpha}{2} \qquad \text{------ (eq. 8)}$$

By substituting (eq. 8) into (eq. 4) we get the expression

$$\Delta\lambda = \frac{b_{img}}{f_2} \cdot d \cdot \cos\left(\arcsin\left(\frac{\lambda}{2 \cdot d \cdot \cos\left(\frac{\alpha}{2}\right)}\right) + \frac{\alpha}{2}\right) \qquad \text{------ (eq. 9)}$$

Normally, Raman band absolute positions are expressed as ω in wavenumber units. In order to derive a practical expression in wavenumber units, we apply these conversions:

$$\omega = \frac{1}{\lambda} \quad \Rightarrow \quad \frac{\partial\omega}{\partial\lambda} = -\frac{1}{\lambda^2}$$

Hence, for small absolute values of $\Delta\omega$ one gets the approximation:

$$\Delta\omega = \omega^2 \cdot \Delta\lambda = (\omega_L - \omega_R)^2 \cdot \Delta\lambda \qquad \text{------ (eq. 10)}$$

where ω is the Raman scattering absolute wavenumber position, ω_L is the laser line absolute wavenumber value and ω_R is the Stokes wavenumber shift of the scattered light.

Instead of specifying the separation between the grating grooves (*d,* not shown in Fig. 4.1), one often uses the density of the grating grooves (number G of grooves per unit length) to classify the grating:

$$d = \frac{1}{G} \qquad \text{------- (eq. 11)}$$

After substitution and unit conversion, the spectral resolution function becomes

$$\Delta\omega\left[\omega_L, \omega_R, G, f_2, \alpha, b_{img}\right] = (\omega_L - \omega_R)^2 \cdot \frac{b_{img}}{G \cdot f_2} \cdot \cos\left(\arcsin\left(\frac{G}{2 \cdot (\omega_L - \omega_R) \cdot \cos\left(\frac{\alpha}{2}\right)}\right) + \frac{\alpha}{2}\right)$$

------- (eq. 12)

It should be noted, because the unit of wavenumber is usually cm^{-1}, when (eq. 12) is applied for numerical calculations, the units of length for all the parameters must be transformed to *cm*.

In the above expression, there are six variables; five of these variables correspond to five of the factors (items 1-5) that were mentioned in the beginning. The items 6-9 must also have influence on the relationship between the widths of the entrance slit (b_{ent}) and the image thereof (b_{img}), thereby affecting the spectral resolution. For monochromatic light, the limiting FWHM of the peak of the image is governed by the diffraction effects and the aberrations (items 8-9). However, this is not easily expressed and we therefore seek an empirical relationship between b_{img} and b_{ent}. Hence, considering the experimental results as shown later, it seems that the spectral resolution ($\Delta\omega$) *versus* the width of the entrance slit (b_{ent}) looks like a hyperbola curve. Furthermore, $\Delta\omega$ and b_{img} have a direct proportional relationship. Therefore we propose to use a hyperbola function (b_{ent} *versus* b_{img}) as a model for the relationship between b_{ent} and b_{img}. If so, we would have a relationship between b_{img} and b_{ent} of the kind:

$$b_{img} = M \cdot \sqrt{(b_{ent})^2 + (b_{limit})^2}, \quad \text{where} \quad M = \frac{f_2}{f_1} \qquad \text{------- (eq. 13)}$$

In this expression, *M* is the system magnification, defined by the focal length f_2 of the *second concave mirror,* divided by focal length f_1 of the *first concave mirror*, (see Fig. 4.1). b_{limit} can be defined as the smallest possible limitation FWHM of the slit image when *M* = 1. The limitation is caused by the system diffractions and the aberrations. In practice the system diffractions play a more important role than the aberrations. According to the diffraction equation of a grating and a circular aperture [4.13], a reasonably approximate expression of b_{limit} would be

$$b_{limit} = A \cdot \lambda = \frac{A}{(\omega_L - \omega_R)} \qquad \text{------ (eq. 14)}$$

where *A* is a constant for a spectrometer with a certain setup. Considering that *A* is depending on the system diffractions and aberrations, we denote *A* as the *Diffractions and Aberrations Compensation Factor (DACF)* of the used spectrometer system.

To resume the results so far: In the above equations (eq. 12) and (eq. 13), the values of all the factors except *A* can easily be determined for a particular Raman instrumental situation.

When the width of the entrance slit b_{ent} is broad enough (such as: >100 μm at 500 nm), the effects of diffraction and aberration become weak, and therefore we may do the approximation:

$$b_{img} \approx M \cdot b_{ent}\,, \quad (b_{ent} > 100\ \mu m) \qquad \text{------ (eq. 15)}$$

This can become the experimental method to verify if (eq. 12) gives a correct description. In addition, we can use a set of measurements to determine *A* and check if the hyperbola approximation, (eq. 13), is indeed a good model.

Concerning the equation (eq. 12), it is worth noting that the CCD pixel width size, for normally adopted Raman instrument layouts, is narrower than the width of common Raman bands. The CCD records the spectrum band as a digital profile from several pixels. The digital profile of the spectrum band will constitute a not very smooth curve, at least when the widths of the CCD pixels and the spectrum band are comparable (see later). The FWHM of a not very smooth curve has a deviation from the true FWHM of the spectrum band, hence affecting the spectral resolution of a spectrometer. This is one reason why the theoretical curves – as we shall see – do not fit well with the experimental curves in the range of narrowly opened slits (b_{ent} < 20 μm).

In practice the spectrum band not only is broadened by the limited resolution of the spectrometer, but also by the line width of the exciting laser. In general the FWHM of the spectrum band will be determined by the convolution of these two causes of broadening. Assuming a Gaussian line profile, an approximation of the FWHM can be provided by this relationship (see Appendix 4):

$$\Delta\omega_M = \sqrt{(\Delta\omega_R)^2 + (\Delta\omega_S)^2 + (\Delta\omega_L)^2} \qquad \text{------ (eq. 16)}$$

Here $\Delta\omega_M$ is the measured spectrum bandwidth, $\Delta\omega_R$ is the true Raman spectrum bandwidth, $\Delta\omega_S$ is the spectral resolution of the spectrometer and $\Delta\omega_L$ is the linewidth of the excited laser.

This equation (eq. 16) is an interesting result. As the laser line width, $\Delta\omega_L$, is typically known (e.g. given by manufacturer), and $\Delta\omega_M$ is the experimental value, we can calculate the spectral resolution $\Delta\omega_S$ of the spectrometer if the true Raman bandwidth, $\Delta\omega_R$, is also known. On one hand, this is an experimental method to find the spectral resolution of the spectrometer at a certain absolute wavenumber. To do this the Spectral Resolution Compensation Factor *A, or the DACF parameter,* can be determined by the equations (eq. 12), (eq. 13), and (eq. 14), and then the spectral resolution of the spectrometer in the whole wavenumber range can be determined. On the other hand, we can use (eq. 16) to determine the true Raman bandwidth for the testing sample, as soon as the spectral resolution is totally known.

4.3 Experiments

- **Samples**

A monocrystalline diamond that did not emit fluorescence was used. Diamond has a characteristic strong Raman band, located at 1332.4 cm^{-1}, that was acting as a suitable narrow line source. The band width of the diamond line is known to be $\Delta\omega_R$ = 1.2 cm^{-1} [4.16]. Another useful source was a low pressure Hg(Ar) pencil style calibration lamp from Oriel Instruments.

- **Instrumentation**

As exciting light source we used a *Lexel* 95-SHG-QS Argon gas ion laser (from Cambridge Laser Laboratories, Inc.) working in direct or second harmonic generation (SHG) mode. The wavelengths and powers applied were 514.5 nm (10 mW) and 257.3 nm (1 mW). The linewidth $\Delta\omega_L$ for the 514.5 nm line was 0.17 cm^{-1}. Since the 257.3 nm line is generated from the 514.5 nm line, the width should be narrower but we have also taken the value 0.17 cm^{-1} as approximation for the 257.3 nm line width.

A flexible *InVia Reflex* Raman spectrometer system from *Renishaw, plc*. was used to record the spectra. The schematics of the couplings of the visible and ultraviolet laser beams into the spectrometer and other details of the system are shown in Fig. 4.2. The optical principle of the Renishaw spectrometer is equivalent to a single classical Czerny-Turner monochromator. Instead of concave mirrors, mirrors combined with lenses are used in the Renishaw system. Compared to the concave mirrors, lenses have the well-known problem of chromatic aberrations, and even for achromatic lenses it is not possible to cover the whole range from UV to the visible; therefore the lenses have (like the grating) to be exchanged in order to suit the whole range of wavelengths from UV to visible. The details of the experiments are shown in Table 5.1.

Table 4.1: Experimental details.

Exciting wavelength (nm)	Grating groove density G (mm^{-1})	Diffraction angle α (deg)	Focal length f_1 (mm)	Focal length f_2 (mm)
514.5	2400	37	140	250
257.3	3600	37	155	250

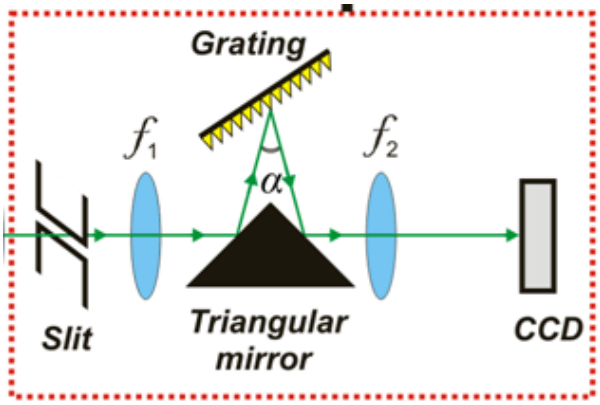

Fig. 4.2: Schematics of the monochromator based on the Renishaw spectrometer.

4.3.1 Examination of the Expression of Spectral Resolution, Equation (eq. 12)

As noted above, when the width of the entrance slit (b_{ent}) is broad enough, the effects of diffraction and aberrations can be ignored, and therefore the spectral resolution can be calculated theoretically by (eq. 12). After that, one can compare with the experimental results to examine if equation (eq. 12) is correct. We take b_{ent} = 140 µm as the condition for a broad slit-width experiment. For this slit width, measurements of the Raman band widths of diamond are shown in Table 4.2. After applying the values of $\Delta\omega_M$ to (eq. 16), the experimental results found for the spectral resolution $\Delta\omega_S$ are shown in Table 4.2. The theoretical results of spectral resolution $\Delta\omega$ are also shown, calculated by equations (eq. 12) and (eq. 13).

Table 4.2: Comparison of the *experimental* and *theoretical* results for the spectral resolution for a wide entrance slit, b_{ent} = 140 µm. [Appendix 6]

Exciting wavelength λ (nm)	The measurements of Raman bandwidth $\Delta\omega_M$ (cm^{-1})	Experimental results of spectral resolution $\Delta\omega_S$ (cm^{-1})	Theoretical results of spectral resolution $\Delta\omega$ (cm^{-1})
514.5	6.77	6.66	6.23
257.3	23.80	23.77	23.24

As shown in the Table 4.2, there is a good correspondence between experimental results ($\Delta\omega_S$) and the theoretical results ($\Delta\omega$); only a few percent differences are seen. This is to be expected because we ignored the effect of the aberrations, as previously noted.

4.3.1.1 Hyperbola Model for the Spectral Resolutions

According to (eq. 13), when the width (b_{ent}) of the entrance slit decreases, the effect of diffraction and aberrations (b_{limit}) becomes of importance. Therefore, these effects cannot be ignored for narrow entrance slits. To investigate the situation, the Raman band width ($\Delta\omega_M$) of a diamond sample was measured for various entrance slit widths (b_{ent}), from 10 µm to 180 µm. The obtained results are shown in Fig. 4.3. In order to compare the FWHMs clearly, the Raman spectra were auto-scaled to have same maximum (set to unity). The analyses of these results are given in Fig. 4.4. Here, the large green points represent the measurements of the Raman *band width versus* the slit width. From these results we can calculate the experimental spectral resolution (the red small points by using (eq. 16).

If one chooses an appropriate number for the *Spectral Resolution Compensation Factor A*, and substitute it to (eq. 14), then one can plot an estimate of the *spectral resolution* by use of (eq. 12). The chosen number for *A* can be varied *by iteration* to find better or worse fits to the experimental red *resolution* points in Fig. 4.4. When *A* = 100, we got the shown approximate model curves (black dotted curves) in Fig. 4.4.

The experimental results (red curves) were fitted well by the theoretical results (black dotted curves) except for narrow slit openings (< 20 µm). One reason is the effect of the CCD spectral resolution. Other reasons are that the effects of diffraction and aberrations become more important. As obvious from Fig. 4.3 the un-smoothed facetted spectrum profiles must be caused by the width of the CCD pixels. One might be tempted from Fig. 4.3 to use narrow slits. However, slits as narrow as < 20 µm are not practical for real measurements because the Raman signals decrease extremely much when so narrow slits are used (the

weakness of the narrow-slit spectra are not obvious from the spectra after setting the auto-scaled intensity to unity).

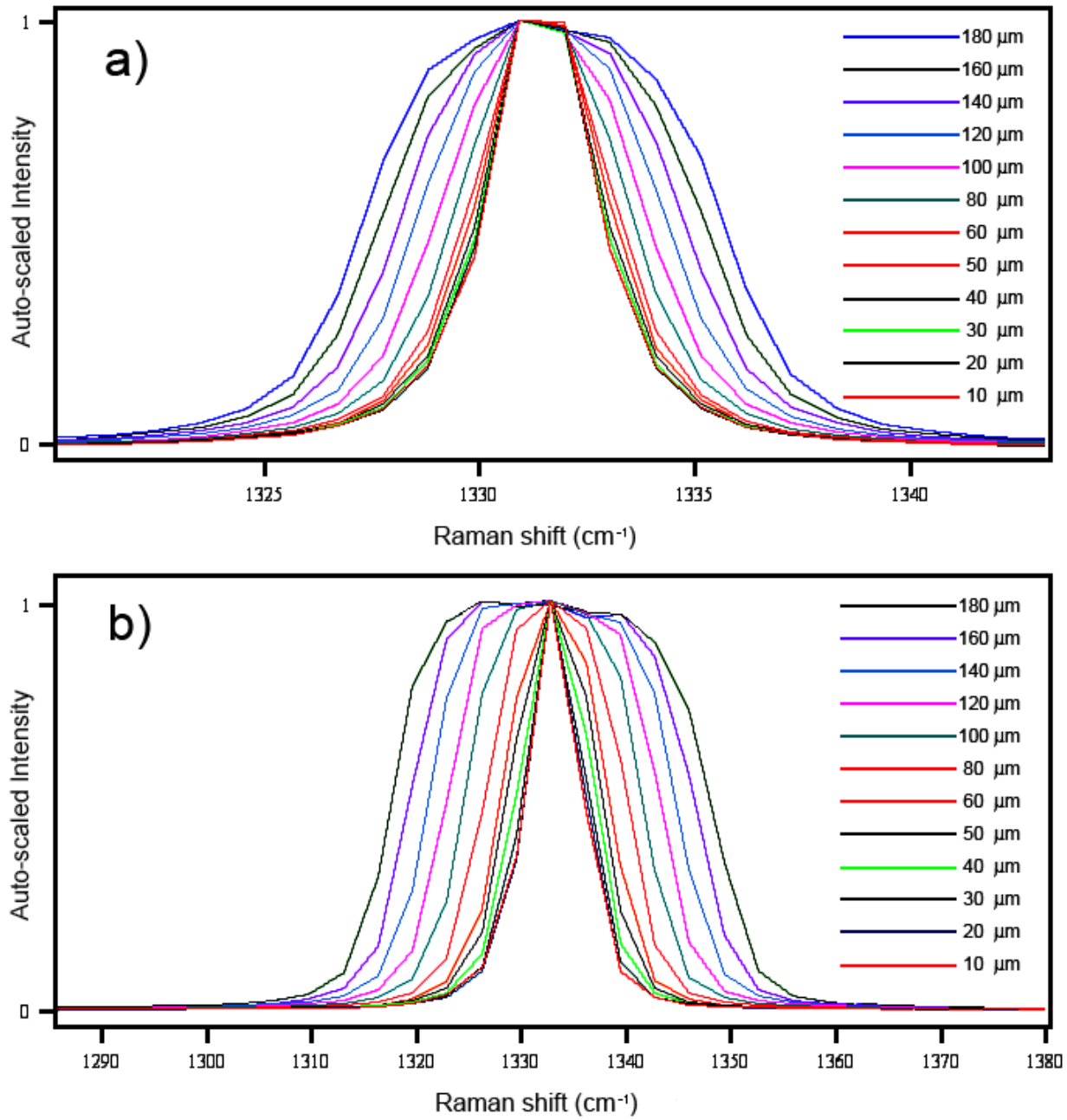

Fig. 4.3: Auto-scaled Raman spectra of the 1332.4 cm^{-1} band of a diamond obtained by use of various slit widths (given in µm) and a) excited with 514.5 nm radiation and b) with 257.3 nm.

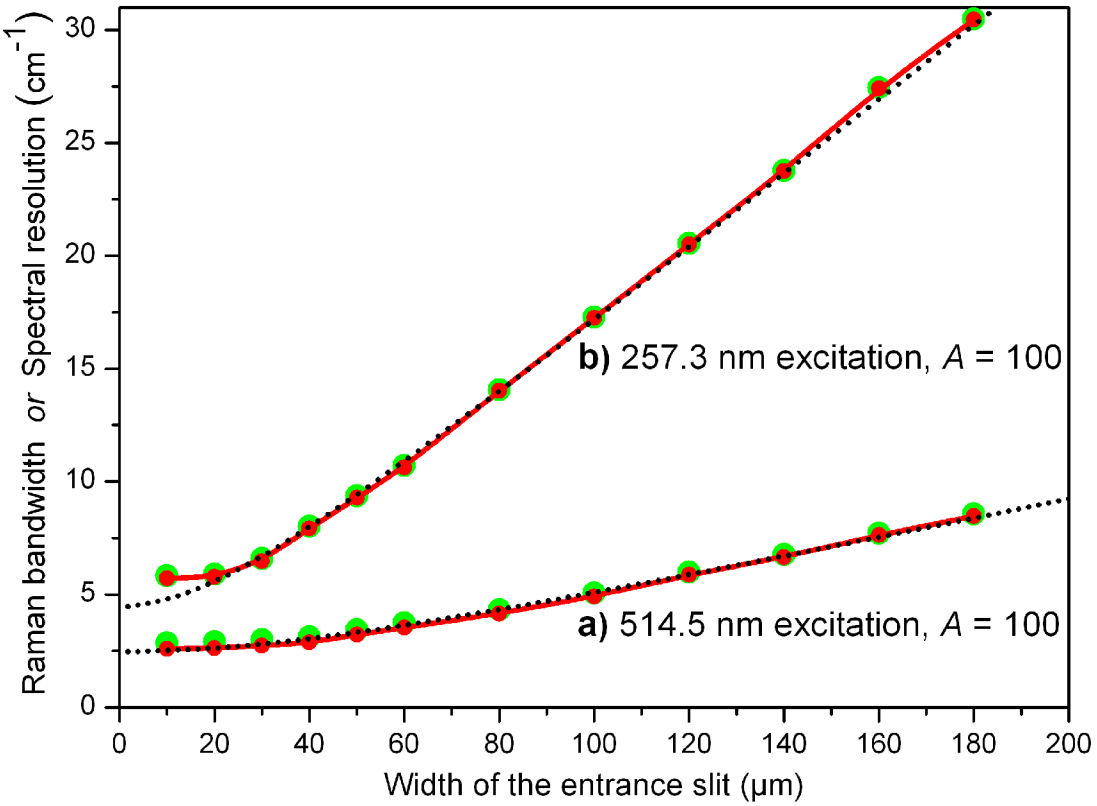

Fig. 4.4: The wide green points are the measurements of Raman **bandwidth** $\Delta\omega_M$ of diamond for various slit widths. The narrow red points, connected by red curves, are the experimental spectral **resolution** data $\Delta\omega$ obtained by means of (eq. 16). The black dotted curve is the spectral resolution modeling results (theoretical spectral resolution) based on the equations (eq. 12), (eq. 13) and (eq. 14). a) The wavelength of the exciting light source was 514.5 nm and *A* was set to 100. b) The wavelength of the exciting light source was 257.3 nm and *A* was set to 100.

4.4 How to Choose a Suitable Width of the Entrance Slit

For a practical Raman spectrum measurement, in order to choose a suitable width of the entrance slit b_{ent}, one needs to consider both the signal intensity and the spectral resolution. Then, the limitation FWHM of the slit image b_{limit} could be used as an importance reference value. According to equations (eq. 13) and (eq. 14), when

$$b_{ent} = b_{limit} = A \cdot \lambda \qquad \text{------ (eq. 17)}$$

we can calculate

$$b_{img} = \sqrt{2} \cdot M \cdot b_{limit} \qquad \text{------ (eq. 18)}$$

This means that the achieved spectral resolution will be $\sqrt{2}$ times of the limitation value.

Using the obtained value of *A,* for the visible laser line 514.5 nm, we get

$$b_{limit} = A \cdot \lambda = 100 \cdot 514.5\, nm = 51.45\, \mu m$$

and for the DUV laser line 257.3 nm,

$$b_{limit} = A \cdot \lambda = 100 \cdot 257.3\, nm = 25.73\, \mu m.$$

For the case of Stokes scattering, the wavelength of the Raman signal is longer than the wavelength of laser line. Therefore as a compromise choice, slit widths of about 60 µm for 514.5 nm and about 30 µm for 257.3 nm are reasonably adopted for practical measurements.

4.5 Dependence of the Spectral Resolution along the Raman Shift Axis

According to the equation (eq. 12), it is possible to plot the theoretical spectral resolution in the range of Raman shifts from 0 to 4000 cm^{-1}, as shown in Fig. 4.5 (green and violet line). Note that the resolution changes significantly along the abscissa. Since (eq. 12) predicts the spectral resolution for the central part of the CCD, it does not describe the situation for the spectral resolution in an exact way in the Raman spectrum recorded by using the whole CCD. In the non-central part of the CCD, the case does not strictly satisfy the equation (eq. 5), $\alpha = \theta - \theta_i$, but rather an approximate version, $\alpha \approx \theta - \theta_i$. Actually, for a static grating measurement, θ_i is a constant (see Fig. 4.1); therefore an expression of the spectral resolution, (eq. 12), can be obtained by using θ_i instead of α (see Appendix 5). The black lines in the Fig. 4.5 show the variation of the theoretical spectral resolution for series of static measured multi-channel spectrograms (static in opposition to so called extended scanning, a feature in the Renishaw spectrometer implemented by moving the grating and the charge detected on the CCD camera synchronously [4.17]).

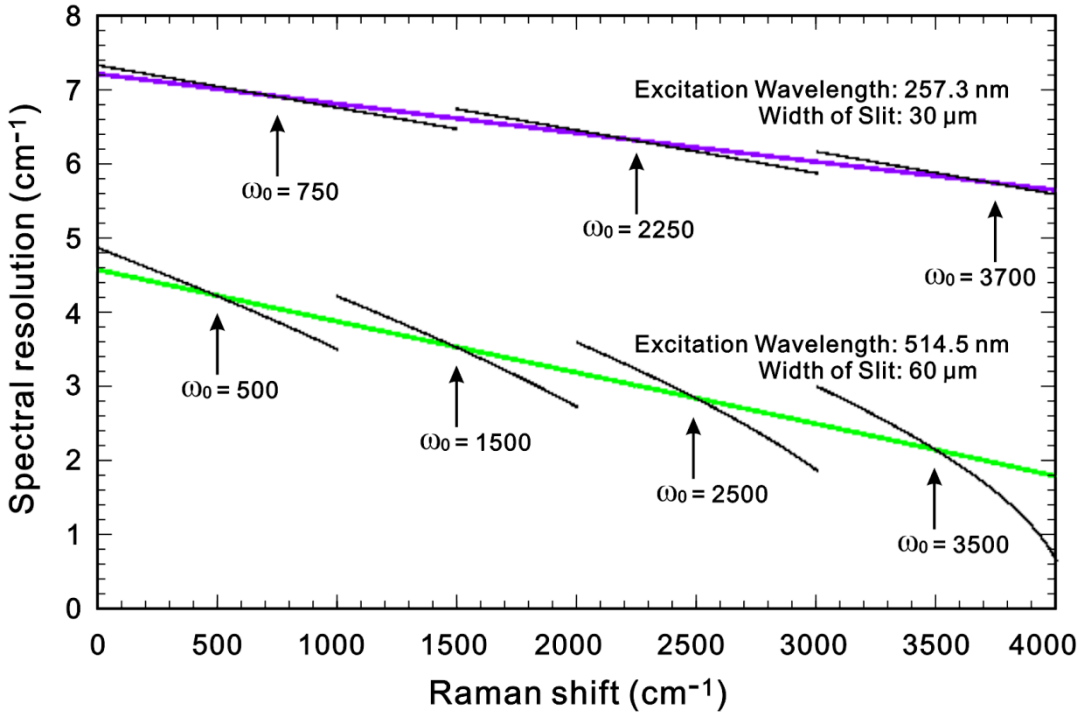

Fig. 4.5: The observed dependence of the spectral resolution along the Raman shift axis. The green and violet lines show the theoretical results calculated by use of (eq. 12) for only the central part of the CCD (in extended scanning mode using only few pixels). The black lines show the spectral resolution increments in four spectrograms and three spectrograms, for 514.5 nm and 257.3 nm laser excitation, respectively, obtained in static mode recordings, using many pixels and settings of the central pixel of the CCD at Raman shift wavenumbers of ω_0 = 500, 1500, 2500 and 3500 cm^{-1} for 514.5 nm excitation, and ω_0 = 750, 2250 and 3750 cm^{-1} for 257.3 nm excitation, respectively. [Appendix 7]

4.6 Experiments with Mercury Lines

The low pressure mercury lamp emits several narrow lines in the DUV range. Therefore it can be used as a wavelength calibration light source for DUV Raman instruments, and furthermore it is well suited for determination of the spectral resolution in the DUV range [4.9]. Particularly, there are three close lines with wavelengths of 265.2042, 265.3681 and 265.5121 nm in air, or 265.2831, 265.4471 and 265.5911 nm in vacuum [4.18] (~0.01 nm larger values have been given in [4.19]). These narrow lines are corresponding to absolute wavenumbers of 37695.57, 37672.29 and 37651.86 cm^{-1}, respectively, and they provide a direct view of the resolution capability of DUV Raman instruments.

These three lines of the low pressure mercury lamp were measured using a spectrometer setup similar to the one used for recording the Raman band of diamond excited with the 257.3 nm laser. The grating was set to the value of 265.2042 nm (the line of 37695.57 cm^{-1}) and various openings of the entrance slit were applied, as shown in Fig. 4.6.

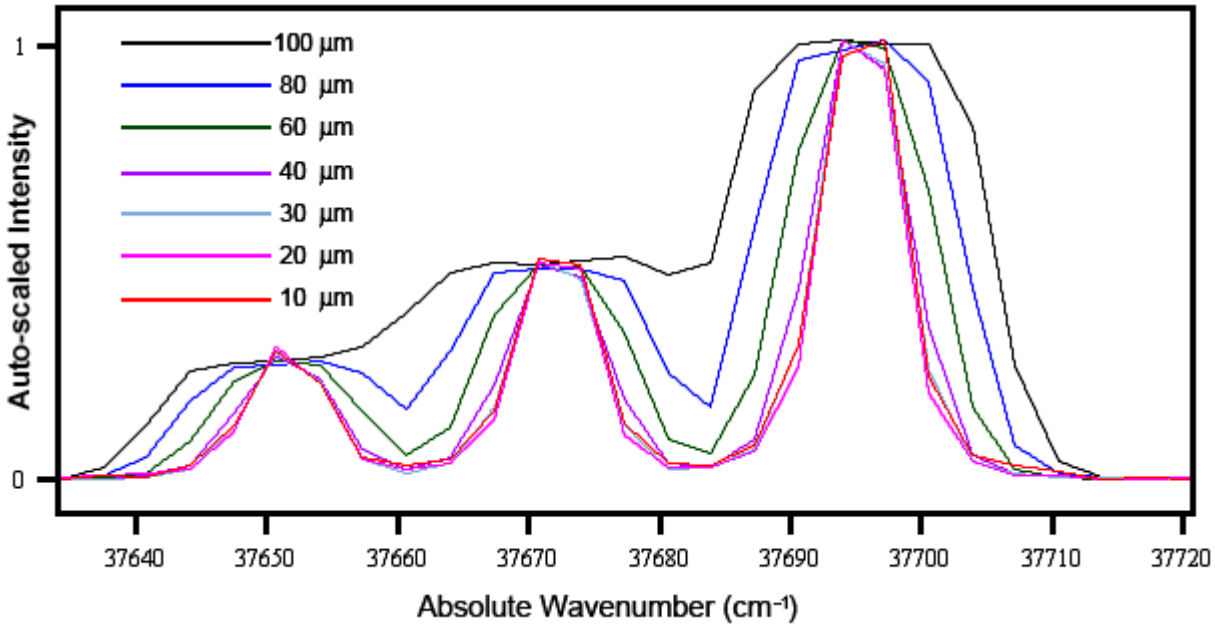

Fig. 4.6: Auto-scaled intensity of mercury lines at 37695.57, 37672.29 and 37651.86 cm^{-1}, obtained by the use of various slit widths (given in µm).

From these spectra we determined the FWHM values of the lines by means of software in the Renishaw WiRE™ 3.0 packet. The principle and the results are shown in Fig. 4.7. Note that a suitable curve resolution algorithm is indispensable during the evaluation of the FWHM values of a *spectrum band* because neighboring lines obviously are affecting each other when the lines are close enough, as seen in Fig. 4.7.

When all the curves in Fig. 4.6 have been curve resolved like for the example in Fig. 4.7, a data set is obtained that forms the basis for Fig. 4.8. Here, wide green points depict a plot of the ***line widths*** for the 265.2042 nm mercury line *versus* the various slit openings.

From these line widths ($\Delta\omega_M$, the wide green points in Fig. 4.8) the corresponding experimental ***spectral resolutions*** of the spectrometer ($\Delta\omega_S$, the narrow red points in Fig. 4.8) are obtained, again as in Fig. 4.4 by means of the (eq. 16), but now with $\Delta\omega_L = 0$ and $\Delta\omega_R \approx 1$ cm^{-1}. Here $\Delta\omega_R$ is the natural (or true) line width of the mercury line. We consider it to be less than 1 cm^{-1} but the approximation of 1 suffices because it is not an important factor when the spectral resolution is much bigger than 1 cm^{-1}.

The experimental spectral resolution curve of the spectrometer (red curve) - determined by this curve resolution technique on the 265.2042 nm mercury line data - compare well with the theoretical spectral resolution results (black dotted curve) obtained by using equations (eq. 12), (eq. 13) and (eq. 14), with A= 100 which determined from diamond experiments as shown in Fig. 4.8.

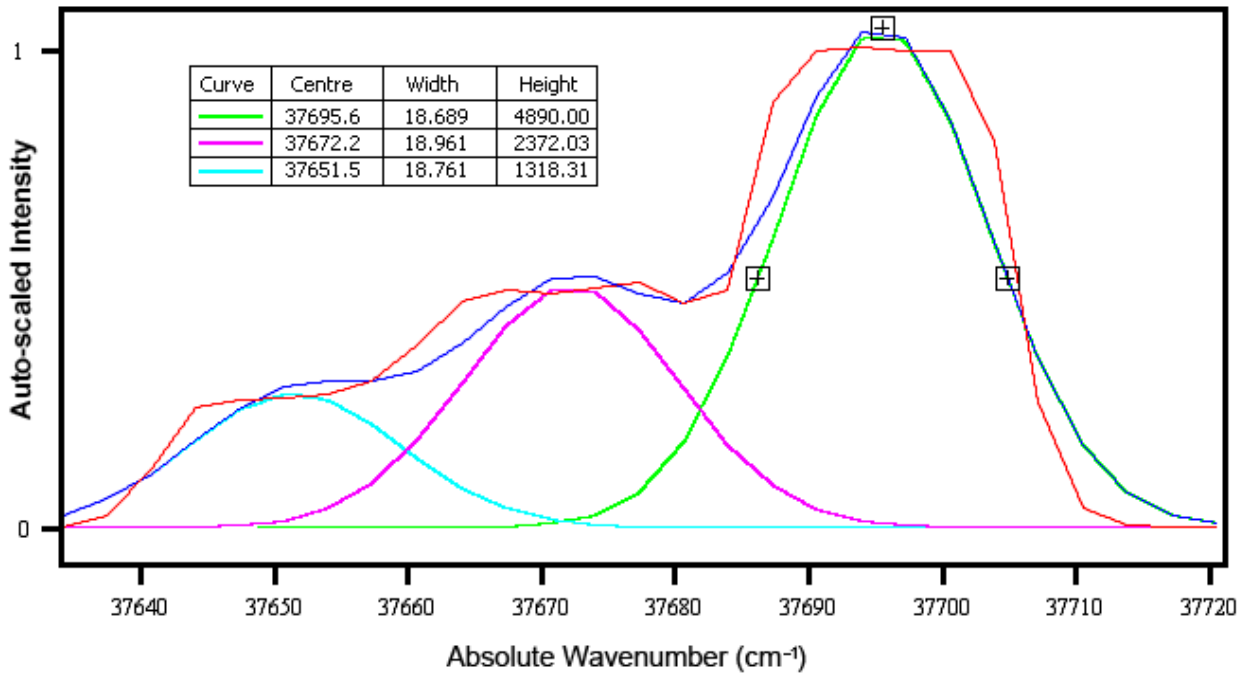

***Fig. 4.7**:* Example showing how to find the FWHM of the mercury line for the spectrum recorded for a slit width of 100 µm (red curve). The FWHMs of the *spectrum bands (main peaks of the curve)* contain the contributions of the neighboring lines. The green, pink and light blue curves and their blue sum are the Gaussian simulations of these three bands. The maximum and FWHM of the mercury line at 37695.57 nm are indicated with [±] signatures (note that the heights are not auto-scaled but the predicted intensities of the model).

As discussed in connection with Fig. 4.5, the resolution will depend on whether spectra measured with a multi-channel Czerny-Turner spectrometer are recorded in static or extended mode. This feature of the dispersive CCD spectrometer systems will cause testing with the same single line to give different spectral resolution results depending on the grating angle setting. As an example we show in Fig. 4.9 spectra for the 265.2042 nm mercury line, recorded for two different central wavenumber settings. An obvious difference is clearly seen.

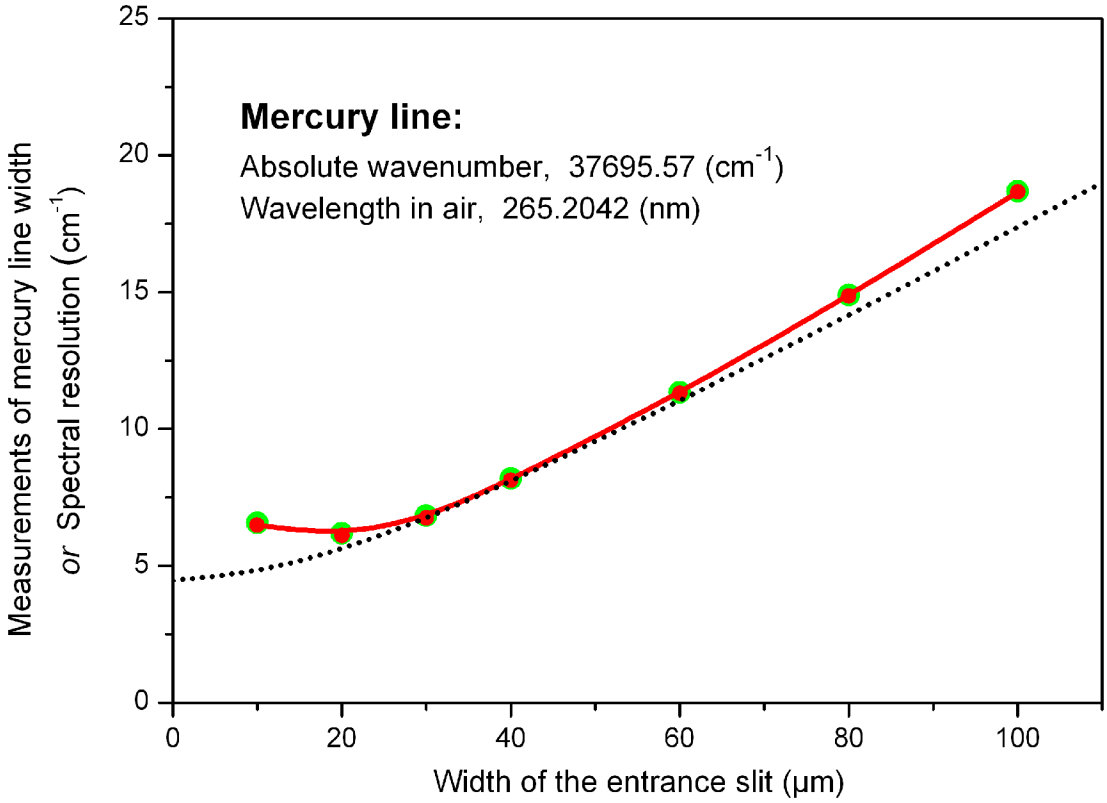

***Fig. 4.8**:* The wide green points are the measurements of the **linewidth** $\Delta\omega_M$ of the low pressure mercury lamp for various slit widths. The narrow red points, connected by the red curve, are the experimental spectral **resolution** data $\Delta\omega$, obtained by means of (eq. 16). The black dotted curve is the spectral resolution modeling results (theoretical spectral resolution) based on equations (eq. 12), (eq. 13) and (eq. 14). A = 100 was determined during the diamond experiments.

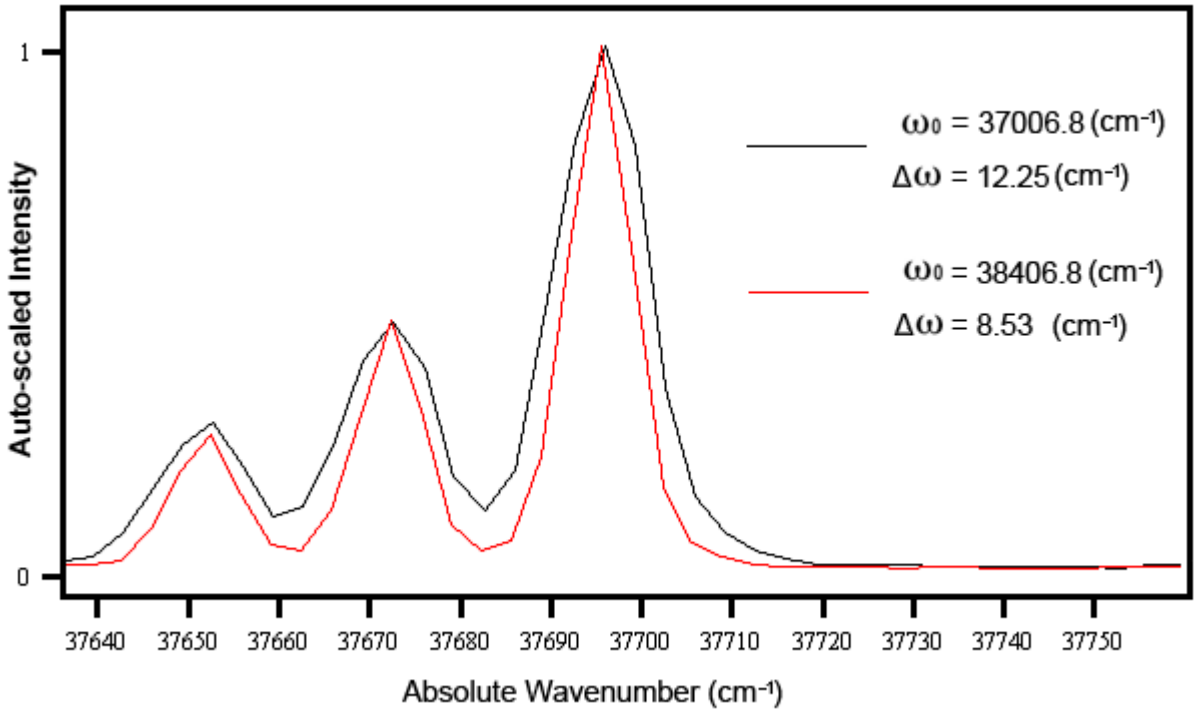

Fig. 4.9: Example of spectra obtained for the three studied mercury lines at 37695.57, 37672.29 and 37651.86 cm^{-1}. Both curves were obtained by use of a slit width of 40 µm in the static recording mode. The black and red curves were recorded in different pixels of the CCD by use of settings of the central pixel at absolute wavenumbers of 37695.57 – 700 = 36995.57, and 37695.57 + 700 = 38395.57 cm^{-1}, respectively. The difference in spectral resolutions, Δω, is significant, as indicated.

4.7 Discussion

According to the expression of the spectral resolution, (eq. 12), the spectral resolution depends strongly (quadratic) on the absolute wavenumber of the Raman scattered light. In DUV the wavenumbers are about twice the values in the visible range. Therefore, in order to get similar spectral resolutions for shorter ultraviolet exciting wavelengths, especially in the extreme DUV, one has to choose high groove-density gratings and narrow entrance slit widths to maintain/obtain high resolution. The wavenumber position of a Raman band also has a significant effect on the spectral resolution. Fig. 4.5 shows this trend of the spectral resolution along the Raman shift axis.

Although equations (eq. 12), (eq. 13) and (eq. 14) reveal the spectral resolution in dependence of all the principal factors, the effect of diffractions and aberrations has not been detailed determined by the present theoretical approximation method. If one would examine these effects it requires information on the actual situation of the optical components and deep optical investigations. Instead of this however, we have introduced a new approximate procedure to handle the situation: By introducing the diffractions and aberrations compensating factor *A*. This *DACF factor*, in (eq. 14), is used to develop a hyperbola function model for the spectral resolution with respect to the width of the entrance slits and for the different

settings of the experimental situation. The experimental data obtained during this work have shown that this procedure is well suited to fit the results, as seen in Fig. 4.4 and checked in Fig. 4.8.

4.8 Conclusion

Often - in Raman spectroscopy - one wants to know what the true width of an observed Raman band is. We here present a generalized method to determine it. At first one has to find out what is the particular spectral resolution of the applied instrument *at the precise position* where the Raman band is located. We have demonstrated that this can been done by using the equations (eq. 12), (eq. 13) and (eq. 14). All the parameters except a new one *A* (*or DACF*) can be easily found, and *A* can be determined by measuring on a given narrow line, *in casu* the diamond Raman fundamental at 1332.4 cm^{-1} or low pressure emission plasma lines from mercury gas. Then, as soon as the spectral resolution at the position of the Raman band in question is known, the band width can be found by means of (eq. 16), as derived in Appendix 4. In order to ensure the measuring accuracy, it should be noted, that the grating should be turned to such an angle that the tested Raman band is located at the central pixel area on the CCD detector – also during recording in scanning mode - because only at the central pixel area is the exact condition for using the equation (eq. 12) strictly fulfilled. Otherwise, there will be deviations as shown in Fig. 4.5 (black lines). At the same grating setting also one takes advantage of the feature that the central area of the CCD is in the optimized position for the slit imaging.

It is to be noted that many CCD-based Raman spectrometric systems apply so-called static recording modes, i.e. spectrometric detection of photons in many pixels of the detector while keeping the grating still (static). Instead of this the Renishaw system can be operated in a so-called extended scan mode, in which the grating is synchronously moved coupled to the charges in the CCD pixels [4.17]. We conclude from our analysis here that the static and the extended recording modes differ with respect to their resolution properties as described. This dependence has been widely overlooked in the literature, but can now be accounted for by use of the new method.

References to Chapter 4

[4.1] S. A. Asher and C. R. Johnson, "*Raman spectroscopy of a coal liquid shows that fluorescence interference is minimized with ultraviolet excitation*", *Science*, New Series *225*, No. 4659, (**1984**), pp. 311-313.

[4.2] S. A. Asher, "*Ultraviolet Raman Spectrometry*", in *Handbook of Vibrational Spectroscopy*, M. J. Chalmers and P. R. Griffiths, Editors, John Wiley & Sons Ltd., New York, *1*, (**2002**), pp. 557-571.

[4.3] D. D. Tuschel, A. V. Mikhonin, B. E. Lemoff, and S. A. Asher, "*Deep Ultraviolet Resonance Raman Excitation Enables Explosives Detection*", *Appl. Spectrosc.* 64(4), (**2010**), pp. 425-432.

[4.4] A. J. Kunov-Kruse, S. B. Kristensen, Chuan Liu and R. W. Berg, "*Experimental and theoretical Raman spectrum of the dye Sudan I*", J. Raman Spectrosc. 42, (**2011**), pp. 1470–1478.

[4.5] A. C. Ferrari, J. C. Meyer, V. Scardaci, C. Casiraghi, M. Lazzeri, F. Mauri, S. Piscanec, D. Jiang, K. S. Novoselov, S. Roth and A. K. Geim, "*Raman Spectrum of Graphene and Graphene Layers*", *Phys. Rev. Lett.* 97(18), (**2006**), pp. 187401.

[4.6] H. Ou, Y. Ou, Chuan Liu, R.W. Berg and K. Rottwitt: "*Formation and Characterization of varied size germanium nanocrystals by Electron Microscopy, Raman spectroscopy and Photoluminescence*", Optical Materials Express 1, Issue 4, (**2011**), pp. 643-651.

[4.7] J. M. Lerner and A. Thevenon, "*The Optics of Spectroscopy, a tutorial V2.0*", Jobin-Yvon ISA Optical Systems Instruments S-A, Inc., (**1988**), pp. 22.

[4.8] I. K. Lednev, V.V. Ermolenkov, Wei He and Ming Xu, "*Deep-UV Raman spectrometer tunable between 193 and 205 nm for structural characterization of proteins*", Anal. Bioanal. Chem. *381*, (**2005**), pp. 431–437.

[4.9] S. Bykov, I. Lednev, A. Ianoul, A. Mikhonin, A. Munro and S. A. Asher, "*Steady-State and Transient Ultraviolet Resonance Raman Spectrometer for the 193-270 nm Spectral Region*" Appl. Spectrosc. 59, (**2005**), pp. 1541-1552.

[4.10] J. D. Ingle and S. R. Crouch, "*Spectrochemical Analysis*", Prentice Hall, Englewood Cliffs, N.J., (**1988**), pp. 70-74.

[4.11] R. L. McCreery, "*Dispersive Raman Spectrometers*", Chpt. 8 in "*Raman Spectroscopy for Chemical Analysis"*, Wiley Interscience, New York, (**2000**).

[4.12] N. Sheppard, "*The Historical Development of Experimental Techniques in Vibrational Spectroscopy*", in *Handbook of Vibrational Spectroscopy*, I. R. Lewis, H. G. M. Edwards (Editors) John Wiley & Sons Ltd, Chichester, *1*, (**2002**), Chpt. 1, pp. 17- 30.

[4.13] E. Hecht, "*Optics*", Addison-Wesley, San Francisco, CA, 4th edition, ISBN: 0-321-18878-0, (**2002**), p. 461, p. 468, pp. 470.

[4.14] P. R. Griffiths, "*Resolution and Instrument Line Shape Function*", *Handbook of Vibrational Spectroscopy*, I. R. Lewis, H. G. M. Edwards (Editors) John Wiley & Sons Ltd, Chichester, *1*, **(2002**), Chpt. 2, pp. 2-8.

[4.15] V. Deckert and W. Kiefer, "*Scanning Multichannel Technique for Improved Spectrochemical Measurements with a CCD Camera and its Application to Raman Spectroscopy*", Appl. Spectrosc. 46(2), (**1992**), pp. 322-328.

[4.16] S. Prawer and R. J. Nemanich, "*Raman Spectroscopy of Diamond and Doped Diamond*", Math. Phys. Engin. Sci, 362, (**2004**), pp. 2537-2565,

[4.17] Renishaw Technology note L-8012-3890-01-F SPD074TN, "*Renishaw's SynchroScan: Artefact- free spectra*", August 2007. See also C. Dyer, B. J. E. Smit, *J. Raman Spectrosc*. 26, (**1995**), pp. 777-783, and patents EP 0638788 A1 (**1992**) and US 5,689,333 (**1997**).

[4.18] F. M. Phelps III, M.I.T. "*Wavelength Tables, Wavelengths by Element*", The MIT Press, Cambridge, Massachusetts, Vol. *2,* 274 (**1982**), based on data by L. Cardaun, *Zeits. f. wiss. Phot. 14*, (**1914**), pp. 56-89.

[4.19] V. Kaufman and B. Edlén, "*Reference Wavelengths from Atomic Spectra in the Range 15 Å to 25000 Å*", *J. Phys. Chem. Ref. Data 3(4),* (**1974**), pp. 825-880.

[4.20] G. B. Airy, "*On the Diffraction of an Object-glass with Circular Aperture*", *Trans. Cambridge Phil. Soc. 5*, (**1835**), pp. 283-291.

Symbols to Chapter 4:

A	The Diffractions and Aberrations Compensation Factor (DACF)
b_{ent}	Width of entrance slit
b_{img}	FWHM of the entrance slit image for $M = 1$
b_{limit}	The limitation FWHM of the slit image for $M = 1$
d	The spacing of the grating grooves
f_1	Focal length of concave mirror 1 or lens 1
f_2	Focal length of concave mirror 2 or lens 2
G	Diffraction grating groove density
$g_L(\omega)$	Spectrum of the exciting laser
g_{L0}	Normalizing constant corresponding to maximum on the Laser peak.
$g_{LR}(\omega)$	Profile of the Raman band excited by a laser
$g_M(\omega)$	Profile of the measured Raman band
$g_R(\omega)$	Profile of an true Raman band
g_{R0}	Constant corresponding to maximum on the true Raman peak.
$g_s(\omega)$	Signal obtained at the detector for a monochromatic line
g_{S0}	Normalizing constant for the spectral contribution (expanded by spectrometer) of a monochromatic light.
$I(r)$	Intensity distribution of an Airy diffraction pattern versus the radius r
$J_1(r)$	Bessel function of the first kind.
$ln2$	Natural logarithm of 2
M	System magnification
r	Radius of the Airy disk diffraction pattern
α	Angle between the incident light and the diffracted light
$\Delta\lambda$	Difference between two close wavelengths
$\Delta\omega$	Theoretical spectral resolution of spectrometer [cm^{-1}]
$\Delta\omega_S$	Experimental spectral resolution of spectrometer [cm^{-1}]
ω_1	Narrow incremental section (a delta function) of the laser spectrum [cm^{-1}]
ω_2	Wavenumber of integration in convolution [cm^{-1}]
ω_s	The variable of the wavenumber difference between the *real* Raman signal and the *measured* Raman signal [cm^{-1}]
$\Delta\omega_M$	Measured bandwidth of Raman band [cm^{-1}]
$\Delta\omega_R$	True Raman bandwidth [cm^{-1}]
ω_r	The variable of Raman shift [cm^{-1}]
$\Delta\omega_L$	Linewidth of the exciting laser [cm^{-1}]
$\Delta\Theta$	Difference between two close diffraction angles
λ_L	Wavelength of the exciting laser
ω_0	Central Raman wavenumber shift for static grating measurement [cm^{-1}]
ω_R	Raman wavenumber shift [cm^{-1}]
ω_L	Absolute wavenumber of the exciting laser [cm^{-1}]
Θ	Grating diffraction angle
Θ_i	Grating incident angle

5 DUV Raman spectroscopic studies of Gasoline.

5.1 Introduction

As a petroleum-based fuel, gasoline consists of a complex mixture of hundreds of hydrocarbons. The performance properties gasoline is closely related to the chemical constituents in the specific hydrocarbon mixture of the fuel. The gasoline octane number is an important property which defines the antiknock quality of the fuel. The content of aromatic compounds is boosting the octane number. On the other hand, the aromatics compounds - such as the common so-called monocyclic BETX group (the 6 compounds Benzene, Toluene, Ethylbenzene, and three isomers of Xylene) - are highly polluting compounds. These chemicals are able to penetrate soil and thus pollute the underground drinking water reserves. On January 1st 2000 a new legislation was introduced in Denmark with respect to aromatics in gasoline: the maximum allowed benzene content was fixed to be 1% and the maximum total content of aromatics was 42% [5.1]. Since the makeup of fuel mixtures requires a careful balance between the components and a reproducible consistency of the mixture, it is essential to be able to determine quickly and reliably the identity and relative content of the active chemical components, present in the fuel batch.

Traditionally gasoline is analysed in many different ways. For instance the total aromatic content is determined by a PIONA analyser, which is based on a gas chromatographic method. The alkanes, iso-alkanes, alkenes, naphthenes and aromatics in the gasoline are separated and analysed. The benzene and MTBE contents are also traditionally determined by gas chromatographic methods [5.1]. Compared with the above motioned analytic methods, Raman spectroscopy has some remarkable advantages such as rapidity, no-contact, milliliter amounts sample and so on. Raman spectroscopic studies of gasoline have occasionally been described in the literature, e.g. with respect to determination of octane number and Reid vapour pressure [5.2]-[5.4], percent content of oxygen [5.5] and amount of aromatics [5.6], [5.7]. The fluorescence interference is a persistent problem for gasoline analysis when the wavelengths of excitation lasers are located in the visible range [5.8]. Therefore, most of the above mentioned applications were implemented by Fourier transform infrared Raman spectrometry in order to reduce the fluorescence.

The difficulty caused by fluorescence interference can be addressed in the opposite way, i.e. shifting the excitation source to the deep ultraviolet (DUV) range. This is because the fluorescence spectra usually prevail in the wavelength range from 300 to 700 nm or longer and there exists a cut-off wavelength at the shorter wavelength side in the UV region for condensed materials. By choosing an excitation wavelength so short, that the excited Raman signals also occur at wavelengths shorter than the fluorescence spectrum, then the Raman signals and the fluorescence spectrum are separated, resulting in the fluorescence interference being greatly diminished. Moreover, the signal intensity is much enhanced because the scattered Raman intensity is proportional to the fourth power of the light frequency [5.9].

Another important advantage of using DUV light sources in Raman spectroscopy is the possibility of a significant improvement in resonance enhancement. The resonance enhancement is realized while the energy of the excitation photon is close to an electronic transition between two states, which often give rise to an absorption band in the absorption spectrum. In the situation of resonance enhancement, the Raman intensity can be increased dramatically. A resonance-enhanced signal can be several orders of magnitude more intense than the normal Raman signal [5.10], [5.11]. Resonance Raman spectroscopy is particularly useful in analytical chemistry when applied to a sample containing a mixture of individual species [5.12], [5.13]. The Raman bands associated with the different components can be selectively enhanced

when excited according to their electronic transitions when in resonance. Therefore such a situation is suitable for analysis of a complex mixture, and it may even make it possible to determine components of small contents.

However, the resonance Raman situation can also become a disadvantage, when the component of interest has no resonance band in the DUV range. As we shall see in the following, such a case is found for MTBE and most of the alkanes in gasoline, and the Raman signals of such components are totally suppressed relatively to the resonating substances, thus making analysis of the components not in resonance difficult to realize by DUV Raman spectroscopy.

5.2 Gas Gap Cell

DUV resonance Raman spectroscopy should be uniquely suited for studies of aromatic species in fuels, coal liquids and in petroleum fractions [5.14], [5.15]. Most aromatic compounds have strong and broad resonance absorption bands in the DUV range, meaning that the test samples are not DUV transparent. Therefore the sampling area is confined to a small spot on the surface of the sample, whether it is in contact with a quartz wall or with a gas atmosphere (a gas gap in a convenient cell). Under a microscope the gathering direction of the Raman signal is normally 180^{o} from the direction of the vertical excitation laser beam (back scattering). This is also practical for the testing of samples absorbing strongly the Raman signal. In the following, we will describe some measuring difficulties for the situation of use of the microscope Raman entrance, and we will introduce a simple device to solve these problems.

Firstly, let's consider the Raman sampling from a surface which contacts with a quartz wall (Fig. 5.1 (a)). Because the entire energy of the excitation light is absorbed in a tiny area "between" the sample and the wall, the amount of undestroyed sample in this sampling area is rapidly going down. Furthermore a bubble is often appearing during the measurement. It most probably is due to decomposition and the heating effect of the DUV light. For a multi-compound mixture, such as a gasoline sample, this behavior is very obvious. It certainly destroys the quality of the measurements. In order to avoid this problem, the magnetic stirring has been used to circulate the sample as shown in Fig. 5.1 (a). However, it did not improve the measurements to any obvious extent. The reason is considered to be due to the laminar flow near the quartz wall. In the sampling area, actually, the liquid moves slowly.

Another method, a setup of a flowing stream of a liquid in a quartz capillary has been constructed and used for several aqueous solutions, wine, etc. [5.15]. A picture of such a quartz capillary tube setup is shown in Fig 5.1(b). However, for most petroleum products, it requires a quite complicated setup because these liquids are volatile, toxic and corrosive. Considering the laminar flow near the quartz wall, the movement of the sample is actually still not realized very well if the liquid has a high absorbance. Another disadvantage of the tube system is that the Raman signal has interference from the quartz material because the wall is very close to the Raman sampling area.

Therefore, we considered Raman sampling from the "naked" sample surface - with a gas gap - as shown in Fig. 5.1 (c). The convection can be obtained by itself because of the disturbances from the laser beam, and the heat and the decomposed compounds will be easily dispersed. Since the sample is often volatile, the

gas gap cell must be airtight. It is not only for keeping the health of the operator but also for the stabilization of the level of the surface, because the excitation beam is supposed to be kept in focus on the surface to stabilize the measuring.

Then a new problem for the measurement of gasoline sample was met. During the DUV laser exposure, a gasoline drop tended to be formed on the sampling window, exactly where the laser beam goes through as shown in Fig. 5.1 (d). Fig. 5.2 (b) shows a photograph of a gasoline drop formed by excitation for 1 minute in a 10 mW 244 nm laser beam. This phenomenon does not occur when the excitation is done with visible light, such as the blue 488 nm line, as shown in Fig. 5.2 (a), or when the samples are simple mixtures, such as e.g. a mixture of toluene and pentane. Our explanation of such an abnormal phenomenon is that the DUV light - when being strongly absorbed in the liquid – destroys some of the molecules. The decomposition products increase the surface tension of gasoline, thus the molecular may be pulled to where the DUV light illuminated.- or the most absorbing species may act as condensation nuclei for the condensation of the vapor. However it seems that the drop is not formed from the vapor. If starting the measurement by use of the more developed cell (see later Fig. 5.3) with a wetted window, after the DUV laser beam exposure, the window turned to dry.

Since the gasoline has a high wettability for quartz, the upper window is wet, already when the cell is half-filled. The wetted upper wall of the cell actually provides the problematic point. The transport of the gasoline to the sampling window is shown with arrows in the Fig. 5.1 (d).

To overcome the problem we surrounded the sampling window with a material having a low surface tension so that it is non-wetted with gasoline. PTFE is presently the best choice, and it is very non-reactive with gasoline and non-soluble in gasoline. Fig. 5.3 shows a gas gap cell with a quartz window surrounded by PTFE. Thereby, the liquid surface cannot reach the window surface, which maintains the sampling window in a “dry” condition during the DUV illumination.

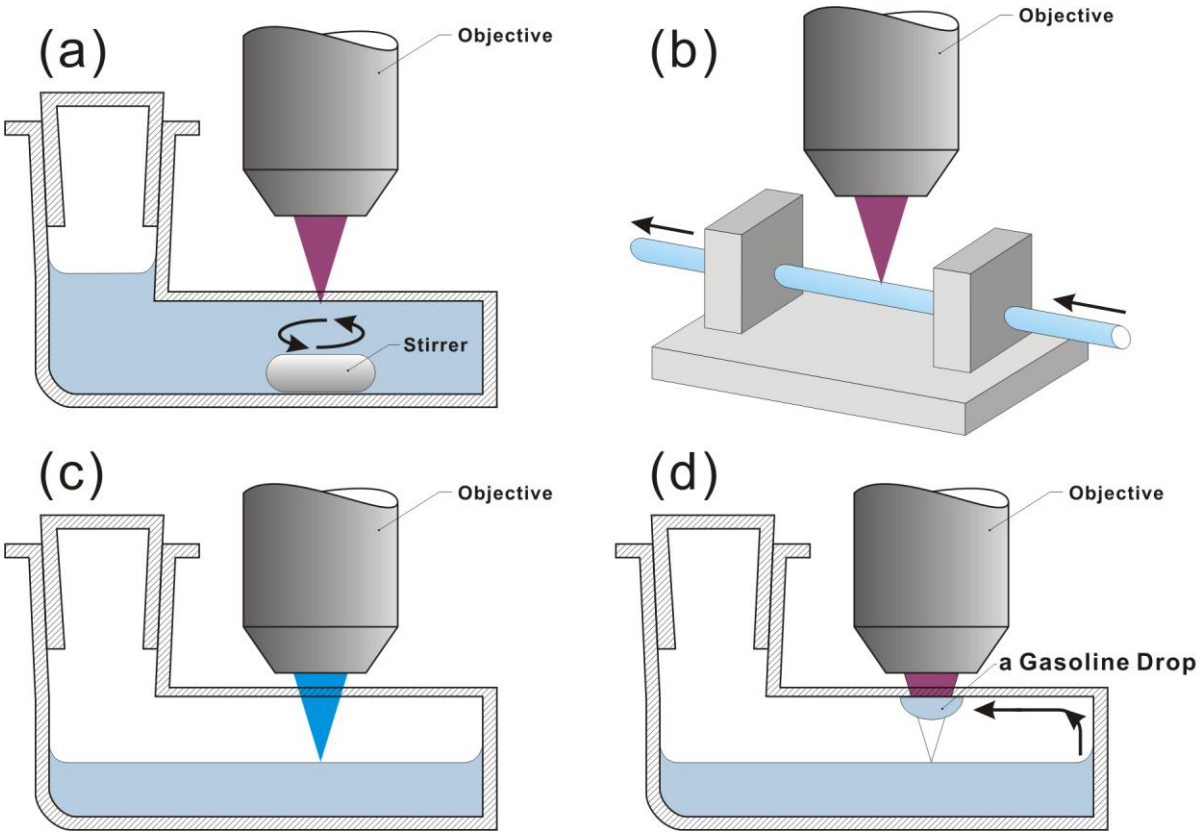

Fig. 5.1: Different versions of sampling cells for liquids, with vapor pressure (a), (c), (d), and for a quartz capillary tube cell for liquids with no vapor pressure and non-absorbing liquids (b). The picture (b) of the tube setup is from [5. 15].

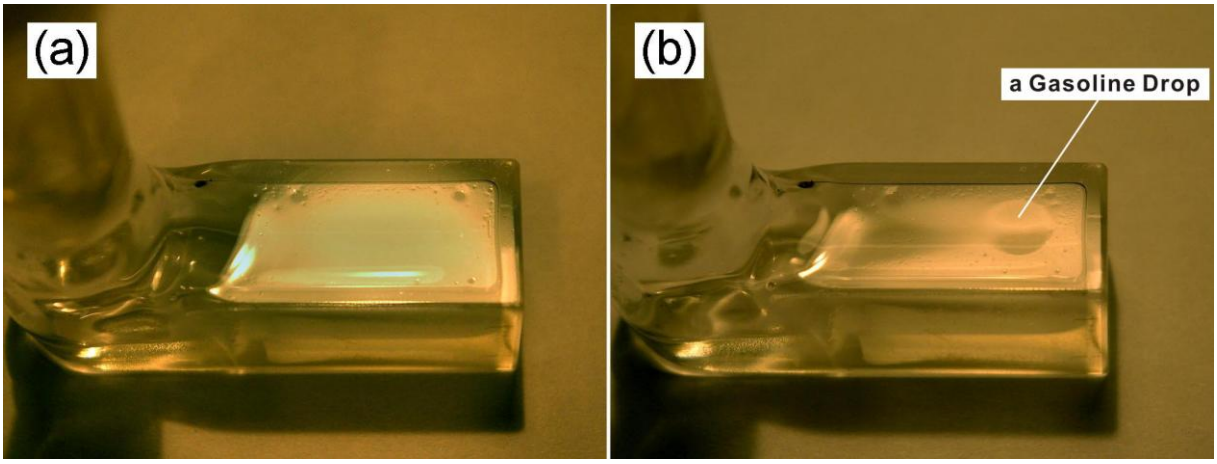

Fig. 5.2: Photographs of the same half-full cell, (a) under blue light excitation and (b) under deep ultraviolet excitation. The drop is hanging where the invisible DUV beam is focused.

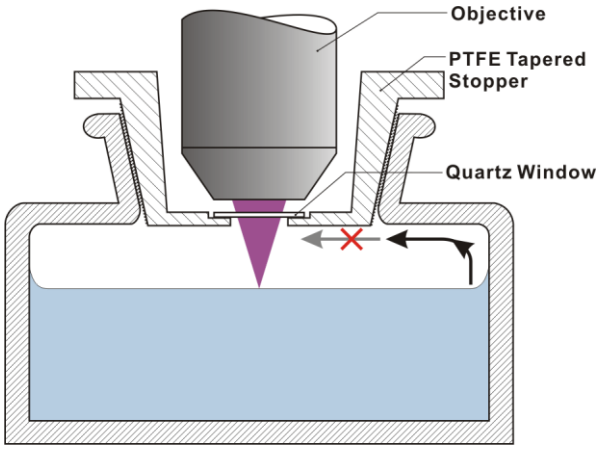

Fig. 5.3: The developed gas gap cell with a quartz window surrounded by PTFE. No drop is formed on the quartz window.

5.3 The experimental setup and the measurement parameters.

In the following entire experiments, except the excitation wavelength all the measurement parameters as well as the laser power, exposure time, objective and the width of the entrance slit are set to be same as below.

The instruments:

- **Spectrometer:**
  An InVia Reflex spectrometer system with micro-entrance (Renishaw plc.);
  Traditional x15 UV objective;
  Acquisition time is 20 second, accumulation 2;
  The lowest cutoff wavenumber of filters are 150, 200 and 550 cm^{-1} for 257.3, 244.0 and 229.0 nm respectively.
  Width of the Entrance slit: 40 µm.

- **Laser:**
  A 95-SHG-QS frequency-doubled Argon ion laser (Cambridge Laser Laboratories Inc.);
  Three DUV laser lines: 257.3, 244 and 229 nm;
  The output power from the laser head was adjusted to 15 mW for each laser lines, about 20 % power (3 mW) reaches the surface of sample.

- **The developed gas gap cell** (as shown on Fig. 5.3).

Samples:

- **Six types gasoline**: Statoil 92, Statoil 95, Statoil 98, Shell 92, Shell 95 and Shell V-power (also named Shell 99), were taken from gas station on 6th August 2010 in the Copenhagen area.

- **Gasoline components:**

Chromatics: Benzene, Toluene, Ethylbenzene, three isomers of Xylene and Naphthalene.
Aliphatics: Butane, Pentane, Hexane and Heptane.
Agent: MTBE and Ethanol.

- **Diamond:**
  All the measurements have been calibrated by the diamond peak at 1332.4 cm^{-1}.

5.4 Overview of the DUV Raman Spectra of Gasoline: The DUV Raman Spectra of Gasoline Excited by Three Different Wavelengths, 257.3, 244.0 and 229.0 nm.

Fig. 5.4 shows the DUV Raman spectra of Shell 92 gasoline excited by the three different wavelengths, 257.3, 244.0 and 229.0 nm, plotted on the same wavenumber shift scale. In the 257.3 nm excited spectrum, no Raman bands can be observed but only the strong fluorescent background. Therefore, the 257.3 nm excitation line must be abandoned for gasoline Raman analysis.

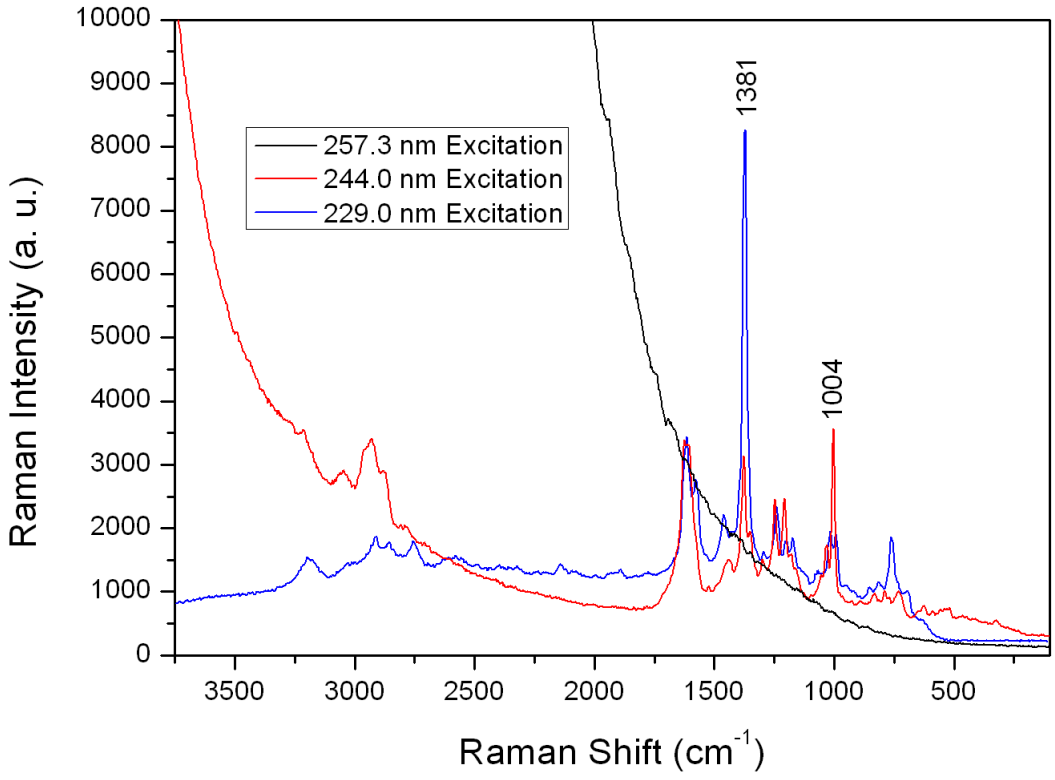

Fig. 5.4: The Raman spectra of Shell92 gasoline excited by three different wavelengths, 257.3, 244 and 229 nm, showing the different results.

As seen in Fig. 5.4 in the 244.0 nm excited spectrum, there are still reminiscences of the fluorescent background. Fortunately, within the range of 0 – 2000 cm^{-1}, in which most of the intense bands are contained, the fluorescent background is much lower than in the range 2000 – 4000 cm^{-1}.

In the 229.0 nm excited spectrum, the fluorescent background is avoided completely. Compared with the 244.0 nm excitation spectrum, the 229.0 nm excitation spectrum obviously has a much different profile. According to the following study, the Raman spectrum excited by 244.0 nm is mainly dominated by the aromatics present in the gasoline, including monocyclic and bicyclic species; and it will be shown that the small content of bicyclic aromatics play an even more important role in the spectrum excited by the 229.0 nm excitation line. Thus, these two excitation lines will have different functions for the analysis of gasoline samples.

5.5 Raman Spectra of Mixtures of Aromatic and Aliphatic Liquids, Represented by Toluene / Heptanes, Toluene / Pentane, Gasoline / Pentane, by use of the 229 nm excitation.

Aromatic components have very high Raman scattering cross-sections owing to large polarizability changes under laser excitation [5.16]. The bands from these components dominate specific Raman spectral regions of aromatic and aliphatic mixture, and analysis of the aromatics in gasoline has previously been performed by visible laser excitation [5.17]. For the case of DUV laser excitation, the situation becomes more delicate because most aromatic components have resonance absorption of DUV light, resulting in resonance Raman scattering, and thus extremely enlarged Raman cross-sections occur. Oppositely, most aliphatic components in the gasoline do not show absorption or resonance Raman scattering affects over the range of 220 – 260 nm.

At first, we started to investigate the behaviour of simple aromatic / aliphatic sample mixtures of Toluene / Heptane and Toluene / Pentane. Fig. 5.5 shows the Raman spectra of Toluene and Heptane mixtures excited by the 229 nm line. It is clear that Toluene dominates the Raman spectra. Only the most intense and relative broad bands of Heptane, at 1300 and 1460 cm^{-1}, corresponding to CH_2 twisting and CH_2 wagging modes [5.20], respectively, can be weakly observed when the Heptane concentrations are high, e.g. 80 vol. % and 60 vol. % of Heptane. In the spectra of concentration lower than 40 vol. %, no bands of Heptane can be observed. The situation is similar for the mixture of Pentane and Toluene as shown in Fig. 5.6.

The aromatic compound Toluene seems to dominate over the aliphatics – Pentane and Heptane - in 229 nm excited DUV Raman spectra.

A typical gasoline mixture - like standard Shell 95 octane gasoline - contains about 5 weigh % Pentane. A 229 nm excited Raman spectrum of such a gasoline does not show any sign of these 5 % Pentane, see Fig. 5.7. Then we considered if we could observe Raman bands of Pentane in the gasoline by increasing the concentration of pentane. As Fig. 5.7 shows, the Raman bands of Pentane are even weaker than for the

mixture with Toluene, meaning that there must be at least one component in the gasoline sample that gives rise to even stronger *resonance* Raman scattering than Toluene for 229 nm excitation.

As the above results shown, the constituent resonance bands dominate the Raman spectra of the mixture. Therefore most of the aliphatic components - without resonance - will not be presented in the 229 nm DUV Raman spectrum. With respect to the aromatic components in a typical gasoline, toluene has the largest content, on the order of around 10 vol. %. However, the 229 nm Raman spectrum of the standard Shell 95 octane gasoline shows its most intense peak at 1381 cm^{-1} at a position which does not correspond to the most intense peak of toluene at 1004 cm^{-1}. This 1381 cm^{-1} peak most probably should be assigned as a bicyclic ring breathing mode in naphthalene, $C_{10}H_8$ [5.18]. This is in accordance with a quantum mechanical calculation [5.21] done in our laboratory, see Fig. 5.8. In the following we will focus on naphthalene in a different mixture.

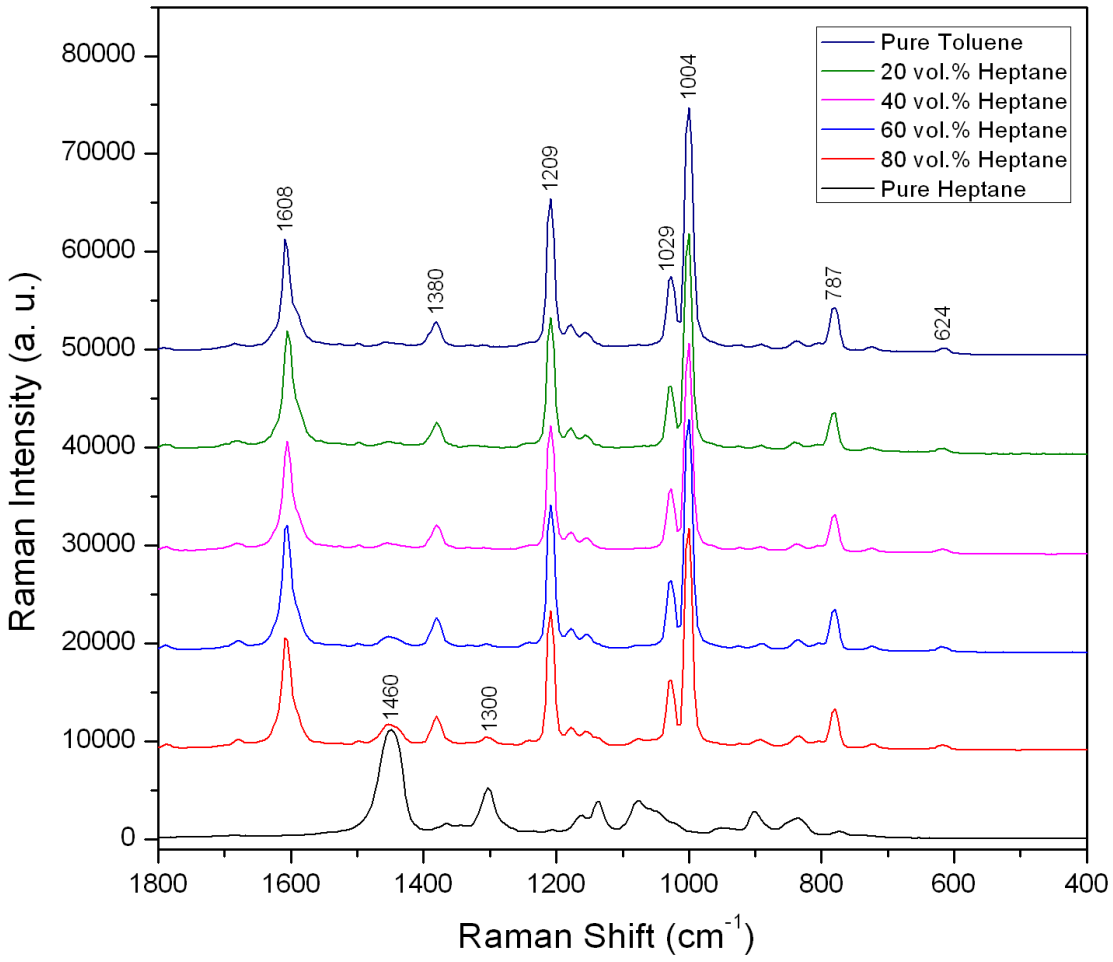

Fig. 5.5: The Raman spectra of a series mixture of Toluene / Heptane excited by the 229 nm laser line.

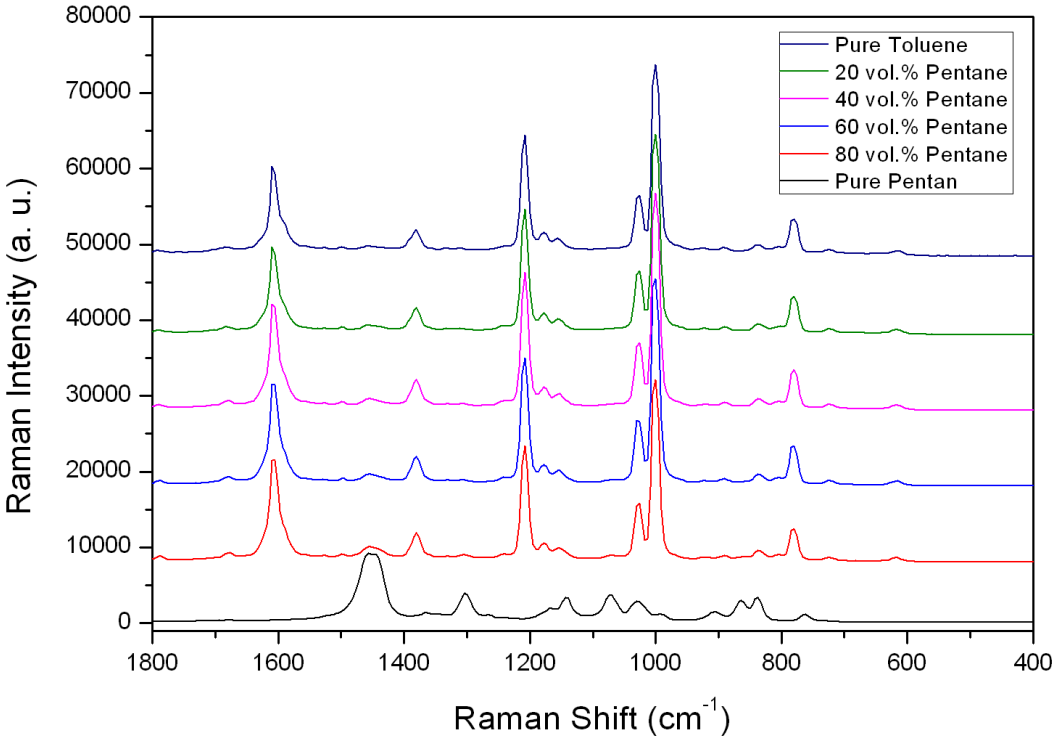

Fig. 5.6: The Raman spectra of a series mixture of Toluene / Pentane excited by the 229 nm laser line.

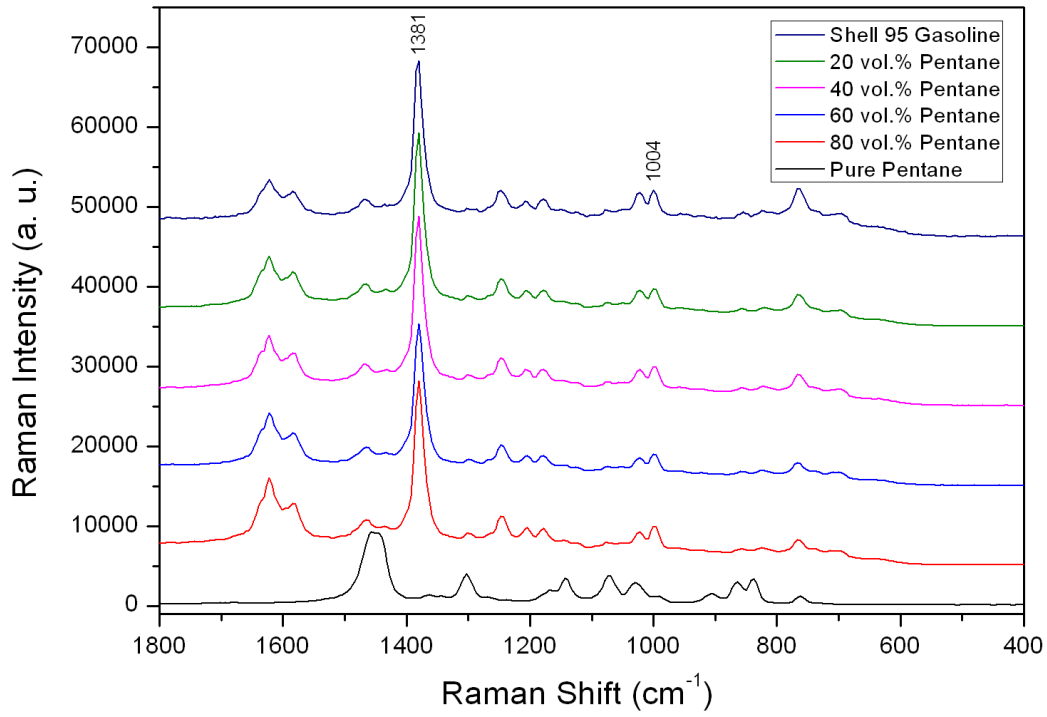

Fig. 5.7: Raman spectra of a series of mixtures of standard Shell 95 octane Gasoline / Pentane, excited by the DUV 229 nm laser line.

5.6 Raman Spectra of Naphthalene and Toluene Mixtures by use of the 244 nm excitation.

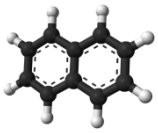

Naphthalene is a highly poisonous compound $C_{10}H_8$, bicyclo[4.4.0]deca-1,3,5,7,9-pentene, CAS number 91-20-3. It occurs in natural carbonaceous materials such as raw oil.

We have calculated the optimized structure and its vibrational spectrum [5.21]. The monocyclic ring breathing mode in Toluene at 1004 cm^{-1} and the bicyclic ring breathing mode in Naphthalene at 1381 cm^{-1} are shown in Fig. 5.8, in accordance with our quantum mechanical calculations [5.21]. In the following we will focus on naphthalene in a different mixture.

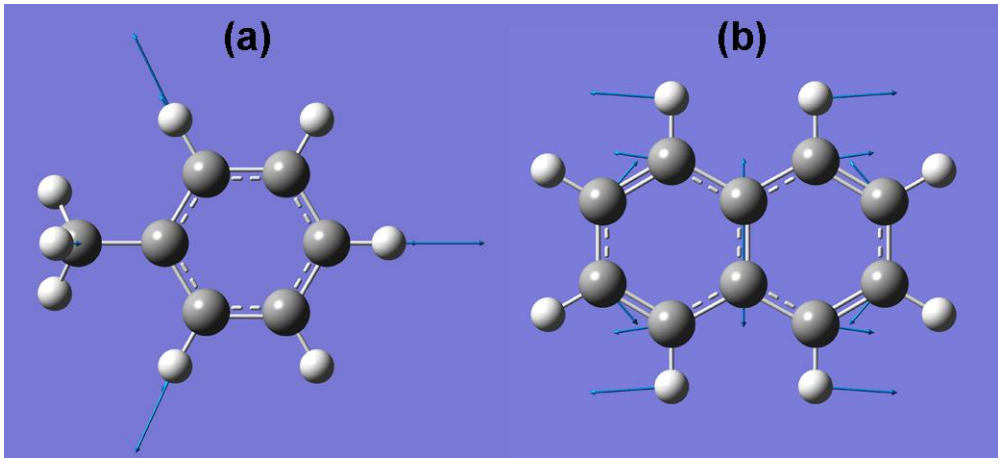

Fig. 5.8: (a) The monocyclic ring breathing mode in Toluene at 1004 cm^{-1}; (b) the bicyclic ring breathing mode in naphthalene at 1381 cm^{-1} [5.21].

Fig. 5.9 shows the 229 nm DUV Raman spectrum of a 2.5 weight % of Naphthalene dissolved in Toluene, and as seen the Naphthalene completely dominates the Raman spectrum. Only the most intense peaks of toluene can be weakly seen in the spectrum of the mixture, meaning that Naphthalene has a much larger Raman cross-section than Toluene when using of the 229 nm excitation. According to the absorption spectra of Toluene and Naphthalene, although both have an absorption peak at 220 nm, Naphthalene has stronger absorption than toluene at 229 nm [5.18], [5.19]. In the gasoline sample, the bicyclic aromatics obliterate the possibility of seeing the presence of aliphatic compounds in the Raman spectrum. With respect to molar fractions, the content of the bicyclic aromatics is much lower than of the monocyclic aromatics, and Naphthalene is the main bicyclic component with a concentration of around 0.5 weight % in the gasoline. Thus the intense bands of Naphthalene, occurring at about 765, 1028, 1237, 1381, 1460 and 1629 cm^{-1}, are present in the spectra of gasoline.

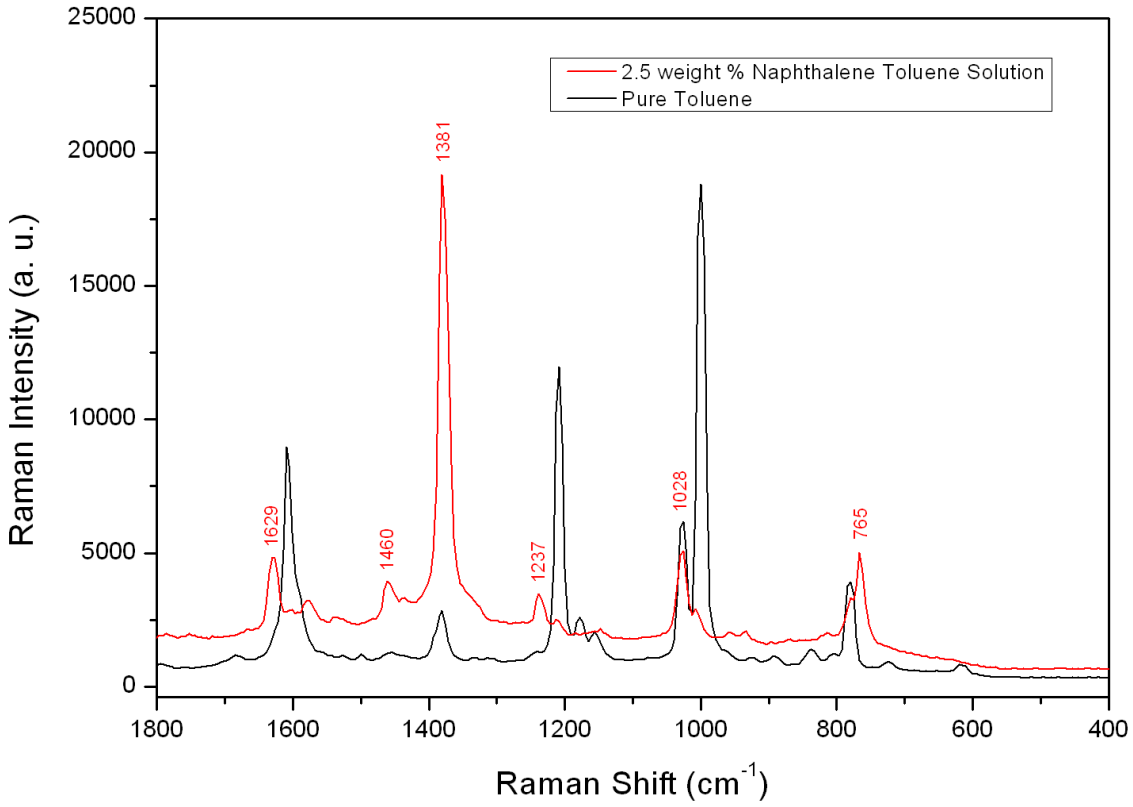

Fig. 5.9: The Raman spectra of Toluene and a 2.5% (weight) solution of Naphthalene in Toluene, excited by the DUV 229 nm laser line.

5.7 Artificial Gasoline

When comparing the Raman spectra of Naphthalene (essential features of the red curve in Fig. 5.9) and gasoline (the upper blue curve in Fig. 5.7), we see that all the peaks of naphthalene are present in the gasoline spectrum. This clearly shows that Naphthalene is dominating the Raman spectrum of gasoline when using the 229 nm excitation. Therefore, it must be concluded that the 229 nm excited spectra are suitable to determine the content of Naphthalene in gasoline, and the band of 1381 cm^{-1} is useful as quick indicator of naphthalene. On the other hand the 229 nm excited spectra are *not* suitable to determine many other other components in the gasoline because of its normal content of Naphthalene and other resonance Raman compounds.

In order to study the detailed behaviour of Naphthalene containing gasoline, we started to prepare and measure an artificial gasoline without Naphthalene, and then we increased the Naphthalene content gradually. The composition of our artificial gasoline was based on common average gasoline analysis reports. The proportion of each component and the corresponding Raman spectrum are shown in Fig. 5.10. The major monocyclic aromatics fractions consist of Benzene, Toluene, Ethyl-benzene, m-Xylen, o-Xylen and p-Xylen (also called BTEX). All the members of the BTEX group of compounds are all in resonance at

229 nm. This is also to be expected when looking at their absorption spectra, shown in Fig. 5.17. Most of the characteristic Raman peaks of the BTEX compounds can be found in the spectra of the mixtures. Heptane and Pentane were used to represent the aliphatic fractions. Because of the high content of n-alkanes – often as high as about 80 % proportion - the bands of CH_2 twisting and wagging modes in n-alkanes, occurring at about 1300 and 1460 cm^{-1}, can be observed in the Raman spectra of many mixtures.

As shown in Fig. 5.10, the spectrum of the artificial gasoline is quite different from the spectrum of the real gasoline (Fig. 5.7). Our explanation for this is that it must because of the lack of small amounts of bicyclic aromatics fractions, that by virtue of their strong resonance Raman spectra have a very dominating influence on the Raman spectra when present. This explanation is further supported in Fig. 5.11, showing the Raman spectra of Naphthalene / Artificial gasoline mixtures as a function of small Naphthalene additions (concentrations given in weight %). A content of Naphthalene as low as 0.01 % obviously has the ability to dramatically increase the Naphthalene peak of 1381 cm^{-1}. Since Toluene also has a Raman band at 1380 cm^{-1}, the determination of Naphthalene in concentrations much lower than 0.01 % is difficult. On the other hand it is clear the small amounts have much influence.

When we further increased the concentration of Naphthalene in the artificial gasoline until reaching concentration levels of about 0.5 % naphthalene, the Raman spectra of the artificial and the real gasoline are very much similar, as shown in Fig. 5.12.

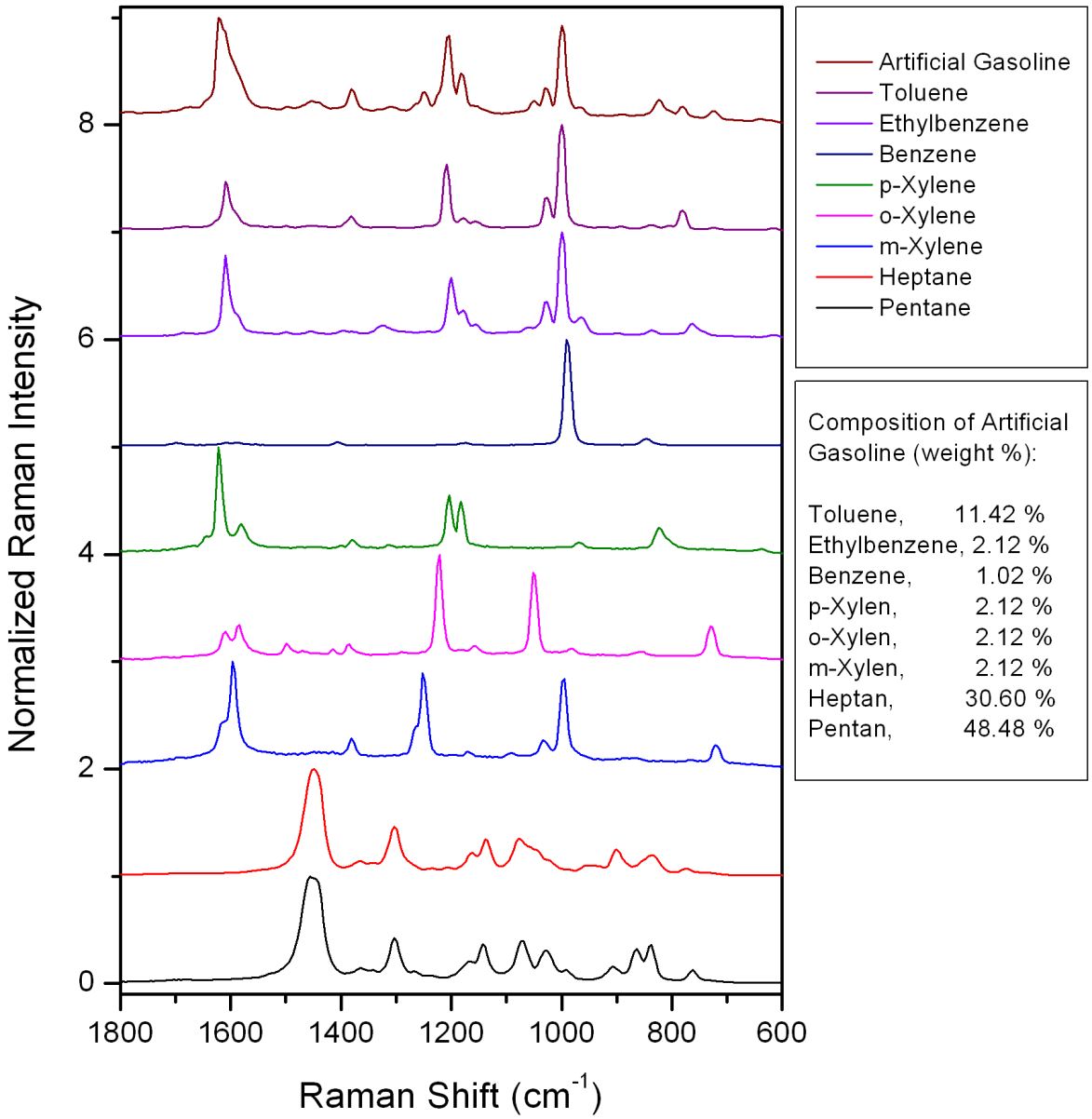

Fig. 5.10: The Raman spectra of the artificial gasoline and the corresponding components, excited by the DUV 229 nm laser line.

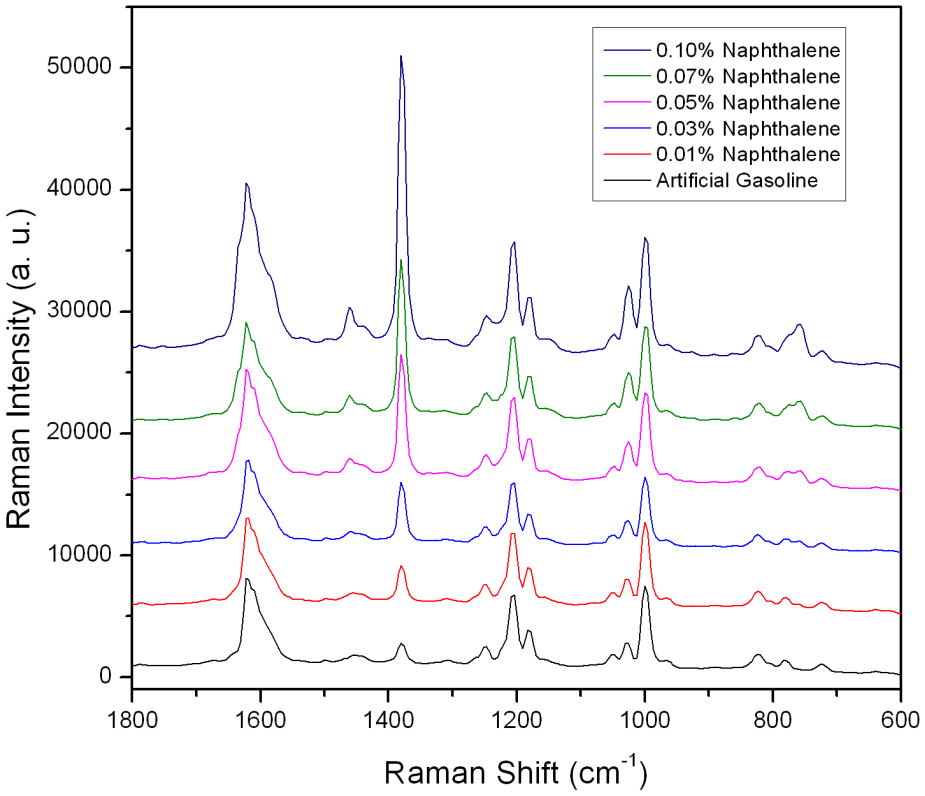

Fig. 5.11: The Raman spectra of the Naphthalene / Artificial gasoline mixtures as a function of Naphthalene concentration (weight %) excited by the DUV 229 nm laser line.

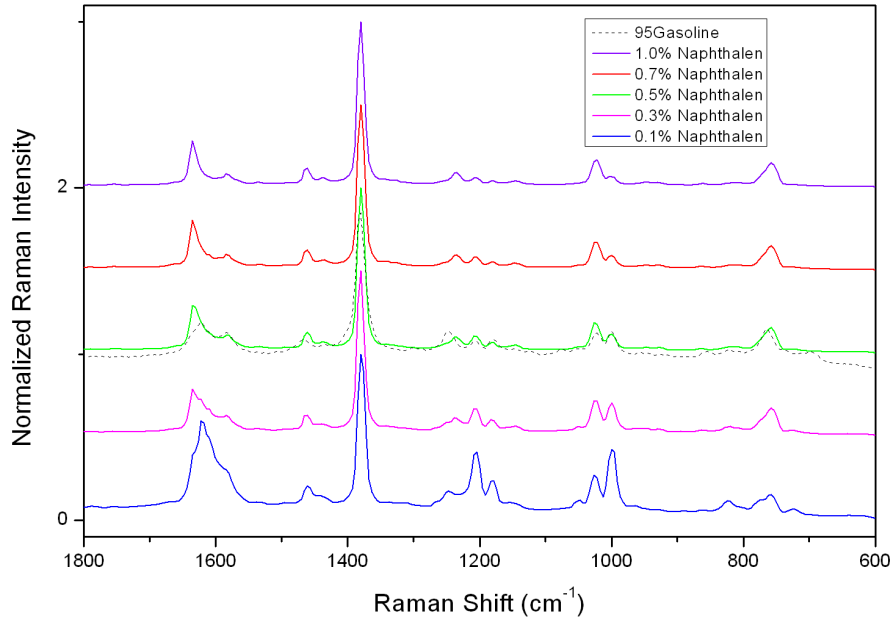

Fig. 5.12: The Raman spectra of Naphthalene / Artificial gasoline mixtures as a function of the Naphthalene concentration (weight %); the dashed line is the spectrum of the standard Shell 95 octane gasoline, excited by the DUV 229 nm laser line.

5.8 Raman Spectra of Gasoline and Toluene Mixtures by Use of the 244 nm Laser Excitation.

As motioned above, the Raman spectra of gasoline are mainly dominated by naphthalene because naphthalene has an extremely strong absorption peak at 220 nm, [5.18]. Compared with the absorption bands of Naphthalene and Toluene, the latter has two broader absorption bands [5.18], [5.19]. Therefore, it is possible to select an excitation wavelength, in which the Raman bands assigned to monocyclic and bicyclic chromatics are comparable to a typical gasoline sample, thus to realize a rapid analysis of the aromatic species, by comparing the different Raman bands. 244 nm is such a wavelength.

The spectra of gasoline, excited by 244 nm, show the significant difference to the 229 nm excited spectra. As shown in Fig. 5.13, two peaks of similar intensity - at 1004 and 1381 cm-1 - could be assigned to the breathing mode of monocyclic and bicyclic chromatics, respectively. For the monocyclic aromatic components in a typical gasoline, Toluene occurs with the highest percentage (contents at around 10 vol. %).

Raman spectra of different concentrations of toluene in gasoline were then measured. The results, the spectra shown in Fig. 5.13, indicate how the increasing content of Toluene dominates the Raman spectra. Compared with the spectra of pure toluene and gasoline, the intense peaks of toluene, at 787, 1004, 1029 and 1209 cm^{-1}, are clearly presented in the gasoline spectrum. The relatively weak peaks at 624, 1380 and 1608 cm^{-1} can also be observed, and the peaks at about 1380 and 1608 cm^{-1} are overlapped with the Raman bands of the bicyclic aromatics.

The spectra of the mixtures in Fig. 5.13 perform interesting behaviours with respect to the background fluorescence noise. The Raman spectra are shown as intensity normalized results; and the fluorescence backgrounds are subtracted. For the original Raman spectra as shown in Fig. 5.14, the spectrum of pure toluene shows a strong fluorescence background. An interesting result is that addition of a small amount of gasoline can reduce the fluorescence background such that some weaker bands, such as 1380 and 1600 cm^{-1}, become more clearly distinguishable.

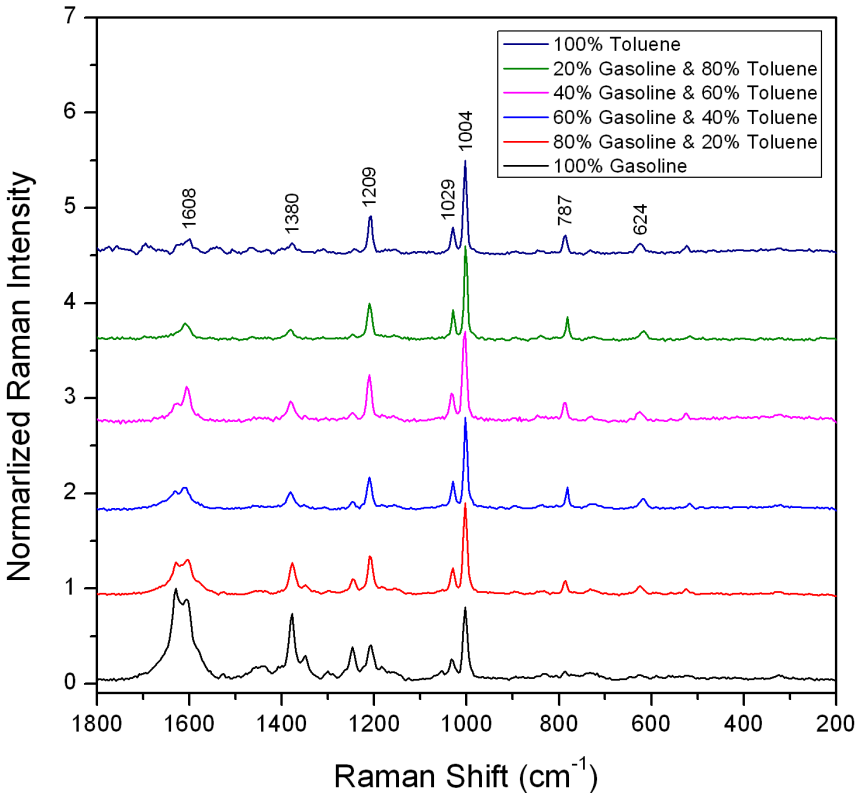

Fig. 5.13: Raman spectra of toluene and Shell 95 gasoline mixtures by use of 244 nm excitation; all the bands of toluene are present in the gasoline spectrum.

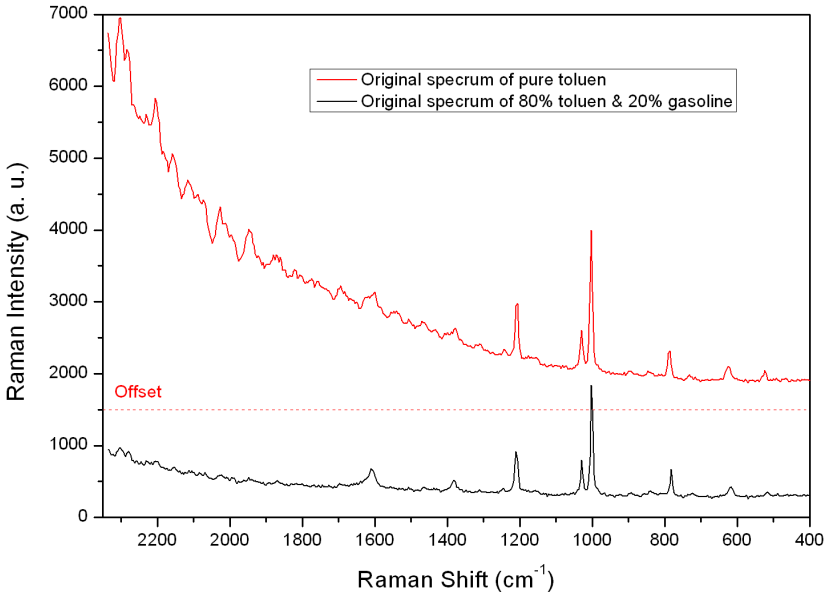

Fig. 5.14: Original Raman spectrum of toluene (top) and a Toluene / gasoline mixture (bottom) by use of the DUV 244 nm laser line excitation; the added gasoline acts to reduce the fluorescence background.

5.9 Raman Spectra of Artificial Gasoline by Use of 244 nm Excitation.

In this section we used the 244 nm excitation laser light. The composition of the artificial gasoline used was the same as above (composition shown in Fig. 5.10). For the 244 nm excitation, the resonance level of naphthalene obviously is reduced. Thus a higher content of naphthalene can suitably be studied. Fig. 5.15 shows the spectra of the artificial gasoline samples containing 0.5, 1 and 2 weight % of Naphthalene, respectively. The relative intensities of the bands at 1004 and 1381 cm^{-1} express the concentrations of the monocyclic aromatics (the BTEX group) and the Naphthalene.

For the artificial gasoline without any Naphthalene content, the Raman spectrum contains the strong fluorescence background as shown in Fig. 5.16 which is the original spectrum (in Fig. 5.15 the fluorescence background has been subtracted for the artificial gasoline curve). The spectra of artificial gasoline with some Naphthalene contents show much lower background noise. Since Naphthalene has no band contribution at 1004 cm^{-1}, it must mean that the added 0.5 % naphthalene actually reduces the fluorescence, and that the presence increases the Raman intensity of the other components (such as e.g. the toluene band of 1004 cm^{-1}).

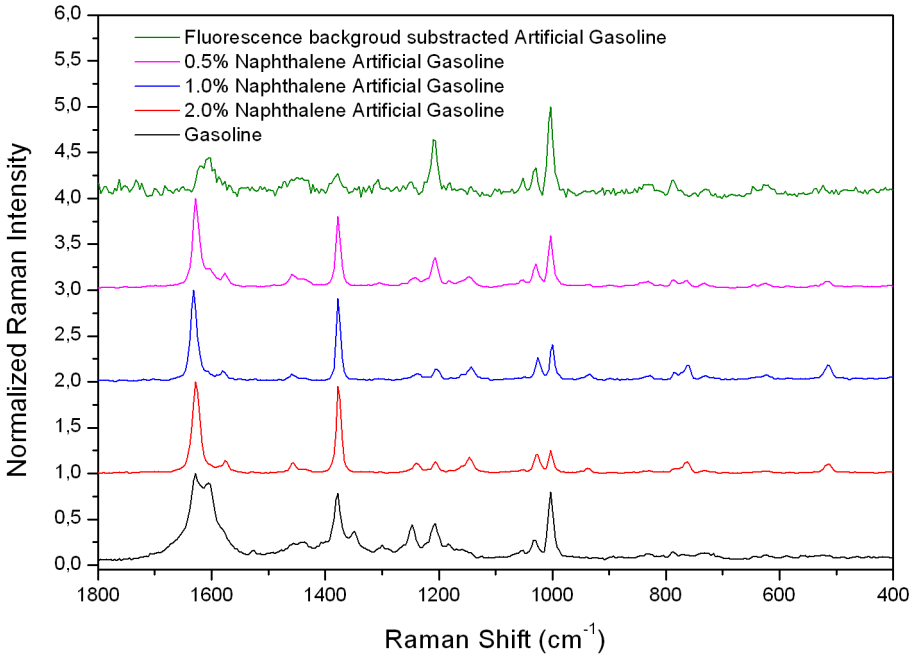

Fig. 5.15: Raman spectra of artificial gasoline with different contents of Naphthalene, excited by use of 244 nm DUV laser line; the spectrum of the real gasoline (Shell 95 octane standard) is also presented for comparison.

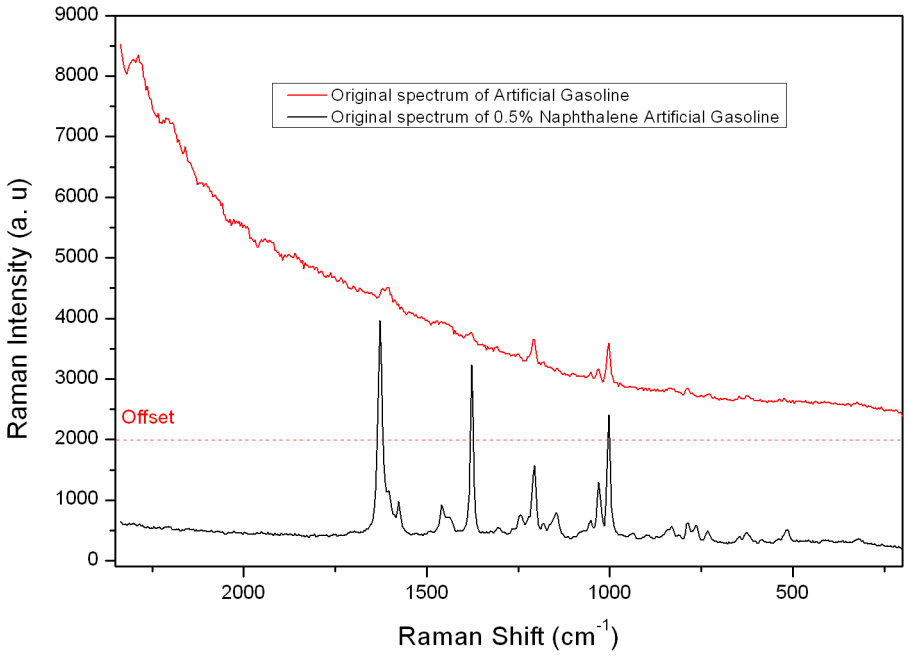

Fig. 5.16: The original Raman spectrum of artificial gasoline without and with a small Naphthalene content excited by use of the 244 nm DUV laser line; the added naphthalene reduce the back ground noise and increase the Raman intensity.

5.10 Raman Spectra of Mixtures of Gasoline and MTBE (an antiknocking Agent), by use of 244 nm laser excitation.

MTBE or methyl-butyl tertiery ether, MTBE has been widely used as an antiknocking agent for automobile engines to substitute the TEP (tetraethyl lead) used in the early-days of the car socities. MTBE is a highly polluting contaminant for the underground water reserves (very small quantities of MTBE gives water a bad taste), and MTBE has now been forbidden to use in many states. Ethanol, the other oxygenate antiknocking agents, have been started to be used by some gasoline producer, such as Shell. In a previous study by visible laser light [5.8], we have reported on the difficulty of fluorescence interferences when trying to use Raman spectroscopy to test gasoline for the content of MTBE.

As obvious from the transmission spectrum shown on Fig. 5.17, MTBE has a quite high absorption at 229 nm (the transmission is about zero) and therefore MTBE is expected to exhibit a resonance Raman behaviour at 229 nm. Therefore we conducted experiments to see if DUV excitation could be of help in this connection.

229 nm Raman spectra of MTBE itself and of high contents of MTBE in gasoline (40 and 80 vol. % mixtures) were measure here as shown in Fig. 5.18. The results show however that the MTBE content does not show up in the Raman spectra of the mixtures. The characteristic bands of MTBE are simply not present in the

spectra of mixtures. We must conclude that it is unsuitable to use the 229 nm excitation and Raman spectroscopy to analyze for the MTBE agent in gasoline.

According to the transmission spectra (Fig. 5.17), Ethanol has lower absorption and hence resonance level than MTBE, meaning the 229 nm excitation should also be unsuitable for ethanol analysis in gasoline.

In addition to this, the transmission spectra of MTBE, ethanol, hexane and heptanes show a same tendency, i.e. the absorption of these compounds are obviously increasing when the wavelength is closing to 200 nm. This may indicate that they are resonance in the further short wavelength range (< 200 nm). Oppositely, the absorption of Toluene shows a contrary tendency as the green line shown on Fig 5.17. This contrary tendency is hardly to be seen because of the saturated absorption.

Following the tendency of these absorption curves, the aliphatic compounds may have stronger resonance then aromatics, meaning, the further shorter wavelength excitation (< 200 nm, so called *vacuum ultraviolet*) is possibly suitable for aliphatic components, ethanol and MTBE analysis.

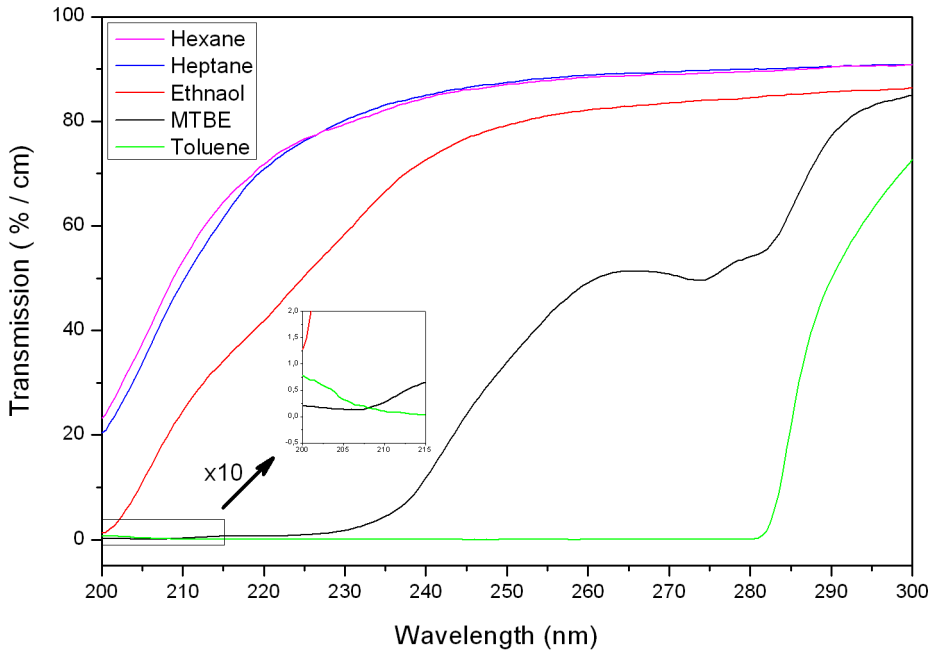

Fig. 5.17: Transmission spectra of Hexane, Heptane, Ethanol and Toluene; the testing samples are no diluted. The propagation distance is 1 cm.

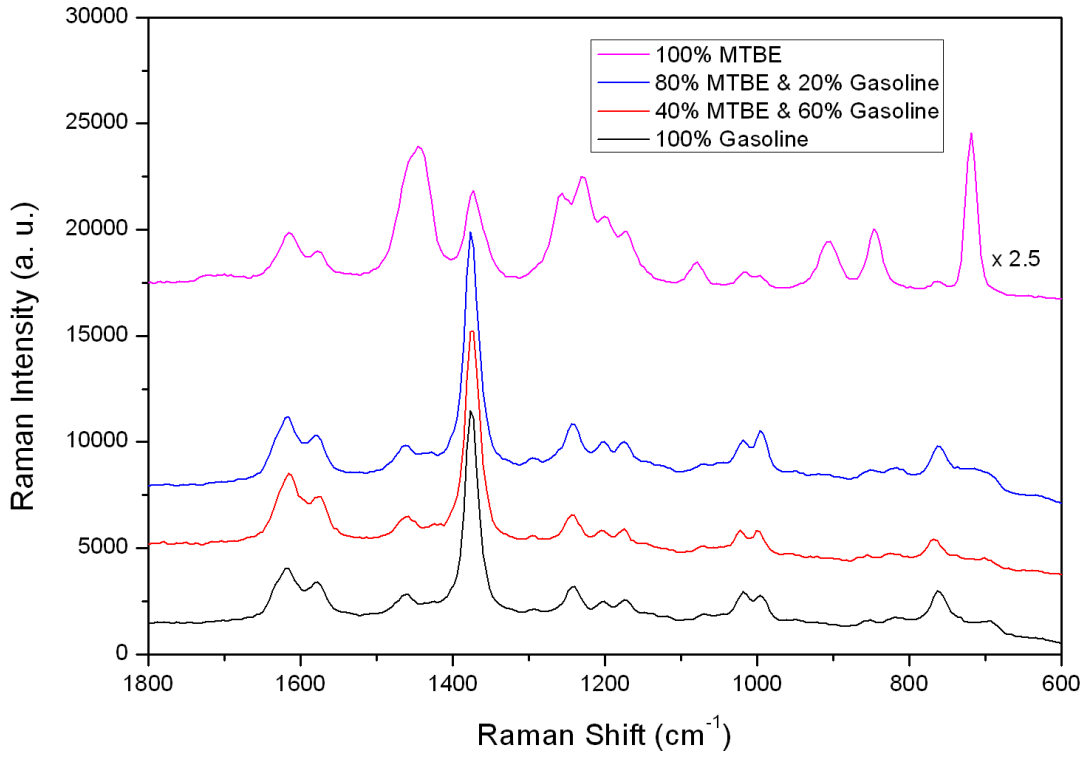

Fig. 5.18: Raman spectra of MTBE and MTBE / gasoline mixture excited by use of the 229 nm DUV laser line. The intensity of MTBE has been multiplied by 2.5, and spectra shifted for clarity.

5.11 Raman Spectra of Six Different Types of Gasoline

The Raman spectra of six types of gasoline excited by 244.0 nm laser are shown in Fig. 5.19. The spectra of the different kinds of gasoline have the same peaks because they are dominated by small amounts the same few species of monocyclic and bicyclic aromatics in strong Raman resonance. The relative intensities are slightly different which may be caused by the different percentages of the aromatic fractions. Especially for the spectrum of the Shell 99 gasoline (commercially called V-power) has a somewhat remarkable difference from the other spectra. The intensities of the bands of 1381 and 1237 cm^{-1}, corresponding to the naphthalene bands (see Fig. 5.9), are relative lower than for the other gasoline samples. Oppositely, the intensities of 1004, 787 and 624 cm^{-1}, corresponding to the toluene bands (see Fig. 5.5), are relatively higher. It indicates that either the concentration of naphthalene is lower, or the concentration of toluene is higher in the V-power gasoline.

In the following we describe a method to estimate the concentration the BTEX group and Naphthalene by comparing of 244 and 229 nm excited spectra. First, the exact concentration of naphthalene can be determined by the 229 nm excited spectra. This is so because the intensity of the 1381 cm^{-1} peak of naphthalene is sensitive for very low concentrations (down to 0.01 %) of Naphthalene as shown in Fig. 5.11. For even lower concentrations of Naphthalene one can dilute the testing sample before the recordings.

Once the exact concentration of Naphthalene has been determined, the 244.0 nm excitation spectrum can be used to determine the concentration of the BTEX group by comparing the intensities of the 1381 and 1004 cm^{-1} bands which were assigned to the characteristic ring breathing modes of bicyclic and monocyclic aromatics, respectively.

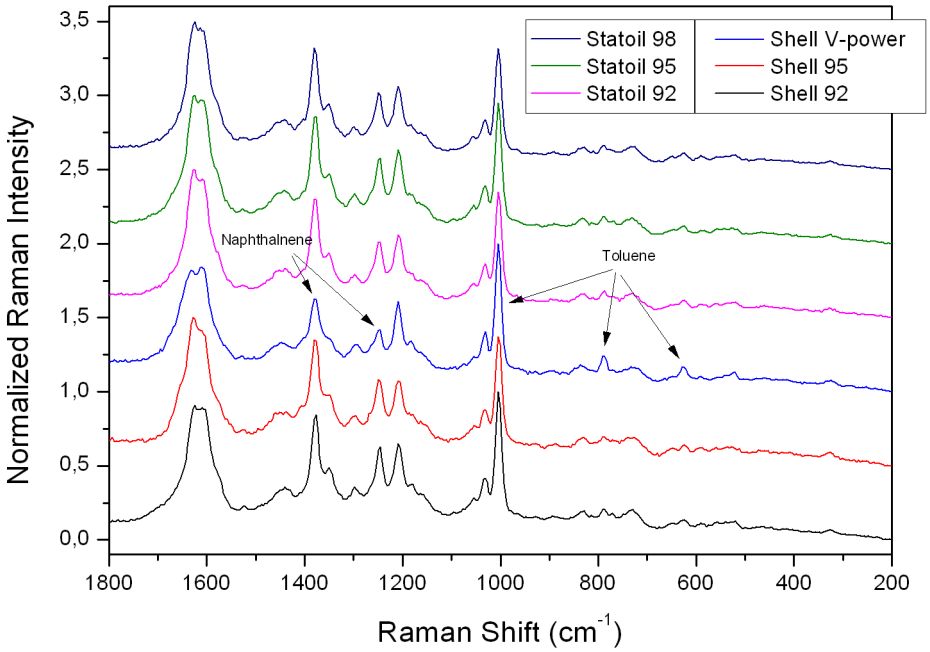

Fig. 5.19: Raman spectra of different types of Gasoline, excited by the 244 nm DUV laser line. Spectra have been shifted for clarity.

The spectra in Fig. 5.20 have been recorded by 229.0 nm laser excitation. Compared with the 244.0 nm excitation spectra (Fig. 5.19), the 229.0 nm excitation spectra obviously have different profiles, and show their most intensive peaks at 1381 cm^{-1}, which we think correspond to the breathing mode of the bicyclic aromatics (see Fig. 5.8). The Raman bands of the other species are strongly suppressed because the resonance Raman intensities are so intensive.

Compared with the spectra of the other different types of gasoline in Fig. 5.20, the spectrum of the Shell 99 V-power gasoline also shows a clear difference with respect to the breathing mode of monocyclic at around 1000 cm^{-1}.

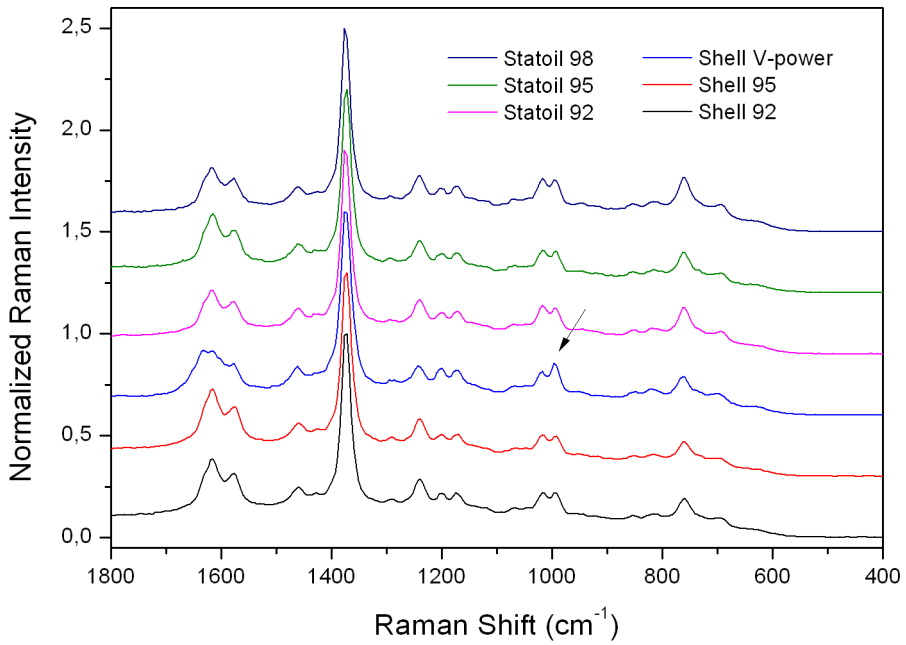

Fig. 5.20: Raman spectra of different types Gasoline excited by 229 nm laser, excited by the DUV 229 nm laser line. Spectra have been shifted for clarity.

5.12 Conclusions

Considerable fluorescence interference problems were previously met when trying to analyse gasoline samples by Raman spectroscopy [5.8]. It was considered that to eliminate the fluorescence for allowing one to perform good gasoline analyses, these problems could be solved by use of deep UV light. It was then found that the sampling was not simple, but a so-called gas gap cell system could be finally developed that allowed recording of good Raman spectra. After that, it was found that the DUV excitation wavelength should be chosen, with wavelengths deeply enough (such as < 244 nm). Actually, some of components still have strong fluorescence interference with the 244 nm excitation. An interesting result was that it could be shown that the small content of naphthalene could reduce the fluorescence interference and increase the Raman intensity of testing samples, such as toluene and artificial gasoline.

By use of the 229 nm excitation, the fluorescence interferences were completely avoided. However new complications were found.

Monocyclic aromatics (members of the BTEX group) and $C_{4\text{-}10}$ saturated aliphatic hydrocarbons are two classes of major species components in a typical gasoline. The Raman spectra of these components were studied as well as different proportion mixtures of the two classes, respectively, toluene and heptane or pentane. The results show that toluene dominates the Raman spectra of mixtures under 229 nm excitation because of the resonance Raman scattering of toluene. The different mixtures have almost the same spectrum, rather independently of the proportions. All the bands of toluene, positioned at about 624, 787,

1004, 1029, 1209, 1380 and 1608 cm^{-1}, are clearly represented; and the 1004 cm^{-1} band is the intensive band corresponding to the breathing mode characteristic of monocyclic aromatics. With respect to bands of heptane or pentane, only two broad bands of 1300 and 1460 cm^{-1} could be observed, even for high composition ratios, such as 80 vol. % and 60 vol. %. These two bands, at about 1300 and 1460 cm^{-1}, are corresponding to the CH_2 twisting and wagging mode transitions. They are appearing in the spectra of most of saturated aliphatic hydrocarbons, and thus they cannot be used to identify definitively the heptanes or pentanes in a complex mixture but only to determine a rough guess on the amount of the saturated aliphatic hydrocarbons species. The Raman spectra of the gasoline mixtures have representative significance because most of the monocyclic aromatics components are at resonance in the DUV range; oppositely, most saturated aliphatic hydrocarbons are not at resonance in the DUV range.

Further it was discovered that Naphthalene, a minor constituent of gasoline, oil and coal fuels, has an even larger Raman cross-section than what is the case for the monocyclic aromatics under the 229 nm excitation. This became clear by measurements of the Raman spectrum of 2.5 weight % Naphthalene in toluene solution. All the intensive bands, observed at 765, 1028, 1237, 1381, 1460 and 1629 cm^{-1} are belonging to Naphthalene. Therefore, it must be the case that Naphthalene is dominating the gasoline spectrum under the 229 nm excitation.

Also it was realized that the content of Naphthalene in a gasoline could be determined by Raman spectroscopy with 229 nm DUV excitation. An artificial gasoline mixture without Naphthalene was made, composed by mixing Heptane, Pentane and the members of the BTEX group. By measuring the spectra of Naphthalene and artificial gasoline / Naphthalene mixtures as a function of the Naphthalene concentration, the spectrum of a 0.5 weight % content mixture is close to the spectrum of a real gasoline, standard Shell 95 gasoline. Finally it has been demonstrated that a concentration of the Naphthalene as low as 0.01 % by weight can be determined by means of DUV Raman spectra using the 229 nm excitation.

When using different DUV excitation wavelengths, the spectra of gasoline are dominated by the presence of different species of aromatics. For the 244 nm excitation the spectra of gasoline are equally dominated by monocyclic and bicyclic aromatics. Thus these spectra contain more information than for the 229 nm case: the intense bands of 1004 and 1381 cm^{-1} are respective characteristic bands for the monocyclic and bicyclic aromatics. The broad low intensity bands at around 1300 and 1460 cm^{-1} can be assigned as vibrational mode transitions of series of CH_2 group twistings and waggings in saturated aliphatic hydrocarbons species (Pentane, Hexane, Heptane etc.). Therefore, one could realize a more precise analysis by a combined use of spectra of both 229 and 244 nm excitation.

Regarding the anti-knocking agents, such as MTBE and ethanol, it was found that they are difficult to analyze by means of DUV Raman spectroscopy because of lack the resonance Raman scattering in these compounds. However, the absorption spectra indicate that it possibly could be implemented by use of excitation by even shorter wavelengths, i.e. in the vacuum UV range.

References to Chapter 5

[5.1] Private communations with technical staff in the product service departments of Shell, refinery in Kalundborg, Denmark.

[5.2] C. J. de Bakker and P. M. Fredericks, "*Determination of petroleum properties by fiberoptic Fourier transform Raman spectrometry and partial least-squares analysis*", Appl. Spectrosc. 49, (**1995**), pp. 1766-1771.

[5.3] J. B. Cooper, K. L. Wise, J. Groves and W. T. Welch, "*Determination of octane numbers and Reid Vapor pressure of commercial petroleum fuels using FT-Raman spectroscopy and partial least-squares regression analysis*", Anal. Chem. 67, (**1995**), pp. 4096-4100

[5.4] P. E. Flecher, W. T. Welch, S. Albin and J. B. Cooper, "*Determination of octane numbers and Reid vapor pressure in commercial gasoline using disperse fiber-optic Raman spectroscopy*", Spectrochim. Acta 53A, (**1997**), pp. 199-206.

[5.5] J. B. Cooper, K. L. Wise, W. T. Welch, R. R. Bledsoe and M. B. Sumner, "*Determination of weight percent oxygen in commercial gasoline: A comparison between FT-Raman, FT-IR and dispersive near-IR spectroscopies*", Appl. Spectrosc. 50, (**1996**), pp. 917-921.

[5.6] R. H. Clarke, W. M. Chung, Q. Wang, D. DeJesus and U. Sezerman, "*Determination of aromatic composition of fuels by laser Raman spectroscopy*", J. Raman Spectrosc. 22, (**1991**), pp. 79-82.

[5.7] J. B. Cooper, K. L. Wise, W. T. Welch, M. B. Sumner, B. K. Wilt and R. R. Bledsoe, "*Comparison of near-IR, Raman and mid-IR spectroscopies for the determination of BTEX in petroleum fuels*", Appl. Spectrosc. 51, (**1997**), pp. 1613-1620.

[5.8] S. Brunsgaard Hansen, R. W. Berg and E. H. Stenby, "*Determination of methyl tertiary butyl ether (MTBE) in gasoline by Raman spectroscopy*", Asian Chem. Letters 4, (**2000**), pp. 65-74.

[5.9] P. R. Griffiths. *Introduction to Vibrational Spectroscopy*. in "Handbok of Vibrational Spectroscopy", eds. J. M. Chalmers and P.R. Griffiths, Wiley, USA, 1st edition, Vol. 1, (**2001**), pp. 33-43.

[5.10] Spiro, T. G. "*Resonance Raman Spectroscopy. New Structure Probe for Biological Chromophores*", *Acc. Chem. Res.* (**1974**), *7*, pp. 339–344.

[5.11] E. Smith and G. Dent. *Modern Raman Spectroscopy - A Practical Approach*. Wiley, England, first edition, (**2005**). Chapter 4.

[5.12] G. Xiong, C. Li, H. Y. Li, Q. Xin, Z. C. Feng, "*Direct Spectroscopic Evidence for Vanadium Species in V-MCM-41 Molecular Sieve Characterized by UV Resonance Raman Spectroscopy*". Chem. Commun., (**2000**), pp. 677–678.

[5.13] S. A. Asher and C. R. Johnson, "*Raman Spectroscopy of a Coal Liquid Shows that Fluorescence Interference is Minimized with Ultraviolet Excitation*", *Science*, *225*, (**1984**), pp. 311-313.

[5.14] C. R. Johnson and S. A. Asher, "*A New Selective Technique for Characterization of Polycyclic Aromatic Hydrocarbons in Complex Samples: UV Resonance Raman Spectrometry of Coal Liquids*", Anal. Chem. 56, (**1984**), pp. 2258-2261.

[5.15] C. K. Hansen, *"Raman spectroscopy for food analysis"*, Exam project (**2011**).

[5.16] G. Herzberg, "Infrared and Raman Spectroscopy", Chap.III, Van Nostrand, New York (**1955**).

[5.17] R. H. Clarke, W. M. Chung, Q. Wang, S. DeJesus and U. Sezerman, "*Determination of Aromatic Composition of Fuels by Laser Raman Spectroscopy*", J. Raman Spectrosc. 22, (**1991**), pp. 79-82.

[5.18] R. Rumelfanger, S. A. ASHER and M. B. Perry, "*UV Resonance Raman Characterization of Polycyclic Aromatic Hydrocarbons in Coal Liquid Distillates*", Appl. Spectrosc. 42, 2, (**1988**), pp. 267-269.

[5.19] G. R. Loppnow, L. Shoute, K. J. Schmidt, A. Savage, R. H. Hall and J. T. Bulmer, "*UV Raman spectroscopy of hydrocarbons*", Phil. Trans. Royal Soc., London. A 362, (**2004**), pp. 2461-2476.

[5.20] J. W. Robinson, *Handbook of Spectroscopy*, CRC Press, Cleveland, OH (**1974**), pp. 119 -124.

[5.21] Unpublished results, Gaussian 03W, DFT/B3LYP/6-31+G optimization.

6 Other Applications

6.1 Sudan I.

The red dye Sudan I is considered to be toxic and carcinogenic. In recent years, several European control authorities have discovered the presence of Sudan I in series of imported food items, such as red canned chili fruits [6.1]. No known threshold limit seems to exist with respect to long-term health risks, and therefore there is a need for further development of the detection methods.

Series of detection methods have been developed, most of them based on liquid chromatogaphy [6.1]-[6.4]. The recently applied methods for Sudan I gave detection limits on the order of around 0.5 ppm [6.5]. Since the food samples normlly consist of miscellaneous organic and inorganic mixtures, the analysis process of the liquid chromatogaphy method is somewhat complicated and slow.

Accordingly we tried to investigate if Raman Spectroscopy could offer a new fast possibility for in-situ and on-location detection of Sudan dyes during food control. For the traditional visible laser excited Raman spectrometry, detection of Sudan dyes in the food sample is difficult because of fluorescence interference. Even for the pure Sudan I, a useful Raman spectrum could not be obtained by visible laser excitation, see Fig 6.1. The detection of Sudan I by SERS (Surface Enhanced Raman Spectroscopy) and SERRS (Surface Enhanced Resonance Raman Spectroscopy) could offer very accurate analysis methods with detection limits below 0.20 ppm. This increased sensitivity comes about because SERRS can selectively and extremly enhance the Raman band of the Sudan I [6.6].

In this way the fluorecence-free DUV Raman spectrometry could provide a convenient method because the method can be applied directly on the food samples in bulk. Thus the DUV Raman spectrometry could be a fast detection method for Sudan I, as an illegal food colorant, but the problem that the radiation does not go through the typical glass containers is a drawback, making the analysis destructive.

Although the detected methods have been demonstrated, the extent of scientific literature on Raman spectra of Sudan dyes is very limited and very few articles have been published so far. A deeper understanding of the chemistry and structure of these molecules is needed to develop a Raman-based precise method that will be able to distinguish the Sudan molecules from other azo-dyes. The current problem of distinguishing Sudan I from natural abundant carotenoids - especially Capsanthin - which is difficult due to almost identical absorption maxima [6.5],[6.7].

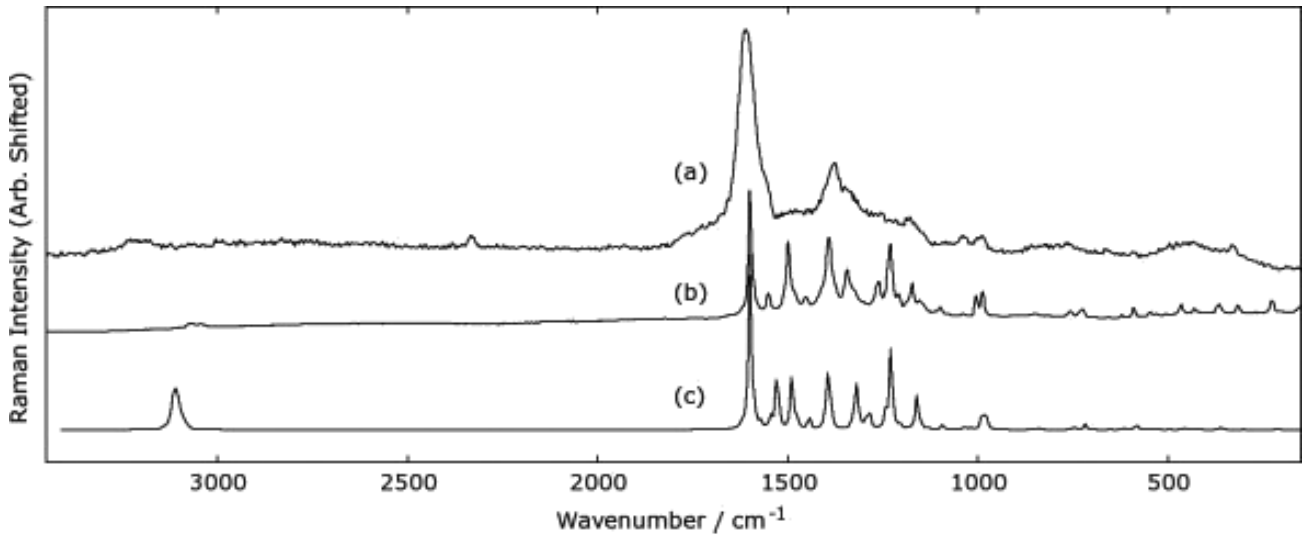

Fig. 6.1: Raman spectra of solid Sudan I obtained with (a) 244 nm UV light and (b) 1064 nm IR light. Useful spectra could not be obtained with green or blue light. The calculated spectrum is shown as (c). The band at 2331 cm^{-1} in (a) is due to N_2 gas, see also Appendix 9.

The structure of azo dyes has been intensely discussed in the chemical literature. The azo dyes formally contain the azo group –N=N–, but are in most cases partly or completely transformed into the tautomeric hydrazo form (Fig. 6.2, b). According to our studies with the Gaussian 03W software package, the azo forms gave poor resemblance to the experiments. In contrast to this, the calculated spectrum for the hydrazo form showed good resemblance to the experimental spectrum. The detailed discussion can be found in our published paper, Appendix 9.

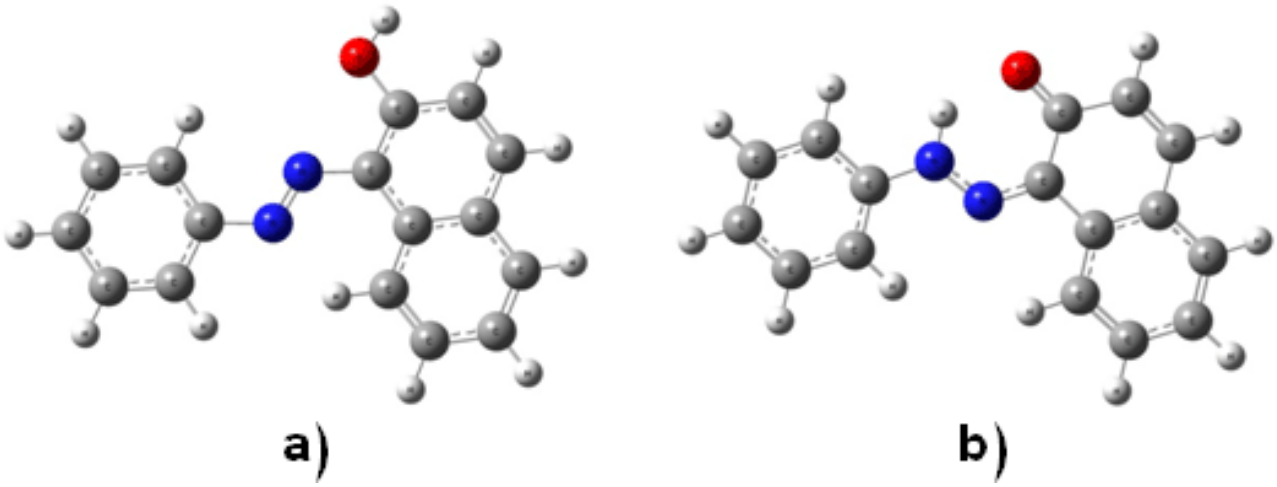

Fig. 6.2: The tautomery of Sudan I: (a) the azo form and (b) the hydrazo form (most stable).

6.2 Characterization of varied size germanium nanocrystals by Raman spectroscopy

Recently, zero-dimensional nanocrystals have been intensively studied in theoretical and experimental research, due to potential applications as light emitters, non-volatile optical memories and enhanced 3rd order optical nonlinear effects, etc. Among these nanocrystals, the high-efficiency germanium light emitter application is receiving much attention because Ge has a 0.80 eV direct bandgap, only slightly larger (by 0.136 eV) than its indirect bandgap (0.664 eV). This puts Ge emission at high efficiency, within the 3rd optical communication window (~1520-1620 nm). Bulk Ge emits with 10% efficiency at a direct bandgap wavelength of 1550 nm when optimized doping and is applied. In Ge nanocrystals usually the emission wavelength is shifted to shorter wavelengths because of the quantum confinement effect (QCE). Therefore, Ge nanocrystals with combined effects of QCE, doping and strain optimization should be very promising high-efficiency light emitters, covering the entire visible and IR wavelength ranges. Different sizes of Ge nanocrystals embedded in a SiO_2 matrix formed by plasma enhanced chemical vapor deposition (PECVD), and analyzed the nanocrystals by transmission electron microscopy (TEM) are shown in Fig. 6.3.

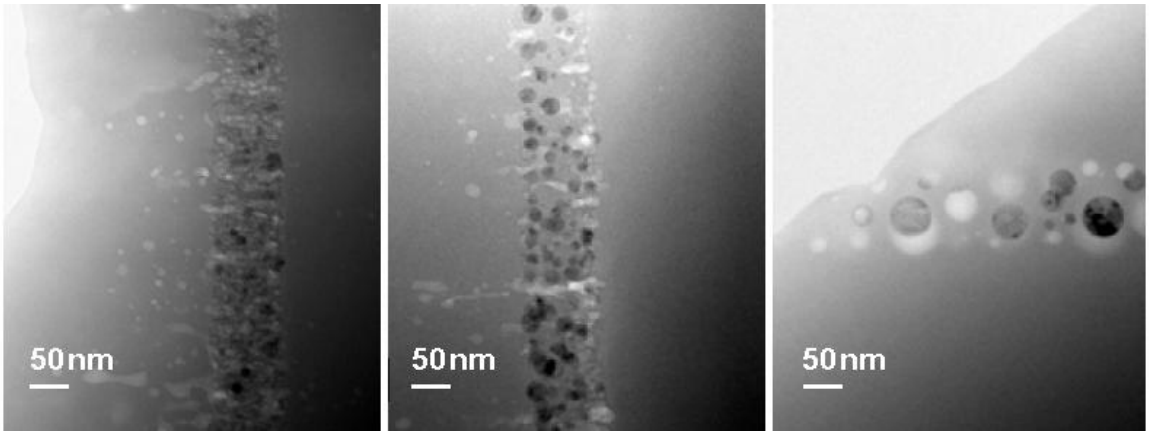

Fig. 6.3: TEM cross-sectional images of samples (from left to right): 0126, 0269 and 0194.

Samples were prepared by standard clean-room techniques on 4 inch diameter oriented Si substrates. First, one layer of Ge doped SiO_2 was deposited. Then a SiGe alloy layer was deposited on top of the SiO_2 layer. The atomic ratios of the Si to Ge were tuned from 1:1 to 1:0.5 and 1:0.25 for samples 0194, 0269 and 0126 respectively. Thirdly, one identical layer of Ge doped SiO_2 was deposited on the SiGe alloy layer. By repeating in this way the deposition of alternate layers of SiGe alloy and Ge doped SiO_2, multilayered structures could readily be made. After deposition the samples were annealed at 1100 ^oC in N_2 for 4 hours. More details of the fabrication parameters can be found in [6.8]. Samples 0126, 0269 and 0194 had 3-layer structures. Sample 0351 (not shown in Fig. 6.3) had a 5-layer structure with 1:1 Si/Ge ratio, made in order to increase the interaction with the light. The Ge nanocrystals (black dots in Fig. 6.3) were found to give Raman peaks at about 295-300 cm^{-1}. A size effect was demonstrated within these Ge nanocystals that gave

peak position and width dependences of the Raman band as shown in Fig. 6.4. The Raman peak of Ge nanocystal can also be shifted by using the different excitation power density due to the thermal effect as shown in Fig. 6.5 (a) and (b).

Fig. 6.5 (a) shows that as the excitation power was increased, the germanium Raman peak position takes a downshift and the line width increases. At low excitation powers (<11 mW), there was no obvious linear relationship between the shift and the excitation power. However, at high excitation powers, the heat effect started to play a dominant role, and a linear relationship was emerging (Fig. 6.5 (b)). Therefore, to be sure that the heat from the Raman excitation light was not disturbing the Raman spectra, we decided to record the spectra by using excitation powers of 5 mW, to reveal the unbiased properties, for example the size-dependent effects and the strain effects [6.9].

It should be noted that the spectral resolution of the Raman instrument is an important factor for these measurements because it directly affects the measured bandwidth and the accuracy of the band position. For our Raman instrument the spectral resolution of the visible laser excited spectra was about 2 cm^{-1}. This spectral resolution is much better than what was the case for the DUV excited spectra (with about 6 cm^{-1} resolution). In the next chapter, the spectral resolution of the Raman instrument will be discussed in detail.

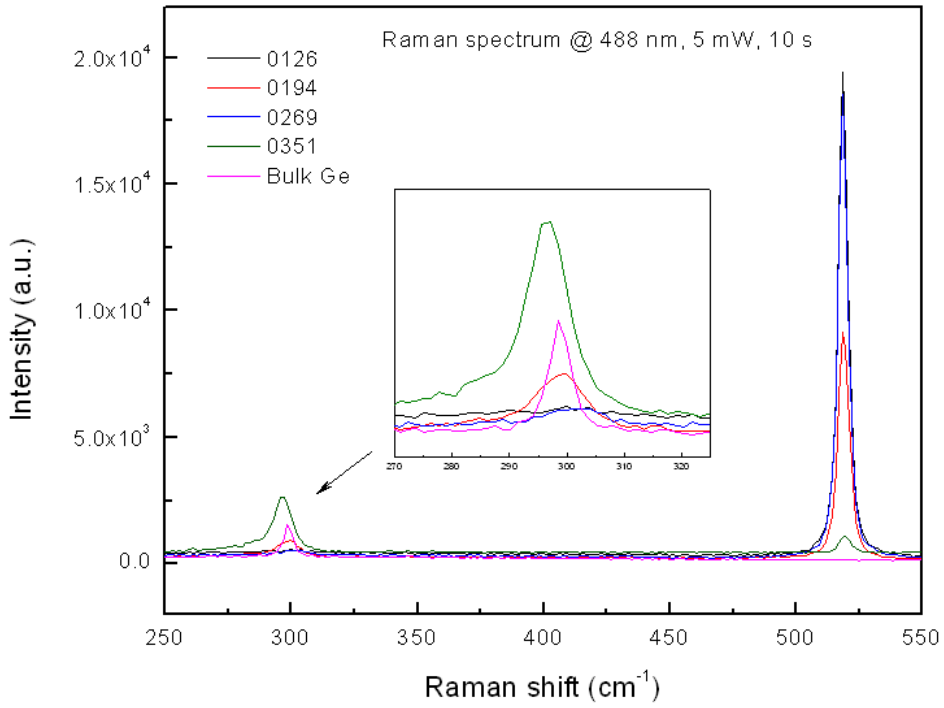

Fig. 6.4: Raman spectra of samples 0126, 0269, 0194, 0351 and a reference sample consisting of a bulk Ge wafer. The inset is a zoom-in on the main peak of the Germanium lattice. The peaks at around 521 cm^{-1} are due to the silicon substrate of the wafer. The spectra were recorded at a sufficient low power level (~5 mW) to avoid heat effects [6.9], [6.10].

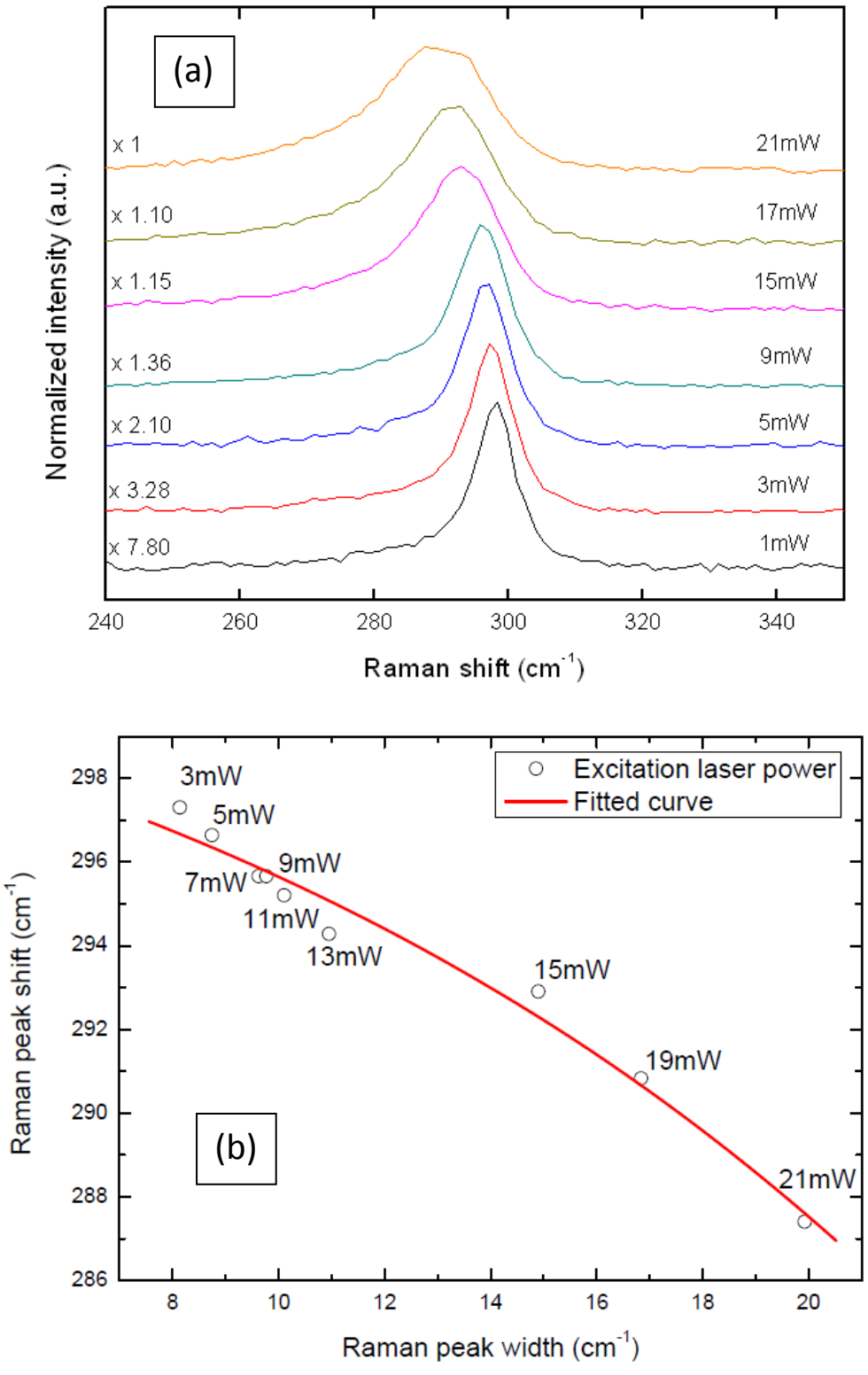

Fig. 6.5: (a) Raman spectra for sample 0351 with varied excitation powers from 1mW to 21mW, (b) Relation between the FWHM and the Raman peak shift, with relation to the excitation powers [5.9].

6.3 Raman spectroscopy characterization of boron- and nitrogen-doped 6H silicon carbide

White light-emitting diodes (LEDs) are promising candidates for the illumination market to replace conventional incandescent lamps as energy-saving and environment friendly new light sources. One common method to realize white light is to use UV or blue light emitting diodes. The light from these is partially or fully used to optically excite wavelength converters. Therefore, such high-efficiency wavelength converters - with long lifetime - are indispensable. SiC is a well established substrate material for nitride growth and has excellent thermal conductivity. Nitrogen (N) and boron (B) doped 6H-SiC has been proven to be a highly efficient wavelength converter. Furthermore, combined donor-acceptor-pair (DAP) band luminescence from N-B and nitrogen-aluminum (N-Al) doped 6H-SiC can cover most of the visible spectral range [6.11]-[6.13].

In this connection characterization of nitrogen and boron doped SiC by Raman spectroscopy was of interest. Doped epilayers were grown at a growth temperature of 1725°C on low off-axis 6H-SiC (0001) substrates (1.4 degree off-orientation in the [1120] direction) and used as samples for Raman studies [6.12], [6.13]. The doping levels are given in Table 6.1.

Table 6.1. Boron and Nitrogen Concentrations for Samples a, b, c, d, and e. Atomic dopant concentrations of the epilayers were measured by secondary ion mass spectrometry (SIMS).

Sample	B acceptor concentration [cm^{-3}]	N donor concentration [cm^{-3}]
a	8.0×10^{18}	4.0×10^{16}
b	6.9×10^{18}	3.2×10^{18}
c	6.9×10^{18}	6.0×10^{18}
d	4.4×10^{18}	9.0×10^{18}
e	5.2×10^{18}	9.2×10^{18}

Raman spectra of longitudinal optical phonon-plasmon coupled (LOPC) modes of the samples are shown in Fig. 6.6. Work by the collaborators in Sweden and in DTU Photonics [6.13] has shown that the N-B doped SiC is a good wavelength converter in white LEDs applications. Also their work showed that dopant concentration differences larger than 4×10^{18} cm^{-3} were favorable to achieve intense photoluminescence [6.13].

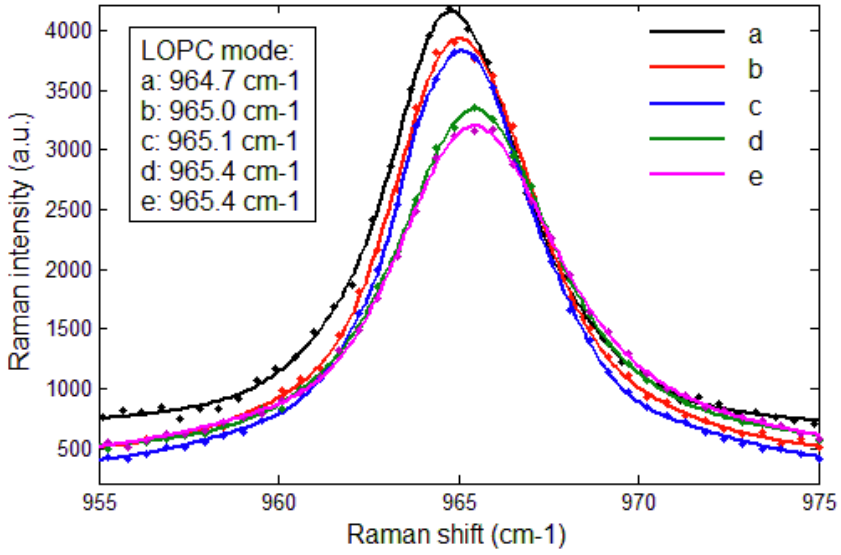

Fig. 6.6: Raman backscattering spectra of 6H-SiC samples with different dopant concentrations, showing the longitudinal optical phonon-plasmon coupled (LOPC) modes. The positions of the LOPC modes in the doped SiC samples are given in the inset frame.

The mechanisms of Raman shifts in p- and n-type samples are different. The LOPC mode would broaden, lower its intensity, and shift toward higher wavenumbers with increasing free carrier concentrations. Usually, it is more sensitive to the amount of free electrons than to free holes. In p-type samples, very few acceptor states are ionized due to the large ionization energy, and the Raman shift is mainly attributed to the atomic size effect [6.13]. Boron atoms usually occupy Silicon lattice positions in SiC. The inter-atomic distance of a Si-C bond is longer than that of a B-C bond due to the smaller atomic size of boron. The biaxial tensile stress will thus be released which results in a decrease of the phonon oscillation frequency. Therefore the LOPC mode shifts toward smaller wavenumbers with higher B concentrations. In n-type samples, the predominant mechanism causing the Raman shift of the LOPC mode is the free carrier (electron) concentration. Although no obvious peak shift has been observed - between sample d and e due to a relatively small concentration difference - the peak intensity of the LOPC mode decreases as expected, when the free electron concentration increases from sample e to d. Furthermore, one can see from Fig. 6.6 as predicted that the LOPC modes of n-type samples occur at significantly higher wavenumbers than the p-type ones [6.13].

6.4 Melamine

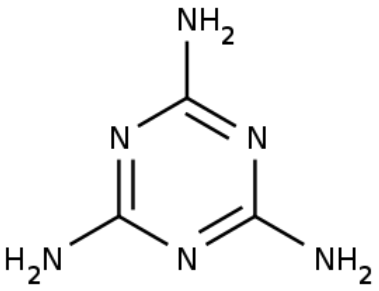

6.4.1 Introduction

Melamine, $C_3H_6N_6$, 2,4,6-triamino-1,3,5-triazine, CAS Reg. no. 108-78-1, is a nitrogen-rich chemical, commonly used e.g. as main raw material of melamine resin, a thermosetting plastic. Recently it has received considerable attention due to numerous incidents of food contamination with this substance [6.14]-[6.16]. In these incidents, melamine was deliberately added to gluten, chicken feed, pet foods, milk etc. to elevate the measured protein content because of melamine's high nitrogen content (66% by mass versus approximation, 10–12% for typical protein). Ingestion of melamine may lead to reproductive damages, or bladder or kidney stones, which can lead to bladder cancer.

Analysis of melamine has been carried out by gas chromatography (GC) [6.17], [6.18], GC-mass spectrometry (GC-MS) [6.19], [6.20], liquid chromatography (LC) [6.21]-[6.23], LCMS and LC-MS-MS [6.24]-[6.26], and Raman spectroscopy [6.27]-[6.30]. As a potential method with advantages of being simple, quick, cost-effective and sensitive, Raman spectroscopy has been intensively applied to melamine detection in food systems in recent years. 83 references (since 2007) can be found with the topics of Raman and Melamine by the Chemical Abstracts search programme *SciFinder*. Most studies have been focused on the surface enhanced (SERS) techniques because of the high sensitivity properties of SERS. About a 10 ppb detection limitation has been reached [6.29]. The traditional Raman spectrometry - excited by 785 nm infrared laser light - is also reported to achieve a successful detection of melamine, although the sensitivity was much lower; the detection limit being about 1% in powdered milk samples [6.30]. However, DUV Raman spectrometry applied to melamine detection has not been reported, and we found that it would be of interest to try it.

Melamine is slightly soluble in water, and the solubility is on the order of 3.24 g/L at room temperature [6.31]. For the melamine contaminated milk and related food products, the melamine was primarily added to the raw milk after water was added - to fraudulently dilute the milk [6.32]. Therefore, it is important to find a way to perform melamine detection in liquid milk in order to obtain food safety control. By use of the traditional Raman spectrometry excited by visible or near infrared laser (including 785 nm) it is difficult to achieve an efficient determination for liquid milk because of the fluorescence interferences and the low Raman scattering intensity. To do the determination in a better way one has to study dried milk samples in solid state to perform a good Raman measurement [6.30].

In the following study it is shown that we have found that by using DUV Raman spectrometry we could avoid the fluorescence interference and improve the detection sensitivity for direct melamine detection in liquid milk. It realizes a true quick detection in seconds without sample preparation.

6.4.2 Experimental Details

6.4.2.1 Experimental setup

Melamin in 99.8 % pure powderous state was bought from Henan Tianfu Chemical and in all experiments used without further purification. Deionized water and Arla milk were used as solvents to dissolve melamine. The dissolving was done by intensive shaking at frequent intervals for 1 hour at room temperature. The water solution did not have any precipitate. The testing samples are shown below:

1. Melamine powder.
2. Deionized water.
3. The milk, brand of Arla 1.5 % fat (08 Dec. 2011)
4. Melamine dissolved in water, 0.1 % by weight.
5. Melamine dissolved in the milk, 0.1 % by weight.

The Renishaw InVia Reflex spectrometer was used in the visible and DUV ranges, applying radiation of wavelengths of 488 and 229 nm at 10 mW (from the Lexel 95-SHG-QS Argon gas ion laser). The optical Leica microscope with an X 20 objective coupled to the instrument through a beam splitter was used to focus the laser beam onto the sample and to collect the back scattered light. We adopted the same *Accumulation* and *Exposure* times (2x20 s) for convenient Raman intensity comparisons between the 488 nm and 229 nm spectra.

6.4.3 Melamine Raman spectrum, Computed and Measured

To calculate a theoretical Raman spectrum of the melamine molecule one has to perform two steps: The optimisation of the structure and the calculation of spectrum. These steps were both performed with the Gaussian 03W software package. The structure of the Melamine molecule and its vibrations were obtained iteratively, in three subsequent calculations, in order to determine the global minimum in an efficient way. Initially the geometry was roughly optimized using the semi-empirical PM3 type procedure, followed next by the *ab initio* Hartree-Fock/DFT method with 3rd order restricted Becke-Lee-Yang-Parr procedure (RB3LYP), at first with the 3-21G basis sets. Then the energy minimum structure and the vibrational IR and Raman spectra were calculated using the 6-31+G basis sets. The vibrational frequencies for each normal mode were calculated without adjusting the force constants and using no frequency scaling. The results are reported in Table 6.2, giving approximate descriptions of dominating group frequency motions.

Table 6.2: Experimental Raman spectrum (cm^{-1}) of Melamine compared to calculated modes. Assignments (approximate descriptions of the modes) have been made on the basis of the calculated gas phase results (Gaussian/DFT/B3LYP/6-31+G model), observing the modes on a computer screen and fitting to the spectral appearance as shown in Fig. 6.7.

Mode no.	Experimental[a] cm^{-1}	Calculated[b] cm^{-1}	Intensity $Å^4$/amu	Assignments[c]
1		190.1	0.01	Ring Twisting
2		190.6	0.01	
3		213.4	0	$(NH_2)_3$ Umbrella
4		336.4	2.15	NH_2 Rocking
5		336.9	2.15	
6		499.9	0.19	NH_2 Wagging *ooph*
7		502.1	0.19	NH_2 Wagging *ooph*
8		528.3	0.00	NH_2 Wagging *iph*
9		530.2	0	NH_2 Rocking
10		557.4	0.00	
11	569	560.3	0.29	NH_2 Twisting
12		561.8	0.27	
13	583	584.1	3.35	Ring Elongation
14		584.2	3.35	
15	677*	682.0*	37.08	C3 Triangle Breathing
16	743	742.3	0.07	Ring *oopl* Twisting
17		742.5	0.07	
18		834.5	0	C *ooph*, N *oopl*
19	985	960.1	10.35	N3 Triangle Breathing
20		985.8	0.07	NH_2 *ipl* Rocking
21		986.2	0.07	
22		1159.0	0	N_3 Triangle Rot. + NH_2 Rocking
23	1191	1179.2	0.42	C-NH_2 Stretching + NH_2 Rocking
24		1179.4	0.42	
25		1308.6	0	C_3 Triangle Rot. + NH_2 Rocking
26	1444	1486.0	1.39	Ring N-C=N asymmetric Stretching
27		1486.9	1.39	
28		1572.6	0.30	
29	1556	1572.9	4.19	Ring C=N Stretching
30		1573.4	4.20	
31	1660	1662.4	3.39	NH_2 Scissoring + C-N Stretching *ooph*
32		1662.7	3.39	
33		1697.6	2.01	NH_2 Scissoring + C-N Stretching *iph*
34		3630.4	27.63	NH_2 Symmetric Streching *ooph*
35	3419	3630.5	28.45	
36		3632.4	469.29	NH_2 Symmetric Streching *iph*
37		3775.7	17.15	
38	3470	3775.9	61.56	NH_2 Asymmetric Streching
39		3776.1	68.66	

[a] *The measured wavenumbers were obtained with 488 nm (10 mW CW) excitation on powdered melamine.*

[b] *The calculated wavenumbers were obtained by modeling of a single molecule in the gas phase.*

[c] *Abbrivations: ipl: in-plane, oopl: out-of-plane, iph: in-phase, ooph: out-of-phase, rot: rotation.*

**Analytically interesting band, see text.*

As seen in Table 6.2 and in Fig. 6.7, it was possible - by use of the 488 nm radiation - to get fairly good correspondences between the calculated and the observed spectra with clear bands. One should not expect complete matches, becase the model is based on a single gas molecule and the measurement is from the solid state where the moleculed interact.

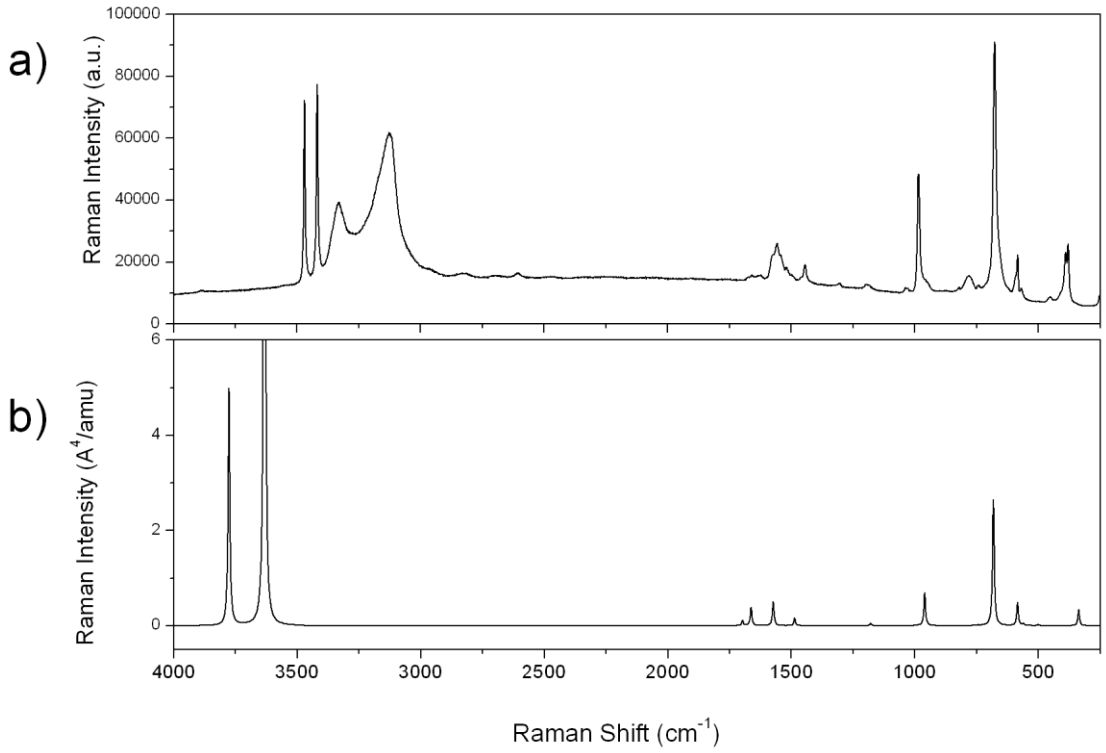

Fig. 6.7: a) Measurement spectrum of Melamine powder by use of 488 nm excitation; b) The calculated spectrum for a single molecule in the gaseous state.

6.4.3.1 Overview of Results

We succeded in measuring the Raman spectrum of 0.1 % melamine in milk, excitated by 229 nm. When comparing to the milk without the melamine, a new band that could be assigned to melamine was present at 677 cm^{-1}, as shown in Fig. 6.9, red line. The same band is also present in the measured Raman spectrum of 0.1 % melamine in water, excitated with the 229 nm line, as shown in Fig. 6.9, blue line. According to the calculated results, Table 6.2, the 677 cm^{-1} band corresponds to the mode 15, which involves three carbon atoms out of the 6-membered ring that are performing a symmetrical breathing-like deformation, resulting in an approach of the ring to a triangular shape, see Fig. 6.8.

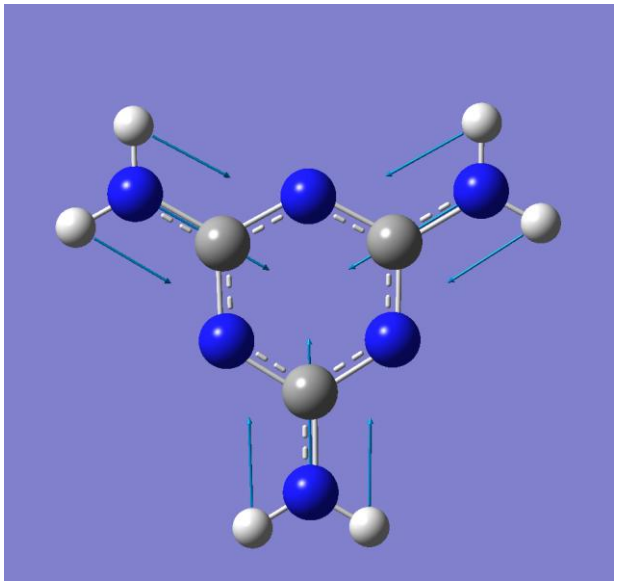

Fig. 6.8: Mode 15, C3 Triangle Breathing mode coupled to NH_2-scissoring (667 cm^{-1} on measurement, 682.0 cm^{-1} on calculation).

6.4.3.2 Detailed Discussion

229 nm Excitation Spectra

As mentioned, the 229 nm excition Raman spectra are shown in Fig. 6.9. A useful Raman spectrum (not shown) of the Melamine powder could not be obtained by regular measurement even at very low excitation levels because the resonance absorption caused melting and decomposition of the Melamine. An improved measuring method could be implemented by spinning a prepared sample with a flat surface, but this method was not tried.

In the Raman spectrum of 0.1 % melamine in water (Fig. 6.9, blue line), a band can be seen near the characteristic band of Melamine, at 677 cm^{-1}. There are also a series of other distinguishable bands appearing in the spectrum of the Melamine-water solution. We have no good explanation of these bands other than decomposition of the melamine. However, these bands are not appearing in the milk sample, so we can neglect to discuss them. We may explain the stability of the melamine-in-milk spectra as due to a possible protective influence of the milk proteins on the melamine molecules so that they avoid decomposition.

Comparing the Raman spectra of milk (black line in Fig. 6.9) and the Melamine contaminated milk (red line), the characteristic band of Melamine can be observed in the spectrum of Melamine contaminated milk on a 0.1 % concentration level. This is a 10 times better sensitivity of the traditional Raman spectrometry - excited by 785 nm infrared laser light – that was found to have a detection limit being about 1 % in powdered milk samples [6.30].

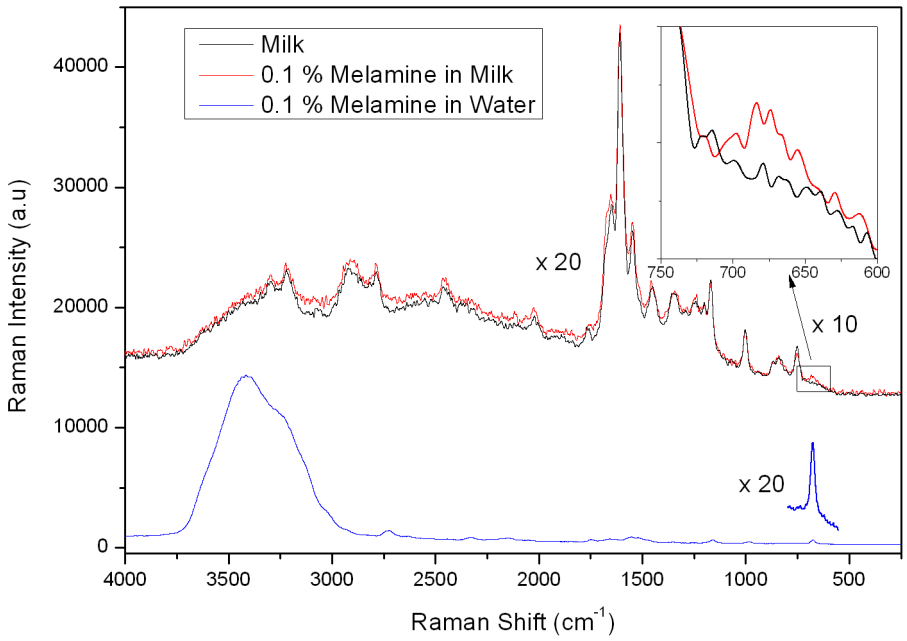

Fig. 6.9: Raman spectra of milk, 0.1 % melamine in water and Milk by use of 229 nm (10 mW) excitation.

488 nm Excitation Spectra.

The Raman spectra of Melamine powder excited by 488 nm is shown on Fig. 6.10 a).

The Raman spectra of 0.1 % Melamine in water and Milk by use of the 488 nm excitation are shown in Fig 6.10. In the Raman spectrum of 0.1 % melamine in water (blue line), the characteristic band of Melamine, 677 cm^{-1} can be hardly seen unless when scaled x 60. However, in the Raman spectrum of 0.1 % Melamine in Milk (red line), no band can be observed; only a strong fluoresence background is obvious (the CCD is saturated in the range of 1000 ~ 3700 cm^{-1}).

We conclude that the 488 nm line cannot be used to detect the Melamine in milk.

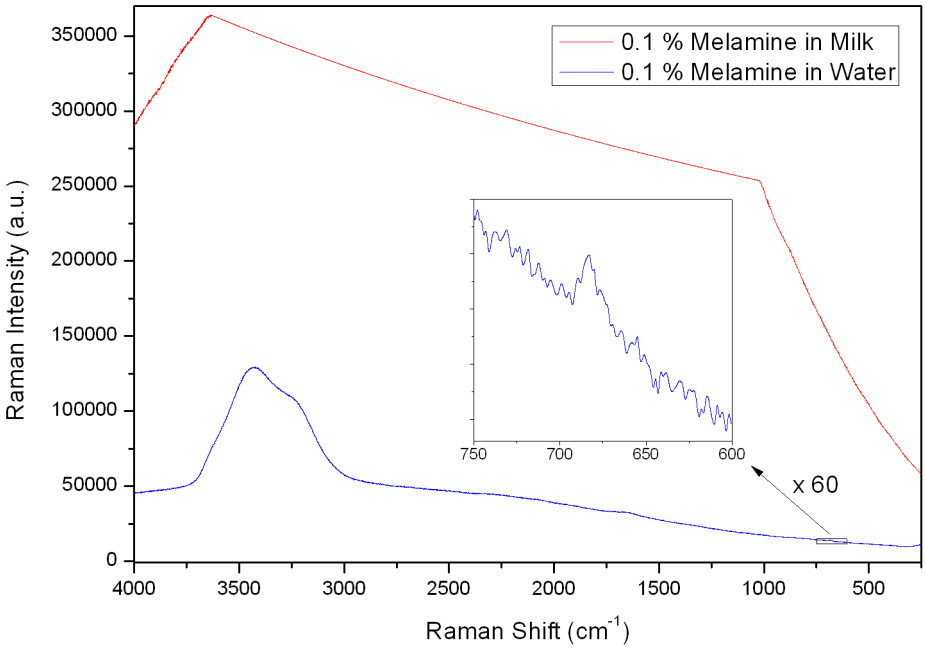

Fig. 6.10: Raman spectra of 0.1 % Melamine in water and in Milk by use of 488 nm (10 mW) excitation. The shape of the red curve is due to saturation of the detector.

6.5 Outlook and future work: DUV Raman spectrometry applied to food analysis

A successful application of Raman spectrometry to food analysis generally requires that one has a Resonance Raman effect to be active for the target compound. This is so because otherwise Raman is a quite weak effect that is against the possibility to realize high sensitivity detection.

The procedure would possibly remind of the work done on finding the UV absorption band of Sudan I and performing the DUV Resonance Raman spectrometry. Such future work could make detection of small amounts of illegal additions possible in food samples. Although the DUV light might not destroy the testing sample by thermal effects, sample degeneration caused by the photochemistry effect may still be a limitation for the use of DUV Raman spectrometry. Some technical tricks, such as rotation of sample, lateral scanning of the sample relative to the laser beam and using suitable solvents for extraction might be used to solve these kinds of problems.

With respect to Melamine, the absorption spectrum (see Fig 6.11) shows a prime resonance peak at 210 nm and a secondary peak at 235 nm, meaning that a more sensitive detection could be achieved by use of 210 nm or 235 nm excited Raman spectrometry. 5th harmonic generation of light from Nd:YAG and Nd:YLF pulsed lasers will emit respectively 213 nm and 211 nm lines that could be affordable laser lines (see Table 2.6). Regarding the 235 nm line, an easy access can be obtained by using the 476.5 nm Argon line in conjunction with a new doubling BBO crystal (see Fig. 2.17).

SHIMADZU

Application News

Rapid Determination of Melamine in Food

Melamine is used as the main raw material of melamine resin, a thermosetting plastic, but recently it is receiving considerable attention due to numerous incidents of food contamination with this substance.
Analysis of melamine in food can be performed using HPLC, LCMS(/MS), and GC/MS, etc., depending on the objective, but among these, HPLC allows for easy, multi-specimen screening analysis.
Here we introduce a rapid analytical technique for determining melamine in food using the ultra-fast LC, Prominence UFLC together with a simple sample preparation procedure.

■ Analysis of Standard Solution

Melamine (Fig. 1) is a high-polarity substance with a triazine ring, but since it is not sufficiently retained using a typical reversed-phase mode, we used the reversed-phase ion pairing mode for this analysis. Detection was conducted with a photodiode array detector, and the Shim-pack XR-ODS high-performance, high-resolution column (particle size 2.2 µm) was used for the analytical column.
Fig. 2 shows the UV spectrum of melamine. Quantitation was conducted at the maximum absorption wavelength of 235 nm.
Fig. 3 shows the chromatogram of a melamine standard solution (1000 µg/L), and Table 1 shows the analytical conditions.

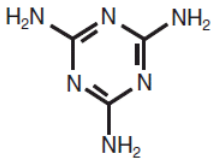

Fig.1 Structure of Melamine

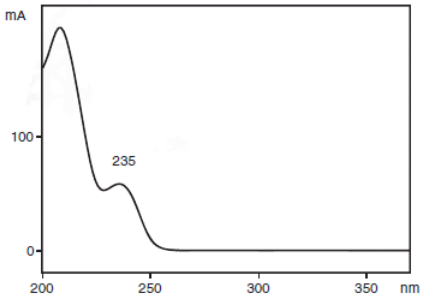

Fig.2 UV Spectrum of Melamine

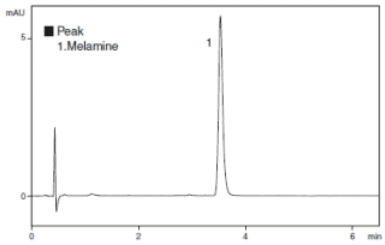

Fig.3 Chromatogram of Melamine Standard Solution (1000 µg/L)

Table 1 Analytical Conditions

Column	: Shim-pack XR-ODS (75 mm L. × 3.0 mm I.D., 2.2 µm)
Mobile Phase	: A; 10 mmol/L (Sodium) phosphate buffer (pH2.6) containing 10 mmol/L Sodium 1-octanesulfonate B; Acetonitrile A / B = 92 / 8 (v / v)
Flow Rate	: 1.2 mL/min
Column Temp.	: 40 °C
Injection Vol.	: 10 µL
Detection	: SPD-M20A at 235 nm
Flow Cell	: Conventional Cell

Fig. 6.11: According to the Shimadzu Company, analysis of melamine (up to 100 microg/L in water) is routinely done by High Performance Liquid Chromatography HPLC using UV absorption detection at 235 nm [6.33].

References to Chapter 6

[6.1] V. Cornet, Y. Govaert, G. Moens, J. V. Loco, J. J. Degroodt, "*Development of a fast analytical method for the determination of sudan dyes in chili- and curry-containing foodstuffs by high-performance liquid chromatography-photodiode array detection*", J. Agric. Food Chem. Vol. 54, Issue 3, (**2006**), pp. 639-644.

[6.2] F. Tateo, M. J. Bononi, "*Fast determination of Sudan I by HPLC/APCI-MS in hot chilli, spices, and oven-baked foods*", Journal of Agricultural and Food Chemistry, Volume 52, Issue 4, (**2004**), pp. 655-658.

[6.3] F. Puoci, C. Garreffa, F. Iemma, R. Muzzalupo, U. G. Spizzirri, N. Picci, "Molecularly imprinted solid phase extraction for detection of sudan I in food matrices", Food Chemistry, Vol. 93, Issue 2, (**2005**), pp. 349-353.

[6.4] M. Mazzetti, R. Fascioli, I. Mazzoncini, G. Spinelli, I. Morelli, A. Bertoli, "*Determination of 1-phenylazo-2-naphthol (Sudan I) in chilli powder and in chilli-containing food products by GPC clean-up and HPLC with LC/MS confirmation*", Food Additives and Contaminants, Volume 21, Issue 10, (**2004**), pp. 935-941

[6.5] H. Buchardt, "*Chili med forbudte farvestoffer*", Dan. Kemi (**2007)**, 88, pp. 28.

[6.6] I. T. Shadi, B. Z. Chowdhry, S. A. Leharne, R. Withnall, *ICORS20, 20th International conference on Raman Spectroscopy, Yokohama, Japan, Wiley*, (**2006)**, pp.247.

[6.7] M. I. Minguez-Mosquera, M. Jaren-Galan, J. Garrido-Fernandez, "*Color quality in paprika*", Journal of Agricultural and Food Chemistry, Volume 40, Issue 12, (**1992**), pp. 2384-2388.

[6.8] H. Ou, T.P. Rørdam, K. Rottwitt, F. Grumsen, A. Horsewell, R.W. Berg, & P. Shi, "*Ge nano-clusters in PECVD-deposited glass caused only by heat treatment*" Appl. Phys. B, 91, (**2008**), pp. 177-181.

[6.9] H. Ou, Y. Ou, Chuan Liu, R.W. Berg and K. Rottwitt: "*Formation and Characterization of varied size germanium nanocrystals by Electron Microscopy, Raman spectroscopy and Photoluminescence*", Optical Materials Express (Optical Society of America), **2011**, Vol.1, Issue 4, pp. 643-651. (ISSN: 2159-3930).

[6.10] H. Ou, Y. Ou, Chuan Liu, R. W. Berg and K. Rottwitt, "*Size-effect of germanium nanocrystals*", part of: Conference proceedings to CLEO:2011 Laser Science to Photonic Applications, Optical Society of America, Baltimore Convention Center, Maryland USA, 1-6 May, (**2011**). Full conference paper publ. in proceedings/book (3 pages).

[6.11] Y. Ou, V. Jokubavicius, Chuan Liu, R.W. Berg, M. Linnarsson, S. Kamiyama, Z. Lu, R. Yakimova, M. Syväjärvi, and H. Ou, "*Photoluminescence and Raman spectroscopy characterization of boron- and nitrogen-doped 6H silicon carbide*", Extended Abstract to the 2011 International Conference on Silicon Carbide and Related Materials (ICSCRM 2011), September 11 – 16, **2011**, Cleveland, Ohio, USA (5 pages).

[6.12] Y. Ou, D. D. Corell, C. Dam-Hansen, P. M. Petersen, H. Ou, "*Antireflective sub-wavelength structures for improvement of the extraction efficiency and color rendering index of monolithic white light-emitting diode*", Optics Express (Optical Society of America), vol. 19 (S2), pp. A166-A172 (**2011**). (ISSN: 1094-4087) (DOI: 10.1364/OE.19.00A166) (paper id: We P-58).

[6.13] Y. Ou, V. Jokubavicius, S. Kamiyama, C. Liu, R. W. Berg, M. Linnarsson, R.Yakimova, M. Syväjärvi, and H. Ou, "*Donor-acceptor-pair emission characterization in N-B doped fluorescent SiC*", OPTICAL MATERIALS EXPRESS, December **2011,** Vol. 1, No. 8, pp. 1439-1446.

[6.14] Food and Drug Administration (USA), (**2007**), *Interim melamine and analogues safety/risk assessment*. Available from: http://www.cfscan.fda.gov/~dms/melamra. Accessed Feb 1, 2008.

[6.15] Chan EYY, Griffiths SM, Chen CW, "*Public-Health Risks of Melamine in Milk Products*", (**2008**), Lancent 372: pp. 1444-1445.

[6.16] Pliny, "Melamine tainted milk re-emerges in northwest China plant", *Xinhua*, http://news.xinhuanet.com/english2010/china/2010-07/09/c_13392414.htm. Retrieved **2010**-07-09.

[6.17] J. J. Cincotta, R. Feinland, "Determination of polyfunctional amines, guanidines, amidinoguanidines, and melamines by gas-liquid chromatography", Anal. Chem., 34, (**1962**), pp. 774–776.

[6.18] P. G. Stoks, A. W. Schwartz, "*Determination of s-triazine derivatives at the nanogram level by gas-liquid chromatography*", J. Chromatogr, 168, (**1979**), pp. 455–460.

[6.19] J. P. Toth, P. C. Bardalaye, "*Capillary gas chromatographic separation and mass spectrometric detection of cyromazine and its metabolite melamine*", J. Chromatogr., 408, (**1987**), pp. 335–340.

[6.20] R. A. Yokley, L. C. Mayer, R. Rezaaiyan, M. E. Manuli, M. W. Cheung, "*Analytical method for the determination of cyromazine and melamine residues in soil using LC-UV and GC-MSD*", J. Agr. Food Chem., 48, (**2000**), pp. 3352–3358

[6.21] T. Inoue, H. Ishiwata, K. Yoshihira, A. "*Tanimura, High-performance liquid chromatographic determination of melamine extracted from cups made of melamine resin*", J. Chromatogr. 346, (**1985**), pp. 450–452.

[6.22] S. Ehling, S. Tefera, I. P. Ho, "*High-performance liquid chromatographic method for the simultaneous detection of the adulteration of cereal flowers with melamine and related triazine by-broducts ammeline, ammelide, and cyanuric acid*", Food Addit. Contam., 24, (**2007**), pp. 1319–1325.

[6.23] R. Muniz-Valencia, S. G. Ceballos-Magana, D. Rosales-Martinez, R. Gonzalo-Lumbreras, A. Santos-Montes, A. Cubedo-Fernandez-Trapiella, R. C. Izquierdo-Hornillos, "*Method development and validation for melamine and its derivatives in rice concentrates by liquid chromatography*", Application to animal feed samples. Anal. Bioanal. Chem., 392, (**2008**), pp. 523–531.

[6.24] J. V. Sancho, M. Ibanez, S. Grimalt, O. J. Pozo, F. Hernandez, "*Residue determination of cyromazine and its metabolite melamine in chard samples by ion-pair liquid chromatography coupled to electrospray tandem mass spectrometry*", Anal. Chem. Acta., 530, (**2005**), pp. 237–243.

[6.25] B. Kim, L. B. Perkins, R. J. Bushway, S. Nesbit, T. Fan, Sheridan R, Greene V, "*Determination of melamine in pet food by enzyme immunoassay, high-performance liquid chromatography with diode array detection, and ultra-performance liquid chromatography with tandem mass spectrometry*". J. AOAC Int., 91, (**2008**), pp. 408–413.

[6.26] M. S. Filigenzi, B. Puschner, L. S. Aston, R. H. Poppenga, "*Diagnostic determination of melamine and related compounds in kidney tissue by liquid chromatography/tandem mass spectrometry*", J. Agr. Food Chem., 56, (**2008**), pp. 7593–7599.

[6.27] C. Srilakshmi, E. Widjaja, B.G. Anderson, M. Garland, "*Fourier transform Raman spectral measurements of powdered quaternary mixtures of organic compounds. Exceptional pure component spectral reconstruction using band-target entropy minimization (BTEM) "*, Talanta, 72, (**2007**), pp. 847–854.

[6.28] M. Lin, L. He, J. Awika, L. Yang, D. R. Ledoux, H. Li, "*Mustapha A Detection of melamine in gluten, chicken feed, and processed foods using surface enhanced Raman spectroscopy and HPLC*", J. Food Sci. 73, (**2008**), pp. 129–134.

[6.29] Qiu Chao, Maingi, T. Alfred, Jiang Chaoyang, "*Surface-enhanced Raman scattering detection of melamine via silver nanostructures, Abstracts of Papers, 241st ACS National Meeting & Exposition*", Anaheim, CA, United States, March 27-31, **2011**.

[6.30] Okazaki Shigetoshi, Hiramatsu Mitsuo, Gonmori Kunio, Suzuki Osamu, Tu Anthony T., "*Rapid nondestructive screening for melamine in dried milk by Raman spectroscopy*", Forensic Toxicology 27(2), (**2009**), pp. 94-97.

[6.31] From the ChemIDplus database:
http://chem.sis.nlm.nih.gov/chemidplus/ProxyServlet?objectHandle=DBMaint&actionHandle=default&nextPage=jsp/chemidlite/ResultScreen.jsp&TXTSUPERLISTID=0000108781
Accessed 19th Dec. 2011.

[6.32] http://www.huffingtonpost.com/2009/11/24/china-executes-2-people-o_n_368657.html
Accessed 19th Dec. 2011.

[6.33] The Fig. 6.11 has been adapted from a Shimadzu application note that is only available after login: http://www.shimadzu.com/an/literature/hplc/l383e.html.

Abbreviations:

AR	Antireflection
BBO	β-barium borate, β-BaB_2O_4
BTEX	Benzene, Toluene, Ethyl-benzene, m-Xylen, o-Xylen and p-Xylen
CCD	Charge-Coupled Device
CLBO	Cesium Lithium Borate, $CsLiB_6O_{10}$
CW	Continuous Wave
CVD	Chemical Vapour Deposition
DAP	Donor-Acceptor-Pair
DACF	Diffractions and Aberrations Compensation Factor
DUV	Deep Ultraviolet
DPSS	Diode-Pumped Solid-State
DFB	Distributed-Feedback
FWHM	Full Width at Half Maximum
GC	Gas Chromatography
GC-MS	Gas Chromatography-Mass Spectrometry
HR	High-Reflector
IEC	International Electrotechnical Commission
LBO	Lithium TriBorate
LC	Liquid Chromatography
LCMS	Liquid Chromatography Mass Spectrometry
LD	Laser Diode
LED	Light Emitting Diodes
LOPC	Longitudinal Optical Phonon-Plasmon Coupled
LP_{01},	fiber 01 order Linear Polarization mode
MTBE	Methyl-butyl tertiery ether
MS	Mass Spectrometry
Nd:YVO4	Neodymium Doped Yttrium Orthovanadate
Nd:YAG	Neodymium Doped Yttrium Aluminum Garnet
Nd:YLF	Neodymium Doped Yttrium Lithium Fluoride
PECVD	Plasma Enhanced Chemical Vapor Deposition
PPNCW	Periodically Poled Nonlinear Crystal Waveguides
QCE	Quantum Confinement Effect
QPM	Quasi Phase Matching
SHG	Second Harmonic Generation
SFG	Sum Frequency Generation
TEP	Tetraethyl lead
TEM	Transmission electron microscopy
TEM_{pl}	p,l order Transverse ElectroMagnetic mode
TE	Transverse-electric
TM	Transverse-magnetic
UV	Ultraviolet
VCSEL	Vertical-Cavity Surface Emitting Laser

Appendix 1:

Mathmatica program for calculating the dispersion of fused silica

```
a1 = 0.69616630; (* Input the constants of dispersion equation of fused silica *)
a2 = 0.40794260;
a3 = 0.89747940;
l1 = 0.068404300;
l2 = 0.11624140;
l3 = 9.8961610;
n = (1 + a1 * λ^2 / (λ^2 - l1^2) + a2 * λ^2 / (λ^2 - l2^2) + a3 * λ^2 / (λ^2 - l3^2))^0.5;
θb = (ArcTan[n] * 180 / π);
θb1 = (ArcTan[n] * 180 / π) / 20 - 1.32;
θt = 180 - 2 * θb;
θ1 = 180 - 45 - θb - 11;
Plot[{n, θb1}, {λ, 0.21, 0.3}, PlotRange → {{0.21, 0.3}, {1.48, 1.54}},
 PlotStyle → {{Thickness[0.003], RGBColor[0, 0, 0]}, {Thickness[0.003], RGBColor[1, 0, 0]}},
 PlotRange → All, TextStyle -> {FontFamily -> "Radius", FontSize → 22}, Frame → True,
 FrameLabel → {"Wavelength (μm)", "Refractive Index"},
  PlotPoints → 80000];
Plot[{θt, θ1}, {λ, 0.21, 0.3}, PlotRange → {{0.21, 0.3}, {66, 68}},
 PlotStyle → {{Thickness[0.003], RGBColor[0, 1, 0]}, {Thickness[0.003], RGBColor[0, 0, 1]}},
 PlotRange → All, TextStyle -> {FontFamily -> "Radius", FontSize → 22}, Frame → True,
 FrameLabel → {"Wavelength (μm)", "θL(degree)"},
  PlotPoints → 80000]
```

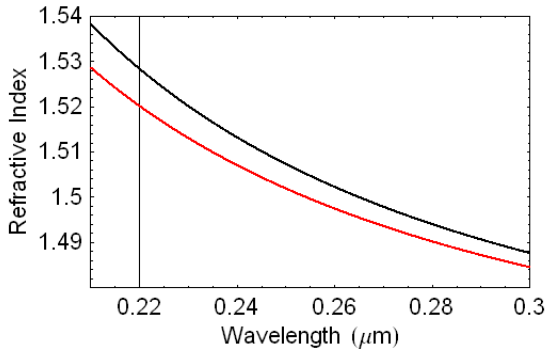

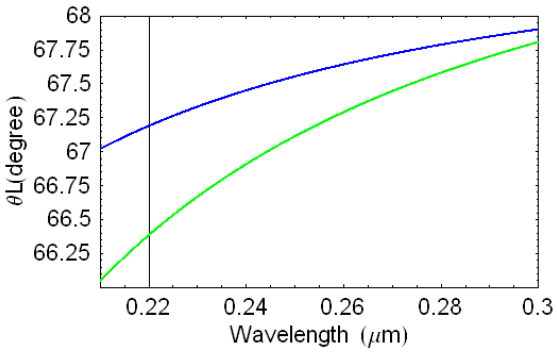

Appendix 2:

Workshop drawings of the horizontal sampling nose

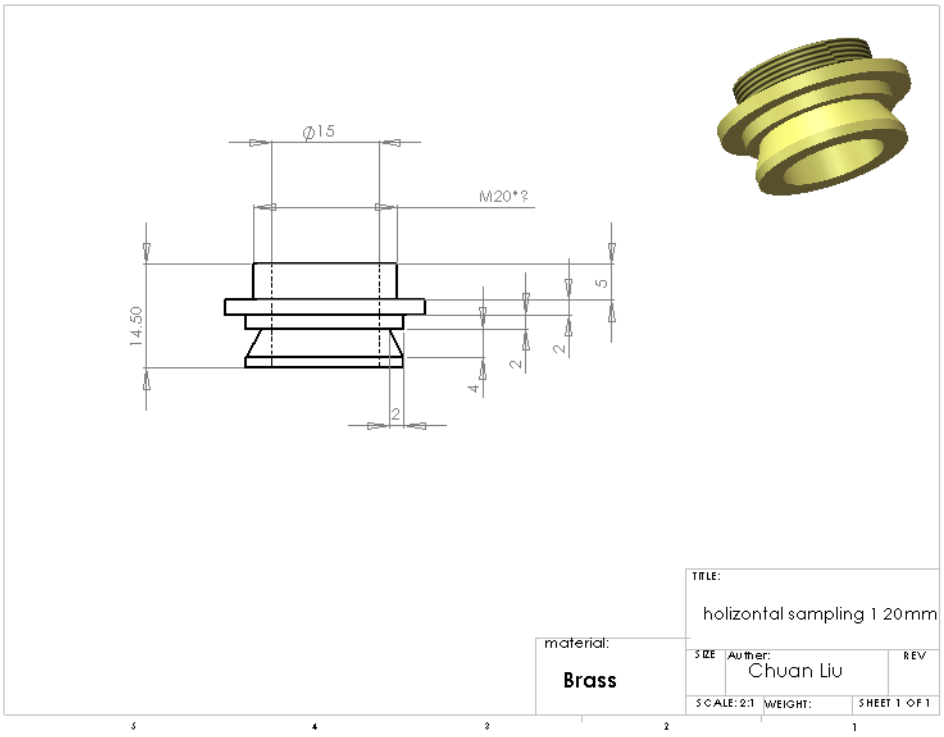

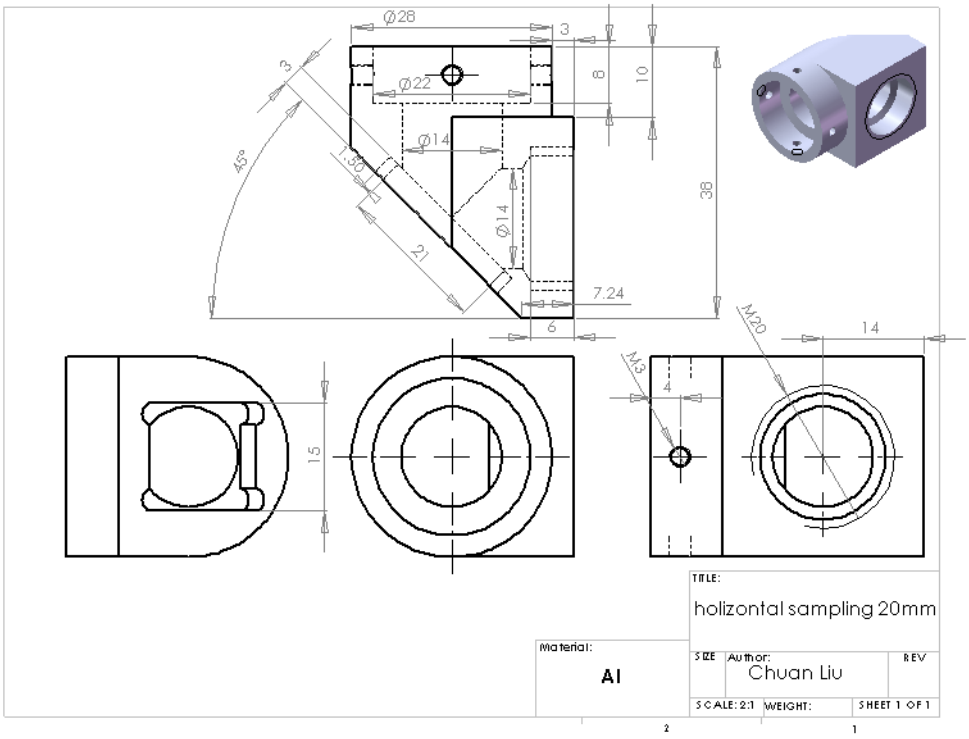

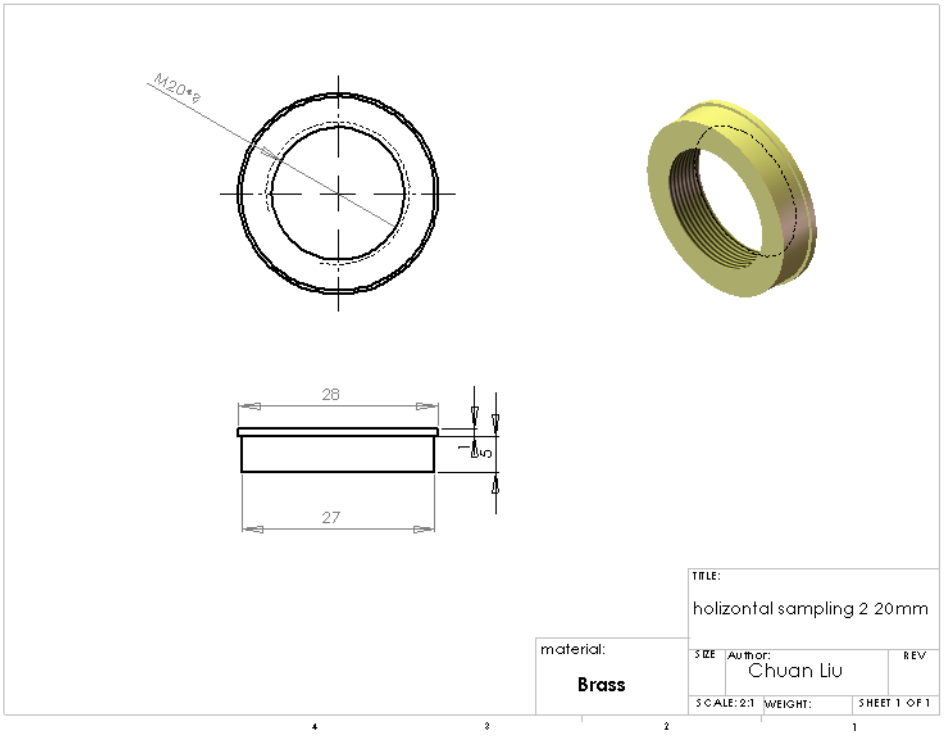
M20*g
28
27
material:
Brass
TITLE:
holizontal sampling 2 20mm
SIZE
Author:
Chuan Liu
REV
SCALE: 2:1
WEIGHT:
SHEET 1 OF 1

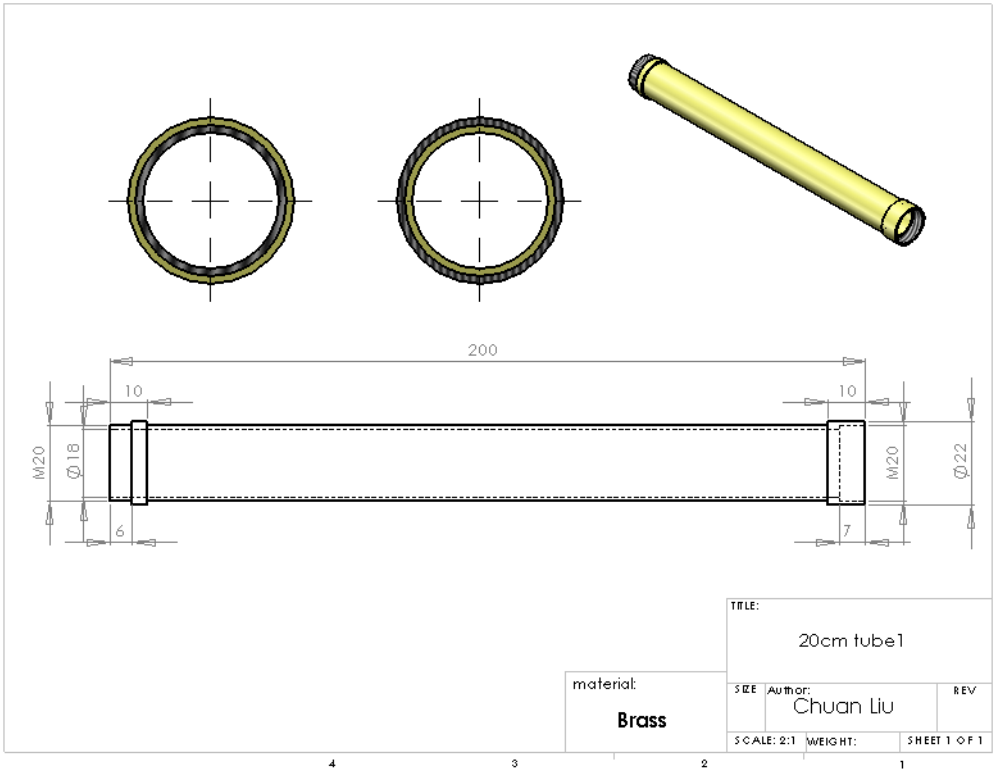
200
10
10
M20
Ø18
M20
Ø22
6
7
material:
Brass
TITLE:
20cm tube1
SIZE
Author:
Chuan Liu
REV
SCALE: 2:1
WEIGHT:
SHEET 1 OF 1

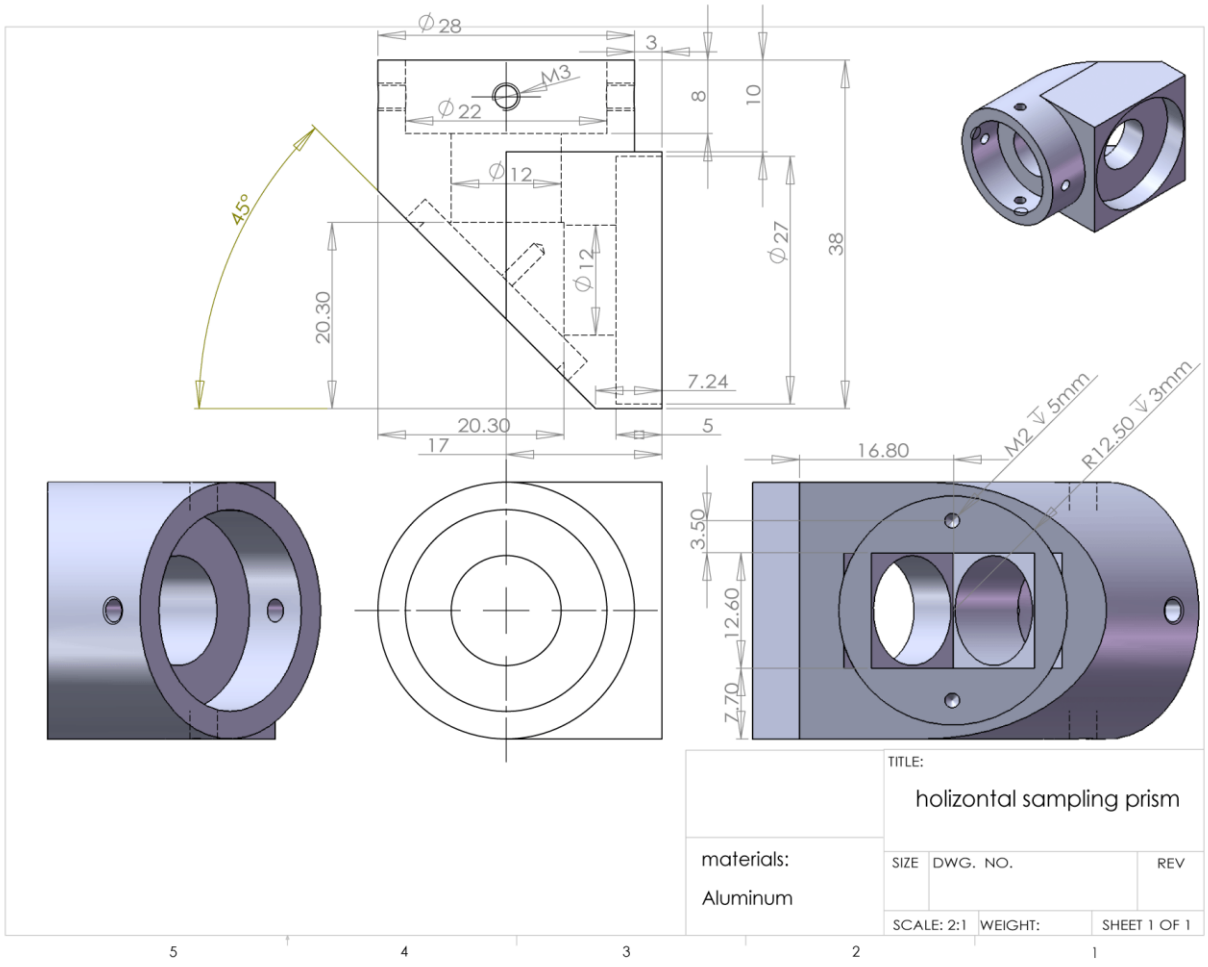
Ø28
3
M3
Ø22
8
10
Ø12
45°
Ø27
38
Ø12
20.30
7.24
20.30
5
17
16.80
M2 ▽ 5mm
R12.50 ▽ 3mm
3.50
12.60
7.70
TITLE:
holizontal sampling prism
materials:
Aluminum
SIZE
DWG. NO.
REV
SCALE: 2:1
WEIGHT:
SHEET 1 OF 1
5
4
3
2
1

Appendix 3:

Comparing Spectral Resolution by using the Rayleigh Criterion and the FWHM

The definition of resolution by the Rayleigh criterion is that two *Airy disk curves* [5.20] (i.e. the diffraction cross section patterns of circular apertures) for two close wavelengths of λ and $\lambda+\Delta\lambda$, are regarded as just resolved when the principal diffraction maximum of one image coincides with the first minimum of the other [5.13], [5.14]. The unity intensity description, *I(r)*, of an Airy disk cross section, shown below in Fig. A3.1 [5.13], is given as

$$I(r) = \left(\frac{2J_1(r)}{r}\right)^2 \qquad \text{------ (eq. A3.1)}$$

where $J_1(r)$ is a Bessel function of the first kind and r is the radius distance from the maximum.

The first minimum of (eq. A3.1) is found at r = 1.22 π = 3.83, therefore the just resolved Airy disk, by the Rayleigh criterion, can be described as

$$I(r - 1.22\pi) = \left(\frac{2J_1(r-1.22\pi)}{r-1.22\pi}\right)^2 \qquad \text{------ (eq. A3.2)}$$

The FWHM of the Airy disk, described by (eq. A1.1), can be shown to be 3.24, a value that was achieved by solving for r letting $I(r)$ be 0.5. Therefore a closely placed Airy disk at a distance of one FWHM unit will be

$$I(r - 3.24) = \left(\frac{2J_1(r-3.24)}{r-3.24}\right)^2 \qquad \text{------ (eq. A3.3)}$$

As shown in Fig. A3.1 a), when two Airy disks are just separated by a distance corresponding to just the FWHM, two maxima can be observed on the overlapped intensity curve (black line), i.e. they are theoretically distinguishable. Compare with Fig. A3.1 b), where two Airy disks are just separated by a distance satisfying the Rayleigh Criterion. In this latter case the peaks are more clearly resolved. Therefore our spectral resolution $\Delta\omega_{FWHM}$, dominated by FWHM, is smaller than the spectral resolution $\Delta\omega_{RC}$ satisfying the Rayleigh Criterion. The scale $\Delta\omega_{FWHM}/\Delta\omega_{RC}$ is 3.24/1.22 π = 0.845.

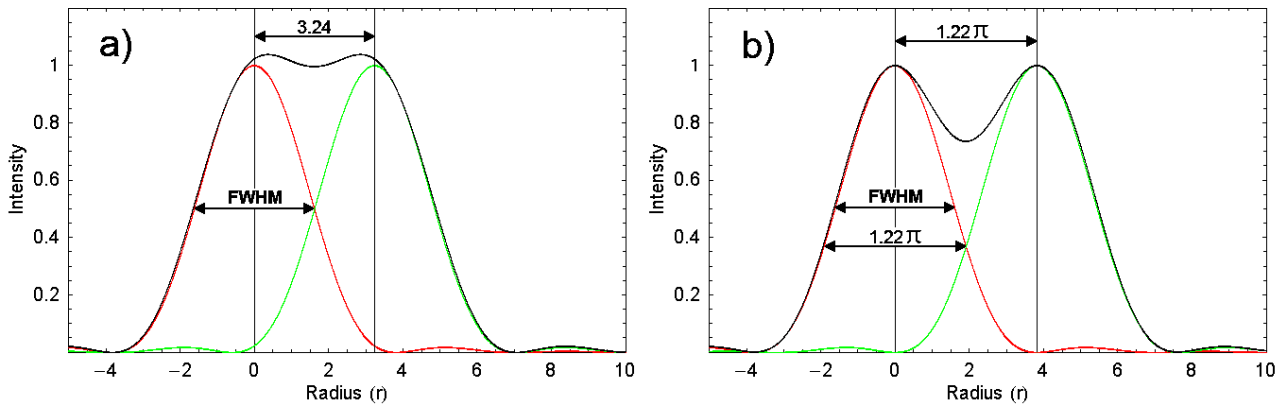

Fig. A3.1: a) Two Airy disks resolved by one FWHM unit, the red curve corresponding to (eq. A1.1), the green curve corresponding to (eq. A1.3), and the black curve corresponding to the intensity overlap, i.e. the sum of equations (eq. A1.1) and (eq. A1.3). b) Two Airy disks just resolved by the Rayleigh criterion. The red curve is corresponding to (eq. A1.1), the green curve is corresponding to (eq. A1.2), and the black curve is corresponding to the intensity overlap, i.e. the sum of equations (eq. A1.1) and (eq. A1.2).

Appendix 4:

Spectral Resolution and True Raman Bandwidth

A true Raman spectrum is here defined as a Raman spectrum excited by a hypothetically monochromatic light source which could be a narrow section (a delta function at ω_1) of the laser spectrum as shown on Fig. A4.1, a). By assuming a Gaussian approximation, the profile of a true Raman band with a FWHM bandwidth of $\Delta\omega_R$ can be described as a Gaussian function $g_R(\omega)$, equation (eq. A4.1), as shown below, corresponding to the Fig. A4.1, b):

$$g_R(\omega_r) = g_{R0} \cdot \exp\left[-\left(\frac{2\sqrt{\ln 2}(\omega_r+\omega_R)}{\Delta\omega_R}\right)^2\right] \qquad \text{------ (eq. A4.1)}$$

Here ω_R is the Raman shift of the peak of the band and ω_r is the variable of the Raman shift, g_{R0} is a constant that corresponds to maximum of the Raman peak.

The laser spectrum can similarly be described as a Gaussian function, $g_L(\omega)$, see (eq. A4.2). Note that for multi-longitudinal mode lasers, which are often used in Raman spectroscopy, this curve of the laser line may - under high resolution - show that it represents an envelopment of several longitudinal mode laser lines. However *at lower resolution* it may still give what looks like one broadened laser line in the spectrum (Fig. A4.1, a).

$$g_L(\omega) = g_{L0} \cdot \exp\left[-\left(\frac{2\sqrt{\ln 2}(\omega-\omega_L)}{\Delta\omega_L}\right)^2\right] \qquad \text{------ (eq. A4.2)}$$

Here ω is the variable of absolute wavenumber; ω_L is the absolute wavenumber of the laser peak; $\Delta\omega_L$ is the FWHM of the laser line spectrum and g_{L0} is a normalizing constant describing the maximum intensity of the laser. $g_L(\omega)$ can be considered as a series of combined monochromatic light sources, ω_1. The wavenumber value, ω, to give significant contributions should be in a range of a suitable size $(0 < \omega < \infty)$. In the corresponding range of negative numbers $(-\infty < \omega \leq 0)$, the values of $g_L(\omega)$ are extremely small because of $\Delta\omega_L << \omega_L$. However, in order to get a convenient way of calculation, the range of ω can still be taken to be $(-\infty < \omega < \infty)$.

Now therefore the Raman spectrum, denoted $g_{LR}(\omega)$, excited by the laser, $g_L(\omega)$, ideally should be created as a convolution result of the equations (eq. A4.1) and (eq. A2.2) as shown in Fig. A4.1, c):

$$g_{LR}(\omega) = g_L(\omega) \otimes g_R(\omega_r) = \int_{-\infty}^{+\infty} g_L(\omega_1) \cdot g_R(\omega-\omega_1) \cdot d\omega_1$$

$$= g_{R0} \cdot g_{L0} \cdot \int_{-\infty}^{+\infty} \exp\left[-\left(\frac{2\sqrt{\ln 2}(\omega_1-\omega_L)}{\Delta\omega_L}\right)^2\right] \cdot \exp\left[-\left(\frac{2\sqrt{\ln 2}(\omega-\omega_1+\omega_R)}{\Delta\omega_R}\right)^2\right] \cdot d\omega_1$$

$$= \frac{g_{R0} \cdot g_{L0} \cdot \sqrt{\pi}}{\sqrt{\left(\frac{2\sqrt{\ln 2}}{\Delta\omega_R}\right)^2 + \left(\frac{2\sqrt{\ln 2}}{\Delta\omega_L}\right)^2}} \cdot \exp\left[-\left(\frac{2\sqrt{\ln 2}(\omega_2-\omega_L+\omega_R)}{\sqrt{(\Delta\omega_R)^2+(\Delta\omega_L)^2}}\right)^2\right]$$

$$= C_1 \cdot \exp\left[-\left(\frac{2\sqrt{\ln 2}(\omega_2-\omega_L+\omega_R)}{\sqrt{(\Delta\omega_R)^2+(\Delta\omega_L)^2}}\right)^2\right] \quad \text{------ (eq. A4.3)}$$

Here ω_1 is the integration variable and C_1 is a constant:

$$C_1 = \frac{g_{R0}\cdot g_{L0}\cdot\sqrt{\pi}}{\sqrt{\left(\frac{2\sqrt{ln\,2}}{\Delta\omega_R}\right)^2+\left(\frac{2\sqrt{ln\,2}}{\Delta\omega_L}\right)^2}} \quad \text{------ (eq. A4.4)}$$

In the next step, the *real* Raman spectrum $g_{LR}(\omega)$ will here be denoted the spectrum of the light as it really is before the light is entering into the spectrometer, i. e. not the *measured* spectrum. Owing to the limited spectral resolution of spectrometer, the *measured* Raman signal could be considered as coming from a series of hypothetic monochromatic light increments that goes through the measuring process. This implies that each element in the $g_{LR}(\omega)$ spectrum would be broadened to contribute a Gaussian-like bell-shaped curve, $g_s(\omega_s)$ (shown on Fig. A4.1, d)) to the measured spectrum. By assuming again a Gaussian approximation then each of these contributions can then be described as $g_s(\omega_s)$ as below:

$$g_S(\omega_s) = g_{S0}\cdot\exp\left[-\left(\frac{2\sqrt{\ln 2}\cdot\omega_s}{\Delta\omega_S}\right)^2\right] \quad \text{------ (eq. A4.5)}$$

Here ω_s is the variable of the wavenumber difference between the *real* Raman signal and the *measured* Raman signal; $\Delta\omega_S$ is the spectral resolution of spectrometer and g_{S0} is the normalizing constant.

By summing the contributions from the all these intervals, the measured Raman spectrum, $g_M(\omega)$, is the convolution result of the equations (eq. A4.3) and (eq. A4.5) as shown in Fig. A4.1, e):

$$g_M(\omega) = g_{LR}(\omega)\otimes g_S(\omega_s) = g_L(\omega)\otimes g_R(\omega_r)\otimes g_S(\omega_s)$$

$$= \int_{-\infty}^{+\infty} g_{LR}(\omega_2)\cdot g_S(\omega-\omega_2)\cdot d\omega_2$$

$$= \frac{g_{R0}\cdot g_{L0}\cdot g_{S0}\cdot\sqrt{\pi}}{\sqrt{\left(\frac{2\sqrt{ln\,2}}{\Delta\omega_R}\right)^2+\left(\frac{2\sqrt{ln\,2}}{\Delta\omega_L}\right)^2}}\cdot\int_{-\infty}^{+\infty}\exp\left[-\left(\frac{2\sqrt{\ln 2}(\omega_2-\omega_L+\omega_R)}{\sqrt{(\Delta\omega_R)^2+(\Delta\omega_L)^2}}\right)^2\right]\cdot\exp\left[-\left(\frac{2\sqrt{\ln 2}\cdot(\omega-\omega_2)}{\Delta\omega_S}\right)^2\right]\cdot d\omega_2$$

$$= \frac{g_{R0}\cdot g_{L0}\cdot g_{S0}\cdot\pi}{4ln\,2\cdot\sqrt{\left(\frac{1}{(\Delta\omega_R)^2}+\frac{1}{(\Delta\omega_L)^2}\right)\cdot\left(\frac{1}{(\Delta\omega_R)^2+(\Delta\omega_L)^2}+\frac{1}{(\Delta\omega_S)^2}\right)}}\cdot\exp\left[-\left(\frac{2\sqrt{\ln 2}(\omega-\omega_L+\omega_R)}{\sqrt{(\Delta\omega_R)^2+(\Delta\omega_L)^2+(\Delta\omega_S)^2}}\right)^2\right]$$

$$= C_2\cdot\exp\left[-\left(\frac{2\sqrt{\ln 2}(\omega-\omega_L+\omega_R)}{\sqrt{(\Delta\omega_R)^2+(\Delta\omega_L)^2+(\Delta\omega_S)^2}}\right)^2\right] \quad \text{------ (eq. A4.6)}$$

Here ω_2 is the integration variable and C_2 is a constant:

$$C_2 = \frac{g_{R0}\cdot g_{L0}\cdot g_{S0}\cdot\pi}{4ln\,2\cdot\sqrt{\left(\frac{1}{(\Delta\omega_R)^2}+\frac{1}{(\Delta\omega_L)^2}\right)\cdot\left(\frac{1}{(\Delta\omega_R)^2+(\Delta\omega_L)^2}+\frac{1}{(\Delta\omega_S)^2}\right)}} \quad \text{------ (eq. A4.7)}$$

According to this expression of the convolution result, equation (eq. A4.6), the measured bandwidth of the observed Raman band must be given by the denominator:

$$\Delta\omega_M = \sqrt{(\Delta\omega_R)^2 + (\Delta\omega_S)^2 + (\Delta\omega_L)^2} \qquad \text{------} \quad \text{(eq. A4.7)}$$

(within the assumption of Gaussian band shapes).

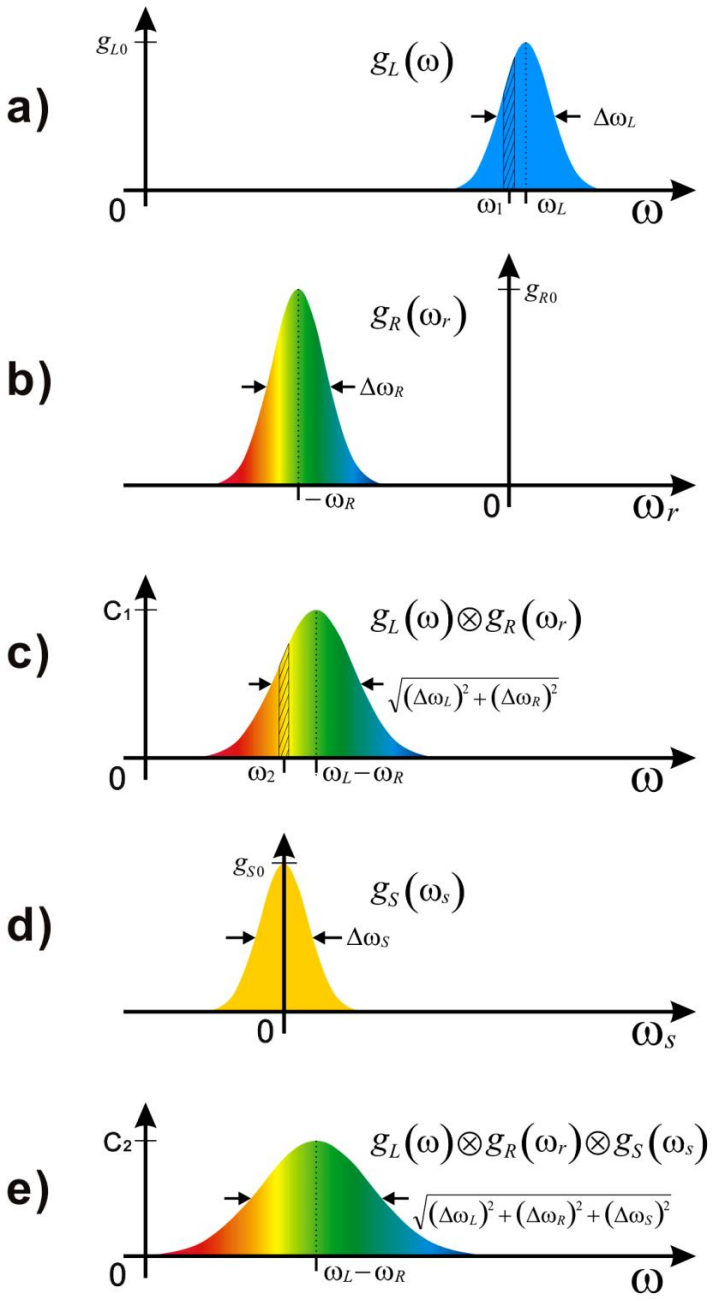

Fig. A4.1: The relationship between the laser spectrum, the true Raman spectrum, the real Raman spectrum, the spectral resolution of spectrometer and the measurement of Raman spectrum under the Gaussian approximation; a) the laser spectrum with a monochromatic incremental section ω_1; b) the true Raman spectrum; c) the real Raman spectrum; d) a hypothetic monochromatic signal broaden by the spectral resolution of spectrometer; e) the measurement of the Raman band.

Appendix 5:

Expression of Spectral Resolution for Static Grating Acquisition

When the grating is static, the angle of Θ_i is kept constant during the measurement of the Raman photons (see Fig. 5.1). The Raman wavenumber shift of signal incident on the center of the CCD is denoted as ω_0 (not shown in Fig. 5.1). Therefore equation (eq. 8) can be modified as

$$\theta = \arcsin\left(\frac{\frac{1}{(\omega_L - \omega_0)}}{2 \cdot d \cdot \cos\left(\frac{\alpha}{2}\right)}\right) + \frac{\alpha}{2} \qquad \text{------ (eq. A5.1)}$$

The constant Θ_i can be found by substituting equation (eq. A5.1) into equation (eq. 5) to get:

$$\theta_i = \arcsin\left(\frac{\frac{1}{(\omega_L - \omega_0)}}{2 \cdot d \cdot \cos\left(\frac{\alpha}{2}\right)}\right) - \frac{\alpha}{2} \qquad \text{------ (eq. A5.2)}$$

By substituting (eq. A5.2) into (eq. 1) we get

$$\theta = \arcsin\left(\frac{\lambda}{d} - \sin\left(\arcsin\left(\frac{\frac{1}{(\omega_L - \omega_0)}}{2 \cdot d \cdot \cos\left(\frac{\alpha}{2}\right)}\right) - \frac{\alpha}{2}\right)\right) \qquad \text{------ (eq. A5.3)}$$

Here it should be noted that Θ in equation (eq. A5.3) is a general expression and not only the condition corresponding to the center of the CCD. Furthermore Θ is a function of λ.

If we substitute (eq. A5.3) into (eq. 4), use unit conversion and equations (eq. 10) and (eq. 11), we get:

$$\Delta\omega\left[\omega_L, \omega_R, G, f_2, \alpha, b_{img}\right]$$

$$= (\omega_L - \omega_R)^2 \cdot \frac{b_{img}}{G \cdot f_2} \cdot \cos\left(\arcsin\left(\frac{G}{(\omega_L - \omega_R)} - \sin\left(\arcsin\left(\frac{G}{2\,(\omega_L - \omega_0) \cdot \cos\left(\frac{\alpha}{2}\right)}\right) - \frac{\alpha}{2}\right)\right)\right)$$

------ (eq. A5.4)

In Fig. A5.1, we show black lines for the resolution *versus* the Raman shift, calculated from the above equation for different values of the static setting ω_0 of the grating. The black lines show the unusual (artifact) behavior, that the spectral resolution can reach 0. Actually, in this case, the grating diffraction angle Θ is simultaneously approaching 90^0. Such an angle, see Fig. 5.1, it is not a condition that can be realized because the grating will be required to have an infinite area to be able to reflect the light.

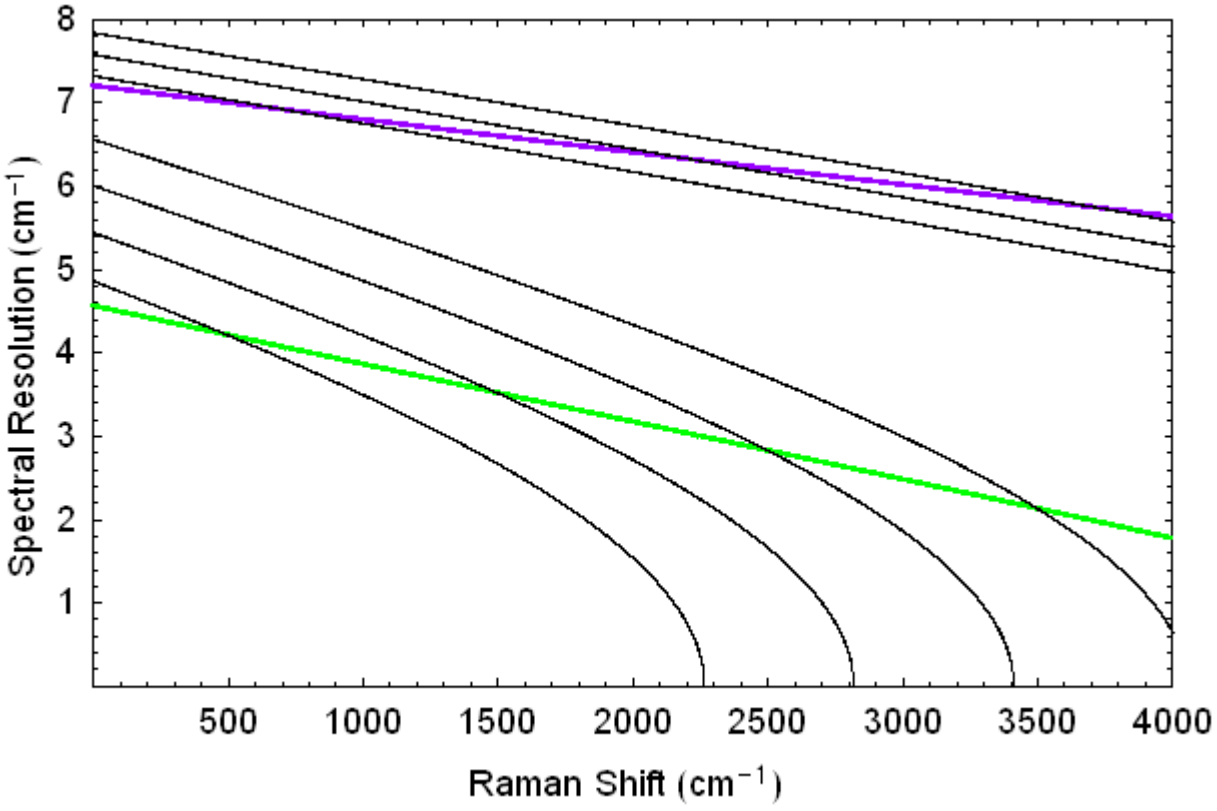

Fig. A5.1: Spectral resolution along the Raman shift axis. The green and violet lines show the theoretical results calculated by use of equation (eq. 12) for the central part of the CCD (in extended scanning mode using only few pixels). The black lines show the spectral resolution in four and three spectrograms excited with 514.5 and 257.3 nm lasers, respectively, recording in static mode, using many pixels and settings of the central pixel of the CCD at Raman shift wavenumbers of ω_0 for 514.5 nm = 500, 1500, 2500 and 3500 cm^{-1}, and ω_0 for 257.3 nm = 750, 2250 and 3750 cm^{-1}.

Appendix 6:

Mathematica program for calculating the spectral resolution.

(1) Excitation wavelength, 514.5 nm; Broad opening width of the entrance slit, 140 μm.

```
α = 37; (* input the angle of α (degree) *)
λl = 514.5 * 10^-7; (* input the wavelength of laser (cm) *)
G = 24000; (* input the groove number of grating (cm^-1) *)
ws = 0 * 10^-4; (* input the width of slit (cm) *)
f = 25; (* input the focal length (cm) *)
m = 25 / 14; (* input the system magnification *)
a = 100; (* input DACF *)
ωrs = 1332.4; (* input diamond Raman band *)
ωl = 1 / λl;
d = 1 / G;
Δωs = N[(ωl - ωrs)^2 * (m * ((ws)^2 + (a * 1/(ωl - ωrs))^2)^0.5) / (G * f) * Cos[ArcSin[G / (2 * (ωl - ωrs) * Cos[α/2 * π/180])] + α/2 * π/180]]
```

```
2.45924
```

(2) Excitation wavelength, 257.3 nm; Broad opening width of the entrance slit, 140 μm.

```
α = 37; (* input the angle of α (degree) *)
λl = 257.3 * 10^-7; (* input the wavelength of laser (cm) *)
G = 36000; (* input the groove number of grating (cm^-1) *)
ws = 200 * 10^-4; (* input the width of slit (cm) *)
f = 25; (* input the focal length (cm) *)
m = 25 / 15.5; (* input the system magnification *)
a = 100; (* input DACF *)
ωrs = 1332.4; (* input diamond Raman band *)
ωl = 1 / λl;
d = 1 / G;
Δωs = N[(ωl - ωrs)^2 * (m * ((ws)^2 + (a * 1/(ωl - ωrs))^2)^0.5) / (G * f) * Cos[ArcSin[G / (2 * (ωl - ωrs) * Cos[α/2 * π/180])] + α/2 * π/180]]
```

```
33.4991
```

Appendix 7:

Mathematica program for plotting the curves of the spectral resolution vs. Raman shift.

```
α = 37; (* input the angle of α (degree) *)
λ1 = 514.67417; (* input the wavelength of visible laser (nm) *)
λ2 = 257.33709; (* input the wavelength of UV laser (nm) *)
G1 = 2400; (* input the groove number of grating (nm^-1) for 514.5 nm laser *)
G2 = 3600; (* input the groove number of grating (nm^-1) for 257.3 nm laser *)
ws = 140; (* input the width of slit (um) *)
ws1 = 60; (* input the width of slit (um) for 514.5 nm *)
ws2 = 30; (* input the width of slit (um) for 257.3 nm *)
f = 25; (* input the focal length (cm) *)
m1 = 25 / 14; (* input the system magnification for 514.5 nm *)
m2 = 25 / 15.5; (* input the system magnification for 257.3 nm *)
ad = 0; (* input the compesation of aberration *)
ad1 = 100; (* input the compesation of aberration 514.5 nm *)
ad2 = 110; (* input the compesation of aberration 257.3 nm *)
ω01 = 500;
ω02 = 1500;
ω03 = 2500;
ω04 = 3500;
ω05 = 750;
ω06 = 2250;
ω07 = 3750;

ωl1 = 1 / λ1 * 10^7;
ωl2 = 1 / λ2 * 10^7;

Δωs10 = N[(ωl1 - ωrs)^2 * (0.1 * m1 * ((ws)^2 + (λ1 * 10^-3 * ad)^2)^0.5 * 10^-4) / (G1 * f) * Cos[ArcSin[G1 / (0.2 * (ωl1 - ωrs) * Cos[α/2 * π/180])] + α/2 * π/180]];
Δωs20 = N[(ωl2 - ωrs)^2 * (0.1 * m2 * ((ws)^2 + (λ2 * 10^-3 * ad)^2)^0.5 * 10^-4) / (G2 * f) * Cos[ArcSin[G2 / (0.2 * (ωl2 - ωrs) * Cos[α/2 * π/180])] + α/2 * π/180]];
Δωs1 = N[(ωl1 - ωrs)^2 * (0.1 * m1 * ((ws1)^2 + (λ1 * 10^-3 * ad1)^2)^0.5 * 10^-4) / (G1 * f) * Cos[ArcSin[G1 / (0.2 * (ωl1 - ωrs) * Cos[α/2 * π/180])] + α/2 * π/180]];
Δωs11 = N[(ωl1 - ωrs)^2 * (0.1 * m1 * ((ws1)^2 + (λ1 * 10^-3 * ad1)^2)^0.5 * 10^-4) / (G1 * f) * Cos[ArcSin[10 * G1 / (ωl1 - ωrs) - Sin[ArcSin[G1 / (0.2 * (ωl1 - ω01) * Cos[α/2 * π/180])] - α/2 * π/180]]];
Δωs12 = N[(ωl1 - ωrs)^2 * (0.1 * m1 * ((ws1)^2 + (λ1 * 10^-3 * ad1)^2)^0.5 * 10^-4) / (G1 * f) * Cos[ArcSin[10 * G1 / (ωl1 - ωrs) - Sin[ArcSin[G1 / (0.2 * (ωl1 - ω02) * Cos[α/2 * π/180])] - α/2 * π/180]]];
Δωs13 = N[(ωl1 - ωrs)^2 * (0.1 * m1 * ((ws1)^2 + (λ1 * 10^-3 * ad1)^2)^0.5 * 10^-4) / (G1 * f) * Cos[ArcSin[10 * G1 / (ωl1 - ωrs) - Sin[ArcSin[G1 / (0.2 * (ωl1 - ω03) * Cos[α/2 * π/180])] - α/2 * π/180]]];
Δωs14 = N[(ωl1 - ωrs)^2 * (0.1 * m1 * ((ws1)^2 + (λ1 * 10^-3 * ad1)^2)^0.5 * 10^-4) / (G1 * f) * Cos[ArcSin[10 * G1 / (ωl1 - ωrs) - Sin[ArcSin[G1 / (0.2 * (ωl1 - ω04) * Cos[α/2 * π/180])] - α/2 * π/180]]];
Δωs2 = N[(ωl2 - ωrs)^2 * (0.1 * m2 * ((ws2)^2 + (λ2 * 10^-3 * ad2)^2)^0.5 * 10^-4) / (G2 * f) * Cos[ArcSin[G2 / (0.2 * (ωl2 - ωrs) * Cos[α/2 * π/180])] + α/2 * π/180]];
Δωs21 = N[(ωl2 - ωrs)^2 * (0.1 * m2 * ((ws2)^2 + (λ2 * 10^-3 * ad2)^2)^0.5 * 10^-4) / (G2 * f) * Cos[ArcSin[10 * G2 / (ωl2 - ωrs) - Sin[ArcSin[G2 / (0.2 * (ωl2 - ω05) * Cos[α/2 * π/180])] - α/2 * π/180]]];
Δωs22 = N[(ωl2 - ωrs)^2 * (0.1 * m2 * ((ws2)^2 + (λ2 * 10^-3 * ad2)^2)^0.5 * 10^-4) / (G2 * f) * Cos[ArcSin[10 * G2 / (ωl2 - ωrs) - Sin[ArcSin[G2 / (0.2 * (ωl2 - ω06) * Cos[α/2 * π/180])] - α/2 * π/180]]];
Δωs23 = N[(ωl2 - ωrs)^2 * (0.1 * m2 * ((ws2)^2 + (λ2 * 10^-3 * ad2)^2)^0.5 * 10^-4) / (G2 * f) * Cos[ArcSin[10 * G2 / (ωl2 - ωrs) - Sin[ArcSin[G2 / (0.2 * (ωl2 - ω07) * Cos[α/2 * π/180])] - α/2 * π/180]]];

Plot[{Δωs1, Δωs2, Δωs11, Δωs12, Δωs13, Δωs14, Δωs21, Δωs22, Δωs23}, {ωrs, 0, 4000}, PlotRange → {{0, 4000}, {0, 8}},
 PlotStyle → {{Thickness[0.004], RGBColor[0, 1, 0]}, {Thickness[0.004], RGBColor[0.6, 0, 1]}, {Thickness[0.001], RGBColor[0, 0, 0]},
   {Thickness[0.001], RGBColor[0, 0, 0]}, {Thickness[0.001], RGBColor[0, 0, 0]}, {Thickness[0.001], RGBColor[0, 0, 0]},
   {Thickness[0.001], RGBColor[0, 0, 0]}, {Thickness[0.001], RGBColor[0, 0, 0]}, {Thickness[0.001], RGBColor[0, 0, 0]}}, PlotRange → All,
 TextStyle -> {FontFamily -> "Radius", FontSize → 18}, Frame → True, FrameLabel → {"Raman Shift (cm^-1)", "Spectral Resolution (cm^-1)"},
 PlotPoints → 40000]
```

Appendix 8:

Laser Safety

In our laboratory, we have three lasers:

1. A diode laser, external-cavity *grating-stabilized. (*Model : Startbright 785-S)
   Manufacturer*: Torsana Laser Technologies, A/S, DK.*
2. A Nd:YVO_4 solid-state laser, intra-cavity frequency doubled. (Model: Millennia IIS)
   Manufacturer*: Spectra-Physics Lasers, Inc., USA.*
3. Ar-ion laser with Intra-cavity frequency doubling. (Model: Lexel 95-SHG-QS)
   Manufacturer*: Cambridge Laser* Laboratories*, Inc., USA.*

The various emission wavelengths and corresponding powers are shown in Table A8.1. According to the IEC (International Electrotechnical Commission) laser safety standard sheet IEC 60825-1 [A8.1], these three lasers all are classified as Class 4 (so-called high-power) lasers that are hazardous to human eyes under any condition (directly or diffusely scattered) and these lasers are presenting potential skin hazards.

The various wavelengths have different biological effects that cause various injuries. With respect to the skin damage, the UV light can cause erythema, pigment darkening and skin cancer [A8.2], [A8.3]. However, too much near infrared light (e. g. 785 nm) just cause skin burn. With respect to injury of the eyes, the situation is more complicated. The major danger of laser radiation is from beams entering the eye. There are five kinds of known eye injuries (photokeratitis, cataract, aqueous flare, retinal burn and corneal burn) which are caused by radiation with various wavelengths of laser light [A8.2], [A8.3]. In order to evaluate the hazards and achieve effective protection, it is necessary to know the mechanism of injury and the damage thresholds.

The power density will depend very much on how much the laser beam is focused, diverged or diffused. Although a focused beam has a very high power density, it has a quite small chance of entering into the eye. On the other hand there is a likely risk that the direct laser beam or the diffused laser beam may irradiate our skin and even our eyes during the normal operation. In order to evaluate the hazards in this connection we need to estimate the risks. In turn we need to consider the power density of the lasers.

We can reasonably assume that the radius of the direct beam is 1 mm. Then we use the below equation to estimate the power density:

$$\Phi_{\mathrm{d}} = \frac{\mathrm{Power}}{\pi \cdot r^2}$$

Here ϕ_d is the power density of the direct beam, and *r* is the radius of beam. The power densities of our lasers are shown on the Table A8.1.

Table A8.1: The various emission wavelengths and the corresponding power of our lasers, the skin hazards caused by these wavelengths and their damage thresholds (assuming one second of maximum exposure) [A8.2], [A8.3].

Laser	**Wavelength (nm)**	**Power (mW)** (*full power*)	**Power density (W/cm^2)** (*For beam radius=1 mm*)	**Effect on skin & the Damage Thresholds (W/cm^2)**	**Effect on the eyes & the Damage Thresholds (W/cm^2)**
Startbright 785-S	785.0	500	15.9	Skin burn; **28**	Cataract, Retinal burn; **5×10^{-3}**
Millennia IIS	532.0	4000	127.4	Skin burn, Pigment darkening; **4**	Retinal burn; **10×10^{-3}**
95-SHG-QS	514.5	2500	79.6		
	496.5	900	28.7		
	488.0	2100	66.9		
	476.5	870	27.7		
	457.9	420	13.4		
	257.3	213	6.8	Erthema, Skin cancer; **3×10^{-3}**	Photokeratitis; **10×10^{-3}**
	244.0	100	3.2		
	229.0	10	0.32		

Injuries of the Skin.

The layers of the skin that are of concern in a discussion of laser hazards are the epidermis and the dermis. The epidermis layer lies beneath the corneum (that is made of dead, flat skin cells) and is the outermost living layer of the skin. The dermis mostly consists of connective tissue and lies beneath the epidermis. Fig. A8.1 shows the typical three uppermost layers of the skin. The depths of penetration into the skin depend much on the wavelengths. The near infrared light has the maximum depth of penetration. In the range of UV radiation, most of the radiation is absorbed by the outer dead layer of the skin. Even so, the damage threshold for the DUV light is still much smaller than for the visible light, as shown in Table A8.1. This is so, because DUV is highly injuring to the skin by damaging the DNA material in the living cells.

By comparing with the damage threshold and the power density of our laser lines (in Table A8.1), it is clear that all of the laser beams are harmful to the skin. Especially, the power density of the 257.3 nm DUV laser line is two thousand times higher than the damage threshold.

Unlike UVA (400 – 315 nm) or UVB (315 – 280 nm), DUV may be seen as an unnatural kind of light because the aerosphere blocks all of the DUV light from sun. The injury of long term exposure to DUV radiation is still lacking investigation. Therefore, one should avoid the exposure to the DUV radiation as much as possible.

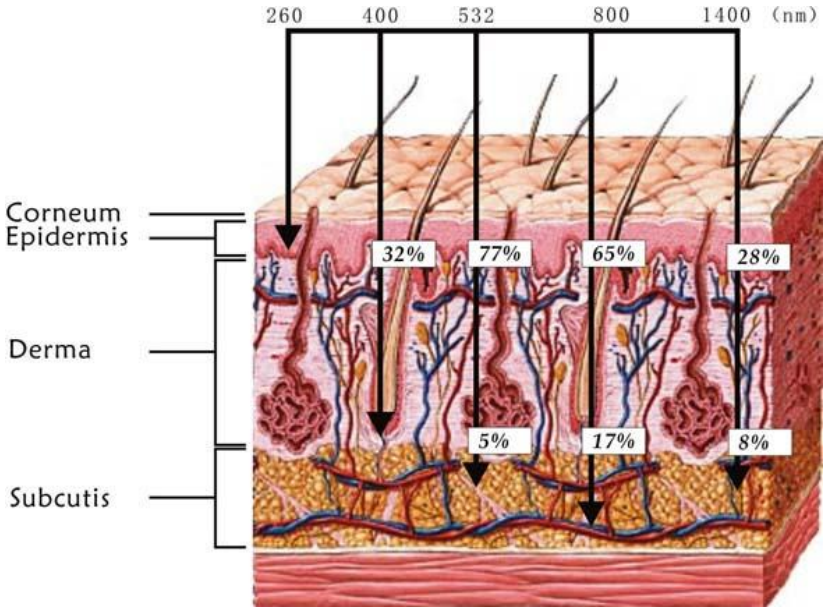

Fig. A8.1: The penetration of various wavelengths to the skin. [A8.3]

Injuries of the Eyes.

Laser radiation injury to the eye is considered more serious than injuries to the skin, since functional loss of an eye is more debilitating than damage to the skin. The eye is the organ most sensitive to light. A laser beam with low divergence entering into the eye - in the worst case - can be focused down to a spot of 10 to 20 µm in diameter on the retina. Thus, even a low-power laser (in the milliWatt range) can cause retina burn.

Example: A 5 mW visible laser beam focused to 100 µm^2 corresponds to

$$\frac{5\ mW}{100\ \mu m^2} = 50000\ \frac{W}{cm^2}$$

In Table A8.1 one sees that this value dramatically exceeds the threshold of retina damage. However, not all kinds of radiation can reach retina. As shown in the Fig. A8.2, almost all of the DUV light is absorbed by the cornea, so overexposure to the UVC and UVB radiation causes *photokeratitis*. Photokeratitis, also called snowblindness, is a burn of the cornea by UV rays. In the range of UVA the principal absorber is the lens, so an overexposure to the UVA radiation causes *cataract*. Cataract is a clouding that develops in the crystalline lens of the eye or in its envelope. A cataract state can also be caused by overexposure of infrared light.

The eye damage thresholds of various wavelengths all are very low, as shown in Table A8.1. We can see that the eye damage threshold of the DUV light is same as for the different kinds of visible light. Comparing the damage thresholds, the eye threshold is even higher than the skin threshold when the wavelength is in the range of DUV. The reason for this might be that the corneal tissues regenerate very quickly, in less than 24 hours.

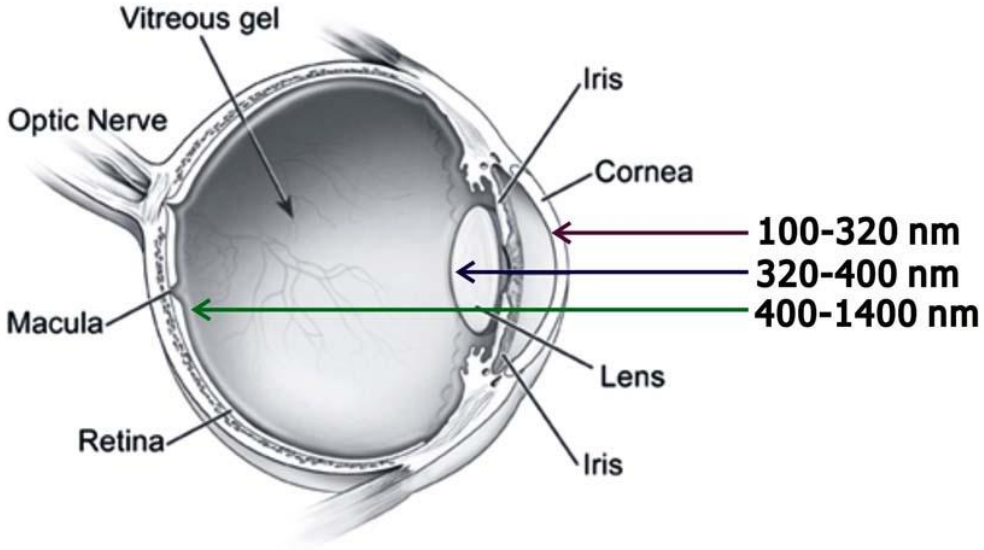

Fig. A8.2: The penetration of various wavelengths into the eye.

The methods of protection

- **Warning signs and Labels**

As mentioned above all direct beams of our lasers are dangerous to the skin and the eyes. The laser entrance and the path of laser beam should therefore be noticed by a warning sign or label. This is especially important for invisible laser beams, such as the DUV radiations.

- **Beam blocks and Dumps**

Beam blocks, backstops, traps, dumps, and stops provide means to terminate unneeded laser energy and to keep beams confined to a particular area, such as the optical table. The beam blocks should preferably be made from aluminium or brass with a rough and blackened surface. Here we introduce a simple and functional beam stop, a reversed J-shaped tube (as shown in Fig. A8.3). Such a simple devise will effectively

trap the laser beam and minimize the diffusive light. It is well suited to stop a harmful DUV laser beam. It also works for the strong visible laser beam.

Fig. A8.3: A simple and functional laser beam stop.

- **Protective Eyewear**

Eyewear is the most important method to protect the eyes in the laboratory. Commercial safety eyewears (laser goggles) are made by treated plastic absorbing particular ranges of the wavelength. In order to make sure that the right eyewear is chosen every time, it is necessary to put a descriptive label on each eyewear. We have chosen laser safety glasses LG3 and LG4 (produced by Thorlabs) which block the light in the range of 190 – 532 nm and 625 – 850 nm, respectively. Therefore, LG3 is suitable for eye protection from the 95-SHG-QS and Millennia IIS lasers, and LG4 is suitable for eye protection from the Starbright 785-S laser.

[A8.1] *Safety of laser products - Part 1: Equipment classification and requirements* (2nd ed.). International Electrotechnical Commission. **2007**.
[A8.2] D.C.Winburn, *Practical laser safety*, Dekker, New York, (**1985**), pp.20-28.
[A8.3] Ken Barat, *Laser safety management*, Taylor & Francis, New York, (**2005**), pp.19-23.

Appendix 9:

Experimental and *ab initio* DFT calculated Raman Spectrum of Sudan I, a Red Dye

Research Article

Journal of RAMAN SPECTROSCOPY

Received: 15 October 2010 Accepted: 23 November 2010 Published online in Wiley Online Library: 23 February 2011

(wileyonlinelibrary.com) DOI 10.1002/jrs.2876

Experimental and *ab initio* DFT calculated Raman spectrum of Sudan I, a red dye

Andreas J. Kunov-Kruse,[a] Steffen B. Kristensen,[a] Chuan Liu[b] and Rolf W. Berg[b]*

The red dye Sudan I was investigated by Raman spectroscopy using different excitation wavelengths (1064, 532 and 244 nm). A calculation of the Raman spectrum based on quantum mechanical *ab initio* density functional theory (DFT) was made using the RB3LYP method with the 3-21G and 6-311+G(d,p) basis sets. The vibrations in the region 1600–1000 cm^{-1} were found to comprise various mixed modes including in-plane stretching and bending of various C–C, N–N, C–N and C–O bonds and angles in the molecule. Below ~900 cm^{-1}, the out-of-plane bending modes were dominant. The central hydrazo chromophore of the Sudan I molecule was involved in the majority of the vibrations through N=N and C–N stretching and various bending modes. Low-intensity bands in the lower wavenumber range (at about 721, 616, 463 and 218 cm^{-1}) were selectively enhanced by the resonance Raman effect when using the 532 nm excitation line. Comparison was made with other azo dyes in the literature on natural, abundant plant pigments. The results show that there is a possibility in foodstuff analysis to distinguish Sudan I from other dyes by using Raman spectroscopy with more than one laser wavelength for resonance enhancement of the different bands

Keywords: azo dye; DFT calculation; Sudan I; resonance enhancement

Introduction

In recent years, public attention has been drawn to a group of red and orange azo dyes comprising Sudan I, II, III and IV. Several European control authorities have discovered the presence of these cheap dyes in a series of imported food items.[1] Especially, Sudan I (Fig. 1) is considered to be toxic, and it has been proven by *in vitro*[2,3] and *in vivo* studies that it is carcinogenic to rats, which are known to have a metabolic system very similar to that of humans. Therefore, Sudan I could be carcinogenic to humans as well.[2–4] A series of detection methods have been developed, most of them based on liquid chromatography.[1,5–7] The recently applied methods for Sudan I give detection limits on the order of around 0.5 ppm.[2] No known threshold limit seems to exist with respect to long-term health risks, and therefore there is a need for further development of the detection methods.

Raman spectroscopy can offer a novel and fast method for *in situ* and on-location detection of Sudan dyes during food control. The detection of Sudan I by surface-enhanced Raman scattering (SERS) spectroscopy and surface-enhanced resonance Raman scattering (SERRS) spectroscopy can offer very accurate analysis methods with detection limits below 0.20 ppm.[8] Although the methods have been demonstrated, the extent of scientific literature on the Raman spectra of Sudan dyes is very limited, with very few articles having been published so far. Thus until recently, only SERS spectra of Sudan II and IV were reported,[9,10] with only two articles dealing with spectra of Sudan I: the first one[11] by using a range of excitation lines, with respect to resonance Raman (RR), SERS and SERRS, as well as a calculated spectrum by the use of low-level PM3 semiempirical methods; and the second one[12] using a portable spectrometer with SERS and multivariate chemometrics to obtain quantitative analysis down to 10^{-4} mol l^{-1}.

A deeper understanding of the chemistry and structure of these planar molecules is needed to develop a Raman-based precise method that will be able to distinguish the Sudan molecules from other azo dyes. The current problem of distinguishing Sudan I from naturally abundant carotenoids – especially capsanthin – is difficult because of the almost identical absorption maxima,[2,13] and this will be treated in the present article.

In the following, first, new and better *ab initio* DFT calculations are presented. Then the experimental Raman spectra of Sudan I with different excitation wavelengths are given, followed by an attempt to correlate the experimental vibrational peaks in the Raman spectrum to the results of the DFT calculations in order to understand the nature of the vibrations in the Sudan I molecule. Finally, we will make some general conclusions about the characteristic vibrations in the Sudan group of molecules, based on the measured spectra, in comparison with the calculations and spectra from the literature.

Structure of Sudan I

The structure of azo dyes has been intensely discussed in the chemical literature. The azo dyes formally contain the azo group –N=N–, but are in most cases partly or completely transformed into the tautomeric hydrazo form (Scheme 1). Initially our geometry optimizations were done on both forms. However,

* *Correspondence to: Rolf W. Berg, Department of Chemistry, Technical University of Denmark, Kemitorvet, Building 207, DK-2800 Kgs. Lyngby, Denmark. E-mail: rwb@kemi.dtu.dk*

a *Center for Catalytic and Sustainable Chemistry; Department of Chemistry, Technical University of Denmark, Kemitorvet, DK-2800 Kgs. Lyngby, Denmark*

b *Department of Chemistry, Technical University of Denmark, Kemitorvet, Building 207, DK-2800 Kgs. Lyngby, Denmark*

Journal of RAMAN SPECTROSCOPY

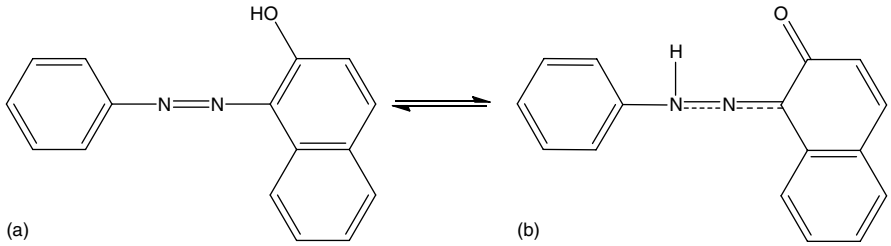

Scheme 1. The tautomeric inversion of Sudan I: (a) the azo form and (b) the hydrazo form. The equilibrium is shifted far to the right.

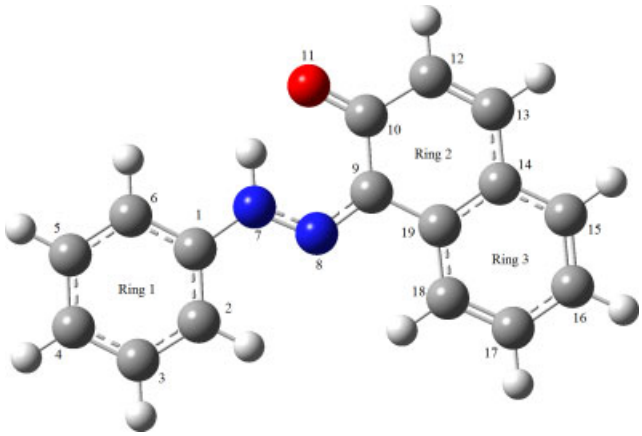

Figure 1. The optimized structure of Sudan I. C: carbon, N: nitrogen and O: oxygen. The numbers 1–19 refer to the numbering of C, N and O atoms in the molecule. The same numbering also refers to the H atoms adjacent to the C, N and O atoms.

the azo forms gave poor resemblance to the experimental spectrum irrespective of whether the H atom on O was pointing away from or toward the nearest N (giving minimum energies of −801.8223 or −801.8449 a.u. and dipole moments of 1.7653 or 1.0586 debye, respectively). In contrast to this, the calculated spectrum for the hydrazo form showed good resemblance to the experimental spectrum (giving a lower minimum energy of −801.8470 a.u. and a dipole moment of 1.6966 debye). These observations are supported by results in the literature,[11] in which Sudan I was found to be exclusively in the hydrazo form. Therefore, we only report our hydrazo results. The recently published work[12] on SERS analysis of Sudan I, unfortunately, does not mention the hydrazo form and the results were discussed as if Sudan I was in the azo form.

Experimental

Sudan I ($C_{16}H_{12}N_2O$, 1-(2-phenyldiazenyl)-2-naphthalenol, CAS Reg. no. 842-07-9) in pure powder form, obtained from Aldrich, was used without further purification in all experiments. Extra virgin olive oil (low acidic, from Italy) and dichloromethane (CH_2Cl_2, CAS Reg. no. 75-09-2) in pure state (Merck, Pro Analysi grade) were used as solvents to dissolve Sudan I. The solutions (nearly saturated) were made to avoid melting and decomposition of the red dye sample during illumination due to its strong absorption of green and blue light.[1] A DILOR-XY (Horiba-JY) Raman spectrometer was used in the visible range by applying a few milliwatts of radiation at 532 nm (from a Nd : YVO_4 laser equipped with a frequency-doubling device based on crystalline LiB_3O_5). A beam-splitter-coupled optical microscope was used to focus the laser beam onto the sample and to collect the light. The Rayleigh scattered light was filtered off by using a notch filter, and the remaining scattered light was dispersed by a 1800 g mm^{-1} grating and collected on a charge-coupled device (CCD) cooled to 140 K with liquid nitrogen. The broad background due to, e.g. fluorescence was stepwise fitted with second- or third-order polynomials and subtracted from each frame before merging to obtain the spectrum. Calibration was done using the Raman lines of cyclohexane. Both the solvent and the saturated solution were measured as drops on an aluminum foil or (for CH_2Cl_2) inside thin-walled quartz capillaries to avoid decomosition. The UV excitation was obtained with a frequency-doubled Ar^+ LEXEL gas laser working at 488 nm to obtain up to 100 mW of 244 nm radiation. The UV-excited spectra (resolution ~8 cm^{-1}) were recorded with a Renishaw InVia Raman microscopy spectrometer with UV optics, high bandpass filters and an UV-enhanced CCD detector cooled to low temperatures. The measurements were repeated in the infrared range on a Bruker-IFS66 FRA-106 Fourier transform Raman spectrometer by using about 100 mW of Nd : YAG IR laser light at 1064 nm. Two hundred scans were recorded and averaged for each spectrum. Further details on the used Raman spectrometers are described elsewhere.[14–17]

Computations

The optimization of the structure and the calculation of spectra were performed with the Gaussian 03 W software package.[18] The structure of the Sudan I molecule and its vibrations (in both its azo and hydrazo forms) were obtained in three subsequent calculations, in order to determine the global minimum in an efficient way. Initially, each geometry was roughly optimized using the semiempirical PM3 type procedure, followed by the *ab initio* Hartree–Fock/DFT method with third order restricted Becke–Lee–Yang–Parr procedure (RB3LYP), first with the 3-21G basis sets and then using 6-311+G(d,p) basis sets to calculate the structure and vibrational spectra. The scaling factor was chosen to be 0.976 on the basis of results from Ref. [19], where a number of calculated and experimental spectra of C-, H-, N- and O-containing compounds were compared using several basis sets to find the best scaling factor.

Results and Discussion

The obtained Raman data can be seen in Fig. 2, showing the spectra of the pure solvents, olive oil (a) and dichloromethane (c) and (e), of Sudan I dissolved in these solvents (b), (d) and (f), and of the pure Sudan I (g), under different kinds of laser excitation, together with the calculated Raman spectrum. The spectra of

dichloromethane were in accordance with those reported in the literature.[20] A summary of the measured and calculated spectra is shown in Table 1, as well as the approximate assignments of the vibrational modes, derived from the calculations and read off a computer screen by the use of the GaussView G03W program.[18]

The spectrum of the Sudan I dissolved in the solvents olive oil (Fig. 2(b)) or in CH_2Cl_2 (Fig. 2(d) and (f)), showed practically no characteristic bands due to the solvents, even though these solvents have very strong bands (Fig. 2(a),(c) and (g)). The reason must be that Sudan I, as a solute, gives a very strong spectrum. Most probably, this is due to RR enhancement effects, which are different for green (b) and (d) and UV excitation (f). The spectra obtained with green excitation resemble the FT-Raman spectrum of pure solid Sudan I obtained with infrared excitation (Fig. 2(g)). The intensities of the peaks in the spectra (b) and (d) obtained with green light were very similar, except in the region below 900 cm^{-1} where some of the bands of dissolved Sudan I appeared stronger. In the spectrum obtained with the UV light, the bands around 1600 cm^{-1} are very strongly and selectively enhanced, whereas the other bands are not seen. One might suspect that Sudan I could be sensitive to photolysis during UV illumination, but this does not seem to be the case, judging from the spectrum of the solid. The observed spectrum, as shown in Fig. 3(a), appeared stable and had bands resembling those from the infrared experiment (b) and the calculated spectrum (c).

Assignment of Vibrational Modes

The C–H/N–H stretching transitions appear weakly in both experimental and theoretical spectra. Two very weak bands at 3067 and 3039 cm^{-1} and a shoulder at 3059 cm^{-1} are present, corresponding to C–H and N–H stretchings, correlating to modes 87–76 in Table 1.

A very strong band is present at 1596 cm^{-1} (with several weaker shoulders), very close to the predicted position. This band is assigned to mainly aromatic C–C stretching in the phenyl ring, in accordance with other studies of azo dyes,[21,22] but C–H as well as N–H in-plane bendings also contribute significantly to the mode. A band of medium intensity at 1546 cm^{-1} could be described by mode 69 and 70 transitions, both of which comprise H–N═N bending, C═C strethcing and C═O stretching. For both modes, a strong contribution from N–H in-plane bending seems probable. A strong band at 1494 cm^{-1} and a shoulder at 1481 cm^{-1} probably correspond to modes 68 and 67, respectively, composed of mainly C═C stretching and C–H in-plane bendings. C═O and N═C stretchings are also contributing to mode 67, which is observed as a shoulder. A band at 1448 cm^{-1} of weak to medium intensity is accurately predicted by mode 65, comprising mainly in-plane C–H bending and C═C stretching in the naphtalene unit, as well as in-plane bending of the N–H bond. A very strong peak is located at 1388 cm^{-1} with a significant shoulder at 1410 cm^{-1} and a poorly resolved shoulder at around 1370 cm^{-1}. These features could be explained by modes 63 and 64, which are rather complex and share similarities such as strong C–N stretching and C–H and N–H in-plane bendings as well as some C═C strecthing. Significant N═N stretching and some C═O stretching are also contributing to mode 63. The band of medium intensity at 1340 cm^{-1} with a shoulder at 1333 cm^{-1} would correspond to modes 61 and 60, respectively. Mode 61 consists of C═C stretching and in-plane C–H bending in the naphtalene unit and stretching of the C9–N bond. Mode 60 resembles mode 61, but the phenyl unit is more active in the vibration with respect to C═C stretching and C–H bending, and with pronounced stretching of the N═N bond.

The rest of the region down to around 1018 cm^{-1} is very complex, and the spectrum consists of several bands, some of them strong but most of them showing rather low Raman intensity and appearing only as shoulders or weak bands. At least 13 features in this region could be identified, but judging from the asymmetrical shape of several of these bands, it seems that there are even more features hidden underneath some of the more intense bands. The complexity of the experimental spectrum is in accordance with the calculated spectrum of this region, in which 14 different modes are predicted, most of them of extensively mixed origin. The modes 59 and 58, for example, comprise extensively coupled N═N, C═O, C═C stretchings and in-plane C–H and N–H bendings. In the middle part of the region (for modes 57–53) the amount of C–C stretching is gradually descreasing, whereas the amount of C–C–C angle deformations are increasing the lower the wavenumber region. The C–C stretchings still participate and N–C stretchings also contribute to many of the modes. For the lower wavenumber modes in this region, above 1000 cm^{-1}, the C–C stretchings are taking part actively, but now participating in the ring breathings, resulting in asymmetrical deformations of the aromatic rings.

A doublet of medium intensity is found with peaks at 1001 and 984 cm^{-1}, and these bands are predicted very accurately by modes 45 and 43. Both modes include breathing and deformations. Especially, mode 45 could be described by a triangular ring breathing movement. The mode mainly involves three carbon atoms out of the six-membered ring performing a symmetrical breathing-like deformation, resulting in the ring approaching a triangular shape (Fig. 4, mode 45). In this mode, the phenyl ring and ring 3 of the naphtalene unit are both performing triangular breathing, but are out of phase with each other, thereby cancelling out some of the large change of polarizabillity (and intensity) often seen for aromatic breathing modes. Mode 43 comprises conventional breathing of the phenyl ring and triangular breathing of the naphthalene ring 3, as well as C–N═N and N–H in-plane bendings, resulting in a medium intensity band.

The region below 980 cm^{-1} contains serveral weak bands. In general, these are quite accurately predicted in the calculated spectrum with respect to band positions and relative intensities. Many of the modes have been excluded from Table 1 in this region. They generally comprise out-of-plane and in-plane C–C–C, C–H, N–H and C–C–N angle deformations. The Raman active modes are mostly very weak, involving many of the atoms in the molecule in unique movements, typically compressing or elongating parts of the molecule in one direction as well as rotations involving also larger parts of the molecule. However, some of the modes deserve attention, especially the four observed bands at around 721, 616, 463 and 218 cm^{-1}, which are interesting because they may have analytical applications. This is so because their intensities seem to be selectively enhanced by the green laser (Fig. 2 bottom right). Looking at the corresponding modes in the calculation (Table 1), it appears that they all involve displacements around the chromophoric azo group, suggesting strongly that the intensity enhancement is caused by the RR phenomenon related to electronic absorption in the hydrazo group.

To conclude, the calculated spectrum overall fits the experimental results quite well. The calculations suggest that the nature of the bands at around 1600–1500 cm^{-1} are rather complex but have been oversimplified in previous studies. In accordance with these previous studies, we also assign many of these vibra-

Table 1. Experimental Raman spectrum (cm^{-1}) compared to the calculated modes of the Sudan I in the hydrazo form

Mode no.	Experimental[a] cm^{-1}	Intensity	Calculated[b] cm^{-1}	Intensity $Å^2$/amu	Assignments[c]
87			3139	35	C–H stretch (ph)
86			3132	55	C–H stretch (naph)
85	3067	vw	3118	380	C–H stretch (ph)
84			3117	209	C–H stretch (naph)
83			3112	306	C–H stretch (naph)
82	3059	sh	3106	157	C–H stretch (ph) + N–H stretch
81			3105	747	N–H stretch
80			3097	110	C–H stretch (ph)
79	3039	vw	3096	133	C–H stretch (naph)
78			3091	17	C–H stretch (ph)
77			3087	90	C–H stretch (naph)
76			3079	64	C–H stretch (naph)
75	1616	sh	1621	60	C=O + C=C stretch (naph ring 2) + N–H bend
74	1600	sh	1606	101	C–H ip bend (naph) + C=C stretch (naph) + N–H bend + N=N/C–N stretch
73	1596	vs	1598	2378	C–H ip bend (ph) + C=C stretch (ph) + N–H bend + N=N/C–N stretch
72			1590	122	C1–N–H scis + C=C stretch (ph + naph) + C–H bend
71			1572	80	C1–N–H scis + C=O stretch + C=C stretch + C–H bend
70	1546	m	1545	164	C=C stretch (naph) + H–N=N bend + C=O stretch
69			1528	955	H–N=N bend + N=N stretch + N=C9 stretch + C=O stretch
68	1494	s	1488	723	C=C stretch (ph) + C–H ip bend (ph)
67	1481	sh	1475	104	C=C stretch (naph) + C=O stretch + N=H + C–H ip bend
65	1448	s	1444	181	C–H + N–H ip bend + asym C–C stretch (naph)
64	1410	sh	1397	337	C–N stretch (ph + naph) + N–H ip bend + C–H ip bend
63	1388	s	1391	750	C–N stretch (ph + naph) + C=O stretch + C–H ip bend
	1370	sh			
62	1340	m	1328	109	N=N + C=O stretch + C=C (ph) stretch/C–H ip bend (ph)
61	1333	sh	1321	273	C=C stretch (naph)/C–H ip bend (naph) + N–C9 stretch
60	1322	sh	1317	464	C=C–N bend (ph + naph) + N=N stretch + C=C stretch + ip N–H bend
59	1298	vw	1300	46	N=N + C=O + C=C stretch, ip N–H and C–H bend
58			1287	288	N=N stretch + N–H ip bend, N–H ip bend, C=O stretch
57	1257	m	1242	220	C9–C10–C12 stretch and bend + C–H ip. bend (naph)
56	1227	s	1228	1182	C–H + N–H ip bend + N–C1 stretch C=C stretch (naph)
55	1203	w	1205	70	C–H ip bend + C–N stretch + C=C stretch (naph)
54	1184	w/sh	1181	12	C–H + N–H ip bend + N–C1 stretch + C–C–C bend
53	1169	m	1161	403	C–H + N–H ip Bend N–C1 stretch + C–C–C bend
52	1151	w	1154	20	C–H ip bend and C–C–C bend
51	1140	sh.	1151	70	C–H + N–H ip bend and C–C bend
50	1118	Sh	1130	24	C–H ip bend and C–C–C bend (naph)
49	1095	w/m[d]	1093	60	ip C–C–C bend/stretch + C–H bend + C=N stretch

Table 1. (*continued*)

Mode no.	Experimental[a] cm^{-1}	Intensity	Calculated[b] cm^{-1}	Intensity $Å^2$/amu	Assignments[c]
48	1072	vw	1076	9	ip C–H bend + C–C–C bend + stretch
47	1038	vw	1035	38	C–H ip bend + asym breathing + C=C stretch (naph)
46	1018	vw	1018	14	asym breathing + C=C stretch (ph) + ip C–H bend (ph)
45	1001	m	988	167	triang breathing (ph) + N=N–C (naph) + N–H ip bend
43	984	m	980	202	N=N–C (naph) + H–N bend + breathing (ph) + (naph ring 3) breathing + C–C stretch (C9–C10)
34	846	vw	843	21	N–N–H bend + C–N=N (ph) bend + C–H ip bend
30	752	vw	750	6	C–H oop bend (ph)
28			744	20	C–N stretch (ph) + C=C bend (ph + naph) + C=C stretch (naph)
27	721[e]	vw/m[d]	718	59	breathing (naph) + C–C–N + N=N–C + C=C–C ip bend (ph)
	651	vw			
23	616[e]	vw/m[d]	616	14	C=C–C ip bend (ph) + C–C–N ip bend (ph + naph)
22	585	vw	583	57	C=C–C ip bend + ip N–N–C bend (ph + naph) + C=O ip bend
21	525	vw	540	4	C=C–C ip bend + ip N–N–C bend (ph + naph)
	501	vw			
16	463[e]	vw/m[d]	460	19	C=C–N ip bend + C=C–C ip bend + C–C=O ip bend
15			419	12	C=C–N ip bend + C=C–C ip bend (naph)
11	362	vw	361	22	N–C–C ip bend (ph + naph) out of phase
	310	vw			
7	218[e]	vw/m[d]	211	6	N–C–C ip bend (ph + naph) in phase
6	159	vw	179	3	C–C–H, C=C–C, N=N–C oop bend

Assignments (approximate descriptions of the modes) have been obtained from the calculated gas phase results [Gaussian/DFT/B3LYP/6-311+G(d,p)] observing the modes on a computer screen. Certain modes have been omitted to make the table shorter.
[a] The given measured wavenumbers were obtained on the Bruker FT-instrument.
[b] The calculated wavenumbers have been corrected with a factor of 0.976 according to Fairchild *et al.*[19]
[c] Stretch, stretching; bend, bending; ip, in-plane; oop, out-of-plane; asym, asymmetric; sym, symmetric; scis, scissoring; triang, triangular; ph: phenyl ring; naph, naphthyl ring.
[d] These bands were significantly enhanced when using the green laser.
[e] Analytically interesting bands, see text.

tions to modes with pronounced C–C stretching in phenyl and naphthalene rings.[11,22,23] However, our calculations show that other modes such as movements within the hydrazo group also contribute significantly. Our calculations also indicate that the hydrazo group is involved in most of the vibrations through N–H and C–N=N bendings and C–N stretchings. The hydrazo group also is the chromophore in the molecule, and therefore these features make the Sudan I molecule very suitable for RR spectroscopic investigations.

The intensities of the bands below 900 cm^{-1} seem to be quite sensitive to the laser wavelength and the sample environment. A similar effect was reported in Refs [9 and 10] concerning the spectra of the related azo dyes Sudan II and Sudan IV. Sudan II has the same structure as Sudan I, but with two methyl groups substituted on the phenyl ring in ortho and para positions. Sudan IV also has a methyl group on the phenyl ring in the ortho position, but has a further azo-toluene unit on the first phenyl ring in the para posistion. SERS spectra of Sudan II on various nanowire areas with IR excitation (1064 nm) have shown very similar trends, although they depend somewhat on the type of the metal substrate used.[9] Similarly, for Sudan IV the SERS spectrum below 1000 cm^{-1} has been recorded with IR excitation (1064 nm), showing several new features not seen in the regular Raman spectrum.[10]

Similarities between Azo Dyes

The Raman spectrum of Sudan I has striking similarities with the Raman spectra of other similar azo dyes. Because of their low toxicity, many sulfonated azo dyes are widely used in the food industry. The use of Raman spectroscopy for the detection of toxic azo dyes therefore demands a specific knowledge about other similar azo dyes. A typical example is Orange II, which is very similar to Sudan I, the only difference being a single SO_3Na group substituted in para position to the C–N group in the phenyl ring. The spectrum in the region from 1600 to

Journal of RAMAN SPECTROSCOPY

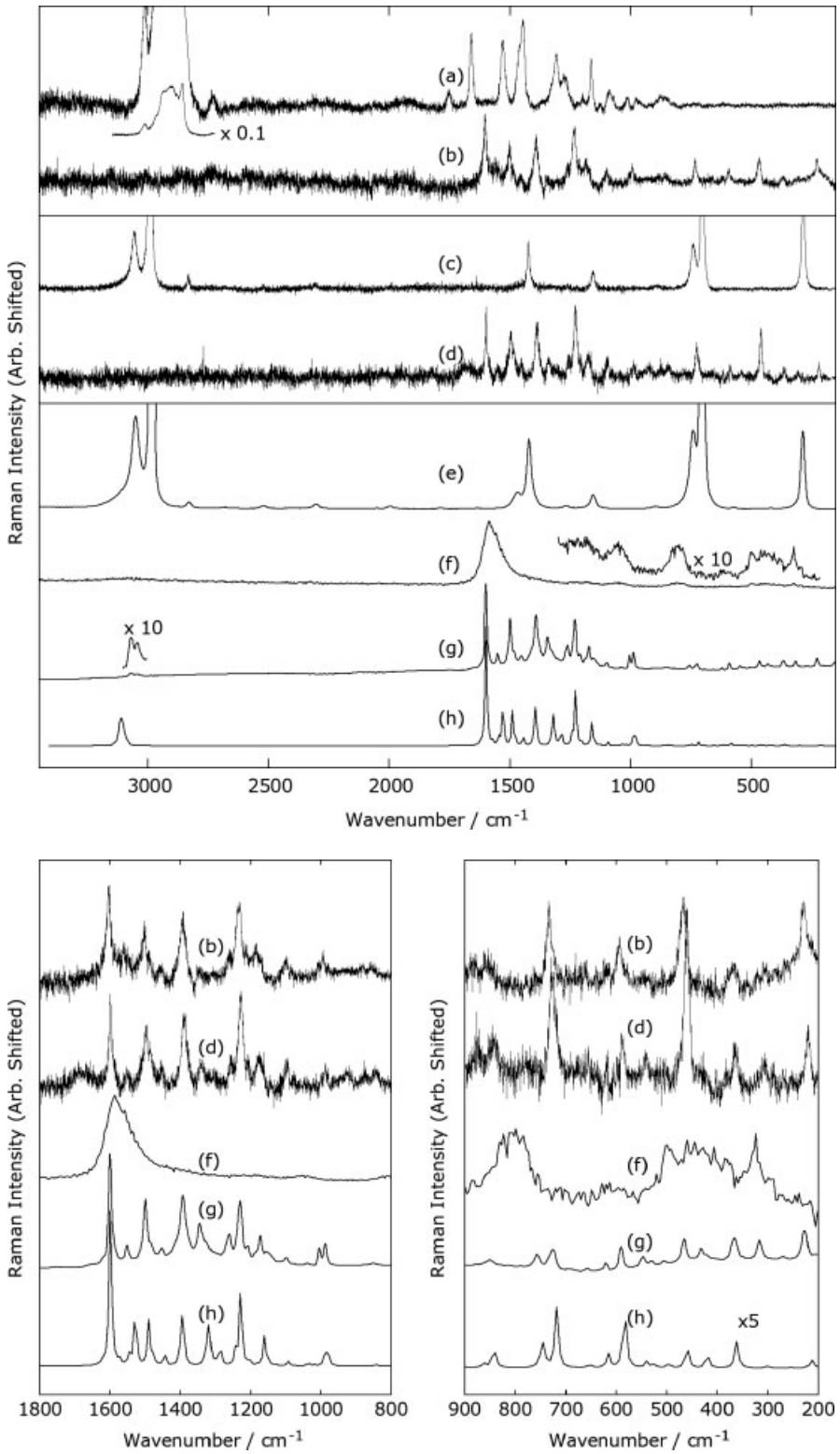

Figure 2. Raman spectra of (a) pure olive oil (excitation: green laser, 532 nm), (b) Sudan I in olive oil (nearly saturated. Excitation: green laser, 532 nm), (c) pure CH_2Cl_2 (excitation: green laser, 532 nm), (d) Sudan I in CH_2Cl_2 (excitation: green laser, 532 nm), (e) pure CH_2Cl_2 (excitation: UV laser, 244 nm), (f) Sudan I in CH_2Cl_2 (nearly satureted. Excitation: UV laser, 244 nm), (g) Sudan I powder (excitation: infrared laser, 1064 nm) and (h) calculated Raman spectrum, wavenumber corrected with a factor of 0.976. Top: Full spectra. Bottom left: Zoom of the region 1800–900 cm^{-1}. Bottom right: Zoom of the region 900–200 cm^{-1}. Note: In the top graph, the spectrum of the C–H stretching region of (a) is also shown, decreased by a factor of 0.1, and for spectra (f) and (g) selected parts are also shown, magnified by a factor of 10. The spectra have also been arbitrarily scaled and shifted. The band at 2331 cm^{-1} in (c) and (e) is due to N_2 gas.

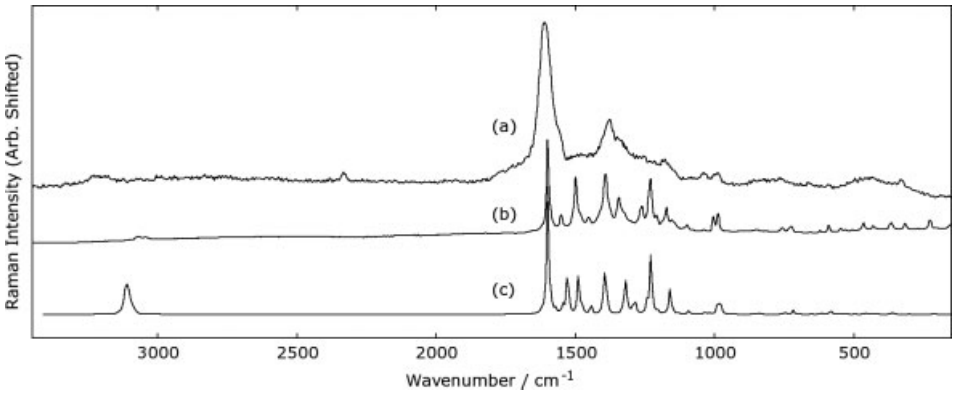

Figure 3. Raman spectra of solid Sudan I obtained with (a) 244 nm UV light and (b) 1064 nm IR light. Useful spectra could not be obtained with green or blue light. The calculated spectrum is shown as (c). The band at 2331 cm^{-1} in (a) is due to N_2 gas.

1300 cm^{-1} shows almost identical features. Below this region, the spectra look very similar, but larger deviations in the wavenumber shift values occur.[23] Also, the azo dye Amaranth (Azorubin S or tri-sodium (4*E*)-3-oxo-4-[(4-sulfonato-1-naphthyl)hydrazono]-naphthalene-2,7-di-sulfonate, CAS Reg. No. 915-67-3), previously much used in foodstuffs, can be described as a triple sulfonated double naphthyl analog of Sudan I. Although the spectra look very similar to that of Sudan I in the region 1600–1100 cm^{-1}, the values of the Raman shifts deviate sufficiently to distinguish them.[22]

The structure of the sulfonated yellow azo dye Tartrazine (1*H*-pyrazole-3-carboxylic acid, 4,5-dihydro-5-oxo-1(4-sulfophenyl)-4-[(4-sulfophenyl)azo] tri-sodium salt, CAS Reg. No. 1934-21-0) differs more from the structure[21] of Sudan I. Although the spectrum in the range 1600–1480 cm^{-1} shows very similar features, many wavenumber shift values deviate considerably. At lower wavenumbers, the spectra deviate more from each other, and below 1000 cm^{-1} the Raman active bands are entirely unique.

Natural abundant cartenoids give colors to biological materials such as plants, and are therefore present in most foodstuffs. Especially capsanthin [(all-*E*,3*R*,3′*S*,5′*R*)-3,3′-dihydroxy-β,κ-caroten-6′-one, CAS Reg. No. 465-42-9] and capsorubin [(all-*E*,3*S*,3′*S*,5*R*,5′*R*)-3,3′-dihydroxy-κ,κ-carotene-6,6′-dione, CAS Reg. No. 470-38-2], found in chili and paprika, makes it difficult to detect Sudan I in samples because they exhibit Raman and absorption maxima at similar wavenumbers as in Sudan I.[2,13] The Raman spectra of capsanthin and capsorubin were investigated by DFT calculations as well as experimentally by Requena *et al.*[24] Even though the structures are very different, many Raman bands for capsanthin and capsorubin are found at more or less the same positions[24] in the region from 1600 to 1100 cm^{-1}. The best way to distinguish these molecules by Raman spectroscopy is to take advantage of some very intense bands in the spectra of capsanthin and capsorubin at around 1100–900 cm^{-1}, where the spectrum of Sudan I only shows weaker features as well as the considerable contribution to the spectra from C–H stretching in the spectra of the cartenoids.

Resonance Raman Effects

Shadi *et al*. at an ICORS conference reported resonance enhancement of the peaks in Sudan I at 1234 and 1598 cm^{-1} when using a 632.8 nm laser.[8] This feature is supported by our calculations, which just show contribution to those bands from C–N bending and stretching modes in the hydrazo chromophore group. The RR effects in Sudan I spectra have systematically been investigated by Munro *et al.*[11] in the range 1180–1618 cm^{-1}. Using different laser wavelengths from 501 to 613 nm, they observed that a 501 nm green laser line gave the strongest RR effect in this region of the spectra.[11] According to their calculations, which were based on the low level semiempirical PM3 method, the vibrations in this part of the spectrum were mostly due to isolated C–C vibration modes, whereas our calculations show rather significant contributions from C–C–N bendings as well as C–N and N═N stretchings in this region. Additional peaks below 1100 cm^{-1} were also amplified because of RR effects when using a 613 nm laser.

The spectrum of Sudan I in olive oil measured with the 532 nm laser clearly showed an enhancement of several orders of magnitude for the intensity of the bands at 721, 616, 463 and 218 cm^{-1}. In Fig. 4(f)–(h), three diagrams of the corresponding calculated modes can be seen (modes 23, 16 and 7), and it is obvious that they all involve extended bending of the C–N–N–C skeleton. Though overtones and progressions could not be found (perhaps due to overlaps with more intense bands), it still is an indication of a RR effect arising from these vibrations. The resonance at these wavenumbers has a potential use as a means to distinguish Sudan I from other azo dyes because this RR pattern is likely to be unique. A procedure involving different laser wavelengths could supply a unique fingerprint for Sudan I due to its specific resonance enhancement at lower wavenumbers, as used widely in the pharmaceutical industry.[25] Also, we believe that this, in combination with the results of Cheung *et al*.,[12] indicates that SERRS with different excitation wavelengths in the fingerprint region, can indeed provide a useful technique for the detection of Sudan I in foodstuffs.

Conclusion

Raman spectra of the red dye Sudan I were recorded using infrared (1062 nm), green (532 nm) and UV (244 nm) laser light. The spectra were interpreted by comparison with *ab initio* DFT (RB3LYP) calculated spectra, based on 6-311+G(d,p) Gaussian orbital basis sets in an isolated molecule approach. The vibrations in the region 1600–1000 cm^{-1} were found to comprise various mixed modes including in-plane stretching of C–C bonds. Especially, the large contributions from N═N core stretching and C–N–N bond bending at higher wavenumbers have not been appreciated previously. Below about 900 cm^{-1}, many out-of-plane bending modes were dominant. Low-intensity bands at 721, 616, 463 and 218 cm^{-1} were selectively enhanced by the RR effect, when using

Journal of RAMAN SPECTROSCOPY

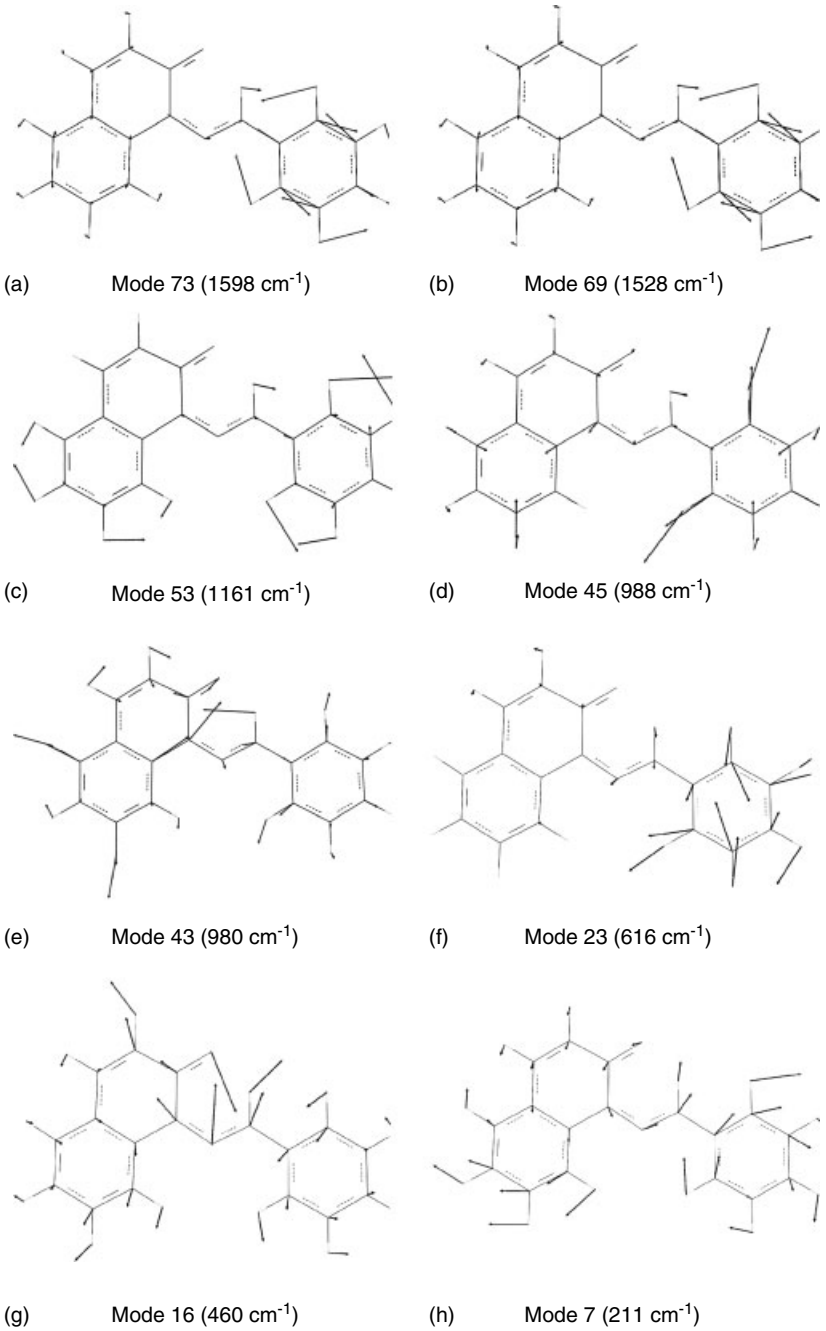

Figure 4. Approximate diagrams of selected vibrations in the hydrazo form of Sudan I. The presented wavenumbers have been corrected with an empirical scaling factor of 0.976[19].

the 532 nm excitation line, relative to those obtained with 1064 or the 244 nm excitation. The spectrum of Sudan I was found to deviate from those of other similar azo dyes, even in the intensive range (1600–1000 cm^{-1}). The spectra of abundant natural food pigments, such as capsanthin and capsorubin showing similar Raman active bands in the same wavenumber range, can be distinguished from those of Sudan I by the spectral differences below 1100 cm^{-1}. The use of differences in the resonance enhancement of various bands (marked with stars in Table 1) with the applied lasers opens up a new sensitive method to detect Sudan I in food based on Raman spectroscopy. Our *ab initio* DFT calculations have indicated that several vibrations in the whole investigated wavenumber range involve bending and stretching modes – at and around the C–N═N–C chromophore – making the molecule obvious for further investigations with SERRS and/or SERS.

Acknowledgements

We would like to thank Lykke Ryelund from University of Copenhagen for help in obtaining the FT-Raman spectra. Udo Jensen at Fødevareregion Øst, Fødevarestyrelsen, Ringsted DK, is thanked for providing the sample of Sudan I. The Danish Agency for Science Technology and Innovation provided a grant (No. 09-065038/FTP) for CL and the UV instrumentation.

References

[1] V. Cornet, Y. Govaert, G. Moens, J. V. Loco, J. J. Degroodt, *J. Agric. Food Chem.* **2006**, *54*, 539.
[2] H. Buchardt, *Dan. Kemi* **2007**, *88*, 28.
[3] P. Møller, H. Wallin, *Mutat. Res. Rev. Mutat. Res.* **2000**, *462*, 13.
[4] M. Stiborova, V. Martinek, H. Rydlova, P. Hodek, E. Frei, *Cancer Res.* **2002**, *62*, 5678.
[5] F. Tateo, M. J. Bononi, *J. Agric. Food Chem.* **2004**, *52*, 655.
[6] F. Puoci, C. Garreffa, F. Iemma, R. Muzzalupo, U. G. Spizzirri, N. Picci, *Food Chem.* **2005**, *93*, 349.
[7] M. Mazzetti, R. Fascioli, I. Mazzoncini, G. Spinelli, I. Morelli, A. Bertoli, *Food Addit. Contam.* **2004**, *21*, 935.
[8] I. T. Shadi, B. Z. Chowdhry, S. A. Leharne, R. Withnall, *ICORS20, 20th International conference on Raman Spectroscopy*, vol. 20 Wiley: Yokohama, Japan, **2006**, pp. 247.
[9] L. S. Zhang, P. X. Zhang, Y. Fang, *J. Colloid Interface Sci.* **2007**, *311*, 502.
[10] X. F. Zhou, Y. Fang, P. X. Zhang, *Spectrochim. Acta, Part A* **2007**, *67*, 122.
[11] C. H. Munro, W. E. Smith, D. R. Armstrong, P. C. White, *J. Phys. Chem.* **1995**, *99*, 879.
[12] W. Cheung, I. T. Shadi, Y. Xu, R. Goodacre, *J. Phys. Chem. C* **2010**, *114*, 7285.
[13] M. I. Minguez-Mosquera, M. Jaren-Galan, J. Garrido-Fernandez, *J. Agric. Food Chem.* **1992**, *40*, 2384.
[14] R. W. Berg, A. Riisager, R. Fehrmann, *J. Phys. Chem. A* **2008**, *112*, 8585.
[15] R. W. Berg, M. Deetlefs, K. Seddon, I. Shim, K. Thompson, *J. Phys. Chem. B* **2005**, *119*, 19018.
[16] M. H. Brooker, R. W. Berg, J. H. von Barner, N. J. Bjerrum, *Inorg. Chem.* **2000**, *39*, 4725.
[17] R. W. Berg, I. M. Ferré, S. C. Schäffer, *J. Vib. Spectrosc.* **2006**, *42*, 346.
[18] M. J. Frisch, H. B. Schlegel, G. E. Scuseria, M. A. Robb, J. R. Cheeseman, J. A. Montgomery Jr, T. Vreven, K. N. Kudin, J. C. Burant, J. M. Millam, S. S. Iyengar, J. Tomasi, V. Barone, B. Mennucci, M. Cossi, G. Scalmani, N. Rega, G. A. Petersson, H. Nakatsuji, M. Hada, M. Ehara, K. Toyota, R. Fukuda, J. Hasegawa, M. Ishida, T. Nakajima, Y. Honda, O. Kitao, H. Nakai, M. Klene, X. Li, J. E. Knox, H. P. Hratchian, J. B. Cross, C. Adamo, J. Jaramillo, R. Gomperts, R. E. Stratmann, O. Yazyev, A. J. Austin, R. Cammi, C. Pomelli, J. W. Ochterski, P. Y. Ayala, K. Morokuma, G. A. Voth, P. Salvador, J. J. Dannenberg, V. G. Zakrzewski, S. Dapprich, A. D. Daniels, M. C. Strain, O. Farkas, D. K. Malick, A. D. Rabuck, K. Raghavachari, J. B. Foresman, J. V. Ortiz, Q. Cui, A. G. Baboul, S. Clifford, J. Cioslowski, B. B. Stefanov, G. Liu, A. Liashenko, P. Piskorz, I. Komaromi, R. L. Martin, D. J. Fox, T. Keith, M. A. Al-Laham, C. Y. Peng, A. Nanayakkara, M. Challacombe, P. M. W. Gill, B. Johnson, W. Chen, M. W. Wong, C. Gonzalez, J. A. Pople, *Gaussian 03 W, Revision E.01*, Gaussian, Inc.: PA, USA, **2006**.
[19] S. Z. Fairchild, C. F. Bradshaw, W. S. Su, S. K. Guharay, *Appl. Spectrosc.* **2009**, *63*, 733.
[20] J. E. Bertie, K. H. Michaelian, *J. Chem. Phys.* **1998**, *109*, 6764.
[21] N. Peica, I. Pavel, S. C. Pinzaru, V. K. Rastogi, W. Kiefer, *J. Raman Spectrosc.* **2005**, *36*, 657.
[22] M. Snehalatha, C. Ravikumar, N. Sekar, V. S. Jayakumar, I. H. Joe, *J. Raman Spectrosc.* **2008**, *39*, 928.
[23] L. C. Abbott, S. N. Batchelor, J. Oakes, B. Gilbert, A. C. Whitwood, J. R. L. Smith, J. N. Moore, *J. Phys. Chem. A* **2005**, *109*, 2894.
[24] A. Requena, J. P. Ceron-Carrasco, A. Bastida, J. Zuniga, B. Miguel, *J. Phys. Chem. A* **2008**, *112*, 4815.
[25] J. A. Zeitler, D. A. Newnham, P. F. Thaday, T. L. Threlfall, R. W. Lancaster, R. W. Berg, C. J. Strachan, M. Pepper, K. C. Gordon, T. Rades, *J. Pharm. Sci.* **2006**, *95*, 2486.

Publications made during the Ph.D project:

(1) ***Determining the Spectral Resolution of CCD Raman Instruments***, Chuan Liu and Rolf W. Berg, Applied Spectroscopy, Accepted.

(2) ***Experimental and ab initio DFT calculated Raman Spectrum of Sudan I, a Red Dye***, Andreas Jonas Kunov-Kruse, Steffen Buus Kristensen, Chuan Liu and Rolf W. Berg, Journal of Raman Spectroscopy, vol: 42, issue: 6, (**2011**), p. 1470-1478,

(3) ***Formation and characterization of varied size germanium nanocrystals by electron microscopy, Raman spectroscopy, and photoluminescence***, Haiyan Ou, Yiyu Ou, Chuan Liu, Rolf W. Berg and Karsten Rottwitt, Optical Materials Express, vol: 1, issue: 4, (**2011**), p. 643-651.

(4) ***Donor-acceptor-pair emission characterization in N-B dopedfluorescent SiC***, Yiyu Ou,Valdas Jokubavicius, Satoshi Kamiyama, Chuan Liu, Rolf W. Berg, Margareta Linnarsson, Rositza Yakimova, and Haiyan Ou, Optical Materials Express, Vol: 1, Issue 8, (**2011**), p. 1440-1446.

(5) ***Size-effect of germanium nanocrystals***, Haiyan Ou, Yiyu Ou, Chuan Liu, Rolf W. Berg and Karsten Rottwitt, Proceedings of CLEO, Optical Society of America, **2011**, Baltimore, USA.

(6) ***Photoluminescence and Raman spectroscopy characterization of boron- and nitrogen-doped 6H silicon carbide***, Ou, Yiyu; Jokubavicius, Valdas; Liu, Chuan; Berg, Rolf W.; Linnarsson, Margareta; Kamiyama, Satoshi; Lu, Zhaoyue; Yakimova, Rositza; Syväjärvi, Mikael ; Ou, Haiyan, Proceedings of ICSCRM, **2011**, Cleveland, Ohio, USA.